Pacific Northwest
NATIONAL LABORATORY

PNNL-29650

Evaluation of the Change in Uranium Mobility in Sediments from the Hanford 300-FF-5 Stage B Polyphosphate Field Injection

January 2020

JE Szecsody
HP Emerson
RD Mackley
CT Resch
BN Gartman
CI Pearce
SA Saslow
O Qafoku
KA Rod
MK Nims
SR Baum
II Leavy

U.S. DEPARTMENT OF ENERGY

Prepared for the U.S. Department of Energy
under Contract DE-AC05-76RL01830

PACIFIC NORTHWEST NATIONAL LABORATORY
operated by
BATTELLE
for the
UNITED STATES DEPARTMENT OF ENERGY
under Contract DE-AC05-76RL01830

Printed in the United States of America

Available to DOE and DOE contractors from the
Office of Scientific and Technical Information,
P.O. Box 62, Oak Ridge, TN 37831-0062;
ph: (865) 576-8401
fax: (865) 576-5728
email: reports@adonis.osti.gov

Available to the public from the National Technical Information Service
5301 Shawnee Rd., Alexandria, VA 22312
ph: (800) 553-NTIS (6847)
email: orders@ntis.gov <https://www.ntis.gov/about>
Online ordering: http://www.ntis.gov

PNNL-29650

Evaluation of the Change in Uranium Mobility in Sediments from the Hanford 300-FF-5 Stage B Polyphosphate Field Injection

January 2020

JE Szecsody
HP Emerson
RD Mackley
CT Resch
BN Gartman
CI Pearce
SA Saslow
O Qafoku
KA Rod
MK Nims
SR Baum
II Leavy

Prepared for
the U.S. Department of Energy
under Contract DE-AC05-76RL01830

Pacific Northwest National Laboratory
Richland, Washington 99354

Summary

The purpose of this study was to evaluate the change in uranium mobility in the periodically re-wetted zone (PRZ) and upper unconfined aquifer of the Hanford Site's 300-FF-5 operable unit as a result of Stage B polyphosphate (PO_4) injections. These 300 Area sediments are beneath or near the former North Process Pond, which has previously been shown to contain metatorbernite [$Cu(UO_2)_2(PO_4)_2 \bullet 8H_2O$] and uranophane [$Ca(UO_2)_2(SiO_3OH)_2 \bullet 5H_2O$], along with aqueous and adsorbed uranium (U), and small amounts of U in calcite as a result of acidic disposal with a significant number of co-contaminants. Previous laboratory-scale studies have identified multiple mechanisms that decrease uranium mobility with polyphosphate injection: (a) precipitation of a low-solubility uranium-phosphate mineral (autunite); (b) precipitation of a Ca-phosphate solid that incorporates U; (c) precipitation of Ca-phosphate mineral (apatite group minerals) that coats existing uranium phases (i.e., U in calcite, U in Fe-oxides), reducing uranium leaching; and (d) aqueous Ca-U-carbonate species adsorption onto apatite.[1,2,3,4] Given the significant amount of apatite precipitation, other U phases such as carbonates could also coprecipitate with apatite. To quantify differences in solubility, leachability, and phases of uranium between pre- and post-PO_4-treated sediments, different types of analyses were conducted, including analysis of uranium in (a) a carbonate solution extraction from sediment over 1000 h (41.67 days), (b) six sequential liquid extractions from sediment over approximately 1 week, (c) leaching of uranium from sediments in one dimensional (1-D) column experiments over 2 months, and (d) solid phase characterization of select sediments. An additional extraction and solid phase measurements were conducted to evaluate phosphate precipitate formation. Metals were also analyzed in sequential liquid extractions as indicators of (a) amendment injection delivery, (b) co-contaminant movement, and (c) changes in solid phases. Aqueous and solid phase carbonate measurements were also conducted to evaluate changes in carbonates.

One-dimensional column leach and batch carbonate extractions were designed to estimate total U mobility in sediments before and after treatment. Uranium mobility measured in 1-D leach experiments showed a 58.9 ± 53.2% (n=26, ± one standard deviation) decrease in uranium leaching, as defined by the fraction leached, after treatment. Of the 10 pre-/post-injection sample pairs (for which column leaching experiments were conducted), 9 pairs showed a decrease in uranium leaching for the post-injection experiment, and 1 pair with low PO_4 treatment showed an increase. In a separate measure of potential uranium mobility, a 1000-h batch extraction using a carbonate solution was conducted on 44 sediments including 19 pre-/post-injection sample pairs and four un-paired post-treatment samples. The mobile (labile) fraction of uranium for pre-injection sediments was 0.425 ± 0.096, and for post-injection samples was 0.156 ± 0.143, or an average of 63 ± 46% less mobile U (per carbonate extractions) as a result of the polyphosphate treatment. The pre- and post- treatment fraction was statistically different based on the

---

[1] Wellman DM, JP Icenhower, and AT Owen. 2006. "Comparative Analysis of Soluble Phosphate Amendments for the Remediation of Heavy Metal Contaminants: Effect on Sediment Hydraulic Conductivity." *Environmental Chemistry* 3:219–224.

[2] Wellman DM, EM Pierce, DH Bacon, M Oostrom, KM Gunderson, SM Webb, CC Bovaird, EA Cordova, ET Clayton, KE Parker, RM Ermi, SR Baum, VR Vermeul, and JS Fruchter. 2008. *300 Area Treatability Test: Laboratory Development of Polyphosphate Remediation Technology for in Situ Treatment of Uranium Contamination in the Vadose Zone and Capillary Fringe*. PNNL-17818, Pacific Northwest National Laboratory, Richland, WA.

[3] Mehta VS F Mailot, Z Wang, JG Catalono, and DE Giammar. 2016. "Effect of reaction pathway on the extent and mechanism of uranium(VI) immobilization with calcium and phosphate." *Environmental Science and Technology* 50:3128-3136.

[4] Lammers L, H Rasmussen, D Adilman, J deLemos, P Zeeb, D Larson, and A Quicksall. 2017. "Groundwater uranium stabilization by a metastable hydroxyapatite." *Applied Geochemistry*, 84:105-113.

Tukey method (95% confidence, $p = 1 \times 10^{-7}$).[1] Phosphate analysis of 19 post-injection sediments that were collected within 3.61 ft (1.1 m) of pre-injection sediments at the same depth showed a consistent increase in phosphate precipitates in the post-injection sediments, average increase 183 ± 132 µg/g (as P in sequential extraction 5). There was a trend between the mass of phosphate precipitates in post-injection sediments and the decrease in uranium mobility in post-injection sediments based on both 1-D leach experiments and 1000-h batch extraction. Based on extractions 6 months after injection, three of the locations show little precipitated phosphate, which accounts for the minimal change in uranium leaching in select pre- and post-injection sample pairs from those locations.

Six sequential liquid extractions were also used to quantify differences in leachable uranium in pre- and post-injection samples and to quantify changes in low- and high-solubility uranium precipitates. These experiments are similar to 1-D column leach and batch carbonate extractions, but they are based on operationally defined extraction solutions of increasing ability to remove U, allowing for binning of solid-phase U into categories of varying mobility. Results of these extractions on 19 pre- and post-injection sediments showed that the most mobile uranium (i.e., aqueous and adsorbed, extractions 1 and 2) decreased from 6.7% to 3.4% (of the total extracted U), high-solubility U minerals decreased from 58.6% to 37.2% (extractions 3 and 4), and low-solubility U minerals increased from 34.8% to 54.3% (extracts 5 and 6) as a result of the phosphate injections. Separate batch experiments with reference mineral phases showed that uranophane, Na-boltwoodite ($Na_2(UO_2)SiO_4 \cdot 1.5H_2O$), and U substituted calcite ($CaCO_3$) are high-solubility U minerals (extractions 1-4), and autunite and torbernite are low-solubility minerals (extractions 5-6). Additional analysis of the inorganic carbon content of sediments showed little calcite (<0.04% for 11 sediments analyzed). Therefore, it is hypothesized that the decrease in high-solubility U minerals from pre- to post-injection sediments (58.6% to 37.2%) was due to dissolution of uranophane or Na-boltwoodite. It is also hypothesized that the large increase in low-solubility U minerals (extraction 6) may be due to (a) precipitation of autunite, (b) apatite coating existing U surface phases, or (c) other U phases (i.e., U carbonates) coprecipitating with apatite. Phosphate extractions show that a significant mass of apatite does precipitate from the polyphosphate solution injection into sediments. Solid phase analysis suggests that there is (a) metatorbernite in pre- and post-injection sediments and (b) significant phosphate precipitates in post-injection sediments. Although some of the aforementioned mechanisms that decrease U mobility are not explicitly identified through extractions; the combination of surface phase analysis, modeling, and the comparison of pre- and post-injection sediments showed a decrease in mobility of uranium (~60%) due to the injected polyphosphate, as demonstrated by 1-D column leach experiments, 1000-h uranium batch extractions, and a series of six liquid extractions.

---

[1] Berthouex PM and LC Brown. 1994. “Multiple Paired Comparisons of k Averages,” in *Statistics for Environmental Engineers*. CRC Press, Boca Raton, FL. p. 123-128.

Acknowledgments

We would like to thank CHPRC and Intera scientists Virginia Rohay, Ryan Nell, Sunil Mehta, Sarah Springer, Elyse Frohling, and Sylvana Bendana for their thoughtful review comments and recommendations, and Matt Wilburn for editing to make this report a more useful document.

Acronyms and Abbreviations

Φ	porosity
μ	gravimetric moisture content
μ-EXAFS	micro extended X-ray absorption fine structure
μ-XANES	micro X-ray absorption near-edge spectroscopy
μ-XRF	micro X-ray fluorescence
1-D	one-dimensional
2-D	two-dimensional
andersonite	$Na_2Ca(UO_2)(CO_3)_3 \bullet 6H_2O$
apatite	a low solubility Ca-phosphate mineral group, $Ca_{10}(PO_4)_6(OH, F, Cl)_2$, with hydroxyapatite [$Ca_{10}(PO_4)_6(OH)_2$] as an end member. Apatite mineral group minerals are referred to generally as apatite in this report.
APS	Advanced Photon Source
autunite	$Ca(UO_2)_2(PO_4)_2 \bullet 10\text{-}12H_2O$
BD	dry bulk density
BGS	below ground surface
Na-boltwoodite	$Na_2(UO_2)SiO_4 \bullet 1.5H_2O$
BSE	backscatter electron
CHPRC	CH2M Hill Plateau Remediation Company
DI	deionized
EDS	energy dispersive detector on SEM
EMP	electron microprobe with elemental detector
ESL	Environmental Sciences Laboratory
EXAFS	extended X-ray absorption structure
FIO	for information only
grimselite	$K_3Na(UO_2)(CO_3)_3 \bullet H_2O$
GWB	Geochemist Work Bench - a geochemical equilibrium model
HASQARD	Hanford Analytical Services Quality Assurance Requirements Document
HEIS	Hanford Environmental Information System
ICP-MS	inductively coupled plasma mass spectrometry
ICP-OES	inductively coupled plasma optical emission spectroscopy
K_d	solid to liquid partitioning coefficient
KPA	kinetic phosphorescence analysis
LCF	linear combination fitting
LIFS	laser induced fluorescence spectroscopy
MDL	minimum detection limit
meta-autunite	$Ca(UO_2)_2(PO_4)_2 \bullet 2\text{-}6H_2O$
metatorbernite	$Cu(UO_2)_2(PO_4)_2 \bullet 8H_2O$
monocalcium phosphate	$Ca(H_2PO_4)_2$
NPP	North Process Pond

PHREEQC	a geochemical modeling tool developed by the U.S. Geological Survey
PNNL	Pacific Northwest National Laboratory
PV	pore volume
PRZ	periodically re-wetted zone
QA	quality assurance
SI	saturation index
SEM-EDS	scanning electron microscopy with energy dispersive spectroscopy detector
SPP	South Process Pond
torbernite	$Cu(UO_2)_2(PO_4)_2•8\text{-}12H_2O$
uranophane	$Ca(UO_2)_2(HSiO_4)_2•5H_2O$
USGS	U. S. Geological Survey
vanadate	U-VO_4 mineral phases, e.g. tyuyamunite $Ca(UO_2)_2(VO_4)_2•5\text{-}8H_2O$ and carnotite $K_2(UO_2)_2(VO_4)_2•3H_2O$
XANES	X-ray near edge structure
XAS	X-ray absorption-spectroscopy
XRD	X-ray diffraction
XRF	X-ray fluorescence

Contents

Figures

Tables

1.0 Introduction

The purpose of this study is to evaluate the changes in uranium mobility in the periodically re-wetted zone (PRZ) and upper portion of the unconfined aquifer of the Hanford Site's 300-FF-5 operable unit as a result of polyphosphate solution injections. The low-to-moderate concentration of uranium in 300 Area subsurface sediments is present as aqueous and adsorbed uranium species and multiple precipitates, including hydroxides, silicates, phosphates, carbonates, and U substituted in calcite and Fe oxides (see Section 2.0 for greater detail).

Previous laboratory-scale studies identified multiple mechanisms that decrease uranium mobility: (a) precipitation of low-solubility uranium-phosphate minerals (e.g., autunite); (b) precipitation of Ca-phosphate minerals (e.g., apatite) that structurally incorporate U; (c) precipitation of Ca-phosphate minerals that coat existing uranium phases (i.e., U in calcite, U in Fe-oxides) and reduce uranium leaching; and (d) adsorption of aqueous Ca-U-carbonate species onto apatite (Wellman et al. 2006, 2008a-c; Mehta et al. 2016; Lammers et al. 2017). Given the significant amount of apatite precipitation, other U phases such as carbonates could also coprecipitate with apatite. In addition, over time, apatite is expected to continue to be a source of phosphate, allowing for additional autunite group mineral formation (shown in Figure 1.1). These changes in uranium mobility can be characterized by methods that quantify the functional ability to remove uranium from sediments (e.g., liquid extractions and 1-D leach experiments) and by direct identification of uranium phases that have differing solubility (and mobility).

For this study, sediment samples from six boreholes were taken prior to field injections and uranium mobility was compared to samples taken from nine post-injection boreholes. Uranium mobility was evaluated through (a) batch sequential liquid extractions, (b) 1000-h carbonate batch leach extraction, (c) 1-D column leach testing, and (d) solid phase characterization, as described in detail in Section 2.0. Additional extractions were conducted to evaluate the phosphate precipitate in sediments. Metals were also analyzed in sequential liquid extractions as indicators of (a) amendment injection delivery, (b) co-contaminant movement, and (c) changes in solid phases.

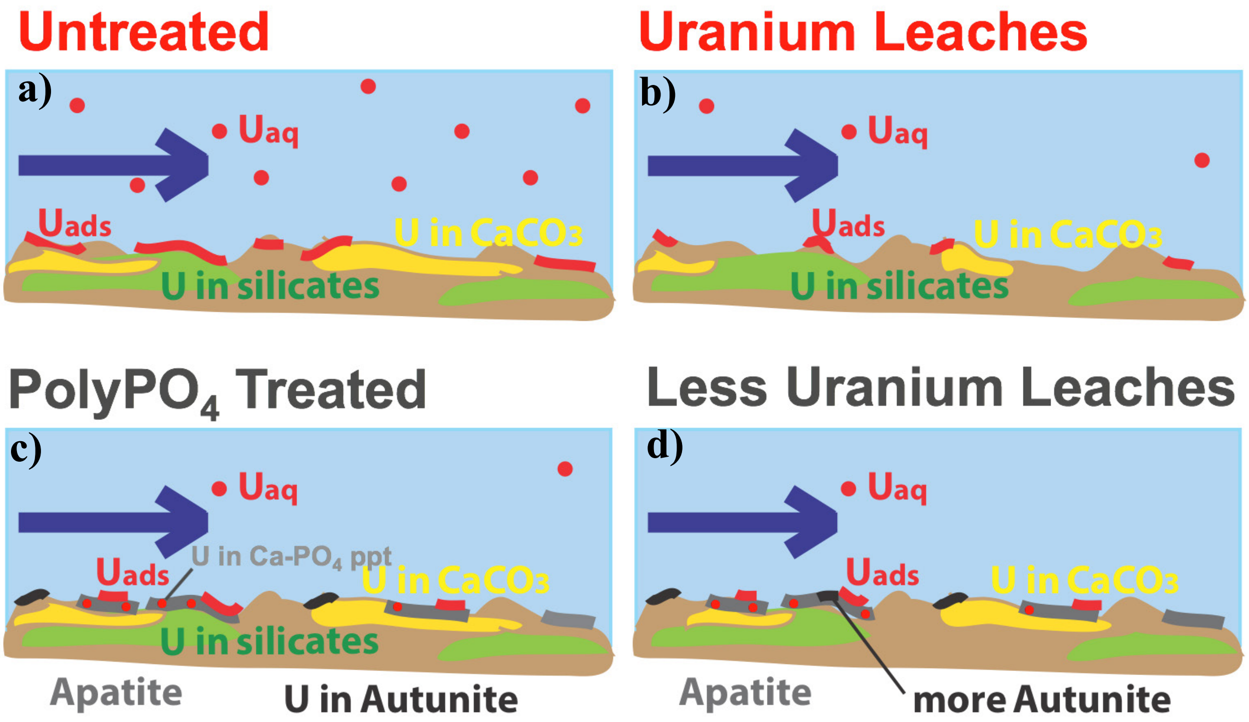

Figure 1.1. Mechanisms for change in uranium mobility with the addition of a polyphosphate solution to sediments where *red* represents potentially mobile aqueous (U_{aq}) and adsorbed (U_{ads}) U; *yellow* and *green* represent soluble U-carbonate and U-silicate (e.g., Na-boltwoodite) species, respectively; *black* represents sparingly soluble autunite (U-phosphate) group minerals; and *gray* represents phosphate precipitates that can incorporate U (e.g., apatite [Ca-phosphate]) that may (i) coat other U phases, (ii) increase available U sorption sites, and (iii) release additional phosphate to promote autunite formation, further decreasing U mobility.

2.0 Background and Objectives

Natural (< 1.5 µg/g) and anthropogenic (up to 150 µg/g) uranium is present in Hanford 300 Area subsurface sediments as aqueous and adsorbed uranium species, and in a variety of minerals that differ significantly in solubility (i.e., leachability) (Zachara et al. 2007). Aqueous uranium is present in the +6 valence state (U^{IV} is only sparingly present in some minerals) primarily as anionic or neutrally-charged Ca-uranyl (UO_2^{2+})-carbonate species: $Ca_2UO_2(CO_3)_3$ (aq), $CaUO_2(CO_3)_3^{2-}$ (and to a lesser extent Mg equivalent phases), with smaller concentrations of $(UO_2)_2CO_3(OH)_3^-$ and $UO_2(CO_3)_2^{2-}$. Anionic Ca-uranyl-carbonate species dominate at a pH > 8, and neutrally charged species dominate at a pH of 7 to 8 (Figure 2.1a).

The U^{VI} sorption distribution coefficient (sorbed U concentration in µg/g divided by U concentration in aqueous solution in µg/mL, K_d) in 300 Area sediments averages 0.8 mL/g (range 0.2 to 4.0; Zachara et al. 2007), with $K_d < 0.2$ for Ringold Formation gravels and K_d ranging from 1.8 to 4.2 mL/g for the Ringold lower mud. For 300 Area sediments, the uranium desorption K_d averages 8.0 ± 8.3 (n = 17; Zachara et al. 2007) for < 2-mm size fraction, in groundwater. Moreover, desorption K_d values are higher due to sorption not being completely reversible. Characterization of sediments in and under the 300 Area North Process Pond (NPP), under which a portion of the Stage B injections occurred, has identified the existence of metatorbernite [$Cu(UO_2)_2(PO_4)_2{\cdot}8H_2O$], uranophane [$Ca(UO_2)_2(SiO_3OH)_2{\bullet}5(H_2O)$], and adsorbed U (Wang et al. 2005; Arai et al. 2007; Zachara et al. 2007).

The historical 300 Area liquid waste disposal operations were active from 1945 until 1975 (Gerber 1993). The main process pond or South Process Pond (SPP), built in 1945, was active until 1948 and received approximately 11 tons (9.98×10^3 kg) of U. The pH of waste disposed of in the 300 Area ranged from 2 to 11, and infiltration of acidic water likely dissolved some to all of the calcite (and U substituted in calcite) in sediments, depending on the infiltration rate and acid neutralization capacity of the sediment (Szecsody et al. 2013; Wang et al. 2005). As such, in these highly contaminated sediments, U was not observed to be associated with calcite (Arai et al. 2007). In 1948, disposal cribs (300 North Cribs or 316-4 Crib, adjacent to the 618-10 burial ground) were built approximately 5 miles north of the 300 Area with two inverted tanks above gravel and substrata as well as a NPP north of the SPP. The North Cribs were active until 1956 and received approximately 2070 pounds (939 kg) of U. A total of 30 tons (2.7×10^4 kg) of U was disposed of in the NPP, along with 50 tons (4.5×10^4 kg) of Cu, 800 tons (7.26×10^5 kg) of nitrate, 900 tons (8.16×10^5 kg) of nitric acid, 800 tons (7.26×10^5 kg) of NaOH, and 2000 tons (1.81×10^6 kg) of sodium aluminate (Gerber 1993; Wang et al. 2005; Arai et al. 2007). In 1955, the NPP was dredged to remove approximately 10,300 pounds (4.67×10^3 kg) of U (Gerber 1993). However, in 1975, two 300 Area process trenches were constructed on a north-south axis just northwest of the NPP (as shown in Figure 3.1) near Stage A and B poly-phosphate injection zones.

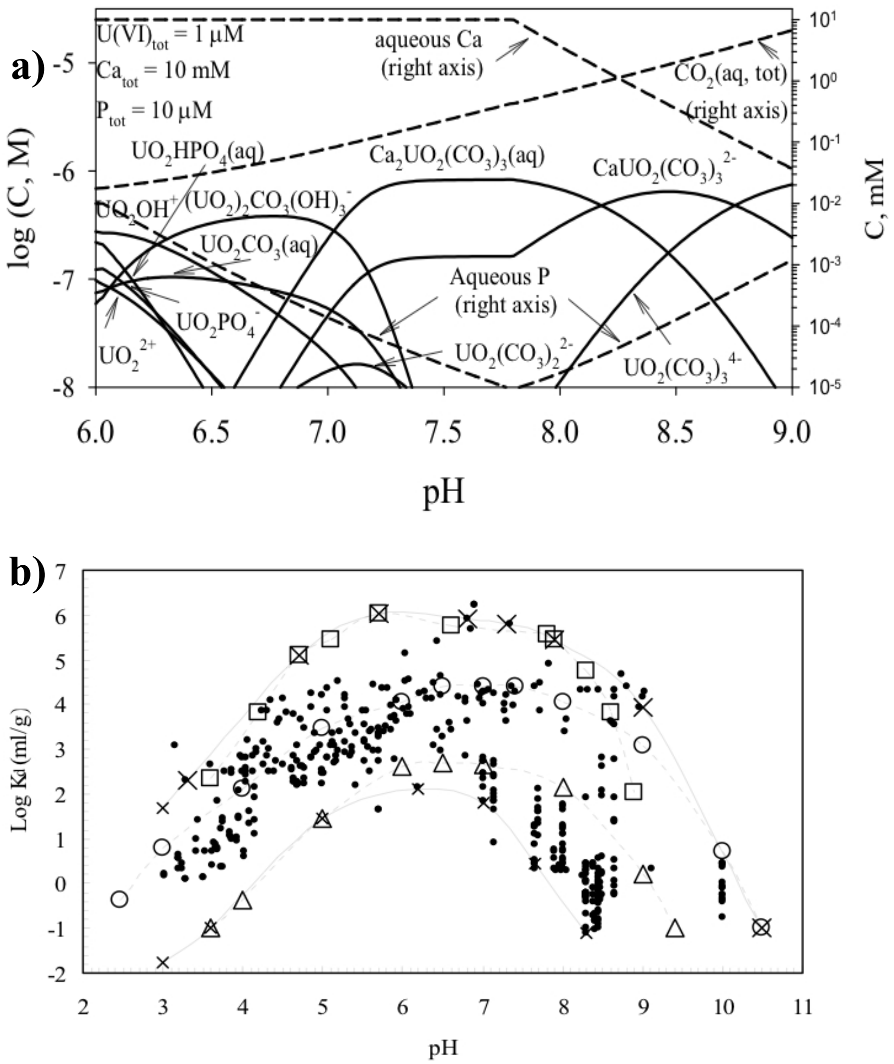

Figure 2.1. (a) Aqueous U^{VI} speciation in the presence of Ca, P, and CO_3 as log concentration (mol/L) versus pH, and (b)- U^{VI} adsorption to sediments (*dots*), ferrihydrite (*open squares*), kaolinite (*open circles*), and quartz (*triangles*) as log K_d versus pH (Zachara et al. 2007; Waite et al. 1994).

The polyphosphate solution injected into 48 wells in the 300-FF-5 Stage B area consisted of 87 mM total phosphate (target concentration) that was 90% orthophosphate and 10% pyrophosphate or 78.4 mM Na, K-phosphate and 4.1 mM Na-pyrophosphate (i.e., dissociates into 8.2 mM PO_4 at a pH of ~7.5, see Appendix F, Table F.1 for targeted and actual injection concentrations of major elements) (Wellman et al. 2008a-c). The Na^+ and K^+ concentrations were ~106 and ~47 mM, respectively. The solution was mixed from concentrated phosphoric acid, NaOH, KOH, and sodium pyrophosphate to have a final pH of 7.5 to 7.7. The cations in the injected solution were 67% sodium and 33% potassium (Wellman et al. 2008a-b). The pyrophosphate does not precipitate initially, but over weeks it hydrolyzes into orthophosphate. After initial precipitation of amorphous monocalcium phosphate, recrystallization occurs, forming di- to octa-calcium phosphate, and eventually hydroxyapatite (Sumner 2000) over periods of months to years. This slow transformation uses a greater proportion of calcium compared to the initial amorphous precipitate (hydroxyapatite, $Ca_{10}(PO_4)_6(OH)_2$, Ca:P = 1.67).

As the polyphosphate solution reacts with in situ aqueous and adsorbed calcium, amorphous Ca-phosphate and autunite [$Ca(U^{VI}O_2)_2(PO_4)_2{\cdot}6H_2O$] precipitate over time using aqueous and adsorbed Ca^{2+} and possibly some from dissolving calcite (if any). Uranium sequestration occurs by a combination of mechanisms including formation of autunite, aqueous uranium species sorption to apatite, and apatite coating of existing uranium surface phases (Figure 1.1). Apatite precipitation occurs with the polyphosphate solution, as confirmed in previous experimental studies and through thermodynamic modeling. Autunite formation has also been shown to occur experimentally at high U and PO_4 concentrations where surface phase analysis was possible (Wellman et al. 2008b; Lammers et al. 2017). Thermodynamic modeling can be used in this study to define the geochemical conditions in which autunite precipitation is favored in different field conditions (Section 4.4.3). Initially, two effects occur as a result of the polyphosphate solution injection and compete with U removal from solution by precipitation and/or adsorption: (i) the higher ionic strength of the injected solution relative to groundwater causes some uranium desorption (short time scale, days); and (ii) the pH decrease from Ca-phosphate precipitation results in a decrease in uranium sorption (Figure 2.1). The effect of a higher ionic strength injection solution on uranium species desorption was shown in a previous study comparing uranium leaching in untreated sediments with groundwater (average 7.9 ± 1.8% of U leached in the first 7.5 pore volumes) to polyphosphate (average 0.13 ± 0.06% of U leached) to a KNO_3 solution of equivalent ionic strength to polyphosphate solutions (average 4.3% of U leached) (Szecsody et al. 2012). The desorption in KNO_3 further demonstrated that the maximum U concentration was greater in KNO_3 as compared to low ionic strength groundwater and polyphosphate (560 versus 330 and 360 µg/L, respectively). Therefore, while a higher ionic strength solution should cause uranium species to desorb, the precipitation of uranium with phosphate (or coating by Ca-phosphate precipitates) had a larger effect, even at a short (i.e., hours) time scale. As a result, aqueous and desorbed uranium precipitation as autunite group minerals, coating by Ca-phosphate precipitates, and adsorption onto Ca-phosphate are still expected to dominate in the short term under relatively high phosphate conditions.

Copper and phosphate are co-contaminants in the 300 Area subsurface may influence the effectiveness and/or characterization of the polyphosphate injection. Metatorbernite [$Cu(UO_2)_2(PO_4)_2{\cdot}8H_2O$] has previously been identified in sediments, which is a low-solubility copper uranium precipitate (Arai et al. 2007; McKinley et al. 2007).

To characterize the change in uranium mobility in pre- and post-phosphate injection sediments, different types of analyses were conducted on sediment samples, which included the following:

- **Sequential extractions for uranium and other metals.** Sequential extractions were used to determine the percentage of uranium present in labile phases (aqueous and adsorbed uranium) and in more difficult-to-extract phases as described in Last et al. (2016). Sequential extractions were conducted on 19 pre- and 25 post-injection sediments (with 6 additional duplicate samples) as specified in Section 3.0. Each extraction solution was analyzed for uranium, phosphate, and metals used as geochemical indicators (e.g., calcium, aluminum, iron, and manganese) as specified in Section 3.0. Because there should be a correlation between the change in uranium mobility and phosphate concentration, an additional, separate phosphate extraction was conducted in pre- and post-injection sediments. Since phosphate is present naturally in sediment, and additionally from co-contaminant precipitates, extractable phosphate in pre-injection sediments was subtracted from extractable phosphate in post-injection sediments (from the same paired boreholes and depth) to quantify the mass of aqueous, adsorbed, and solid phase phosphate precipitated as a result of the injections. Changes in extracted uranium in one of the sequential liquid extractions (acetic acid at pH 2.3) suggested dissolution of carbonates, and thus selected sediments were characterized by solid phase inorganic carbon analysis.
- **1000-hour labile uranium batch leach test.** The labile uranium batch leach test is a measure of readily leachable uranium using the method of Kohler et al. (2004). Dissolved uranium concentration

is measured after a 1000-h contact time of the sediment sample with a specified carbonate solution. This 1000-h labile uranium test was conducted on 19 pre- and 25 post-injection sediments with 6 additional duplicates.

- **1-D flow-through column leach tests.** Flow-through column leach tests were performed on the full grain size distribution of sediments (fraction gravel was packed with < 12.5-mm size gravel) to quantify mass of uranium leaching from sediments over time (100 pore volumes, 2 months) and to quantify the uranium release rate from sediments using stop-flow events at selected times during the leach test (i.e., ~ 2, 15, and 100 pore volumes). These 1-D column leach tests were conducted on 10 pre- and 14 post-injection sediments with two additional duplicate experiments. Although uranium is present in multiple phases in the sediment (i.e., aqueous, adsorbed, associated with carbonates, phosphates, silicates, Fe oxides), the uranium release rate at 2 pore volumes most likely occurs during the time period when uranium is desorbing from sediments, and thus represents a uranium desorption rate. By tens of pore volumes, most aqueous and adsorbed uranium has been advected out of the sediment column; thus, the uranium release rate at 15 pore volumes likely represents the dissolution rate of high-solubility minerals that may contain uranium, such as calcite and iron oxides. By 100 pore volumes, a large fraction of high-solubility minerals has been dissolved and the remaining uranium in the sediment is incorporated into low-solubility minerals. Therefore, the uranium release rate at 100 pore volumes represents a long-term uranium release rate from the sediment. These 1-D column tests also included injection of a bromide tracer to evaluate transport characteristics in the column (i.e., breakthrough time and dispersion). All effluent samples were analyzed for U by kinetic phosphorescence analysis (KPA), U by inductively coupled plasma optical emission spectroscopy (ICP-OES) (selected samples, for confirmation), pH, specific conductivity, and selected effluent samples were analyzed for aqueous phosphate.
- **Uranium solid phase characterization**. Although direct identification of the formation of autunite group minerals [e.g., $Ca(U^{VI}O_2)_2(PO_4)_2 \cdot 6(H_2O)$] or Ca-phosphate coatings on existing uranium precipitates provides the best evidence of mechanisms that decrease uranium mobility, solid phase characterization techniques are limited by the low uranium concentrations in sediments. For the 300-FF-5 Stage B pre- and post-injection sediments, the total uranium concentration ranged from 0.3 to 140 µg/g, so only specific techniques were possible. Uranium phases for both pre- and post-injection sediments were quantified at the Advanced Photon Source (APS) at Argonne National Laboratory using micro X-ray fluorescence (µ-XRF), micro extended X-ray absorption structure (µ-EXAFS), and X-ray near edge structure (µ-XANES, for U valence state). The µ-XRF was also used to identify some associated elements present in uranium precipitates. A scanning electron microscope (SEM) at Pacific Northwest National Laboratory (PNNL) was additionally used on the same sediment thin sections to quantify additional elements (i.e., P, Ca, C, Cu, Fe) to provide better insight into the likely phases with which uranium was associated.

3.0 Experimental Methods

Laboratory experiments were conducted on pre- and post-injection sediments to characterize total uranium, fraction of highly and partially mobile uranium, uranium solid phases, phosphate, and metals in the sediment, as described in Table 3.1. The total uranium and uranium in varying mobility states was characterized using sequential liquid extractions on 19 pre- and 25 post-injection samples with 6 additional duplicates (Section 3.2) that also included analysis of 33 metals (measured by ICP-OES, Section 3.8.2). A separate extraction that used a carbonate solution in a 1000-h batch experiment was also conducted on 19 pre- and 25 post-injection samples with 6 additional duplicates to quantify the mass of labile uranium (Section 3.3).

Leaching of groundwater through sediments to quantify mobile uranium in a 1-D column system is an idealized representation of groundwater flow through sediments at field scale and was used to quantify the mass and rate of uranium release from sediments at different stages of leaching. These 1-D leach experiments were conducted on 10 pre- and 14 post-injection sediments with two additional duplicates (Section 3.7). Sequential extractions were conducted on selected sediments after the 1-D leach experiments to evaluate the lability of the remaining uranium. The aqueous uranium concentration in batch extractions and 1-D leach experiments was measured by KPA (Section 3.8.1), with selected samples analyzed by ICP-OES for confirmation (Section 3.8.2). Sediment grain size distribution analysis was also conducted on the 26 sediments used in 1-D column leach studies (Section 3.10). Solid phase inorganic carbon analysis was conducted on selected pre- and post-injection sediment pairs to evaluate the potential of carbonate dissolution by the polyphosphate injection solution (Section 3.6). Uranium solid phases were characterized in selected pre- and post-injection sediments by µ-XRF, µ-XANES, µ-EXAFS, and elemental analysis on a scanning electron microscope (Section 3.9). Finally, to quantify the mass of precipitated phosphate in sediments, 61 phosphate extractions were conducted on pre- and post-injection sediments (Section 3.5). These separate phosphate precipitate extractions were compared to phosphate measured during sequential extractions (Section 3.2), which estimated aqueous, adsorbed, and precipitated phosphate.

3.1 Sediments Analyzed in Pre- and Post-Injection Boreholes

PNNL and CH2M Hill Plateau Remediation Company (CHPRC) jointly selected samples for testing from six pre-injection boreholes and nine post-injection boreholes (Table 3.1, Figure 3.1). The sediment samples were all loose samples (not cores) that were the full grain size distribution of a 2.5 ft vertical interval. There are six pre-/post-injection borehole pairs that are within 3.61 ft (1.1 m) of each other: C9683/C9732, C9673/C9728, C9667/C9729, C9647/C9733, C9646/C9731, and C9677/C9730. Unpaired post-injection boreholes are C9734, C9735, and C9736. Distances between post-injection boreholes and pre-injection boreholes and the nearest three injection wells are given in Table 3.2. The post-injection boreholes were drilled approximately 6 months after Stage B injections to allow the polyphosphate solution to precipitate initially as amorphous Ca-phosphate/Ca-uranyl-phosphate and crystallize into apatite [$Ca_{10}(PO_4)_6(OH)_2$] and autunite [$Ca(UO_2)_2(PO_4)_2 \cdot 10H_2O$]. The time between the last injection and the start of different laboratory experiments was 6.5 to 6.9 months.

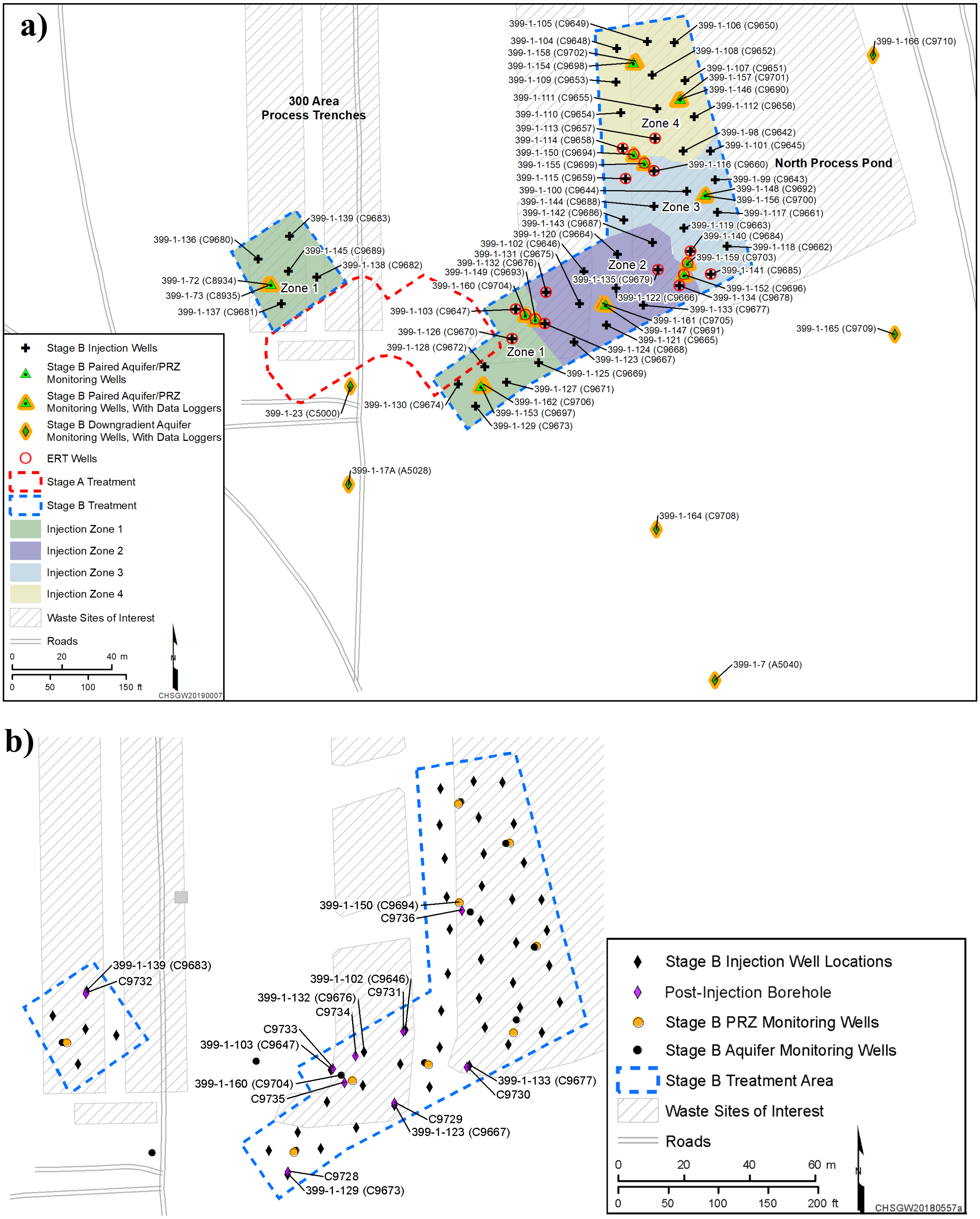

Figure 3.1. Location of Stage B pre-injection boreholes and injection wells (a) and paired pre-injection (*black diamonds*) and post-injection boreholes (*purple diamonds*) sampled for laboratory experiments (b).

Table 3.1. Analysis conducted on 300-FF-5 Area pre- and post-injection vadose zone sediments.

Bore Hole	Pre or Post Injection?	Start Depth (ft)	End Depth (ft)	HEIS #(a)	Pre/Post Borehole Pair(b)	1000-h CO_3 Extract PNNL #	Seq. Extract(c) PNNL #	1-D Leach Column(d) PNNL #	PO_4 Extract PNNL #	Post Leach Seq. Extract PNNL#	Inorganic Carbon	Organic Carbon	U Solid Phases
C9683	Pre	20.0	22.5	B389J4	C9732				G28				
	Pre	22.5	25.0	B389J7		G52C	G52	G29	G29				
	Pre	25.0	27.5	B389K0		G53C	G53		G30				
	Pre	27.5	30.0	B389K6					G31, G33				
	Pre	30.0	32.5	B389K9					G32				
C9732	Post	22.5	25.0	B3P2W2	C9683	A118	S118	G118	P118				
	Post	25.0	27.5	B3P2W6		A119	S119		P119				
C9673	Pre	20.0	22.5	B388W1	C9728				G17				
	Pre	22.5	25.0	B388W4					G18				
	Pre	25.0	27.5	B388W7		G45C	G45		G18				
	Pre	27.5	30.0	B388X3		G36C	G46	G20	G20, G22		G20ic	G20oc	
	Pre	30.0	32.5	B388X6		G47C	G47	G21	G21		G21ic	G21oc	G5
C9728	Post	25.0	27.5	B3P2K6	C9673	A111	S111		P111				
	Post	27.5	30.0	B3P2L0		A112	S112	G112	P112		G112ic	G112oc	
	Post	30.0	32.5	B3P2L4		A1113	S113	G113	P113		G113ic	G113oc	G6
C9667	Pre	20.0	22.5	B388M1	C9729				G12				
	Pre	22.5	25.0	B388M4		G41C	G41		G13				
	Pre	25.0	27.5	B388NO		G42C	G42	G14	G14				G3
	Pre	27.5	30.0	B388N6		G43C, G43CD	G43, G43dup		G15				
	Pre	30.0	32.5	B388N9		G44C	G44	G16	G16	G16L	G16ic		
C9729	Post	22.5	25.0	B3P2M2	C9667	A107	S107		P107				
	Post	25.0	27.5	B3P2M6		A108, A128	S108, S128	G108	P108, P128				G4
	Post	27.5	30.0	B3P2N0		A109	S109		P109				
	Post	30.0	32.5	B3P2N4		A110	S110	G110	P110	G110L	G110ic		
C9647	Pre	20.0	22.5	B38B65	C9733				G6				
	Pre	22.5	25.0	B38B71		G39C	G39	G7	G7	G7L		G7oc	
	Pre	25.0	27.5	B38B74					G8				
	Pre	27.5	30.0	B38B77		G40C	G40	G9	G9, G11		G9ic	G9oc	
	Pre	30.0	32.5	B38B83					G10				
C9733	Post	22.5	25.0	B3P2Y2	C9647	A105, A124	S105, S124	G105, G105A	P105, P124	G105L	G105ic	G105oc	
	Post	27.5	30.0	B3P300		A106	S106	G106	P106		G106ic	G106oc	
C9646	Pre	20.0	22.5	B38B35	C9731	G35C	G35		G1				
	Pre	22.5	25.0	B38B38		G36C	G36	G2	G2				
	Pre	25.0	27.5	B38B41		G37C, G37CD	G37, G37dup		G3				
	Pre	27.5	30.0	B38B47		G38C	G38	G4	G4				
	Pre	30.0	32.5	B38B50					G5				
C9731	Post	20.0	22.5	B3P2R8	C9646	A100	S100		P100				
	Post	22.5	25.0	B3P2T2		A101	S101	G101	P101				
	Post	25.0	27.5	B3P2T6		A102, A121	S102, S121		P102, P121				
	Post	27.5	30.0	B3P2VO		A103	S103	G103	P103				
C9677	Pre	20.0	22.5	B38901	C9730	G48C	G48		G23				
	Pre	22.5	25.0	B38907		G49C	G49	G24, G24A	G24				
	Pre	25.0	27.5	B38910		G50C, G50CD	G50, G50 dup		G25				
	Pre	27.5	30.0	B38913		G51C	G51		G26				
	Pre	30.0	32.5	B38919					G27				
C9730	Post	20.0	22.5	B3P2N8	C9677	A114	S114		P114				
	Post	22.5	25.0	B3P2P2		A115	S115	G115	P115				
	Post	25.0	27.5	B3P2P6		A116	S116		P116				
	Post	27.5	30.0	B3P2R0		A117	S117		P117				
C9734	Post	22.5	25.0	B3P312	none	A120	S120		P120				
	Post	27.5	30.0	B3P320	none	A127	S127	G127	P127				
C9735	Post	22.5	25.0	B3P340	none	A122	S122		P122				
	Post	27.5	30.0	B3P340	none	A123	S123	G123	P123		G123ic		
C9736	Post	22.5	25.0	B3P352	none	A125	S125	G125	P125				
	Post	25.0	27.5	B3P356	none	A126	S126	G126	P126	G126L			

(a) HEIS = Hanford Environmental Information System
(b) Pair with pre- and post-borehole sediment analysis
(c) Sequential extractions with uranium and 33 metals analysis
(d) Particle size distribution conducted on sediments used in 1-D column leach

Table 3.2. Distance of post-injection boreholes from the closest three or four pre-injection boreholes.

Post-Inj. Borehole	Pre-Inj. Borehole and/or Injection Well	Distance (m)	Distance (ft)
C9728	C9673	0.961	3.154
	C9674	10.56	34.66
	C9671	15.10	49.54
C9729	C9667	0.910	2.986
	C9668	13.41	44.00
	C9665	14.35	47.08
C9730	C9677	0.858	2.813
	C9666	12.59	41.32
	C9665	15.95	52.32
C9731	C9646	0.871	2.858
	C9666	14.74	48.35
	C9676	16.55	54.31
C9732	C9683	0.778	2.552
	C9689	13.31	43.67
	C9680	14.95	49.04
C9733	C9647	1.048	3.439
	C9668	12.60	41.34
	C9670	12.67	41.58
	C9676	12.91	42.36
C9734	C9676	3.373	11.07
	C9647	10.58	34.72
	C9668	11.41	37.44
C9735	C9668	6.783	22.26
	C9647	6.848	22.47
	C9670	9.609	31.52
C9736	C9658	7.563	24.81
	C9660	7.982	26.19
	C9659	8.174	26.82

3.2 Sequential Uranium and Metals Extractions

Six sequential liquid extractions were conducted in series on selected pre- and post-injection sediment samples based on targeted species. These extractions are operationally defined and may not necessarily be representative of the targeted fraction depending on sample conditions, although previous research suggests some association. Each extraction is listed with the reaction time in parenthesis. Extraction 1 is the aqueous contaminant fraction (1 h), extraction 2 is the adsorbed contaminant fraction (1 h), and the remaining extractions, 3 through 6, are operationally defined and designed to remove metals from precipitates (Hall et al. 1996; Gleyzes et al. 2002; Chao and Zao 1983; Larner et al. 2006; Mossop and Davison 2003; Sutherland and Tack 2002). Extraction 3 is a weak acid (pH 5 acetate for 1 h) that dissolves some carbonates and Fe oxides, extraction 4 is acetic acid (pH 2.3 for 5 days) designed to dissolve carbonates (if present) and other phases, extraction 5 is an ammonium oxalate extraction designed to dissolve Fe oxides (1 h), and extraction 6 is 8 M HNO_3 at 95°C (2 h) designed to dissolve a portion of sediment minerals. The 8 M HNO_3 extraction is a strong but incomplete digestion that is expected to dissolve elements that are potentially environmentally available. For example, previous research has shown that an 8 M HNO_3 acid extraction may remove 70% of total trace metals, 40-60% of Fe and Mn, 25% of major alkaline earth metals (Ca and Mg), 15% of Al and Ti, and negligible Si (< 0.03%) based on a comparison of acid extracts with quantitative XRF measurements (Serne et al. 2002; 2008). These sequential extractions are conducted at a 1:2 sediment:liquid ratio at room temperature (20°C to 25°C). The extractions use reagents 1 through 6, defined as follows:

- **Reagent 1 - Artificial groundwater (Table 3.3)**

Table 3.3. Artificial groundwater composition (Szecsody et al. 1998).

Constituent	Conc. (mg/L)	Mass for 1 L (g)
$H_2SiO_3 \cdot nH_2O$, silicic acid	15.3	0.0153
KCl, potassium chloride	8.20	0.0082
$MgCO_3$, magnesium carbonate	13.0	0.0130
NaCl, sodium chloride	15.0	0.0150
$CaSO_4$, calcium sulfate	67.0	0.0670
$CaCO_3$, calcium carbonate	150	0.1500

This provides a composition of 53 mg/L Ca^{2+}, 26 mg/L Na^+, 13 mg/L Mg^{2+}, 8.0 mg/L K^+, 166 mg/L HCO_3^-, 66 mg/L SO_4^{2-}, and 24 mg/L Cl^- (ionic strength 11.5 mM).

- **Reagent 2 - 0.5 mol/L $Mg(NO_3)_2$**: 128.2 g $Mg(NO_3)_2 \cdot 6H_2O$ + 30 µL 2 mol/L NaOH to pH 8.0, balance deionized (DI) H_2O to 1.0 liters
- **Reagent 3 - Acetate solution: 2 liters**: 136.1 g sodium acetate•$3H_2O$ + 30 mL glacial acetic acid (17.4 mol/L), pH 5.0, balance DI H_2O to 2.0 liters
- **Reagent 4 - Acetic acid solution**: concentrated glacial acetic acid, pH 2.3; 2 liters: 50.66 mL glacial acetic acid (17.4 mol/L) + 47.2 g $Ca(NO_3)_2 \cdot 4H_2O$, pH 2.3, balance DI H_2O to 2.0 liters
- **Reagent 5 - Oxalate solution**: 0.1 mol/L ammonium oxalate, 0.1 mol/L oxalic acid; 1 liter: 9.03 g anhydrous oxalic acid + 14.2 g ammonium oxalate•H_2O, balance DI H_2O to 1.0 liters
- **Reagent 6 - 8.0 mol/L HNO_3**: 502 mL conc. HNO_3 (15.9 mol/L) + 498 mL DI H_2O

In the first extraction, 6 mL of artificial groundwater (reagent 1) was mixed with 3.0 (±0.5) g of sediment for 50 min; the tube was then centrifuged at 3000 rpm for 10 min, and liquid was drawn off the top of the sediment and filtered (0.45 µm) for analysis. Extractions 2 and 3 were conducted on the same sediments with the same procedure in series except using reagents 2 and 3, respectively. The fourth extraction followed extraction 3 with a contact time of 5 days with reagent 4. The fifth extraction was conducted the same as extraction 1 except using reagent 5. In the sixth extraction, 6 mL of nitric acid (reagent 6) was added and mixed for 2 h at 95°C with the sediment; the tube was then centrifuged at 3000 rpm for 10 min, and liquid was drawn off the top of the sediment and filtered (0.45 µm) for analysis.

3.3 1000-Hour Carbonate Batch Extraction

This extraction exchanges carbonate in aqueous solution with calcite, so any uranium in calcite (and other minerals that may dissolve in the carbonate solution) will be solubilized into aqueous solution over time (Kohler et al. 2004). This 1000-h extraction may also dissolve other high-solubility U minerals such as uranophane. The carbonate extraction solution consisted of 0.0144 M $NaHCO_3$ and 0.0028 M Na_2CO_3 at pH 9.3 and was reacted with sediment (2 g/mL ratio) for 1000 h at room temperature. Sediment and the carbonate solutions were placed in 45-mL polytetrafluoroethylene or polycarbonate centrifuge tubes, mixed for 1000 h at 6 rpm, and centrifuged at 3000 rpm for 10 min. Liquid was drawn off the top of the sediment and filtered (0.45 µm) for analysis.

3.4 Dissolution of Uranium Minerals in the Polyphosphate Solution

Three high solubility uranium minerals (uranophane $Ca(UO_2)_2(HSiO_4)_2 \cdot 5H_2O$, Na-boltwoodite $Na_2(UO_2)SiO_4 \cdot 1.5H_2O$, and uranyl carbonate $K_2(UO_2)_2CO_3$) were reacted in a batch system containing the targeted 70-mM polyphosphate injection solution to evaluate the rate of dissolution of the mineral and release of uranium to solution to approximate conditions that would occur at field scale. For the first 16 h of the experiment, just the 70-mM polyphosphate injection solution was present with each uranium mineral. This approximates early times during a field scale injection (and near the injection well), where phosphate is in excess to any available calcium. During this time interval, multiple aqueous samples were collected, and the aqueous uranium and pH measured. At 16 h, sufficient calcium (as calcium sulfate) was added to precipitate all of the phosphate, approximating polyphosphate solution reaction with adsorbed Ca^{2+} in sediment minerals at field scale. Aqueous samples were taken to measure uranium and pH at selected times up to 300 h. During this second stage, the uranium initially dissolved was incorporated into phosphate precipitates (likely autunite).

3.5 Phosphate Injection Solution, Precipitation, and Extraction

A weak nitric acid solution (0.1 M HNO_3) for a short time (15 min) was used to dissolve anthropogenic phosphate precipitates and some natural phosphate minerals (Szecsody et al. 2009). For this extraction, 6 mL of 0.1 M HNO_3 was mixed with 3.0 (±0.5) g of sediment, then the sample was gently shaken for 15 min by placing the tube on a slow (6-10 rpm) rotary mixer or orbital shaker at room temperature (20°C to 25°C). The solution was then filtered (0.45-µm nylon/PVDF) for analysis. The solution was analyzed for total phosphate by ICP-OES (Section 3.8.2). Phosphate (as P) was additionally analyzed in the six sequential extractions (Section 3.2).

3.6 Inorganic and Organic Carbonate Analysis

The inorganic carbon in sediment was analyzed in selected pre- and post-injected sediments (Table 3.1, columns 11 and 12) using a Shimadzu TOC-5000A carbon analyzer with solid sample module. In this process, the inorganic carbon was digested by phosphoric acid at 200°C, then CO_2 gas analyzed. The detection limit was 0.01% carbon, and analytical precision was 0.005%. Selected sediments were additionally analyzed for organic carbon to evaluate whether organic co-contaminants were present. This analysis consisted of a total carbon pyrolysis of the sediment at 900°C (both organic and inorganic carbon), followed by CO_2 gas analysis. Organic carbon content was calculated as the total carbon minus inorganic carbon content.

3.7 1-D Column Leach Experiment

Leaching groundwater or artificial groundwater through untreated and phosphate-treated sediments (Table 3.1, column 8) provides a quantitative measure of the uranium concentration, mass, and release rate from sediments (Szecsody et al. 2013, 2014, 2016, 2017, 2019; Qafoku et al. 2004; Truex et al. 2017). In these 1-D column experiments, sediment was reacted with artificial groundwater (reagent 1) for different time periods as water flowed through the sediment (at the approximate rate of groundwater flow through contaminated sediment). Each column experiment was unique in terms of the exact flow rate, mass of sediment, size of column, and the change in concentration of contaminant(s) leaching from the sediment (Szecsody et al. 2013), so every aspect of the column experiment – from packing the column, to column flow operations, to various measurements made on the effluent liquid – was recorded in a spreadsheet.

The 1-D flow experiments were conducted with the full grain size distribution of the gravel fraction < 12 mm in the 25-mm-diameter columns and was packed as moist sediment into columns. The weight of the moist sediment in the column was quantified by difference from empty column weight and packed weight. In a small pan, the gravimetric moisture content (μ) of a sample of the moist sediment was quantified by weighing 3 to 5 g of moist sediment, drying for at least 48 h at 105°C, and weighing the dry sediment. The moisture content was calculated by Eq. (3.1):

$$\mu = \frac{(M_{moist} - M_{dry})}{M_{dry}} \tag{3.1}$$

where M_{moist} is the moist sediment mass and M_{dry} is the dry sediment mass. The packed column was water-saturated by injecting artificial groundwater (reagent 1) into the lower end of the column (which is mounted vertically) until water was present at the effluent end of the column. The dry bulk density of the sediment was calculated from Eq. (3.2) (where V_{column} is the column volume and BD is the dry bulk density). The pore volume, PV or total water weight in the column, was calculated from Eq. (3.3) (where $M_{sat,column}$ is the mass of the column after saturation). The porosity (φ) was calculated from the total water weight in the column divided by the column volume per Eq. (3.4).

$$BD = \frac{M_{dry,column}}{V_{column}} = \frac{(M_{moist}) - (\mu \times M_{moist})}{V_{column}} \tag{3.2}$$

$$PV = (\mu \times M_{moist}) + \left(M_{sat,column} - M_{moist}\right) \tag{3.3}$$

$$\varphi = \frac{PV}{V_{column}} \tag{3.4}$$

The actual column experiment consisted of injecting artificial groundwater (reagent 1) into one end of the column at a constant flow rate to achieve a 1- to 4-h residence time for a total of 100 pore volumes. The residence time is defined as the time it takes for 1 pore volume of water to travel through the column, as measured by effluent volume. At the effluent end of the column, liquid samples were collected in sufficient number and frequency to measure the change in contaminant concentration, (i.e., 36 to 40 for these experiments). Samples were automatically collected using a timed fraction collector (Isco Foxy 200), which contained 4.5-mL BD falcon tubes to collect effluent. Contaminant(s) typically leaches from the sediment at a high initial rate (i.e., at high initial concentration, which decreases over time), then at a slower rate at later pore volumes. Because of this general "breakthrough curve" behavior, more effluent samples are collected in the first 2 pore volumes, with less frequent sample collection for subsequent pore volumes. More specifically, for these leach experiments, the sample frequency was (a) 0 to 2 pore volumes, 12 effluent samples; (b) 2 to 10 pore volumes, 12 effluent samples; (c) 10 to 30 pore volumes, 6 effluent samples; and (d) 30 to 100 pore volumes, 6 effluent samples (for a total of 36 effluent samples, and a few influent and duplicate samples). Effluent samples were measured for aqueous uranium, pH, specific conductance, and metals/cations (on selected effluent samples).

Stop-flow events were additionally used in the 1-D leach experiments with durations ranging from 10 to 1000 h without flow, providing time for contaminants in one or more surface phases to partition into pore water (i.e., from diffusion from intraparticle pore space or time-dependent dissolution of precipitate phases or slow desorption). The stop-flow events were at approximately 16 h (at 2 pore volumes), 150 h (at 10 pore volumes), and 500 h (at 100 pore volumes). The different times were selected to target leaching of different uranium phases. Initially, aqueous and sorbed uranium was leaching (i.e., < 10 pore volumes), so the release rate from the sediment was relatively rapid (so a 16-h stop-flow is used). Over a larger number of pore volumes, uranium was released from carbonate dissolution and phosphate dissolution, so longer stop-flow times are used. Operationally, initiating a stop-flow event involves turning off the pump, plugging both ends of the column (to prevent water movement out of the sediment column), and turning off the fraction collector. Ending a stop-flow event involved reconnecting the column to the pump, turning on the fraction collector, and then turning on the pump. The calculation of the contaminant release rate from sediment (µg contaminant/g of sediment/day) uses the change in contaminant effluent concentration before and after the stop-flow event, and the length of time of the stop flow event.

3.8 Aqueous Sample Analysis

3.8.1 Analysis of Aqueous U^{VI} in Extractions and Column Effluent by Kinetic Phosphorescence Analysis

The aqueous uranium concentration in batch extractions and 1-D leach column influent and effluent was measured by kinetic phosphorescence. Selected aqueous samples were additionally measured by ICP-OES, as described in Section 3.8.2. For quantification of aqueous U^{VI} species, the 0.45-µm filtered sample is measured by reaction with a phosphate buffer, Uraplex (Chemchek, Richland, WA), using light from a pulsed nitrogen laser with an excitation wavelength of 425 nm and measurement of the UV emission at 515 nm (KPA-11 system; Brina and Miller 1992). A total of 1000 pulses were used with a duration of 13 microseconds. The average lifetime of the U^{VI} as uranyl (UO_2^{2+}) compound emission was 200 to 300 microseconds. Uraplex was used to increase phosphorescence of U and decrease quenching probability. The analytical range of uranium measurement is 0.01 to 30 µg/L on the low range.

Before samples were analyzed for uranium, the daily routine included (i) laser warmup, (ii) uranium calibration curve, then (iii) sample analysis. The KPA laser was warmed up by loading four (or more) DI water samples into the autosampler and running the samples. Then, the set of U^{VI} standards (minimum of five standards) covering the analytical range of interest (0.01 to 30 µg/L) was loaded into the autosampler and analyzed. There are two types of U^{VI} standards used: *calibration standards* mixed from a U^{VI} standard from one supplier (typically 1000 mg/L, NIST traceable), and a *verification standard* from a second supplier (also NIST traceable).

The 0.45-µm-filtered aqueous samples were loaded into the KPA autosampler. A minimum of 3 mL of sample is needed, in 2% HNO_3 by volume. Samples containing Cl^-, Br^-, and HCO_3^- were diluted to be less than 10 mmol/L of each of these anions to minimize quenching (i.e., dilute concentrated samples). After every 10 samples, a U^{VI} verification standard was measured to confirm reliability of measurements. For the uranium analysis to be valid, the reference, all standards, and sample lifetime must be >150 microseconds. If sample lifetimes were too short, the solution was quenched, and a more diluted sample was re-analyzed. If the reported sample U^{VI} concentration was greater than the upper range of the calibration curve (typically 30 µg/L), the sample was also diluted to be within range. For each set of 20 samples, one preparation blank (reagent 1, artificial groundwater) and one blank spike (reagent 1 spiked with 30 µg/L U^{VI}) were conducted. In addition, a duplicate sample was analyzed for every 20 samples.

3.8.2 Analysis of Metals by ICP-OES

The aqueous samples from six sequential liquid extractions of pre- and post-injection sediments were analyzed for uranium (by KPA, previous section) and 33 cations/metals that included Al, As, Ba, Be, B, Cd, Ca, Cr, Co, Cu, Fe, Pb, Mg, Mn, Ni, P, K, Si, Na, Sr, S, Ti, U, V, Zn, and Zr. Of these, 13 metals were reported, as they can directly or indirectly provide information about changes in uranium or major solid phases and/or the injection solution. The extractable P provided additional information as to aqueous, adsorbed, and precipitated phosphate in addition to the separate phosphate extraction (Section 3.5). Changes in calcium and magnesium (and strontium, which substitutes for calcium) between pre- and post-injection sediments indicate whether the aqueous/adsorbed cations are dissolving from calcite and are being precipitated with phosphate. Changes in more acidic extractions indicate dissolution of carbonates (extractions 3 and 4) or anorthite (extraction 6). Extractable iron provides an indication of whether U in Fe oxides is dissolving (in extractions 3, 4, and 5). Both sodium and potassium were in the injection solution, so an increase in these aqueous and adsorbed cations would coincide with delivery of the injection solution. Changes in Si and Al in the acid extractions (3 through 6) indicated the presence of different minerals. As natural minerals predominantly contain only silica or silica and aluminum (at 1:1 or 2:1 concentration), aluminum at a significantly higher concentration than silica in acidic extractions indicated Al from waste. Copper was also present in 300 Area waste (Gerber 1993; Wang et al. 2005; Arai et al. 2007), and torbernite (and other Cu-precipitates) has previously been identified (Wellman et al. 2008c; Arai et al. 2007). Changes in copper in sequential extractions from pre- to post-injection sediments provide an indication of dissolution of previously formed minerals and/or Cu-phosphate precipitation. Both lead and beryllium were used for uranium shielding, so their presence in subsurface sediments is a likely waste indicator. Sulfate was present in the natural Hanford groundwater (67 mg/L) and also as sulfuric acid in historical waste. Titanium may be present in natural titanomagnetite, which can contain uranium. Vanadium may be present as natural U-vanadate minerals carnotite ($K_2(UO_2)_2(VO_4)_2 \cdot 3H_2O$) and tyuyamunite ($Ca(UO_2)_2(VO_4)_2 \bullet 5\text{-}8H_2O$). Therefore, Ti and V were expected at similar concentrations in pre- and post-injection sediments, as these elements were not present in the uranium (and co-contaminant) waste and represent low solubility, naturally occurring mineral phases. Low natural arsenic is present in Hanford sediments and was not present in the waste.

3.9 Uranium Solid Phase Characterization

Untreated and phosphate-treated sediments were evaluated by multiple surface techniques to identify uranium and associated phases (i.e., phosphate) coating uranium. The aqueous and adsorbed fractions (i.e., most mobile) of the sediment are not evaluated by solid phase characterization but are quantified by sequential extractions (see Section 3.2, extractions 1 and 2). Subsurface sediments from the 300-FF-5 Stage B pre- and post-injection sediments have low uranium concentrations (0.3 to 140 µg/g), which limit solid phase characterization of uranium compounds. Possible solid phase characterization with uranium includes the following minimum detection limits (MDLs):

- X-ray diffraction (XRD), MDL 0.5% or 5000 µg/g
- X-ray fluorescence (XRF), MDL 0.1% or 1000 µg/g
- Scanning electron microscope with energy dispersive detector (SEM-EDS), MDL 500 µg/g
- Electron microprobe with elemental detector (EMP), MDL 200 µg/g
- Laser induced fluorescence spectroscopy (LIFS), MDL 200 µg/g
- µ-XRF, µ-XANES, and µ-EXAFS at the APS at Argonne National Laboratory, MDL 1, 10, and 100 µg/g, respectively

All of these techniques have been used in previous laboratory studies reacting high-concentration aqueous, adsorbed, and precipitated uranium with phosphate (Wellman 2005, 2006, 2008a-c; Vermeul et al. 2009; Zachara et al. 2007; Shi et al. 2009; Mehta et al. 2016). In these 300 Area field sediments with low (< 140 µg/g) uranium concentration, uranium phases were identified at the APS using µ-XRF, µ-EXAFS, and µ-XANES (for U valence state). Additional elements were identified using a scanning electron microscope (SEM) to better identify potential uranium minerals. Because these surface phase techniques are not NQA-1 qualified, all solid phase characterization techniques are for information only (FIO).

3.9.1 Thin Section Preparation

Thin sections were prepared from the sediments with samples identified below in Table 3.1. Two pre-/post-injection sediment pairs were prepared with high Cu concentrations (Table 3.4).

Table 3.4. Sediment samples used for solid phase analysis.

Borehole	Start Depth (ft)	End Depth (ft)	Lab #	Pair	Injection	U (µg/g)	Cu (µg/g)
C9667	25	27.5	G3	w/G4	pre	94.1	782
C9729	25	27.5	G4	w/G3	post	48	762
C9673	30	32.5	G5	w/G6	pre	55.7	518
C9728	30	32.5	G6	w/G5	post	136.4	463

Dried < 1-mm-size sediments were mixed with epoxy (EpoThin2 epoxy and hardener, Buehler, Lake Bluff, IL) and placed into a 1.6-cm (inner diameter) aluminum tubing. Samples were then vacuum-degassed multiple times to remove bubbles and air-dried overnight at room temperature. Slices were cut with an Isomet 1000 diamond blade thin sectioning saw with Isocut fluid (Buehler, Lake Bluff, IL) to a thickness of approximately 150 µm. After mounting on a glass microscope slide, thin sections were sanded with silicon carbide sandpaper with Isocut fluid followed by 400 grit sandpaper, then 600 grit sand paper, and finally 1200 grit sand paper (Ted Pella, Inc.), all using a figure eight pattern. Final polishing was conducted with a nylon polishing cloth and 1-µm diamond polish (Metadi II, Buehler). Samples were washed with methanol and dried prior to analysis.

3.9.2 Micro X-ray Fluorescence Mapping and Micro X-ray Absorption Spectroscopy

Sediment thin sections and reference minerals as pressed powders were characterized by synchrotron µ-XRF mapping on beamline 20-ID at the APS. Samples were sealed with multiple layers of Kapton tape and Mylar sheets for containment. µ-XRF images were collected for U, Ca, Ti, Fe, Mn, Zr, Rb, Sr, Cu, Zn, Y, and Bi with a beam size of 2 x 3.5 µm, and at an energy above the U L_{III} edge (17166 eV). A Si (111) monochromator provided an energy resolution of 3 eV at the U L_{III} edge. µ-XRF maps of the thin sections were collected with a step size of 5 µm. The incident beam energy was selected using a Si (111) monochromator, and the X-ray beam was focused to spot size of ~400 µm using a toroidal mirror. The fluorescence signal was monitored using a multi-element, energy dispersive germanium detector. Initial energy calibration was performed using a zirconium foil. Additional spectra were collected of the XANES and EXAFS regions for U at an energy above the L_{III} edge (17166 eV). The µ-XANES data were analyzed using the Athena interface and µ-EXAFS data were analyzed using the Artemis interface to the IFEFFIT program package (Ravel and Newville 2005).

3.9.3 Scanning Electron Microscopy

Scanning electron microscopy energy dispersive X-ray spectroscopy (SEM-EDS) was conducted on thin sections prepared from sediments with 10- to 20-nm coating of carbon on a FEI Quanta 600 FEG environmental SEM instrument. A working distance of 10 to 25 mm was used to identify locations of interest on samples with a 10-mm working distance for imaging and EDS analysis with an operating voltage of 30 keV. A backscatter electron (BSE) detector was used for imaging and identification of areas with higher molecular weight elements (e.g., U) as they appear brighter in BSE mode.

3.10 Sediment Grain Size Distribution

Sediments used in the 1-D column experiments were analyzed for particle size distribution using laser diffraction (< 0.5-mm size) following a standard procedure (ASTM D4464-15) using a Horiba laser particle size analyzer over a range of 0.01 µm to 2 mm. The weight fractions of larger particle sizes (2, 4, 12 mm, > 12 mm) were measured by sieves following ASTM D6913-04. The laser particle size analysis for each sample was conducted in triplicate, with average particle size analysis shown.

3.11 Equilibrium Speciation Modeling

3.11.1 Uranium Speciation

A geochemical equilibrium model, Geochemist's Workbench version 10 (GWB), was used to model the speciation of uranium within groundwater and remediation solutions. The Visual Minteq database that was previously converted for GWB by Jon Petter Gustafsson was used for model development with several additions to update uranium species based on new thermodynamic data as described within recent reviews (Guillamont et al. 2003; Gorman-Lewis et al. 2008, 2009). Meta-autunite and metatorbernite species were not included in the model as constants were not available, but autunite and torbernite species were included in predictions. The Davies equation was used for calculation of activity coefficients. The Davies method is applicable up to 0.7 mol/kg (Langmuir 1997) and solutions in this research are within this range. The total bicarbonate (HCO_3^-) concentration was fixed at 166 mg/L and saturated with oxygen (8.4 mg/L) in the model to represent previous groundwater measurements at the Hanford Site based on the average of 11 monitoring wells in the 100D Area from 1987 to 1990 (Table F.1 in Appendix F). Elevated concentrations of sodium, potassium, bicarbonate, and phosphate were added based on the remediation solution components included in Section 2.0 and actual delivered solution composition. Simulations were conducted where the pH varied from 6 to 8 to consider changes during apatite precipitation with Na^+ for the charge balance. Further, modeling was conducted with mineral precipitation suppressed to allow for comparison of saturation indices as Q/K (reaction quotient divided by the equilibrium constant). Then, models allowed for precipitation in order to compare equilibrium aqueous speciation. Because this modeling is not NQA-1 qualified, simulation results are for information only.

3.11.2 Phosphate precipitation

Batch systems were simulated using a geochemical equilibrium model (PHREEQC Interactive 3.5.0.14000) that was developed by the U.S. Geological Survey with the standard database. The model included the components from GWB with the additional equilibration with a partial pressure of $10^{-2.8}$ carbon dioxide gas, which is similar to air ($10^{-3.4}$) but slightly saturated as has been observed at the Hanford Site previously. As with the GWB model, precipitation was allowed to change pH as precipitation occurred. In subsequent model runs, precipitation was suppressed to calculate saturation indices. In addition, calcium was added to the system in two different ways: (1) as a variable content of calcite, up to 0.1%; and (2) as aqueous calcium, which may adsorb or exchange from local minerals, up to 50 mg/L.

4.0 Results

Four different types of analyses were conducted to quantify differences in solubility and leachability of uranium between pre- and post-PO_4-treated sediments. These included (a) a Na-carbonate solution (pH 9.3) extraction of uranium from sediment over 1000 h (Section 4.1), (b) a series of six sequential liquid extractions of uranium from sediment over a week (Section 4.2), (c) leaching of uranium from sediment in 1-D column experiments over the course of 2 months (Section 4.3), and (d) solid phase analysis of uranium minerals and apatite formation (Section 4.4). Additional extractions were conducted to evaluate the phosphate precipitate in sediments (Section 4.5). Metals were also analyzed in sequential liquid extractions as indicators of (a) amendment delivery via injection, (b) co-contaminant movement, and (c) change in solid phases (Section 4.6).

4.1 Batch Carbonate Extraction of Uranium for 1000 h in Pre- and Post-PO_4 Treated Sediments

The pH 9.3 carbonate extraction (0.0144 M $NaHCO_3$ and 0.0028 M Na_2CO_3, see Section 3.3) of sediment for 1000 h is designed to mobilize adsorbed uranium as well as exchange uranium in calcite, due to dissolution of U-laden carbonate and precipitation of $CaCO_3$ (i.e., no net dissolution; Kohler et al. 2004). This 1000-h extraction may also dissolve other high-solubility U minerals such as uranophane. Over the 1000-h batch extraction, other moderate-solubility U solid phases (such as uranophane and Na-boltwoodite) may also partially dissolve. Carbonate extraction results are presented in pre- and post-injection pairs, which are in boreholes ~ 3.28 ft (1 m) apart (Table 3.2). The spatial location is shown in the map in each set of graphs (Figure 3.1 for borehole location details).

There are 19 pre- and 25 post-injection pairs of samples in six boreholes shown with pre-injection samples as the upper plots in each figure and post-injection samples as the lower plots in each figure (Figure 4.1, Figure 4.2, Figure 4.3, and Figure 4.4). A comparison of the pre- to post-injection extractions shows a decrease in the labile uranium (i.e., the labile uranium is in µg/g), although the *fraction* labile uranium is a better measure of pre- to post-injection difference, as it removes differences in the total uranium between samples. The comparison of the fraction of labile uranium for each of the 19 pairs (Figure 4.5a) shows that the mobile uranium fraction for pre-injection (i.e., untreated) sediments is 0.425 ± 0.096, and for post-injection samples is 0.156 ± 0.143, or an average of 63% less mobile U as a result of the polyphosphate treatment, based on results of this 1000-h carbonate batch extraction. The pre- and post-treatment labile fraction was statistically different based on the Tukey method (95% confidence, $p = 1 \times 10^{-7}$) (Berthouex and Brow 1994). For the 10 pairs of pre- and post-injection sediments used in 1-D column leach studies, the results are similar (Figure 4.5b), with an average of 68.2% less mobile U from the polyphosphate treatment, indicating that a representative pool of samples were chosen for 1-D column leach studies presented in Section 4.3.

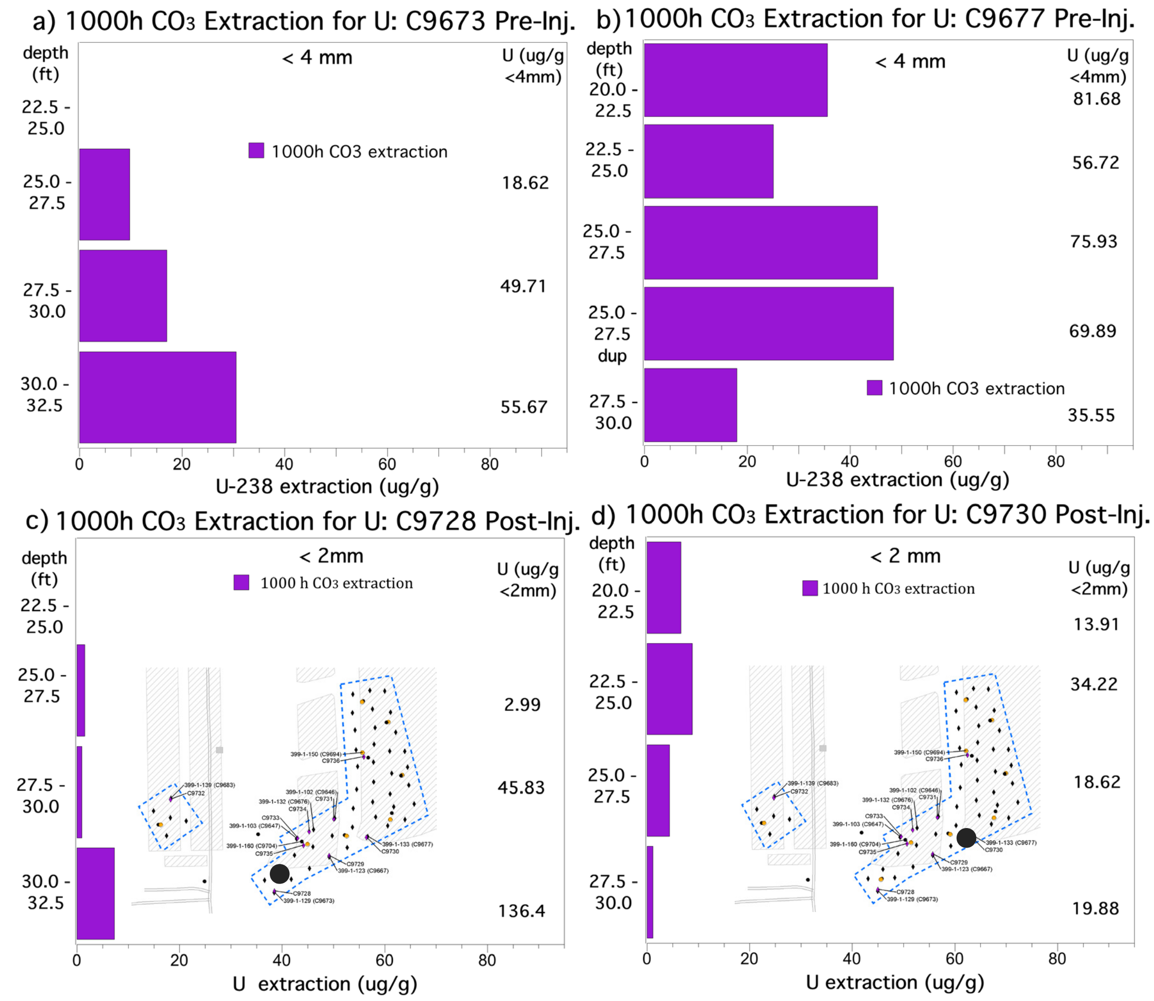

Figure 4.1. Carbonate extraction (1000 h) of uranium in pre- and post-injection borehole pairs: C9673 (a) and C9728 (c), and C9677 (b) and C9730 (d). Borehole locations are shown in (c) and (d).

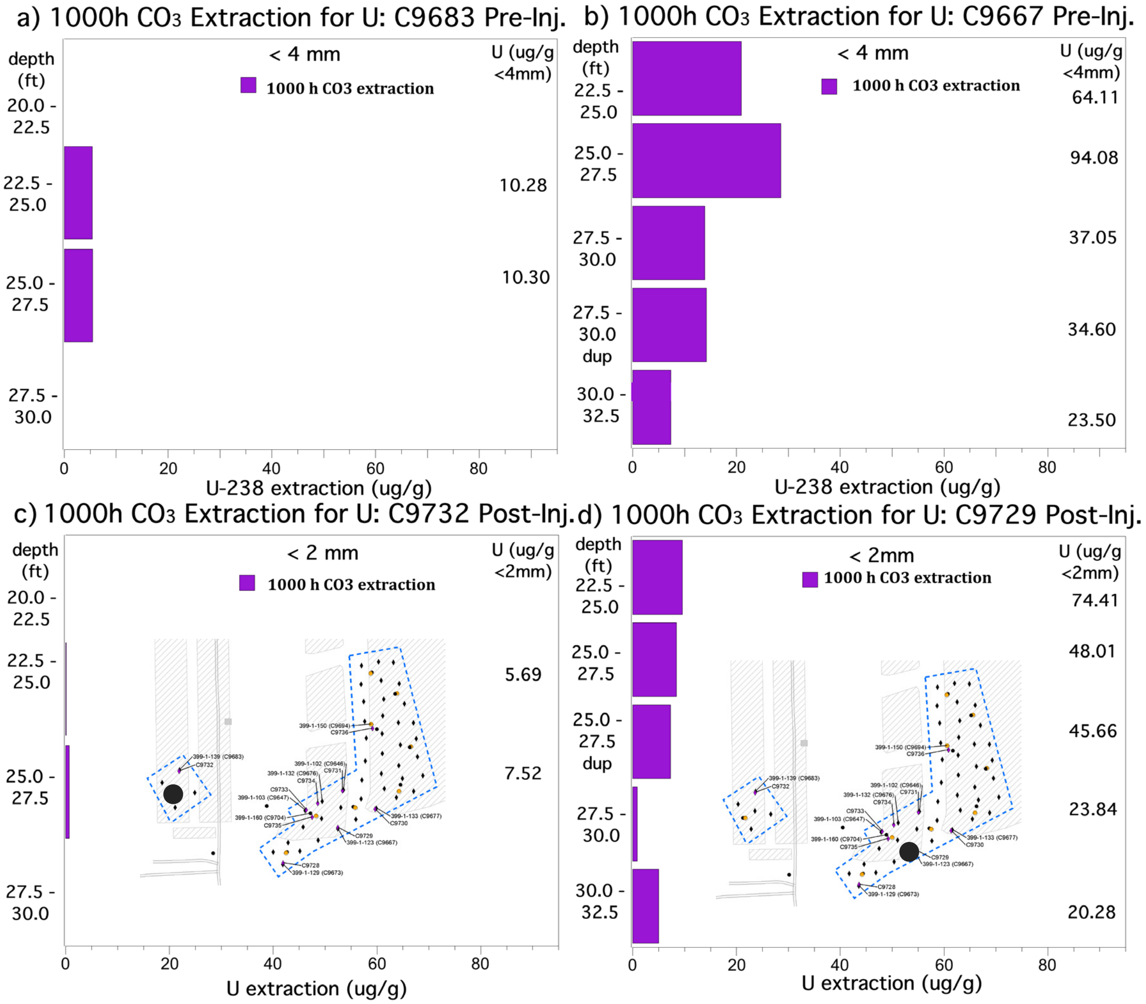

Figure 4.2. Carbonate extraction (1000 h) of uranium in pre- and post-injection borehole pairs: C9683 (a) and C9732 (c), and C9667 (b) C9729 (d). Borehole locations are shown in (c) and (d).

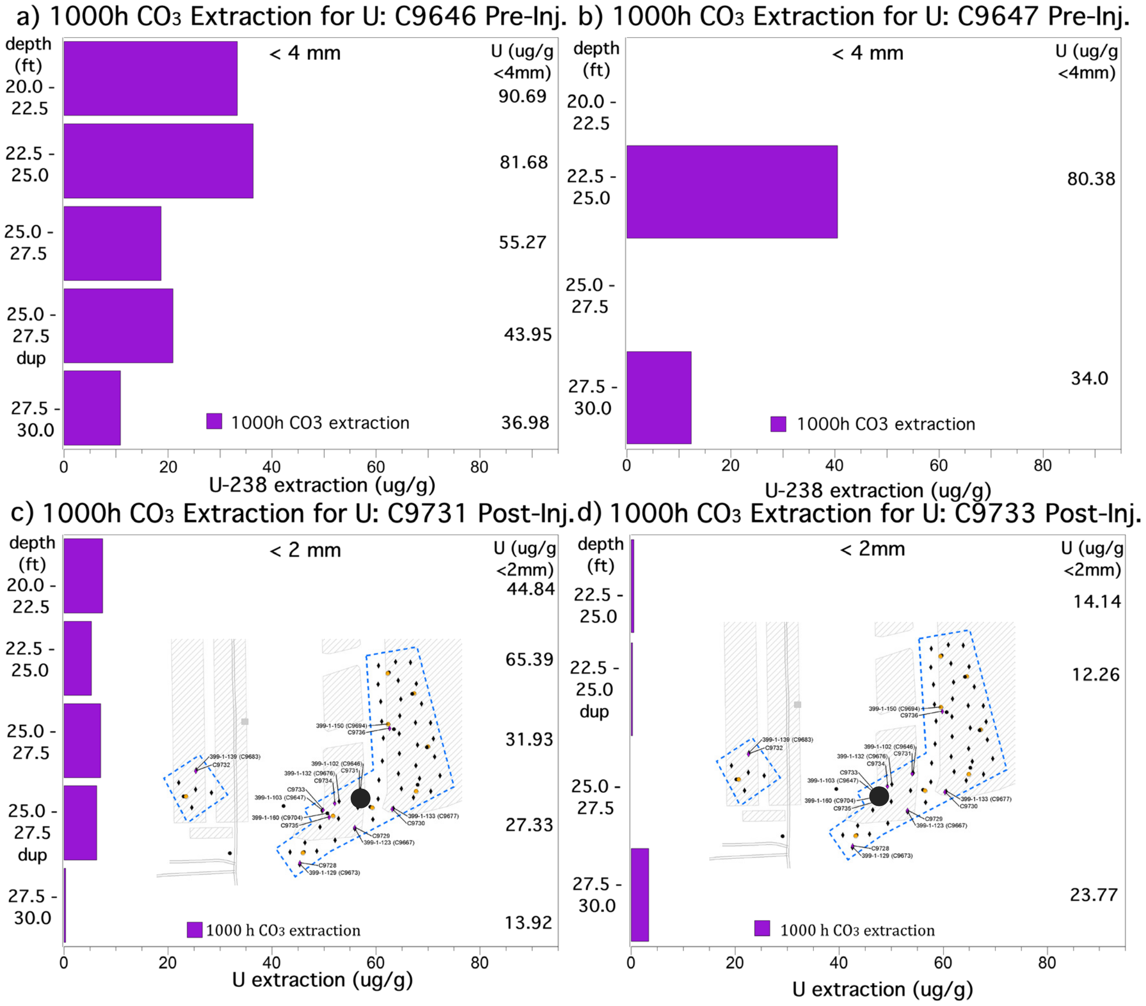

Figure 4.3. Carbonate extraction (1000h) of uranium in pre- and post-injection borehole pairs: C9646 (a) C9731 (c), and C9647 (b) C9733 (d). Borehole locations are shown in (c) and (d).

a) 1000h CO_3 Extraction for U: C9734 Post-Inj. b) 1000h CO_3 Extraction for U: C9735 Post-Inj.

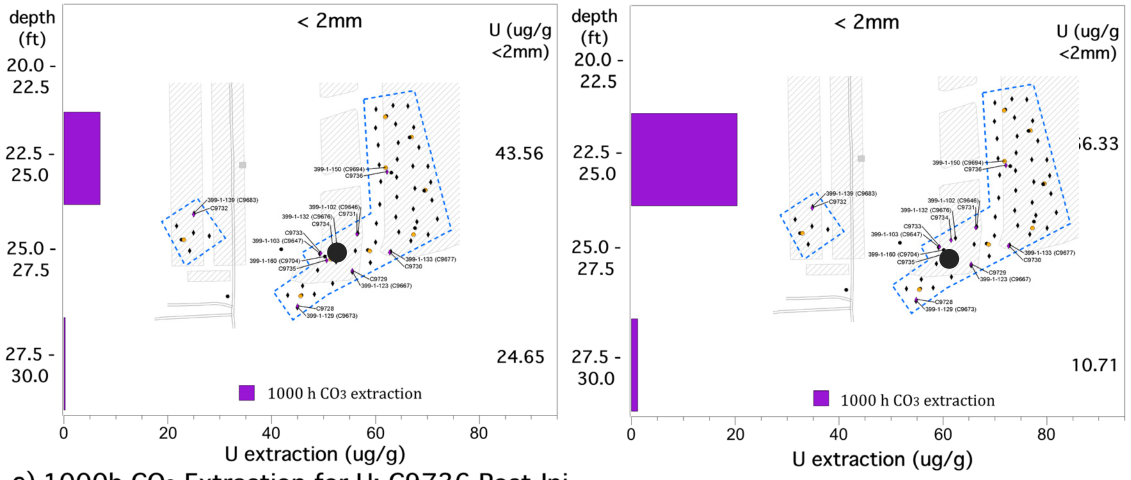

c) 1000h CO_3 Extraction for U: C9736 Post-Inj.

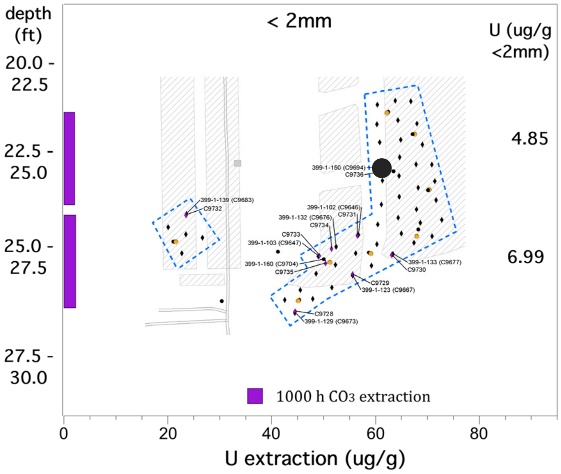

Figure 4.4. Carbonate extraction (1000 h) of uranium in unpaired post-injection boreholes C9734 (a, 35 ft from C9647), C9735 (b, 22.5 ft from C9647), and C9736 (c).

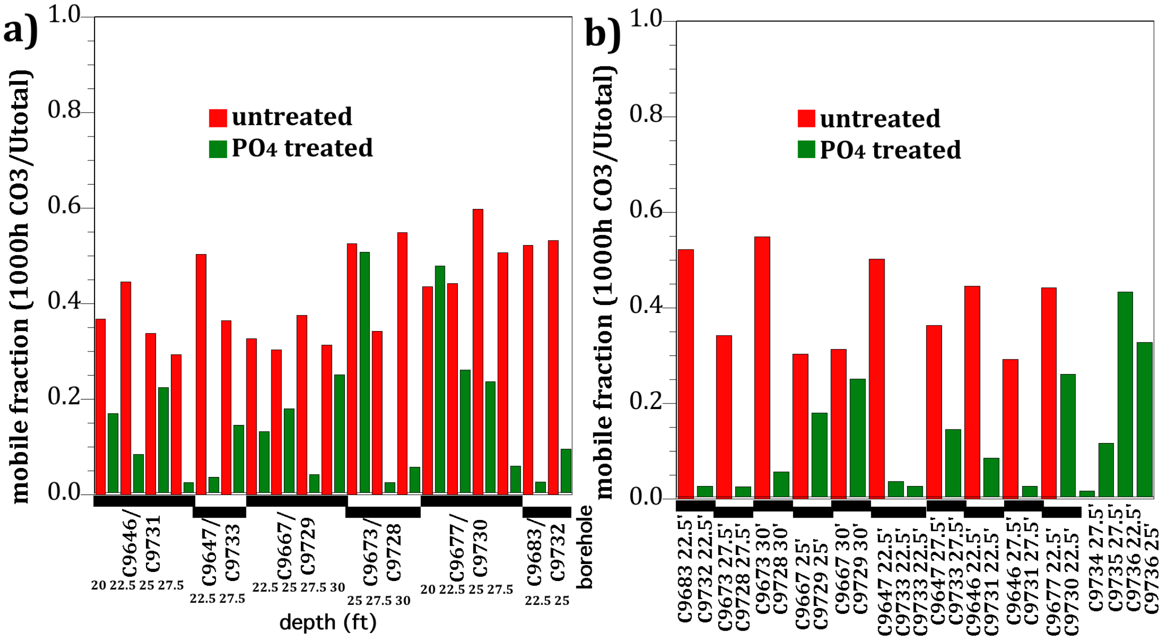

Figure 4.5. Carbonate extraction (1000 h) of uranium in post-injection boreholes in (a) 19 pre-/post-injection borehole pairs, and (b) 10 pre-/post-injection pairs used in 1-D leach columns.

4.2 Uranium Sequential Liquid Extractions in Pre- and Post-PO_4 Treated Sediments

Sequential liquid extractions were used to quantify uranium in sediment that is aqueous (extraction 1), adsorbed (extraction 2), and in progressively lower-solubility precipitates (extractions 3 through 6, Table 4.1). Results of uranium in sequential extractions for pre- and post-injection sediments are presented in this section, and metals/cations measured in sequential extractions are presented in Section 4.5. For comparison, the stack bar graphs of sequential extractions are shown (Figure 4.6 through Figure 4.9) with the 1000-h carbonate extraction (described in detail in Section 4.1). Sequential extraction data are shown as uranium concentration (i.e., µg/g in each phase, < 2-mm size fraction in Table 4.2; whole sediment size in Appendix A, Table A.1) and also as the fraction of total uranium.

Table 4.1. Sequential extraction of contaminants from sediment samples.

Extraction Solution	Hypothesized Targeted Sediment Components	Interpreted Contaminant Mobility of Extracted Fraction	Color Code
1. Aqueous: uncontaminated Hanford groundwater	Contaminants in pore water and a portion of sorbed uranium	Mobile phase	🟥
2. Ion exchange: 1 M Mg-nitrate	Readily desorbed contaminants	Readily mobile through equilibrium partitioning	🟥
3. Acetate pH 5: 1 h in pH 5 sodium acetate solution	Contaminants associated with surface-exposed carbonate precipitates and other readily dissolved precipitates	Moderately mobile through rapid dissolution processes	🟧
4. Acetate pH 2.3: 1 week in pH 2.3 acetic acid	Dissolution of most carbonate compounds, and hydrous uranium silicates: Na-boltwoodite and uranophane	Slow dissolution processes for contaminant release from this fraction; mobility is low with respect to impacting groundwater	🟨
5. Oxalic acid: 1 h	Dissolution of some aluminosilicates and Fe oxides	Slow dissolution processes are associated with contaminant release; mobility is very low with respect to impacting groundwater	🟩
6. 8 M HNO_3: 2 h in 8 M nitric acid at 95°C	Low-solubility uranium precipitates: torbernite and autunite	Very slow dissolution processes are associated with contaminant release; functionally immobile; some or all of the contaminants in this phase may be naturally occurring	🟩

4.2.1 Uranium Mass in Sequential Extractions

The sequential extraction data for all pre- and post-injection sediments (< 2 mm size fraction) is shown in Table 4.2, with the data shown for the whole sediment size in Appendix A. For the 19 pre- and post-injection pairs of sediment samples from six borehole pairs, the post-injection sediments show significantly less mobile uranium compared with pre-injection sediments (Figure 4.6 through Figure 4.8). The aqueous and adsorbed (extractions 1 and 2, respectively, red bars on figures) are the most mobile, and part of the acetate (extractions 3 and 4, respectively, orange and yellow bars on figures) extractable uranium is mobile, as uranium dissolved in these extractions is from high-solubility minerals such as U in calcite, Na-boltwoodite, and uranophane. A direct comparison of the uranium extracted in different phases (in µg/g) between pre- and post-injection samples is difficult because the total uranium varies between each sediment sample due to spatial heterogeneities (both chemical and physical grain size), even though pre- and post-injection pairs are <3.28 ft (1 m) apart. For that reason, these pre- and post-injection comparisons of sequential extractions shown in uranium concentration (i.e., µg/g) in Figure 4.6 through Figure 4.9 are also shown in fraction in each extraction in Figure 4.11 through Figure 4.14.

More specifically, after phosphate treatment aqueous and adsorbed uranium (extractions 1 and 2, highly mobile U fraction) decreased from 6.7% to 3.4% of the total extracted U, acetate/acetic acid extractable U (extractions 3 and 4, soluble U precipitates) decreased from 58.6% to 37.2%, and the oxalate/nitric acid extractable U (extractions 5 and 6, low-solubility U precipitates) increased from 34.8% to 54.3%. It should be noted that because pre-injection boreholes are injection wells, and most post-injection boreholes are located within 3.61 ft (1.1 m), some decrease in aqueous and adsorbed U is caused by advection during injection, although aqueous U in the polyphosphate solution will precipitate (Mehta et al. 2016; Mehta 2017; Szecsody et al. 2012). The average percent change of uranium in pre-injection and post-injection extractions in Table 4.3. is the average change in each of the 19 pre- and post-injection pairs. While most locations of pre-/post-injection pairs received polyphosphate treatment, some received minimal phosphate, which accounts for poor performance in some areas and increased standard deviations for averages (described in Section 4.5). Average uranium mass changes in extractions show a net decrease in extractions 1, 2, 3, and 4, with the greatest changes in extractions 1, 2, and 4 (Table 4.2). There is a net U gain in extraction 6, likely due to (i) the precipitation of autunite, (ii) coating of U phases with apatite, or (iii) co-precipitation of aqueous U with apatite.

Table 4.2. Uranium sequential extraction data for pre- and post-injection boreholes for the < 2 mm size fraction.

Borehole	Depth (ft)	Extract 1 (µg/g)	Extract 2 (µg/g)	Extract 3 (µg/g)	Extract 4 (µg/g)	Extract 5 (µg/g)	Extract 6 (µg/g)	Sum (µg/g)	1000h CO_3 (µg/g)	Extr. 1 fraction	Extr. 2 fraction	Extr. 3 fraction	Extr. 4 fraction	Extr. 5 fraction	Extr. 6 fraction
C9646 pre	20 - 22.5	5.614	4.072	4.870	31.96	16.20	27.99	90.7	33.35	0.0619	0.0449	0.0537	0.352	0.179	0.309
C9731 post	20 - 22.5	0.238	0.161	7.793	12.31	8.659	15.68	44.8	7.45	0.0053	0.0036	0.174	0.275	0.193	0.350
C9646 pre	22.5 - 25	2.614	3.079	6.265	36.23	15.18	18.31	81.7	36.4	0.032	0.0377	0.0767	0.444	0.186	0.224
C9731 post	22.5 - 25	0.340	0.046	10.26	12.88	13.74	28.13	65.4	5.28	0.0052	0.0007	0.1569	0.197	0.210	0.430
C9646 pre	25 - 27.5	1.553	1.487	12.44	29.48	3.333	6.98	55.3	18.66	0.0281	0.0269	0.225	0.533	0.060	0.126
C9646 pre dup	25 - 27.5	0.907	1.59	3.79	25.71	3.325	8.62	43.9	20.97	0.0206	0.0363	0.086	0.585	0.076	0.196
C9731 post	25 - 27.5	0.393	0.680	5.572	11.51	2.835	10.95	31.9	7.05	0.0123	0.0213	0.1745	0.360	0.089	0.343
C9731 post dup	25 - 27.5	0.296	0.474	6.032	9.004	2.608	8.92	27.3	6.27	0.0108	0.0174	0.221	0.329	0.0954	0.326
C9646 pre	27.5 - 30	0.270	0.078	1.080	17.02	6.790	11.75	37.0	10.84	0.0073	0.0021	0.0292	0.460	0.184	0.318
C9731 post	27.5 - 30	0.010	0.072	1.697	2.677	2.812	6.65	13.9	0.300	0.0007	0.0052	0.1219	0.192	0.202	0.478
C9647 pre	22.5 - 25	3.135	3.625	13.01	35.40	8.577	16.63	80.4	40.45	0.039	0.0451	0.1619	0.440	0.107	0.207
C9733 post	22.5 - 25	0.011	0.168	1.171	1.620	2.405	8.77	14.1	0.464	0.0008	0.0119	0.0828	0.115	0.170	0.620
C9733 post dup	22.5 - 25	0.025	0.137	1.012	1.693	2.264	7.13	12.3	0.284	0.0021	0.0112	0.0825	0.138	0.185	0.581
C9647 pre	27.5 - 30	0.503	0.265	1.357	17.08	3.488	11.31	34.0	12.4	0.0148	0.0078	0.0399	0.502	0.103	0.333
C9733 post	27.5 - 30	0.050	0.266	1.961	3.283	4.390	13.82	23.77	3.37	0.0021	0.0112	0.0825	0.138	0.185	0.581
C9667 pre	22.5 - 25	0.974	2.372	5.110	34.15	8.264	13.23	64.11	20.96	0.0152	0.037	0.0797	0.533	0.129	0.206
C9729 post	22.5 - 25	0.424	0.052	10.60	15.98	16.050	31.31	74.41	9.56	0.0057	0.0007	0.142	0.215	0.216	0.421
C9667 pre	25 - 27.5	2.089	3.170	5.842	59.36	15.288	8.33	94.08	28.6	0.0222	0.0337	0.0621	0.631	0.163	0.089
C9729 post	25 - 27.5	0.389	0.226	6.957	15.66	8.531	16.25	48.01	8.46	0.0081	0.0047	0.145	0.326	0.178	0.338
C9729 post dup	25 - 27.5	0.0570	0.143	6.288	14.66	8.009	16.5	45.7	7.27	0.0012	0.0031	0.138	0.321	0.175	0.361
C9667 pre	27.5 - 30	1.204	1.586	7.347	18.77	3.060	5.076	37.05	13.89	0.0325	0.0428	0.198	0.507	0.083	0.137
C9667 pre dup	27.5 - 30	1.212	1.682	1.398	18.36	5.095	6.853	34.60	14.23	0.0350	0.0486	0.0404	0.531	0.147	0.198
C9729 post	27.5 - 30	0.007	0.012	3.781	3.981	5.116	10.94	23.84	0.900	0.0003	0.0005	0.159	0.167	0.215	0.459
C9667 pre	30 - 32.5	0.160	0.120	4.115	12.27	1.901	4.933	23.5	7.37	0.0068	0.0051	0.175	0.522	0.081	0.210
C9729 post	30 - 32.5	0.322	0.489	4.898	6.818	1.809	5.942	20.28	5.03	0.0159	0.0241	0.242	0.336	0.089	0.293
C9673 pre	25 - 27.5	0.773	0.343	2.447	9.705	1.376	3.977	18.62	9.78	0.0415	0.0184	0.131	0.521	0.074	0.214
C9728 post	25 - 27.5	0.703	0.160	0.537	0.580	0.386	0.625	2.99	1.51	0.235	0.0535	0.180	0.194	0.129	0.209
C9673 pre	27.5 - 30	0.338	0.124	5.901	17.91	3.505	21.93	49.71	17.02	0.0068	0.0025	0.119	0.360	0.071	0.441
C9728 post	27.5 - 30	0.050	0.147	3.886	4.006	6.86	37.74	45.83	0.984	0.0011	0.0032	0.0848	0.087	0.131	0.823
C9673 pre	30 - 32.5	1.815	1.748	10.52	28.76	3.897	8.924	55.67	30.54	0.0326	0.0314	0.1889	0.517	0.070	0.160
C9728 post	30 - 32.5	0.041	0.314	6.493	11.42	15.45	102.70	136.4	7.27	0.0003	0.0023	0.0476	0.084	0.113	0.753
C9677 pre	20 - 22.5	2.875	5.693	10.94	34.05	10.44	17.68	81.68	35.55	0.0352	0.0697	0.134	0.417	0.128	0.217
C9730 post	20 - 22.5	1.168	1.480	3.197	4.722	1.252	2.091	13.91	6.63	0.084	0.1064	0.230	0.340	0.090	0.150

Borehole	Depth (ft)	Extract 1 (µg/g)	Extract 2 (µg/g)	Extract 3 (µg/g)	Extract 4 (µg/g)	Extract 5 (µg/g)	Extract 6 (µg/g)	Sum (µg/g)	1000h CO_3 (µg/g)	Extr. 1 fraction	Extr. 2 fraction	Extr. 3 fraction	Extr. 4 fraction	Extr. 5 fraction	Extr. 6 fraction
C9677 pre	22.5 - 25	2.768	5.230	5.456	28.52	4.657	10.08	56.72	25.09	0.0488	0.0922	0.0962	0.503	0.082	0.178
C9730 post	22.5 - 25	0.202	0.387	11.655	11.28	5.020	5.677	34.22	8.83	0.0059	0.0113	0.3406	0.330	0.147	0.166
C9677 pre	25 - 27.5	3.432	3.781	5.733	41.64	9.704	11.64	75.93	45.34	0.0452	0.0498	0.0755	0.548	0.128	0.153
C9677 pre dup	25 - 27.5	3.252	2.764	3.876	40.994	7.176	11.825	69.89	48.42	0.0465	0.0396	0.0555	0.587	0.103	0.169
C9730 post	25 - 27.5	0.091	0.171	4.890	6.450	2.720	4.297	18.62	4.35	0.0049	0.0092	0.2626	0.346	0.146	0.231
C9677 pre	27.5 - 30	3.263	3.448	1.358	17.82	4.078	5.588	35.55	17.99	0.0918	0.097	0.0382	0.501	0.115	0.157
C9730 post	27.5 - 30	0.030	0.080	3.225	5.089	4.964	6.493	19.88	1.12	0.0015	0.004	0.1622	0.256	0.250	0.327
C9683 pre	22.5 - 25	0.171	0.117	0.473	4.673	1.965	2.881	10.28	5.37	0.0166	0.0114	0.046	0.455	0.191	0.280
C9732 post	22.5 - 25	0.009	0.075	0.910	0.954	1.113	2.630	5.69	0.125	0.0015	0.0131	0.1599	0.168	0.196	0.462
C9683 pre	25 - 27.5	0.301	0.064	0.204	4.376	2.258	3.097	10.3	5.48	0.0292	0.0062	0.0198	0.425	0.219	0.301
C9732 post	25 - 27.5	0.030	0.046	1.066	1.730	1.739	2.910	7.52	0.687	0.0040	0.0061	0.1418	0.230	0.231	0.387
C9734 post(a)	22.5 - 25	0.237	0.011	3.050	3.326	6.010	30.92	43.56	7.015	0.0055	0.0002	0.0700	0.0764	0.138	0.710
C9734 post(a)	27.5 - 30	0.043	0.051	1.935	3.226	7.222	12.17	24.65	0.285	0.0017	0.0021	0.0785	0.131	0.293	0.494
C9735 post(a)	22.5 - 25	0.080	0.023	16.93	12.18	11.28	25.83	66.33	20.35	0.0012	0.0003	0.2553	0.184	0.170	0.389
C9735 post(a)	27.5 - 30	0.010	0.012	1.944	2.462	2.662	3.617	10.71	1.207	0.0009	0.0011	0.182	0.230	0.249	0.338
C9736 post(a)	22.5 - 25	0.136	0.312	1.666	1.533	0.361	0.838	4.847	2.092	0.0281	0.0645	0.344	0.316	0.0745	0.173
C9736 post(a)	25 - 27.5	0.182	0.364	1.841	2.606	0.573	1.427	6.993	2.267	0.0260	0.0521	0.2633	0.3727	0.0819	0.204

(a) Unpaired post injection sample

Table 4.3. Average change uranium in sequential extractions.

Extraction	Pre-Injection (% U)	Post-Injection (% U)	Change (% U)	Pre-Injection U (µg/g)	Post-Injection U (µg/g)	ΔU (Post-Pre) in U (µg/g)
1	3.20 ± 2.09	1.97 ± 0.55	-1.12 ± 5.69	1.78 ± 1.49	0.225 ± 0.299	-1.54 ± 1.48
2	3.48 ± 2.82	1.47 ± 2.53	-1.94 ± 3.47	2.13 ± 1.87	0.252 ± 0.340	-1.86 ± 1.76
3	10.3 ± 6.32	15.4 ± 6.99	5.99 ± 9.41	5.50 ± 3.96	4.53 ± 3.44	-0.732 ± 4.56
4	48.3 ± 6.73	21.78 ± 9.16	-25.4 ± 9.33	25.2 ± 13.9	6.65 ± 5.11	-18.2 ± 10.9
5	12.4 ± 4.94	15.9 ± 5.01	4.36 ± 4.39	6.52 ± 4.84	5.29 ± 4.85	-0.953 ± 5.21
6	22.4 ± 8.69	39.1 ± 18.4	18.8 ± 16.3	11.1 ± 6.88	15.7 ± 23.3	5.43 ± 23.1
1000-h CO_3	42.5 ± 9.60	15.6 ± 14.3	-26.9 ± 11.8	21.8 ± 12.4	3.97 ± 3.34	-17.7 ± 11.4

The total uranium extracted in pre-injection sediments averaged 52.21 ± 26.93 µg/g (minimum 10.28, maximum 94.08 µg/g), whereas the total uranium extracted in post-injection sediment (most of which was from pre-/post-borehole pairs, so within 3.28 ft) averaged 33.98 ± 31.68 µg/g (minimum 2.99, maximum 136.4 µg/g). A comparison of 19 pre- and post-injection sediment pairs (i.e., boreholes within 3.28 ft, at the same depth) indicates that the total U in post-injection sediments was 33.2 ± 50.8% less than in pre-injection sediments, or 19.9 µg/g. This is consistent with extraction 4, showing an 18.6 µg/g decrease from pre- to post-injection samples. This decrease in extraction 4 (acetic acid pH 2.3) from pre- to post-injection samples indicates that one or more phases that contain uranium are decreasing due to the polyphosphate injection solution. This was evaluated in batch experiments, which showed that the moderate-solubility hydrous U silicates (e.g., uranophane and Na-boltwoodite) and U substituted in calcite are somewhat soluble in the polyphosphate solution (Figure 4.21). These results confirm that the polyphosphate injection solution did not advect mobile and other labile uranium out of the injection area (leaving only immobile U in extraction 6), as extraction 6 (8 M HNO_3) from pre- to post-injection samples in 19 pre/post pairs increased on average from 11.1 ± 6.9 to 15.7 ± 23.3 µg/g.

As noted above, because pre-injection boreholes are injection wells, and most post-injection boreholes are located within 3.61 ft (1.1 m), some decrease in aqueous and adsorbed U is caused by advection during injection, although aqueous U in the polyphosphate solution will precipitate (Mehta et al. 2016; Mehta 2017; Szecsody et al. 2012). In addition, most solubilized U from U carbonates and hydrous U silicates would also likely precipitate with phosphate at greater distance from the injection well, or at greater depth (see Figure 4.11 and Figure 4.19). In a previous laboratory study of polyphosphate treatment of 300 Area sediments, a complete mass balance of uranium was possible (Szecsody et al. 2012). In that study, the average of 20 1-D leach experiments with the same sediment showed that untreated sediments leached 7.9 ± 1.8% of the total extracted uranium in the first 7.5 pore volumes, whereas polyphosphate-treated sediments leached 0.13 ± 0.06% of the total extracted uranium in the first 7.5 pore volumes (including leaching during polyphosphate treatment).

There are some slight trends with depth for the uranium sequential extraction data (Figure 4.10 and Figure 4.11). Given the injection well injection screens are at 16 to 21 ft depth and 26 to 31 ft depth, the pre- to post-injection total uranium from sequential extractions increases slightly with depth likely due to the downward movement of solutions (Figure 4.11a). The 1000-h carbonate extraction pre- to post-injection uranium from 1000-h carbonate extraction also increases slightly with depth (Figure 4.11b). However, changes in individual sequential liquid extractions 1 through 6 show no trend with depth (Figure 4.11a to f). Trends are more apparent with fraction uranium in different extractions, as shown in the Section 4.2.2 likely due to the ability to normalize based on the total U in each sample as U is not evenly distributed within the subsurface.

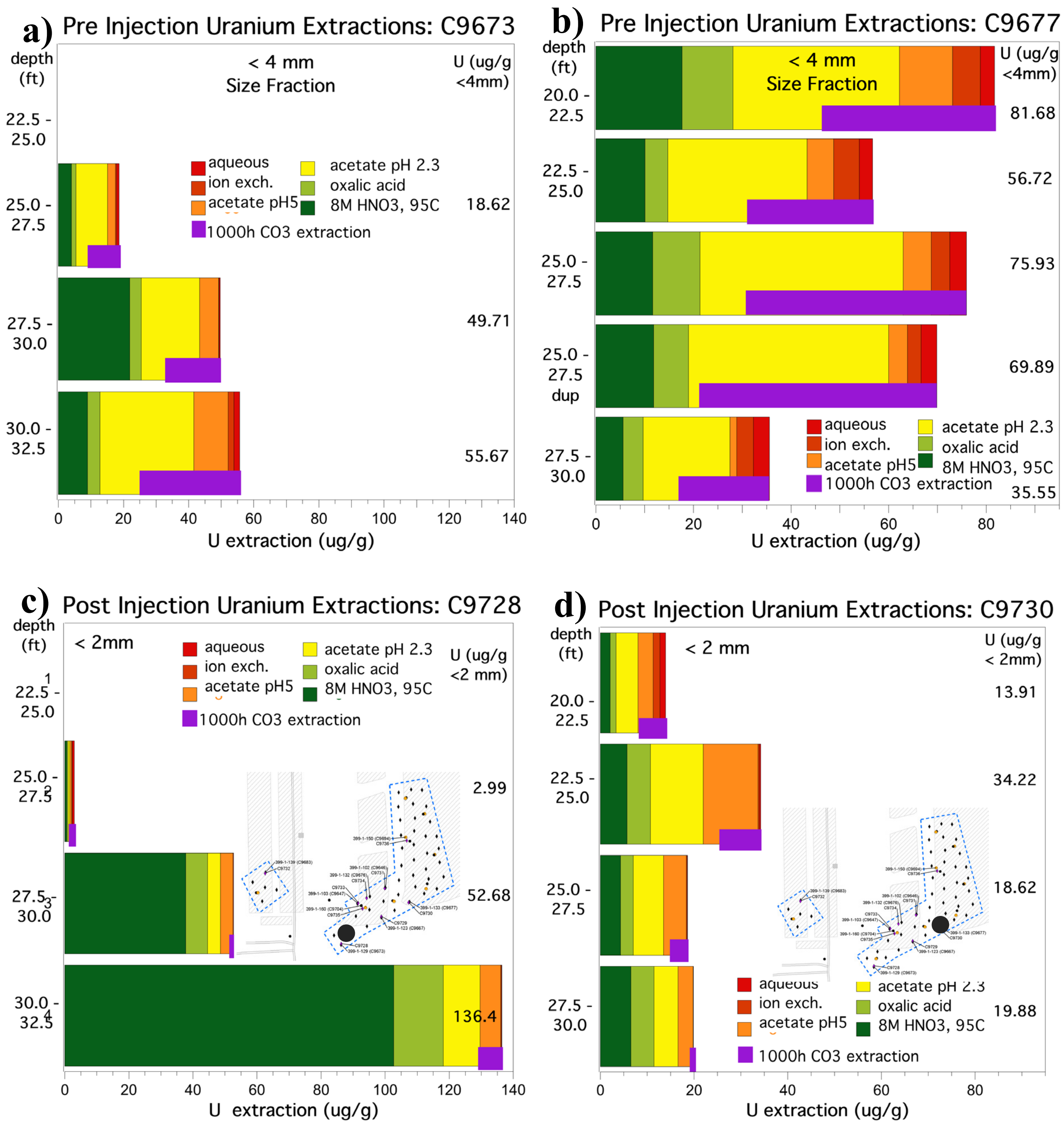

Figure 4.6. Sequential extraction (multicolored stack bar graphs) and carbonate extraction (purple) of uranium in pre- and post-injection borehole pairs: C9673 (a) and C9728 (c), and C9677 (b) and C9730 (d). Borehole locations are shown in (c) and (d).

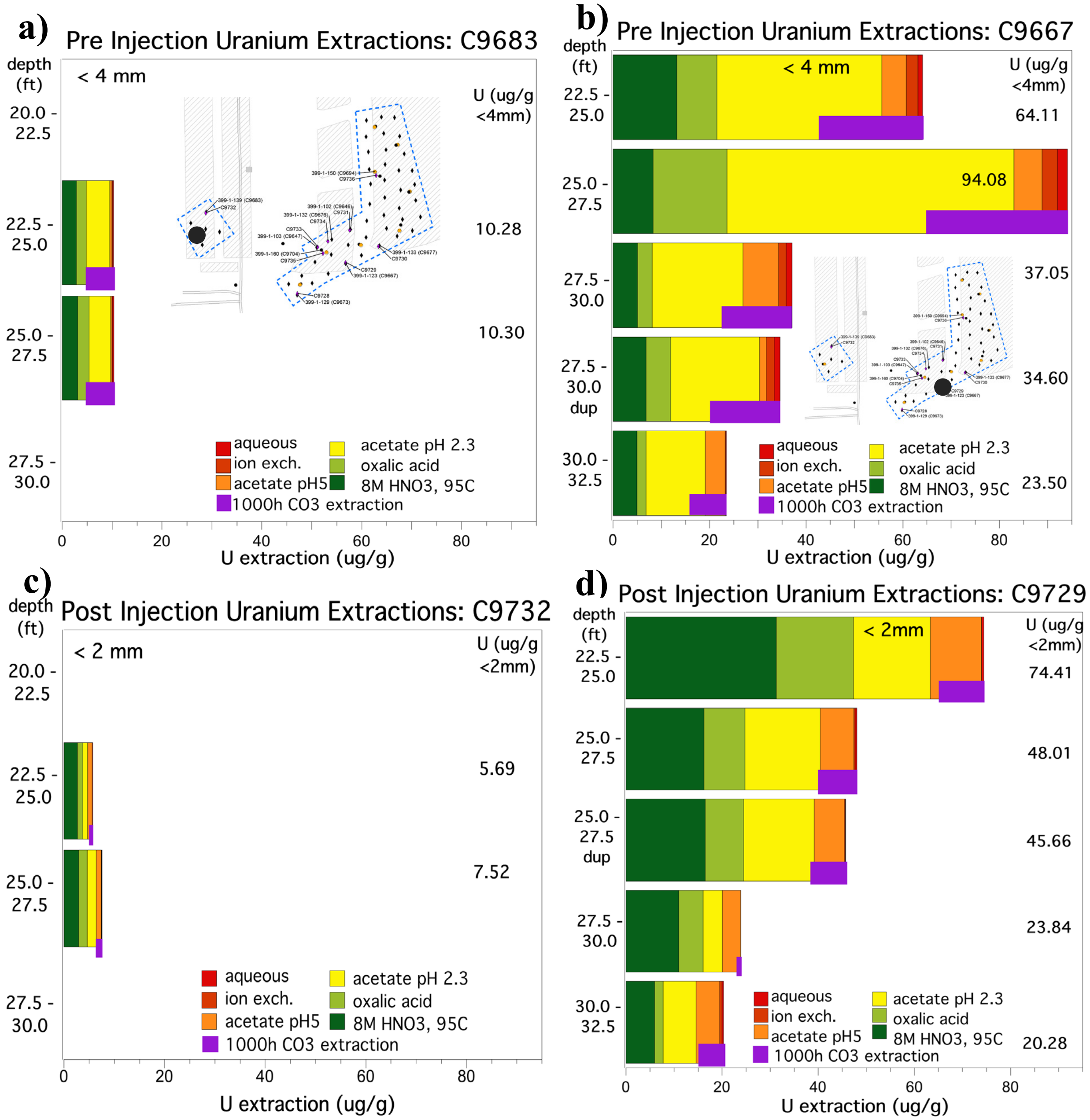

Figure 4.7. Sequential extraction (multicolored stack bar graphs) and carbonate extraction (purple) of uranium in pre- and post-injection borehole pairs: C9683 (a) and C9732 (c), and C9667 (b) and C9729 (d). Borehole locations are shown in (a) and (b).

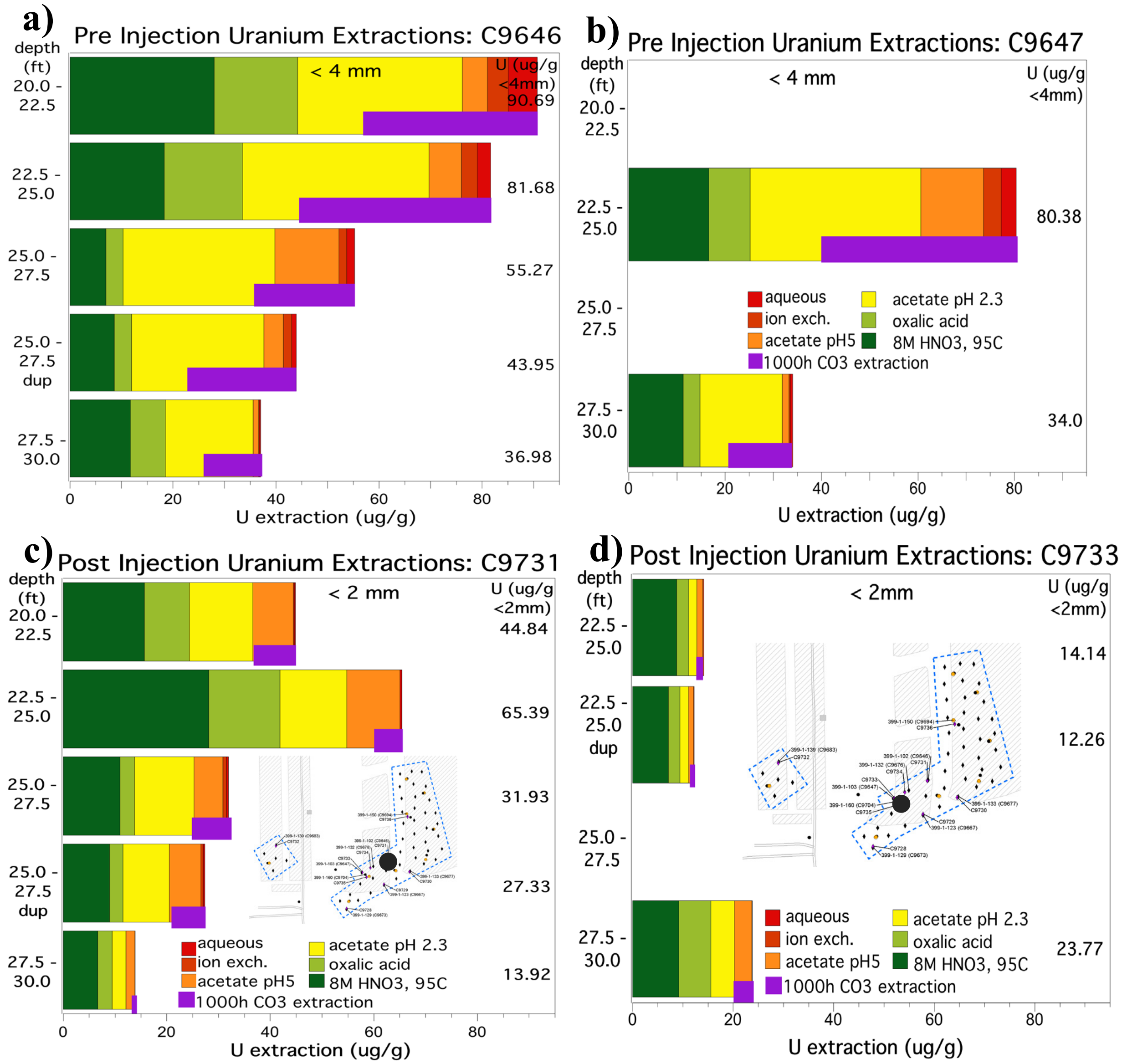

Figure 4.8. Sequential extraction (multicolored stack bar graphs) and carbonate extraction (purple) of uranium in pre- and post-injection borehole pairs: C9646 (a) and C9731 (c), and C9647 (b) and C9733 (d). Borehole locations are shown in (c) and (d).

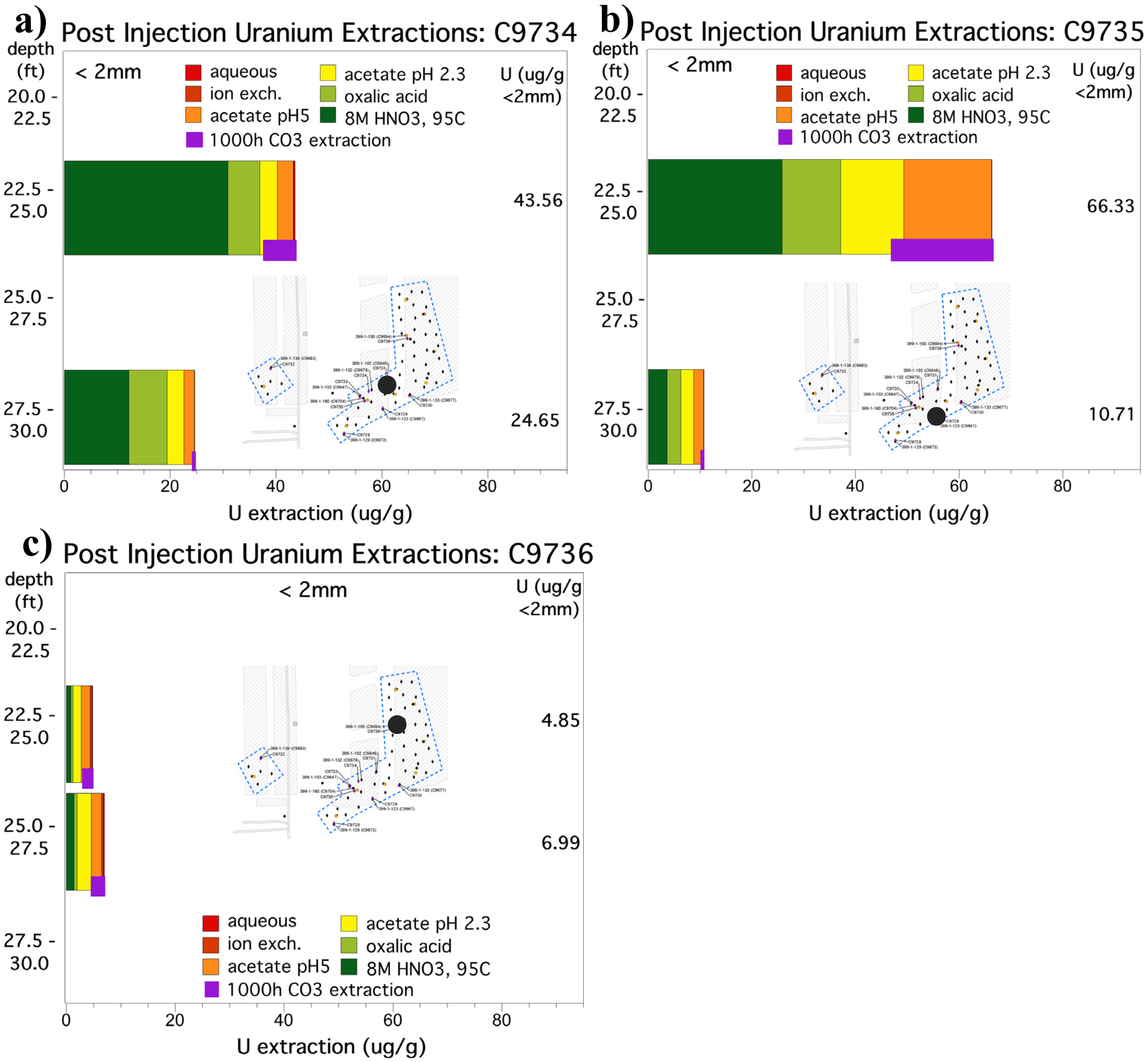

Figure 4.9. Sequential extraction (multicolored stack bar graphs) and carbonate extraction (purple) of uranium in unpaired post-injection borehole: C9734 (a), C9735 (b), and C9736 (c).

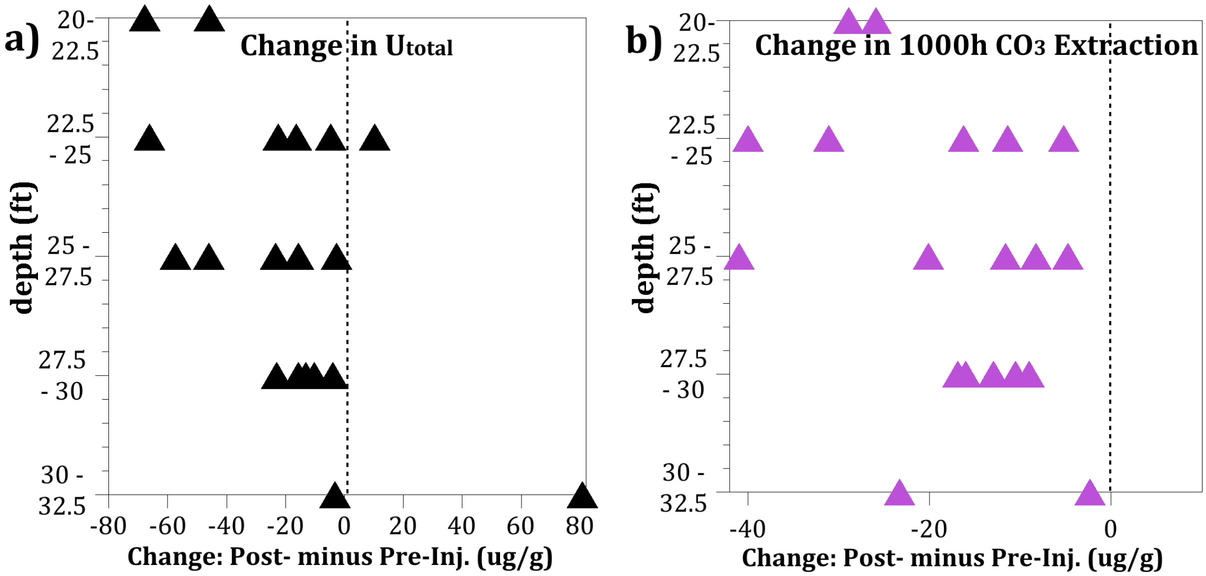

Figure 4.10. Depth discrete changes in sequential liquid extraction of: a) total U (in µg/g) and b) 1000-h carbonate extraction with the dotted line shown as a reference line representing zero change based on total U in post minus pre injection extractions.

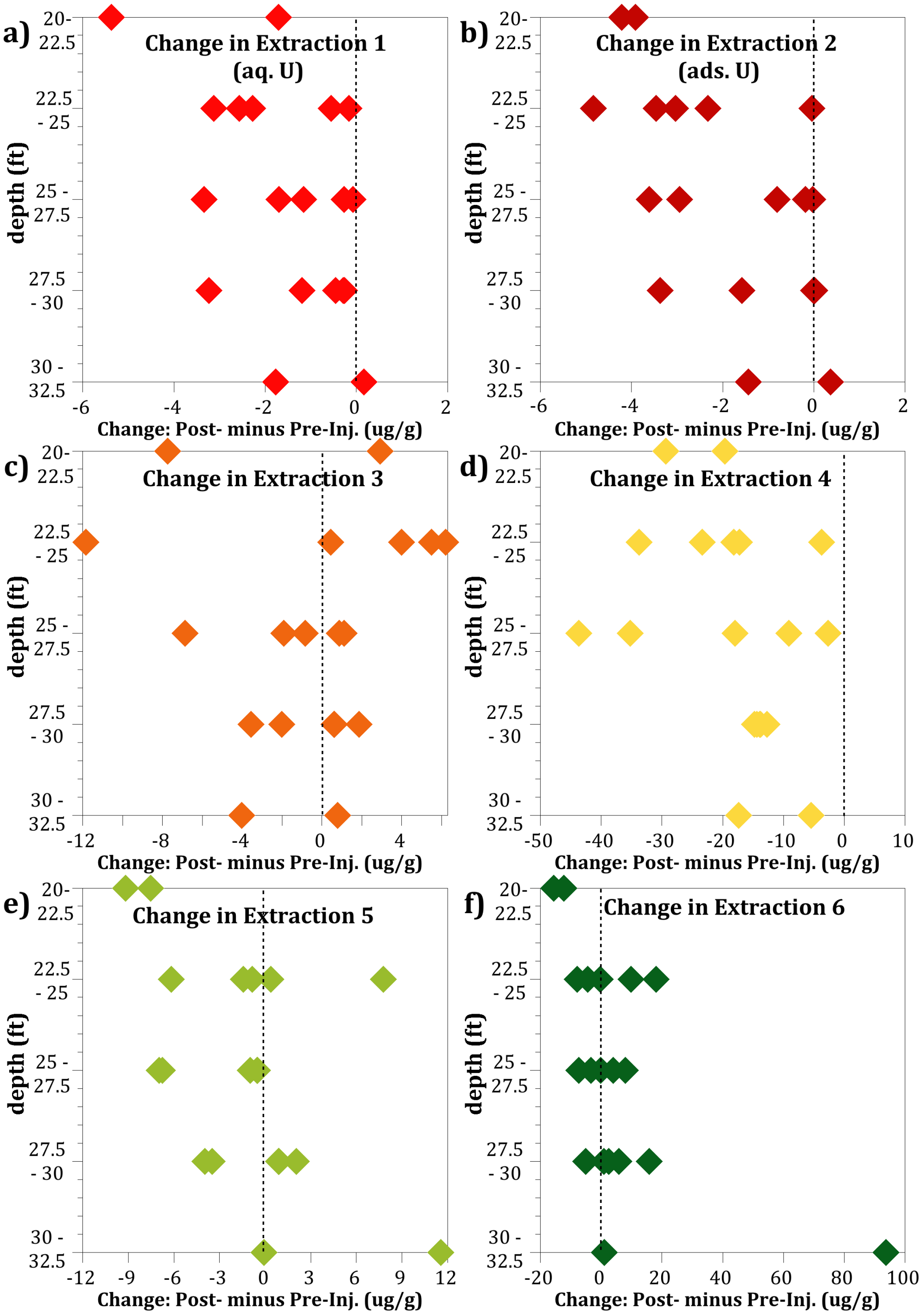

Figure 4.11. Depth discrete changes in individual sequential liquid extractions of U (in µg/g) for extractions 1 (a), 2 (b), 3 (c), 4 (d), 5 (e), and 6 (f) from pre to post-injection sediments with the dotted line shown as a reference line representing zero change based on total U in post minus pre-injection extractions.

4.2.2 Fraction of Uranium in Different Phases from Sequential Extractions

The fraction of uranium in the different sequential extractions enables a direct comparison of pre- and post-injection data (Figure 4.12 through Figure 4.15). In nearly all cases, the most mobile uranium (i.e., in aqueous and adsorbed extractions 1 and 2) decreased from 6.7% to 3.4% with polyphosphate treatment (Table 4.3.), and the least mobile (i.e., lowest solubility) uranium (i.e., extraction 6, 8 mol/L nitric acid at 95°C) increased from 22.4% to 39.1%, likely due to (a) precipitation of autunite group minerals, (b) apatite coating on U phases, and (c) adsorption of aqueous U complexes onto apatite (described further in Section 5.2). Although the fraction of aqueous and adsorbed uranium is small (total 6.7%), this fraction has the potential to migrate offsite. Extraction 4 (pH 2.3 acetic acid) also decreased by 26.5%, which is likely from the dissolution of Na-boltwoodite, uranophane, or other higher-solubility U precipitate (Table 4.3., also described further in Section 5.1). Uranium in extractions 3 and 4 (acetate and acetic acid) is only partially mobile as shown by carbonate extractions (previous section) and leach experiments (Section 4.2.3, Figure 4.20).

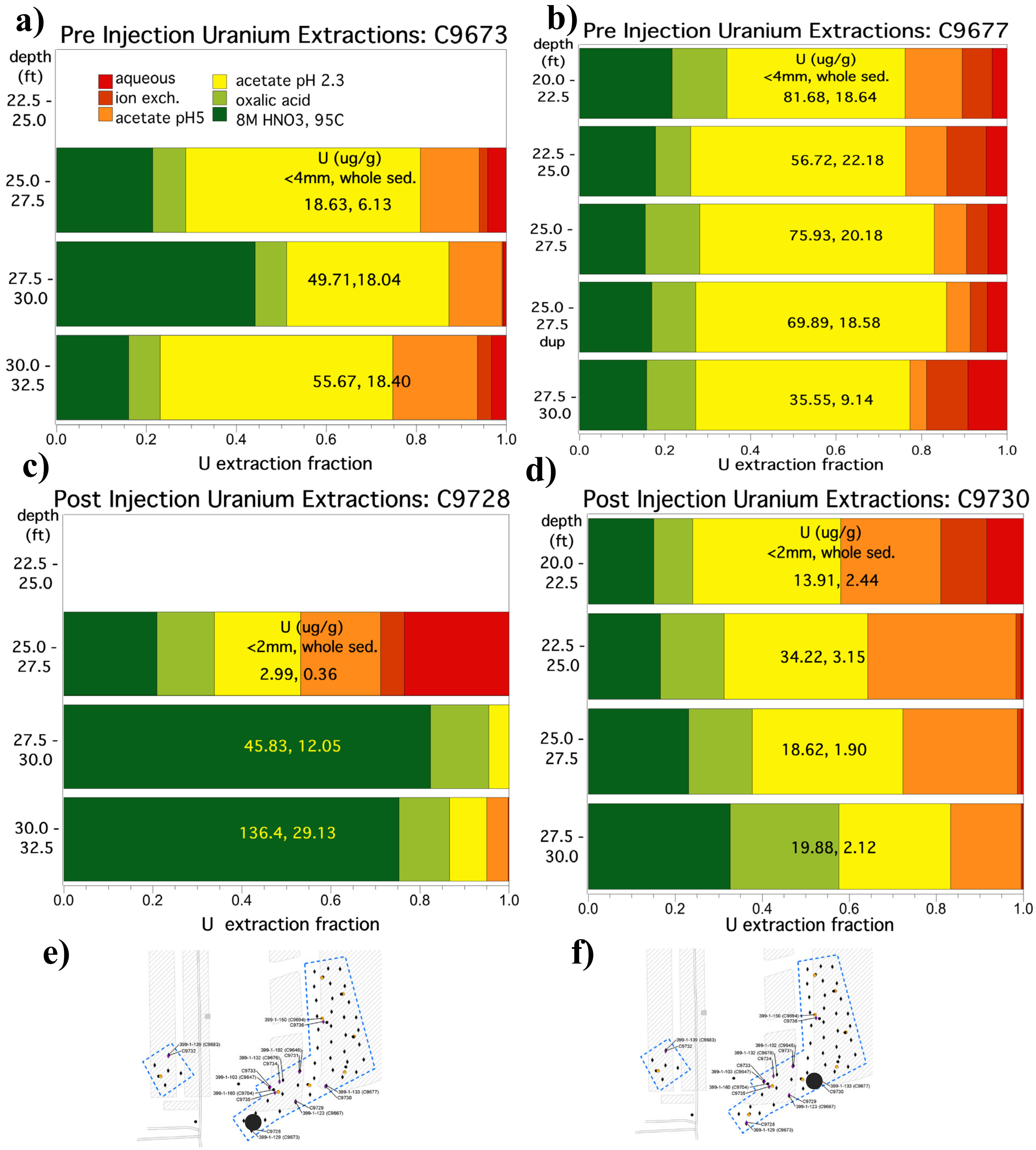

Figure 4.12. Fraction uranium in different sequential extractions in pre- and post-injection borehole pairs: C9673 (a) and C9728 (c), and C9677 (b) and C9730 (d). Borehole locations are shown in (e) and (f).

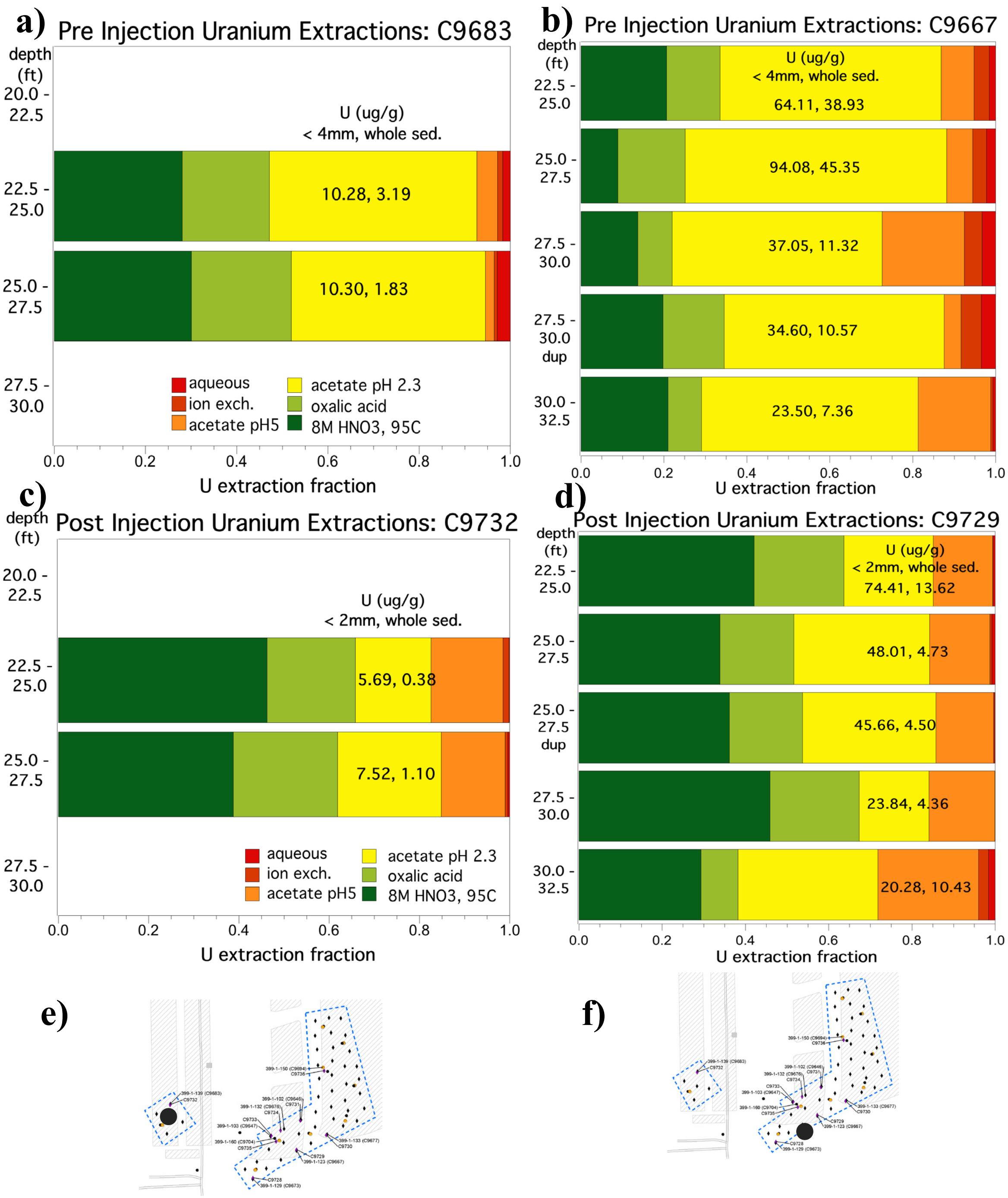

Figure 4.13. Fraction uranium in different sequential extractions in pre- and post-injection borehole pairs: C9683 (a) and C9732 (c), and C9667 (b) and C9729 (d). Borehole locations are shown in (e) and (f).

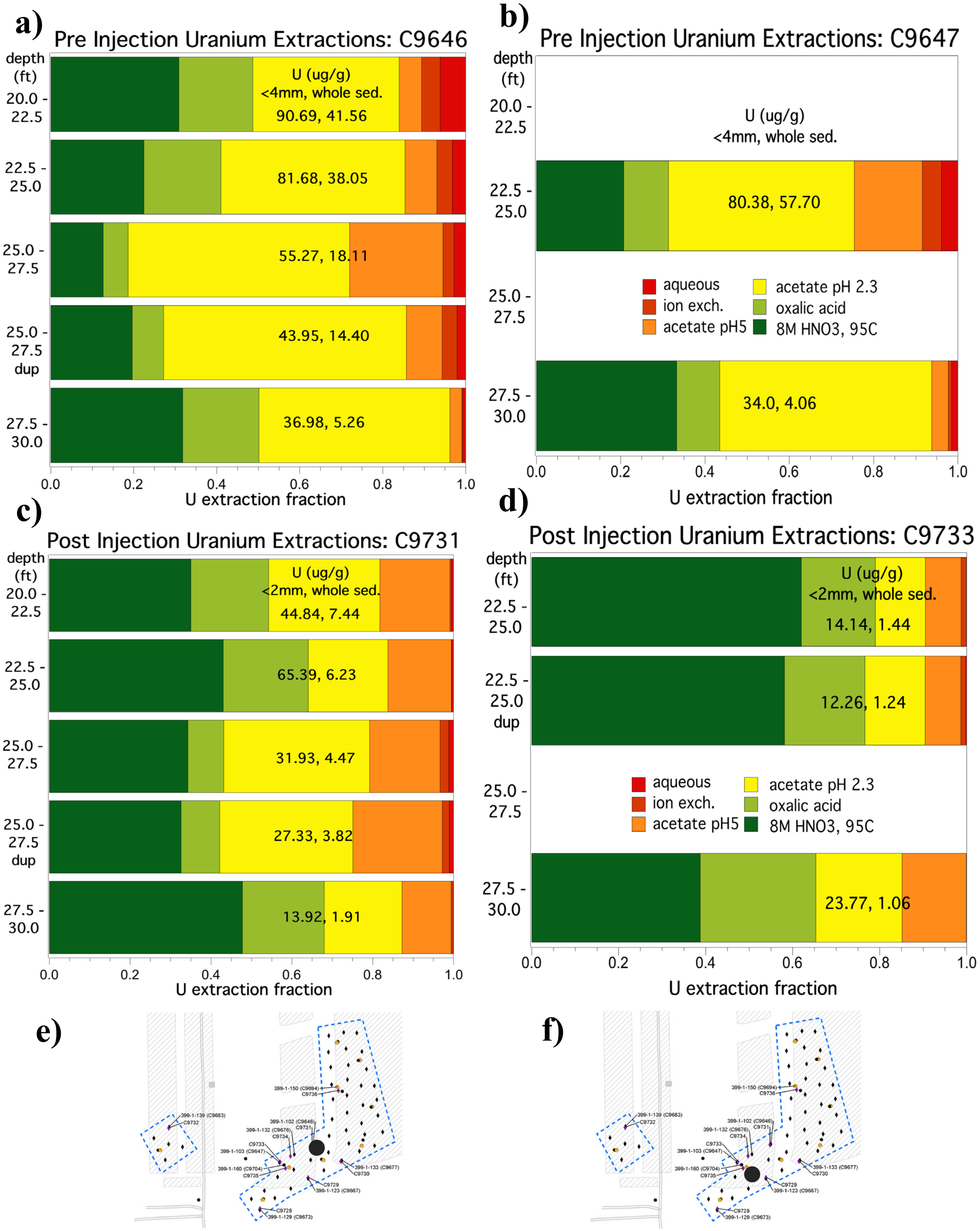

Figure 4.14. Fraction uranium in different sequential extractions in pre- and post-injection borehole pairs: C9646 (a) and C9731 (c), and C9647 (b) and C9733 (d). Borehole locations are shown in (e) and (f).

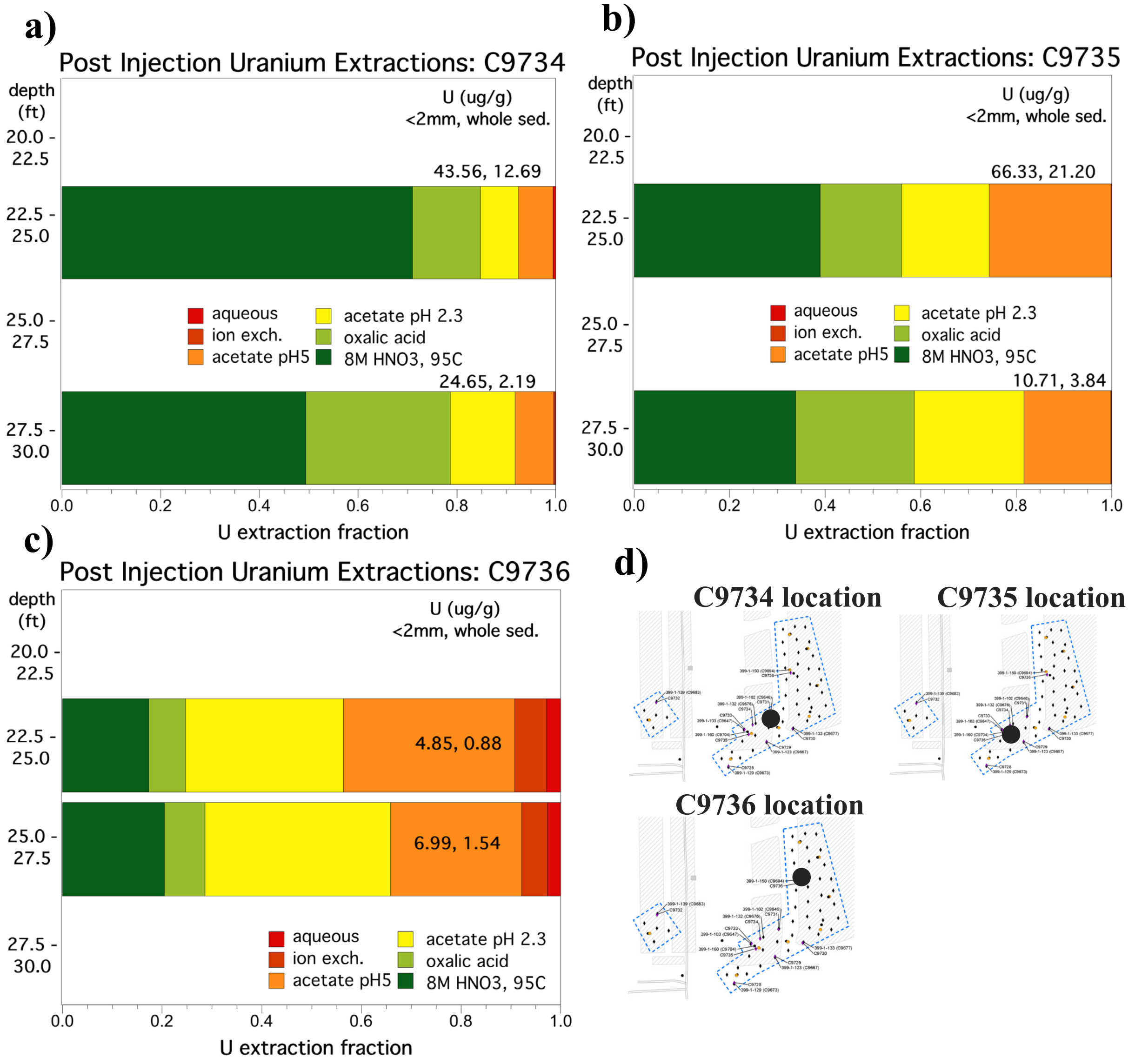

Figure 4.15. Fraction uranium in different sequential extractions in unpaired post-injection boreholes: C9734 (a), C9735 (b), and C9736 (c). Borehole locations shown in (d).

Tracking changes in each of the sequential extractions for pre- and post-injection pairs shows that the average changes (as indicated in Table 4.3.) vary to some extent between sediment pairs, but are consistent (Figure 4.16 and Figure 4.17). Extractions 1, 2, and 4 showed a decrease in contrast to extractions 5 and 6 with an increase from pre- to post-injection (Figure 4.17). Although all boreholes had sediment samples at different depths and generally shallower (i.e., 20 ft) depths had a higher uranium concentration, there was no trend with depth between pre- and post-injection total uranium (Figure 4.18). There are some slight trends with depth for the uranium sequential extraction data (Figure 4.19). Given the injection well injection screens are at 16 to 21 ft depth and 26 to 31 ft depth, the pre- to post-injection total uranium from sequential extractions (in fraction of total U) increases slightly with depth (Figure 4.19a). However, changes in individual sequential liquid extractions 1 through 6 and the 1000-h carbonate extraction show no trend with depth (Figure 4.19b and Figure 4.19a to f). These results are consistent with observations based on U mass.

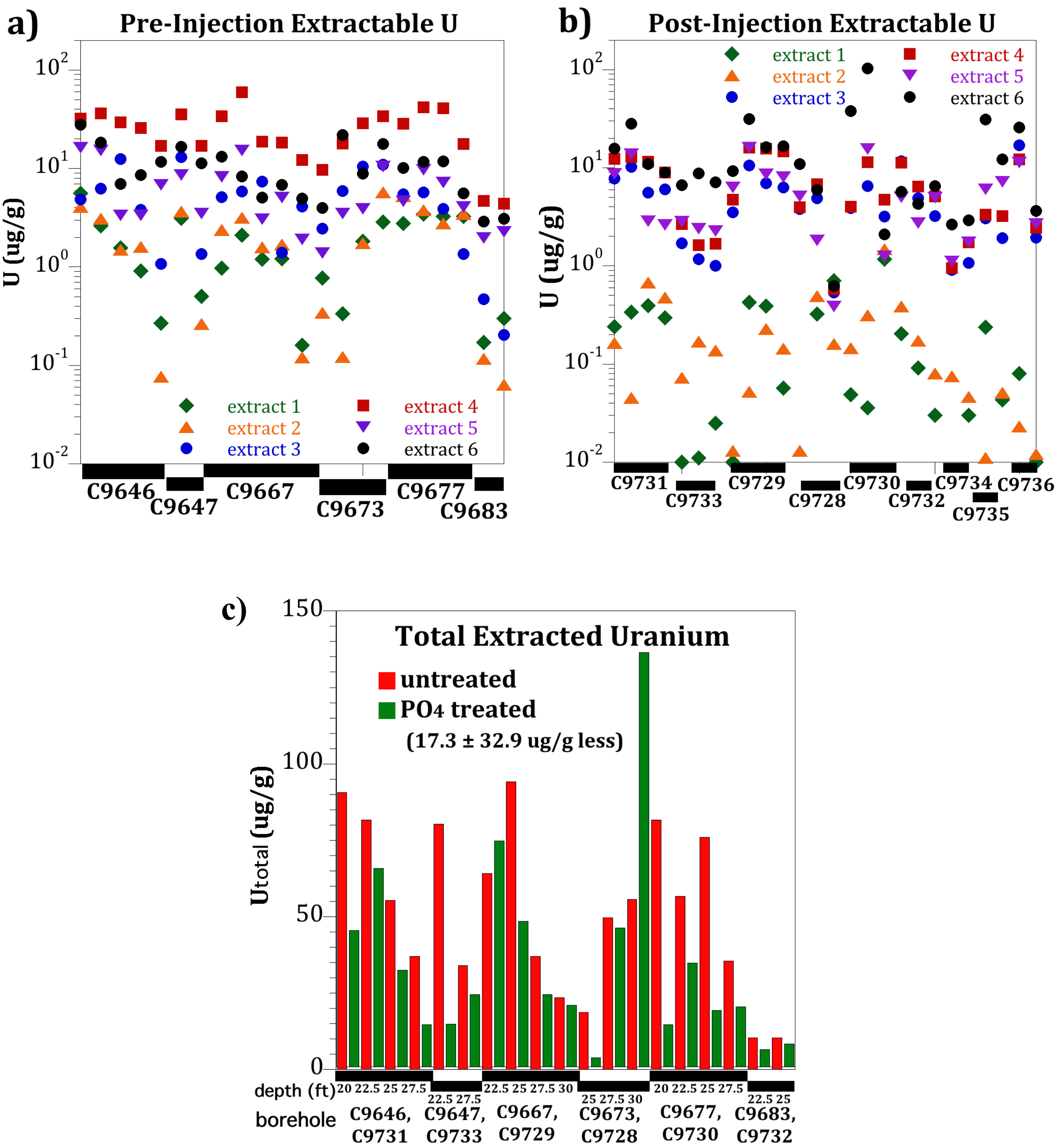

Figure 4.16. Uranium sequential data for 19 pre- (a) and post-injection (b) pairs (in µg/g), with the total uranium in (c) [average ± one standard deviation of all pairs inset into figure in (c)].

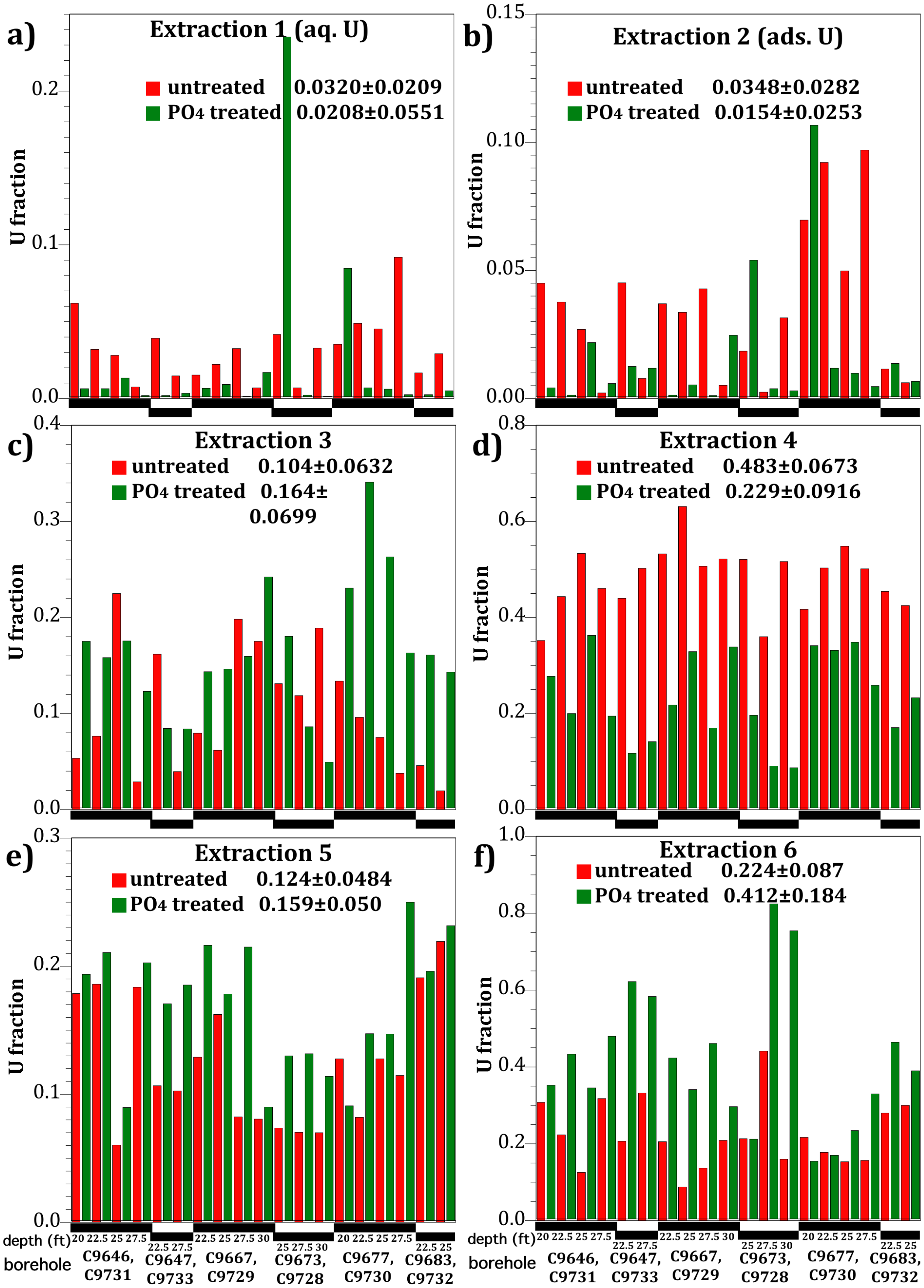

Figure 4.17. Average change of the fraction uranium in 19 pre- and post-injection pairs of sequential extractions for (a) extraction 1, (b) extraction 2, (c) extraction 3, (d) extraction 4, (e) extraction 5, and (f) extraction 6 for untreated sediments (red) and post-treated sediments (green) with the average ± one standard deviation for all pairs inset into each graph for both treated and untreated sediments.

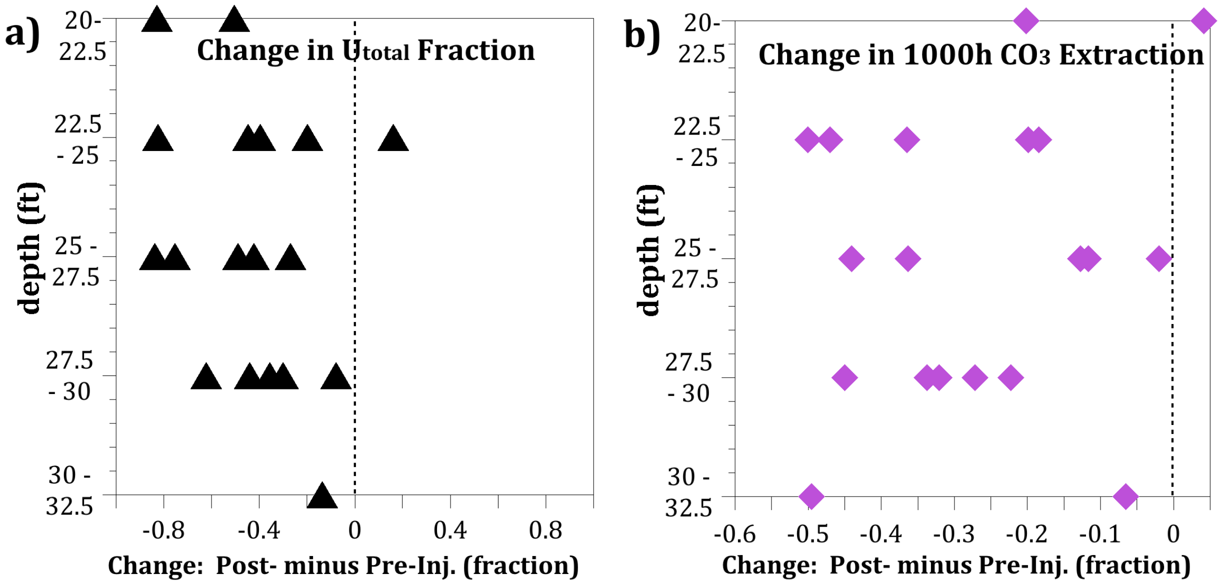

Figure 4.18. Depth discrete changes in sequential liquid extraction (as fraction of total U) (a), and 1000-h carbonate extraction (b), reported as post- minus pre-injection U fraction.

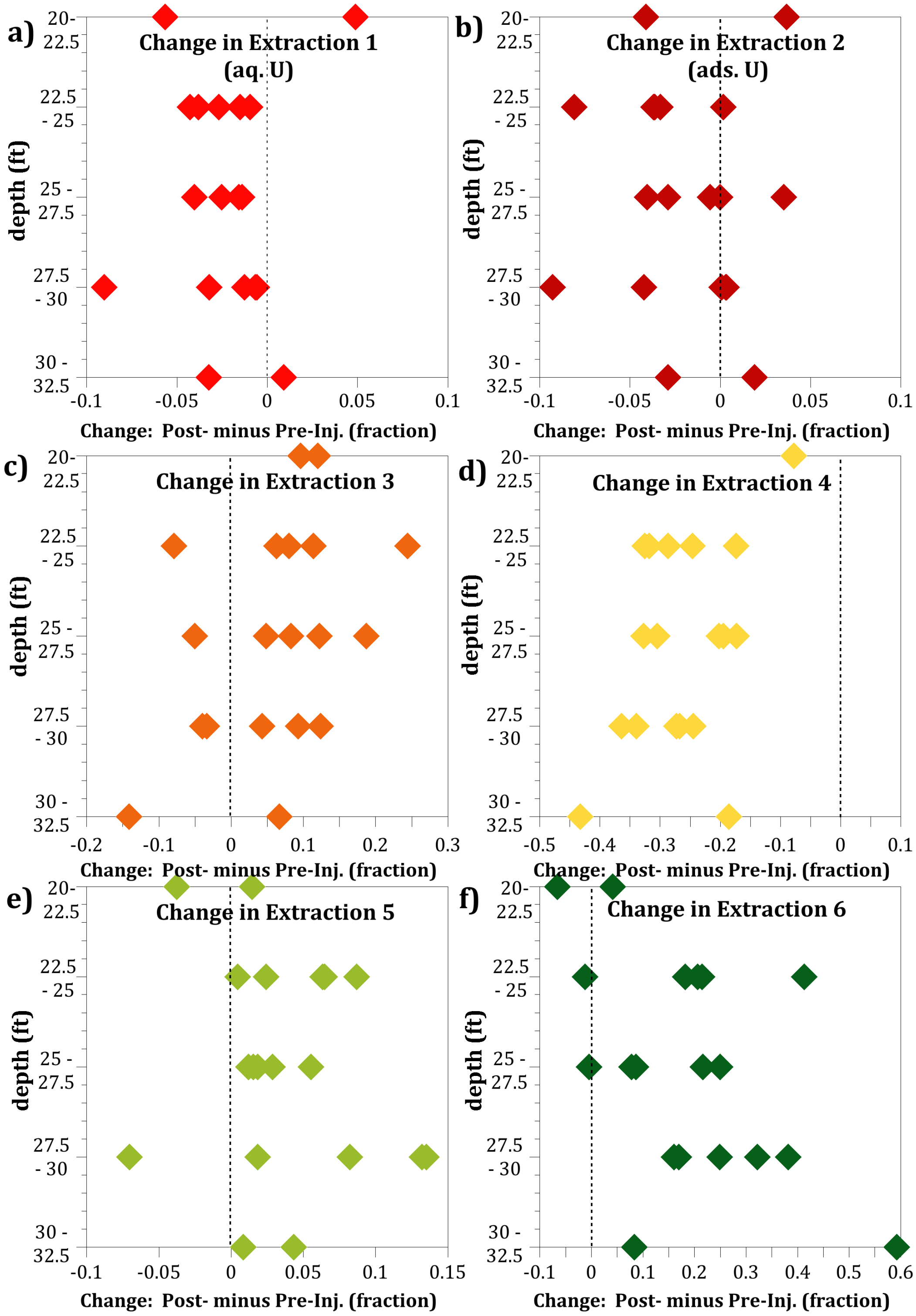

Figure 4.19. Depth discrete changes in individual sequential liquid extractions (as fraction U): extraction 1 (a), extraction 2 (b), extraction 3 (c), extraction 4 (d), extraction 5 (e), and extraction 6 (f) from pre to post-injection sediments with the dotted line representing zero change in U fraction based on post- minus pre-injection extraction results.

4.2.3 Measurement of Solid and Liquid Phase Carbonate in Sediments

Given the significant decrease that occurred in extracted uranium between pre- and post-injection sediments, further analysis of sediments was done to quantify the carbonate minerals (e.g., calcite) that can incorporate uranium. Inorganic carbon analysis was conducted on five pre-/post-injection pairs to evaluate whether calcite was decreasing as a result of the polyphosphate injection. The inorganic carbon analysis of five pre-/post-injection pairs shows nearly all sediments were below detection limits (< 0.01% inorganic C), which was surprising as Hanford groundwater is naturally Ca- and Mg-carbonate-saturated Natural Hanford formation samples average 1.91 ± 1.71% calcite, and Ringold Formation sediment samples average 0.68 ± 0.92% calcite (Xie et al. 2003). It is possible that the acidic co-contaminants in the waste (i.e., 900 tons of nitric acid; see Section 2.0 for additional description of co-contaminants) have dissolved a significant portion of the calcite. In addition, previous characterization of NPP sediments also showed little calcite (Arai et al. 2007). Therefore, the inorganic carbon analysis of pre- and post-injection sediments indicates it is unlikely that uranium-carbonates are dissolving with polyphosphate injection, within the detection limits of this analysis technique (i.e., 0.01% C). The 0.01% carbon detection limit (8.33×10^{-6} mol C/g) is still higher than the highest uranium concentration in the sediment (i.e., 136 µg U/g is 5.71×10^{-7} mol U/g), so U could still be present as U carbonates as well as hydrous silicates.

Table 4.4. Inorganic and organic carbon analysis of selected sediments.

Borehole	Start Depth (ft)	End Depth (ft)	HEIS #	Inorganic C %C(a)	Organic C %C(a)
C9673	27.5	30.0	B388X3	< 0.01	0.0169
C9728	27.5	30.0	B3P2L0	< 0.01	0.0087
C9673	30.0	32.5	B388X6	< 0.01	0.031 ± 0.0035
C9728	30.0	32.5	B3P2L4	< 0.01	0.0094
C9647	22.5	25.0	B38B71	< 0.01	0.038 ± 0.008
C9733	22.5	25.0	B3P2Y2	< 0.01	0.0098
C9647	27.5	30.0	B38B77	< 0.01	0.023 ± 0.003
G9733	27.5	30.0	B3P300	< 0.01	0.036 ± 0.008
C9667	30.0	32.5	B388N9	< 0.01	
C9729	30.0	32.5	B3P2N4	0.038 ± 0.009	
C9735	27.5	30.0	B3P340	< 0.001	

(a) Each sample run in duplicate or triplicate; MDL 0.01

Organic carbon analysis was additionally conducted on four pre-/post-injection sediment pairs to evaluate any potential influence of organic co-contaminants, but values are of moderate concentration (i.e., 0.01% to 0.036%) compared to background organic carbon in the 100N sediments of 0.001% (Szecsody et al. 2010), so there may be some organic contaminants.

Because the solid phase inorganic carbon analysis indicated that low calcite concentration was present, the significant decrease in uranium in extraction 4 from pre- to post-injection sediments is unlikely to be caused by a decrease in U in carbonates. To confirm which uranium minerals dissolve in which extractions, sequential extractions were also conducted with five uranium minerals. Results show that (a) most U in carbonates dissolves in extraction 3 and the balance in extraction 4, (b) the hydrous U-silicates uranophane and Na-boltwoodite dissolve slightly in extraction 3 and mainly in extraction 4, and (c) U-phosphate minerals autunite and torbernite do not dissolve until extraction 6 (i.e., 8 M nitric acid, Figure 4.20a, first three minerals from Szecsody et al. 2012). This indicates that it is possible that if

U were not present in carbonates in the 300 Area but were present as hydrous silicates, these phases would be dissolved in extraction 4. As an additional test, if uranophane and other minerals (or adsorbed U) are present in Hanford sediments, the uranophane is still extracted primarily in extraction 4, indicating that the presence of other sediment minerals was not influencing uranophane dissolution (i.e., uranophane was not coated by less soluble non-U minerals) (Figure 4.20b, data from Szecsody et al. 2012).

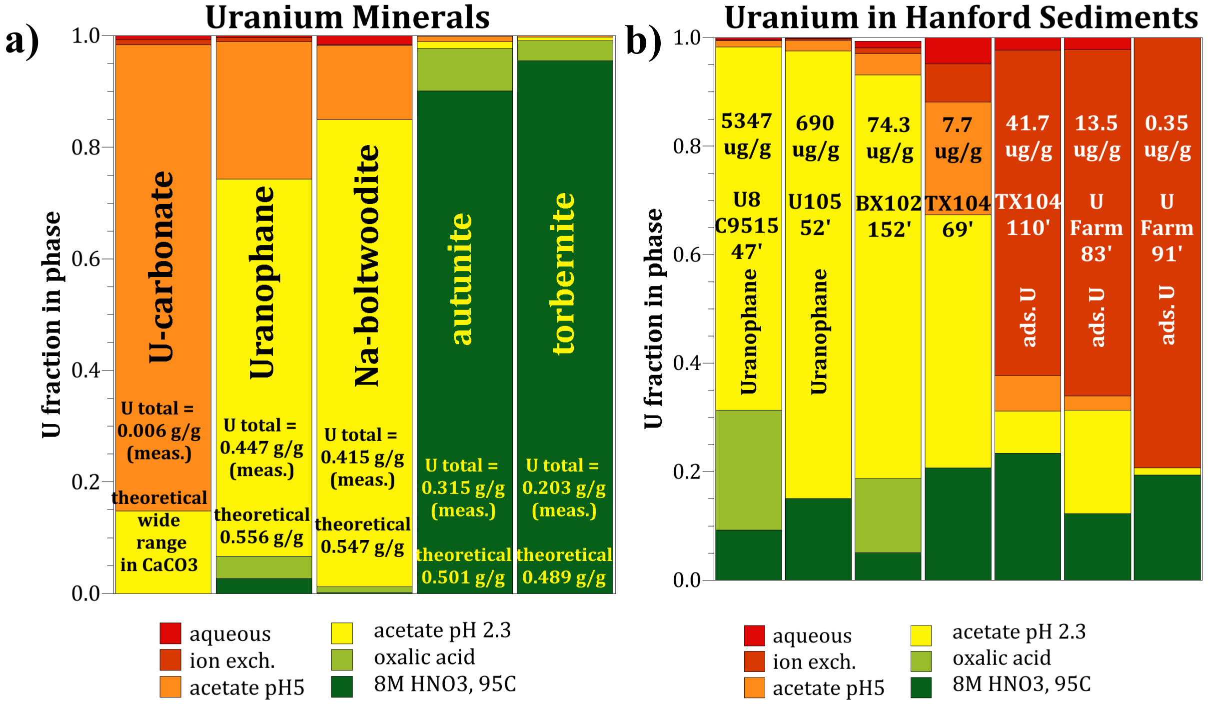

Figure 4.20. Sequential extraction of (a) uranium minerals, and (b) uranium-contaminated 300 Area Hanford sediments.

Extractions were additionally conducted on post-injection sediments to measure the pore water carbonate remaining 6 months after injection. These extractions were conducted with 20 g of wet sediment with 20 mL of DI water. The measured aqueous inorganic carbon values in the diluted water were then calculated back to pore water concentration, given the moisture content and inorganic carbon measured in the DI water. The eight post-injection sediments that were measured had the highest specific conductance in the 1-D leach experiments (Section 4.3) and showed pore water carbonate ranging from 52.5 to 837 mg/L (Table 4.5). For comparison, two pre-injection samples had pore water carbonate ranging from 60.2 to 1060 mg/L, with natural groundwater at 165 mg/L. The 1060-mg/L carbonate in C9647 may be from Stage A injections. The low aqueous carbonate values in post-injection sediments in most boreholes indicate that the high carbonate in the injection water (median HCO_3^- during injection of 3680 mg/L, respectively, as measured by CHPRC) either precipitated (but post-injection solid phase carbonate values were low, Table 4.4) or advected downgradient. Further, conductivity of samples further indicates that either precipitation or advection of injection solutions occurred due to the relatively low conductivity as compared to injection solutions (median of 11510 µS/cm during injection, as measured by CHPRC).

Table 4.5. Aqueous pore water carbonate and conductivity in pre- and post-injection sediments based on 1:1 DI water to sediment suspensions (carbonate) and 1-D leach columns (specific conductivity).

Borehole	Depth (ft)	Pre- or Post- Inj.	Pore Water CO_3 (mg/L)[(a)]	SpC[(b)] (µS/cm)
C9732	22.5-25'	Post-	87.6	1525
C9728	27.5-30'	Post-	81.9	2190
C9729	25-27.5	Post-	106.	1323
C9733	22.5-25'	Post-	74.7	2280
C9731	22.5-25'	Post-	837	1318
C9731	27.5-30'	Post-	71.0	1432
C9734	27.5-30'	Post-	52.5	1468
C9736	25-27.5'	Post-	576	468
C9673	27.5-30'	Pre-	60.2	615
C9647	22.5-25'	Pre-	1062	792
C9647	22.5-25'	Pre-	1058	792
Groundwater[(c)]	-	-	127. ± 6.3	480 ± 33.3
Columbia River[(d)]	-	-	70 ± 7.0	138 ± 10.3
Inject Solution[(e)]	-	-	5048 ± 233	11377 ± 1552

(a) MDL = 0.5 mg/L
(b) Maximum specific conductivity (SpC) in 1-D leach column
(c) Monitoring during injection at well 399-1-2, NW of injection site, CHPRC, HCO_3^- instead of total CO_3
(d) Quarterly water monitoring in 2004 by USGS near Richland Pump House, HCO_3^- instead of total CO_3
(e) Monitoring skid during injection, CHPRC, HCO_3^- instead of total CO_3

4.2.4 Reaction of Uranium Minerals with the Polyphosphate Solution

Given that most post-injection boreholes were within 1 m (3 ft) of injection wells and the ~19-µg/g decrease in total U (pre- to post-injection sediment average) was similar to the ~18-µg/g decrease in extraction 4, it is possible that uranophane, Na-boltwoodite, and U in calcite (if present) are partially dissolved in the polyphosphate solution. Experiments conducted to evaluate the rate of dissolution of U-carbonate, uranophane, and Na-boltwoodite in the 70-mM polyphosphate injection solution showed that significant uranium carbonate is dissolved within 16 h in the polyphosphate solution (2.6%), but hydrous U silicates are also dissolved (maximum 0.16%) by 16 h (Figure 4.21). In this experiment, only the polyphosphate solution at pH 7.7 was reacted with the U minerals initially, approximating early times of solution injection at field scale. At 16 h, sufficient calcium (as calcium sulfate) was added to precipitate all of the phosphate, approximating polyphosphate solution reaction with desorbed Ca^{2+} from sediment minerals at field scale. During this second stage, the uranium initially dissolved was incorporated into phosphate precipitates (likely autunite group minerals), as the aqueous U concentrations for all experiments was < 12 µg/L.

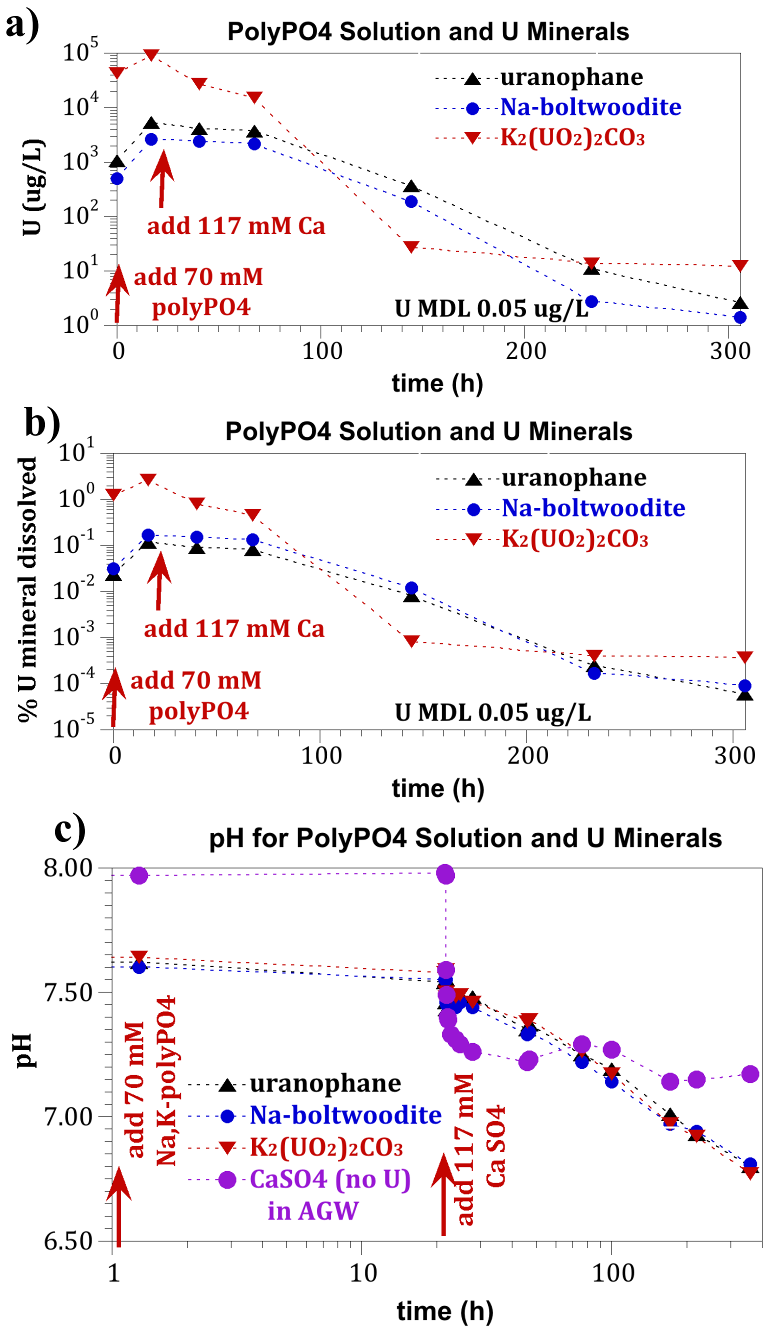

Figure 4.21. Dissolution of uranium carbonate and hydrous silicate minerals in a 70 mM polyphosphate solution (0 to 16 h), then with Ca^{2+} addition (>16 h): (a) aqueous U concentration, (b) fraction mineral dissolved, and (c) pH.

Given that high solubility uranium minerals (U in calcite, Na-boltwoodite, uranophane) can dissolve in the polyphosphate solution (Figure 4.21), field post-injection sediments that were collected at different distances from an injection well were evaluated to quantify whether some uranium was removed near the injection well as a result of the injection and precipitated at greater distance from the injection well. The uranium extraction results from one pre-injection borehole (C9647, which was also an injection well) are compared to post-injection boreholes with increasing distance (C9733, 3.4 ft lateral distance from C9647, Table 3.2 and C9735, 22.47 ft lateral distance from C9647). Results at the 22.5 to 25 ft depth (in all three boreholes) show that significant phosphate was injected (i.e., 1.2 to 2 mg/g in post-injection boreholes compared with 0.4 mg/g in the pre-injection borehole), and the total uranium is less at 3.4 ft lateral distance (Figure 4.22b) compared to the pre-injection borehole (Figure 4.22a), and somewhat elevated at 22.47 ft lateral distance (Figure 4.22c). In contrast, at the 27.5 ft depth, there is decreasing uranium with distance from the borehole, which is not consistent with the hypothesis. It is likely that the natural spatial heterogeneity of uranium in the sediment accounts for the significant variability observed, so this possible trend related to the polyphosphate injection is difficult to evaluate. In terms of the fraction of uranium at distance, there was also no trend of post-injection sediment uranium in extraction 6 (least mobile) or in extractions 1 and 2 (aqueous and adsorbed U, the most mobile U), or in extraction 4.

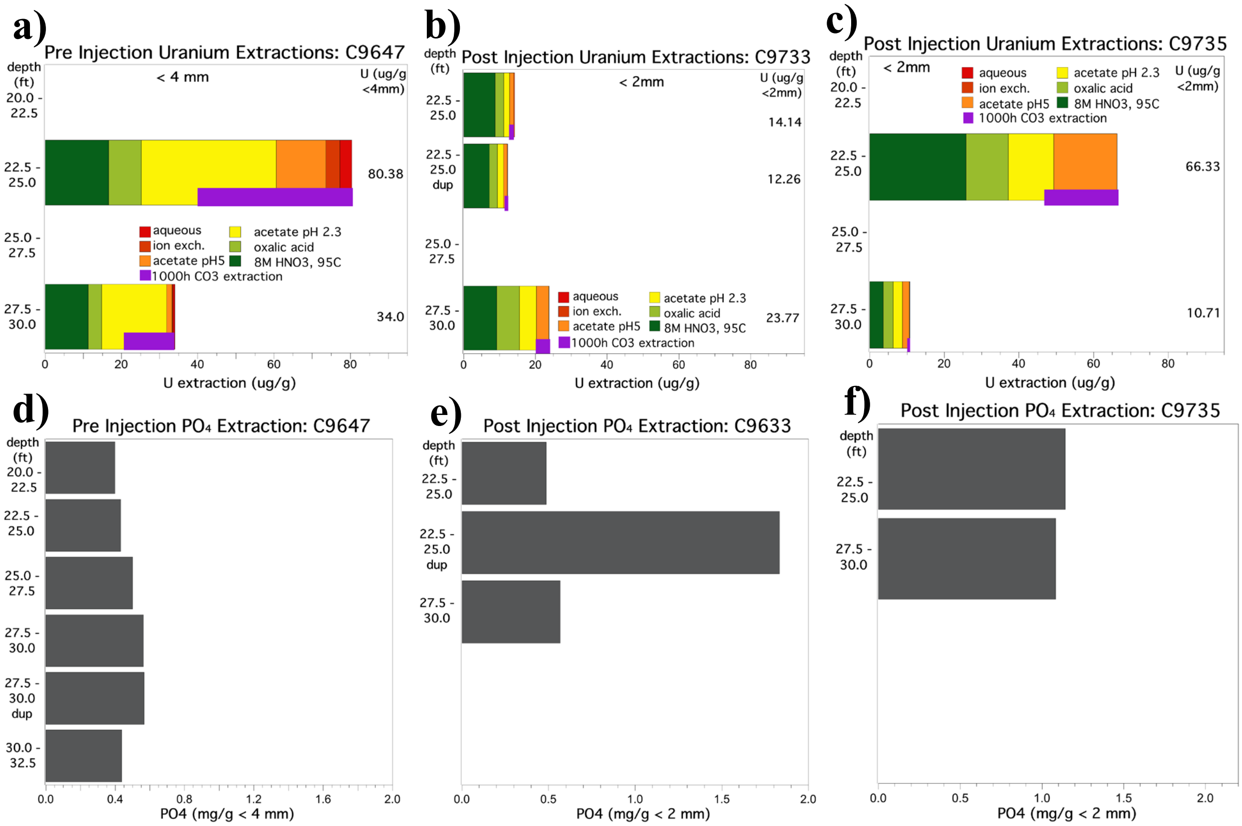

Figure 4.22. Comparison of uranium and phosphate in pre-injection borehole (and injection well) C9647 to post-injection boreholes C9733 (3.4 ft lateral distance) and C9735 (22.47 ft).

4.3 Uranium Leaching in Pre- and Post- PO_4-Treated Sediments

1-D leach experiments were conducted with pre- and post-injection sediments to measure the change in uranium mobility (i.e., uranium mass and concentration released) as a result of the field-injected phosphate treatment and to measure the rate of uranium release from the sediment. The post-injection sediments were collected 6 months after injection of phosphate (total phosphate targeted 8000 mg/L, median measured injection value of 8294 mg/L by CHPRC). At 6 months post injection, the phosphate would have (a) precipitated as apatite and/or autunite, (b) advected downgradient, and (c) remained aqueous in groundwater as phosphate. In these experiments, approximately 100 pore volumes of artificial groundwater were injected into the sediments and effluent samples were collected and analyzed for uranium concentration, pH, and specific conductivity. A bromide tracer was added to the artificial groundwater to track breakthrough of the injected groundwater, so the first few effluent samples (i.e., within 3 pore volumes) were measured for bromide, and additionally for phosphate. The effluent data during continuous flow show the uranium concentration over time (about 2 months) and the cumulative uranium as the total mass released from the sediment. Although the leach experiments were 2 months in length, 100 pore volumes are equivalent to a few years to tens of years at field scale, depending on the pore water or groundwater flow rate (i.e., sediment samples in the PRZ will have considerably less pore water flux than sediment samples in groundwater). Three stop-flow intervals ranging from 16 to 500 h were conducted in 1-D leach experiments at 2, 10, and 100 pore volumes to quantify the rate of uranium release from the sediment when (a) uranium is desorbing (at 2 pore volumes), (b) uranium is desorbing and some high-solubility U precipitates may be dissolving (i.e., at 10 pore volumes), and (c) moderate-solubility U precipitates may be dissolving (i.e., at 100 pore volumes). Uranium leach data are shown in this section, and supporting Br, PO_4, pH, and specific conductivity data are shown in Appendix D. All of the column physical size, sediment porosity, bulk density, and flow rate data are in Appendix C (Table C.1). The water-saturated column was weighed after 10 and 100 pore volumes for calculation of porosity, dry bulk density, and pore volume.

The 1-D columns are 30.48 cm in length and 2.36 cm diameter and filled with approximately 220 g of sediment. The sediment used in the columns is representative of the field sediment, in terms of fractions of clay, silt, sand, and gravel, although the gravel fraction used was < 12 mm (i.e., in order to fit in the column; Appendix B). The average dry bulk density of the 26 columns was 1.67 ± 0.14 g/cm^3, average porosity 0.405 ± 0.061, average pore volume 54.0 ± 8.13 mL, and average residence time 2.02 ± 0.39 h/pore volume (Appendix C, Table C.1). As received, the loose sediment was not fully water saturated when the column was packed. In order to not leach any uranium, the columns were slowly water saturated with artificial groundwater and no bromide tracer before each leach experiment. Artificial groundwater with the bromide tracer was then injected at the start of the leach experiment. The average bromide breakthrough was 0.880 ± 0.104, which indicates there may have been some air trapped in the column during the first few pore volumes. The total uranium reported on the uranium leach plots is the U from sequential extraction for the whole sediment, in contrast to < 2 mm reported for sequential extractions in the previous section. For five 1-D leach columns, sequential extractions were conducted with the post-leach sediments to check for changes in lability of solid phase uranium. These post-leach sequential extractions are shown next to the 1-D leach data. The fraction leaching between pre- and post-injection sediment is compared to remove any difference in the total extractable uranium in the different sediment samples.

4.3.1 Uranium Leaching in 1-D Experiments for Pre-/Post-Injection Pairs of Sediments

For the pre-injection borehole C9673 and corresponding post-injection borehole C9728, 1-D leach experiments at two depths showed that with high phosphate delivered (i.e., 900 mg/L phosphate remaining in the pore water 6 months after injection, Appendix D, Figure D.1), phosphate treatment resulted in significantly less uranium leaching (Figure 4.23). For the pre-injection borehole at 27.5 ft depth, the total extractable uranium was 18.04 µg/g and 1.0 µg/g uranium leached (5.6%), in contrast to the post-injection borehole with a total extractable uranium of 12.05 µg/g with 0.11 µg/g uranium leached (0.9%). For the pre-injection borehole at 30 ft depth, the total extractable uranium was 18.4 µg/g and 8.6 µg/g uranium leached (47%), in contrast to the post-injection borehole with a total extractable uranium of 29.13 µg/g with 0.18 µg/g uranium leached (0.6%).

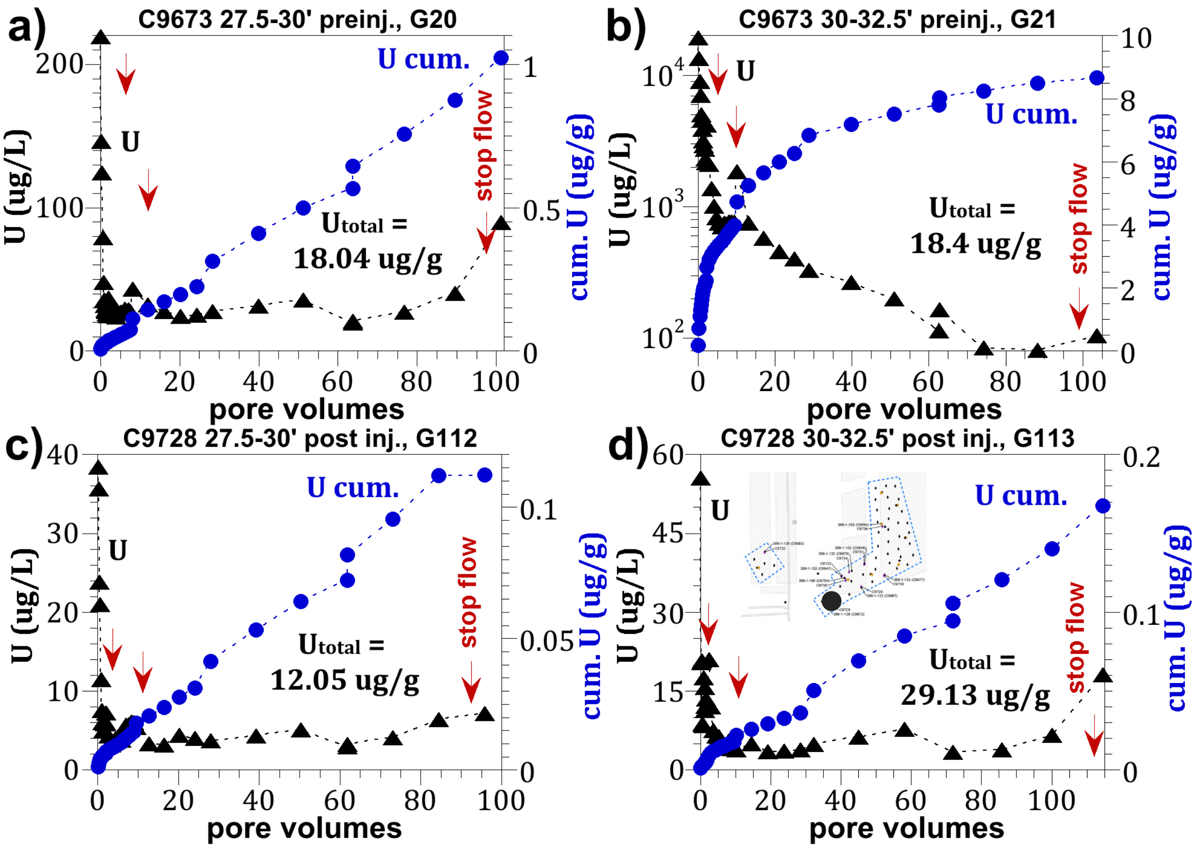

Figure 4.23. 1-D leach of pre-injection sediments from C9673 (a and b) and nearby post-injection sediments from C9728 (c and d). Borehole locations are shown in (d). Note that the U concentration (Y-axis) scales differ.

For the pre-injection borehole C9677 and corresponding post-injection borehole C9730 (3 feet away), 1-D leach experiments at 22.5-to-25 ft depth showed a low concentration of remaining aqueous phosphate (i.e., 90 mg/L; Appendix D, Figure D.2) in the pore water and less uranium leaching in post-injection sediments compared to pre-injection sediments (Figure 4.24). For the pre-injection borehole, the total extractable uranium was 22.2 µg/g and 11 µg/g uranium leached (~50%). In contrast, the post-injection borehole had a total extractable uranium of 3.15 µg/g and 1.1 µg/g uranium leached (35%). The fraction of U leaching is higher than the average in post injection sediments (12.8%), although given the low aqueous PO_4 (Appendix D, Figure D.2) and low precipitated PO_4 extracted (extraction 5, Figure 4.51e), this location may have received low phosphate delivery. Additional discussion of phosphate deliver is in Section 4.5.

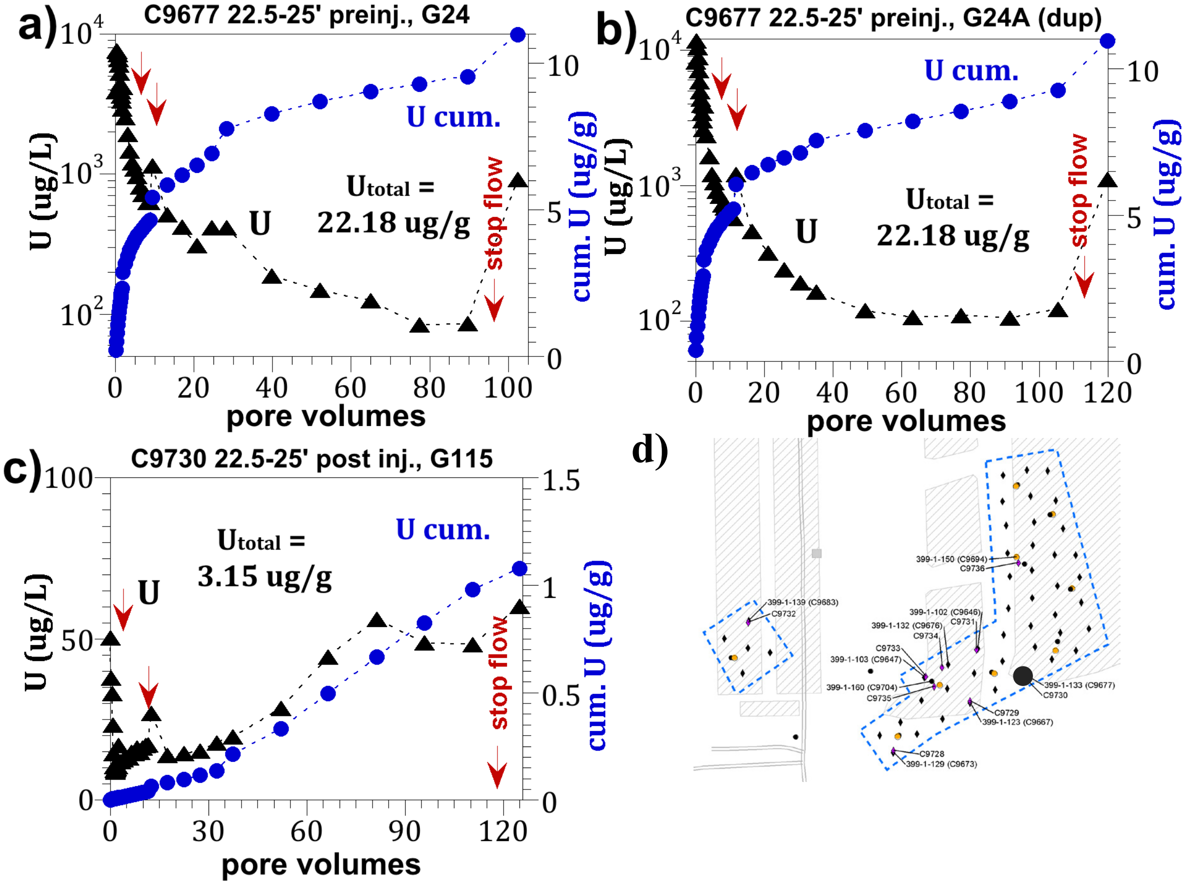

Figure 4.24. 1-D leach of pre-injection sediments from C9677 (a and duplicate experiment b) and nearby post-injection sediments from C9730 (c). Borehole locations are shown in (d). Note that the U concentration (Y-axis) scales differ.

For the pre-injection borehole C9683 and corresponding post-injection borehole C9732, 1-D leach experiments at 22.5 to 25 ft depth showed high remaining aqueous phosphate (i.e., 700 mg/L phosphate in the pore water, Appendix D, Figure D.3) and significantly less uranium leaching in post-injection sediments relative to pre-injection sediments (Figure 4.25). For the pre-injection borehole, the total extractable uranium was 3.19 µg/g and 0.65 µg/g uranium leached (~20%), in contrast to the post-injection borehole with a total extractable uranium of 0.383 µg/g with 0.023 µg/g uranium leached (6%). Note that the average background uranium in Hanford 300 area sediments is ~1.5 ug/g, so these sediments are at or close to background uranium.

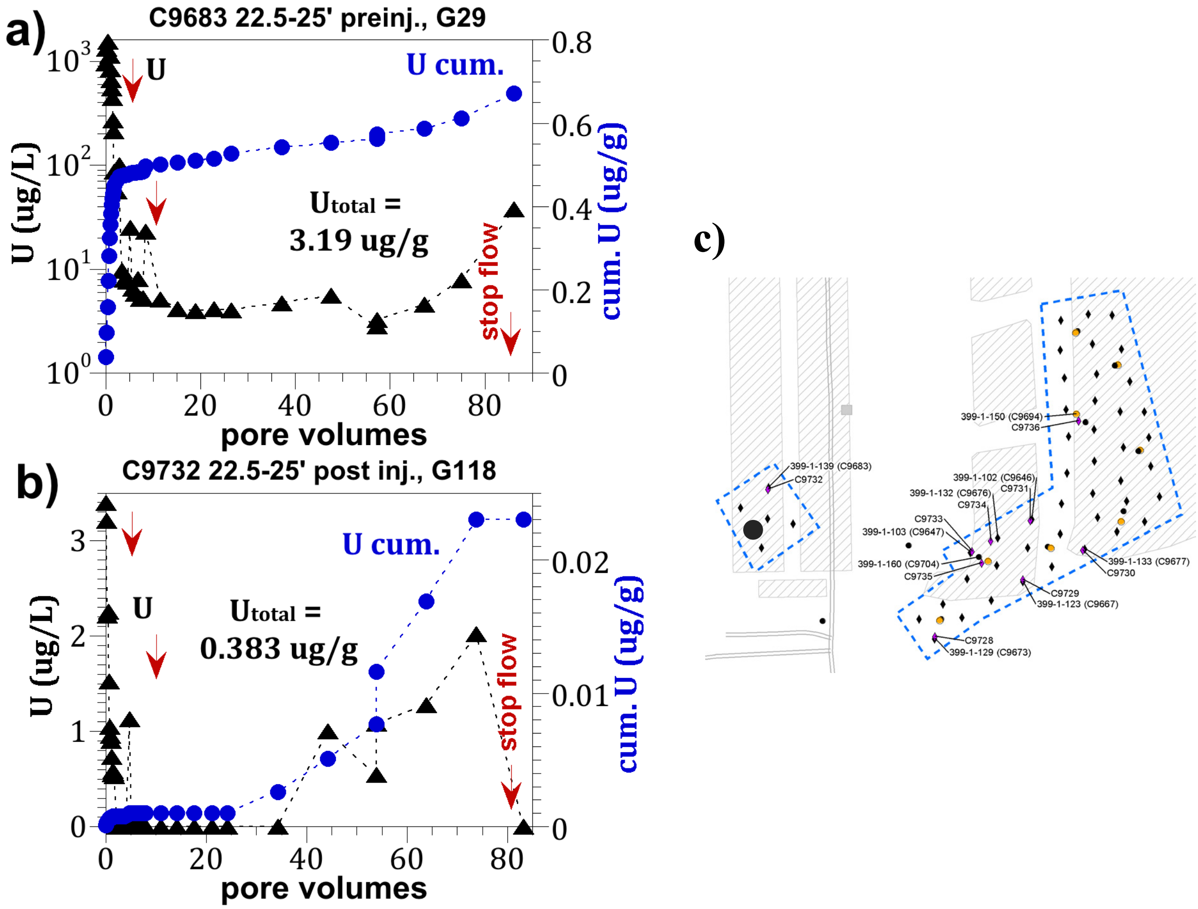

Figure 4.25. 1-D leach of pre-injection sediments from C9683 (a) and nearby post-injection sediment from C9732 (b). Borehole locations are shown in (c). Note that the U concentration (Y-axis) scales differ.

For the pre-injection borehole C9646 and corresponding post-injection borehole C9731, 1-D leach experiments at 22.5 to 25 ft depth showed high remaining aqueous phosphate (i.e., 600 to 800 mg/L Appendix D, Figure D.4), and significantly less uranium leaching in post-injection sediments compared to pre-injection sediments (Figure 4.26). For the pre-injection borehole at 22.5 ft, the total extractable uranium was 38.05 µg/g and 20.5 µg/g uranium leached (54%), in contrast to the post-injection borehole at 22.5 ft with a total extractable uranium of 6.23 µg/g with 0.24 µg/g uranium leached (4%). For the pre-injection borehole at 27.5 ft, the total extractable uranium was 5.26 µg/g and 0.97 µg/g uranium leached (18%), in contrast to the post-injection borehole at 27.5 ft with a total extractable uranium of 1.91 µg/g with 0.04 µg/g uranium leached (2%).

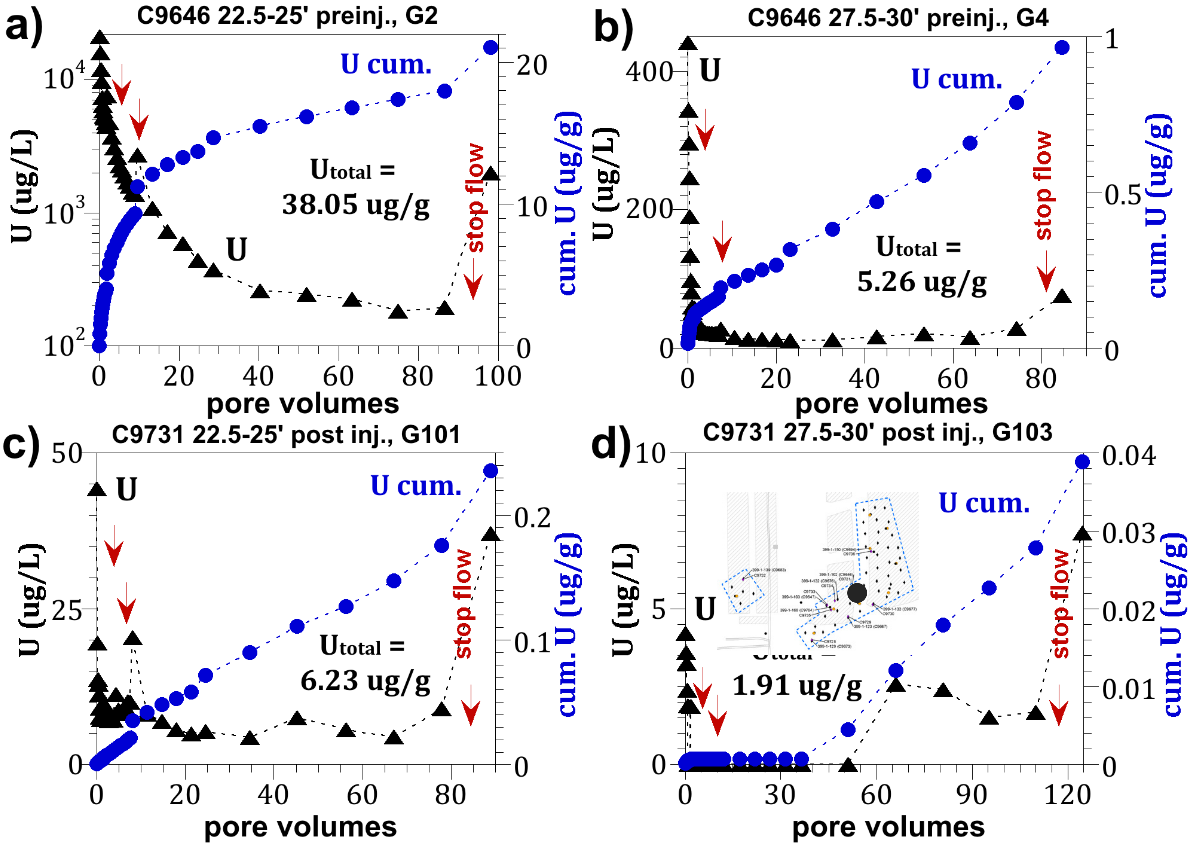

Figure 4.26. 1-D leach of pre-injection sediments from C9646 (a and b) and nearby post-injection sediments from C9731 (c and d). Borehole locations are shown in (d). Note that the U concentration (Y-axis) scales differ.

For the pre-injection borehole C9647 and corresponding post-injection borehole C9733 at a 22.5 to 25 ft depth (27.5 ft depth data shown in Figure 4.28) 1-D leach experiments showed that, with high remaining aqueous phosphate delivered (i.e., 1000 mg/L phosphate, Appendix D, Figure D.5), phosphate treatment resulted in significantly less uranium leaching (Figure 4.27). For the pre-injection borehole at 22.5 ft, the total extractable uranium was 15.97 µg/g (based on the leaching plus post-injection sequential extraction, shown in the bar graphs in Figure 4.27b) and 6.0 µg/g uranium leached (38%), in contrast to the post-injection borehole with a total extractable uranium of 9.54 µg/g (based on the post-leach extraction) with 0.025 ug/g uranium leached (0.3%, Figure 4.27c), with duplicate experiment 0.07 ug/g U leached (Figure 4.27d).

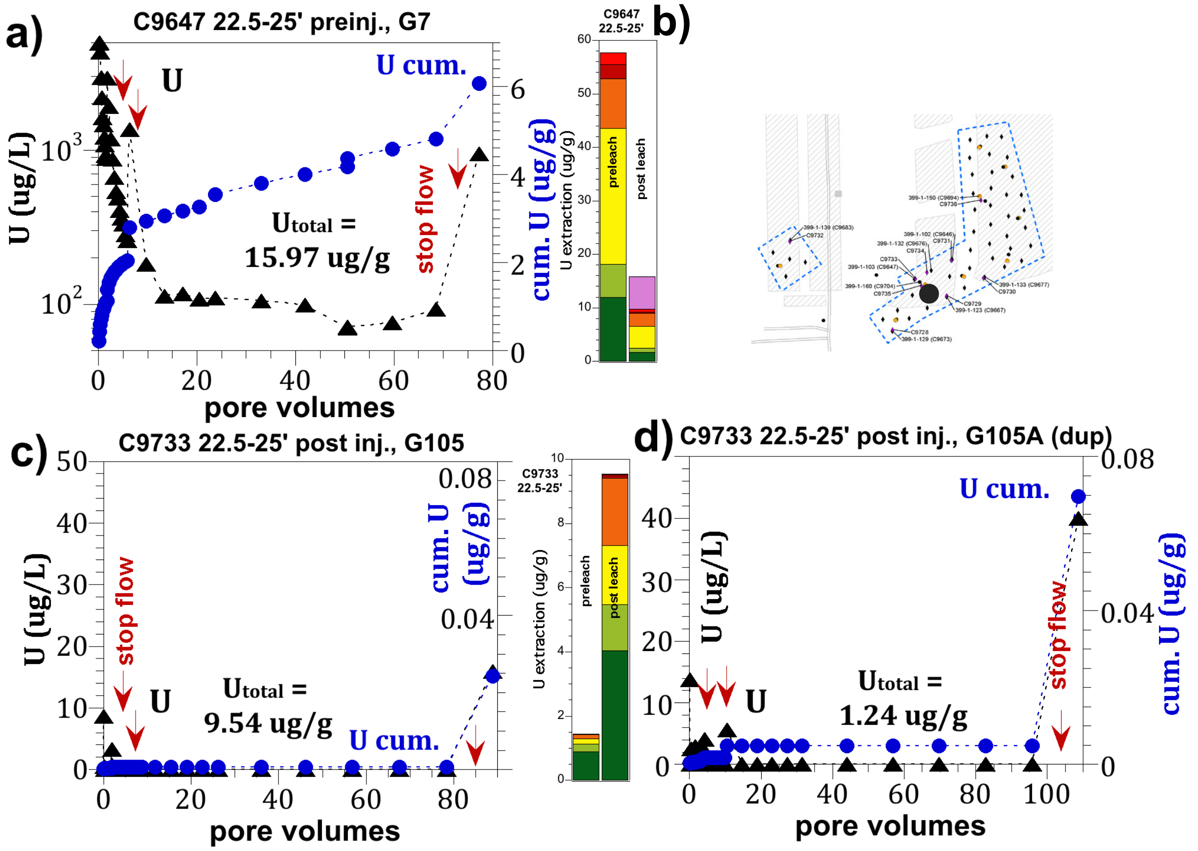

Figure 4.27. 1-D leach of pre-injection sediments from C9647 (a) and nearby post-injection sediments from C9733 (c and duplicate experiment in d) at 22.5 ft depth. Pre- and post-leach sequential extractions shown in (a and c) where red bars are extractions 1 and 2, orange is extraction 3, yellow is extraction 4, and green bars are extractions 5 and 6, while the pink bar in the post leach represents the mass removed during 1-D column leaching experiments. Borehole locations are shown in (b). Note that the U concentration (Y-axis) scales differ between (a) and (c, d). The U concentration scale is the same between (c) and (d).

For the pre-injection borehole C9647 and corresponding post-injection borehole C9733 at a 27.5 to 30 ft depth, 1-D leach experiments showed that with moderate remaining aqueous phosphate (i.e., 180 mg/L, Appendix D, Figure D.5), U-phosphates likely precipitated, and there is significantly less uranium leaching in post-injection sediments (Figure 4.28). For the pre-injection borehole at 27.5 ft, the total extractable uranium was 4.06 µg/g and 0.6 µg/g uranium leached (15%), in contrast to the post-injection borehole with a total extractable uranium of 1.06 µg/g with 0.021 µg/g uranium leached (1.9%).

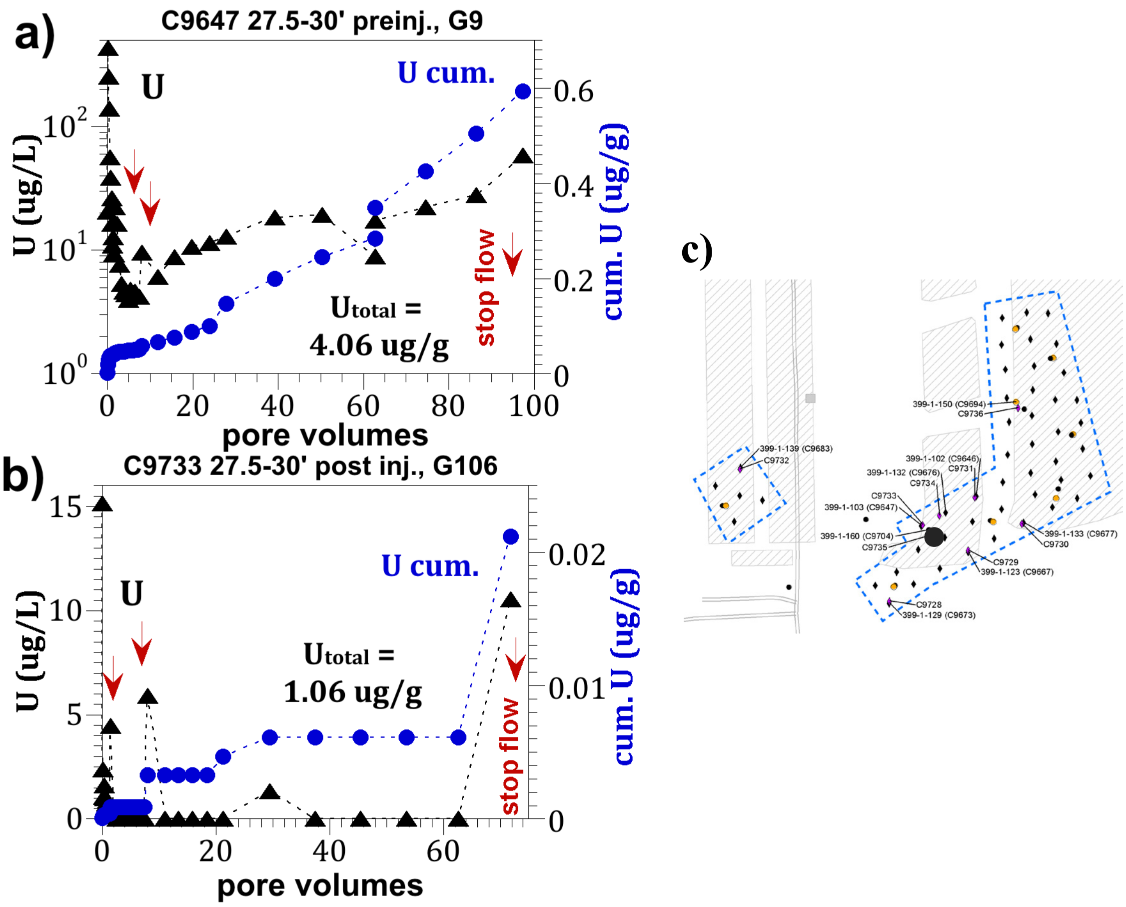

Figure 4.28. 1-D leach of pre-injection sediments from C9647 (a) and nearby post-injection sediments from C9733 (b) at 27.5 ft depth. Borehole locations are shown in (c). Note that the U concentration (Y-axis) scales differ.

For the pre-injection borehole C9667 and corresponding post-injection borehole C9729 at a 25 to 27.5 ft depth (Figure 4.29a and c), 1-D leach experiments showed that with moderate remaining aqueous phosphate delivered (i.e., 180 mg/L phosphate remaining in the pore water; Appendix D, Figure D.6), less uranium leached in post-injection sediments (Figure 4.29c). For the pre-injection sediment, the total extractable uranium was 45.35 µg/g and 14.8 µg/g uranium leached (33%), in contrast to the post-injection borehole with a total extractable uranium of 4.62 µg/g with 0.72 µg/g uranium leached (15%). For the pre-injection sediment at the 30 to 32.5 ft depth Figure 4.29b), the total extractable uranium was 8.70 µg/g and 0.22 µg/g uranium leached (2.5%), in contrast to the post-injection borehole with a total extractable uranium of 12.6 µg/g with 0.41 µg/g uranium leached (3.2%, with 75 mg/L residual PO_4). For this 30 ft depth sediment, post-leach extractions were similar to pre-leach extractions for total uranium (bar graphs right of Figure 4.29b and d).

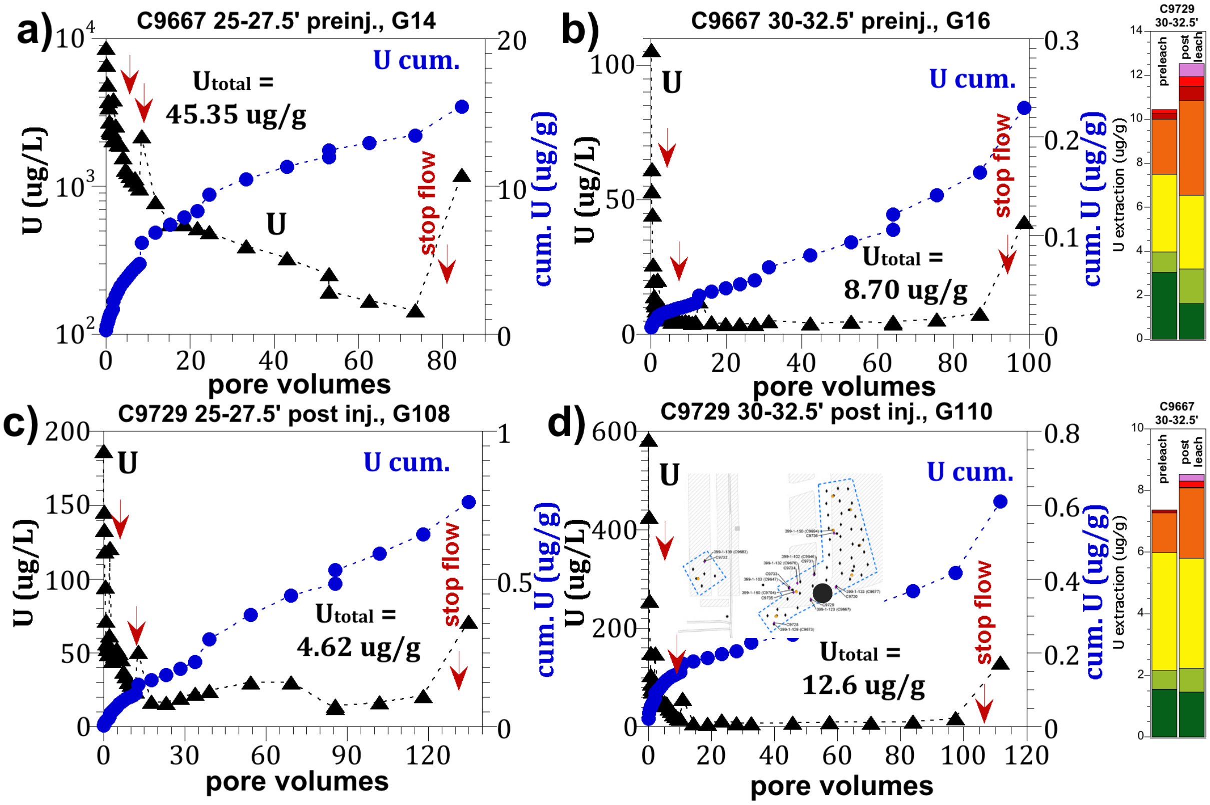

Figure 4.29. 1-D leach of pre-injection sediments from C9667 (a and b) and nearby post-injection sediments from C9729 (c and d). Pre- and post-leach sequential extractions shown on the right side of (b) and (d). Borehole locations are shown in (d). Note that the U concentration (Y-axis) scales differ. The pink bar in the post leach extractions is the leached U mass.

For the post-injection borehole C9734, which showed moderate PO_4 (700 mg/L) remaining (Appendix D, Figure D.7), and the fraction uranium leached was 2.6% (0.048 µg/g leached of 2.19 µg/g total, Figure 4.30a), whereas for the post-injection borehole C9735, which received lower PO_4 (300 mg/L PO_4 remaining; Appendix D, Figure D.7), the fraction uranium leached was 1.0% (0.04 µg/g leached of 3.84 µg/g total, Figure 4.30c). For the post-injection borehole C9736 at a 22.5 to 25 ft depth, which received no detectable PO_4 (0.0 mg/L PO_4 remaining, Appendix D, Figure D.8), the fraction uranium leached was 1.6% (0.014 µg/g leached of 0.88 µg/g total, Figure 4.30b). At this low uranium concentration, most of the uranium present is natural, with a slow release rate from the sediment. Finally, in borehole C9736 at a 25 to 27.5 ft depth, which also received no detectable PO_4 (0.0 mg/L PO_4 remaining after subtraction of background or pre-injection phosphate, Figure 4.30d), the fraction uranium leached was 39% [1.45 µg/g leached of 3.72 µg/g total (total based on post-leach extractions)], Figure 4.30e). Pre- and post-leach sequential extractions were conducted on the C9736, 25 ft depth sediment.

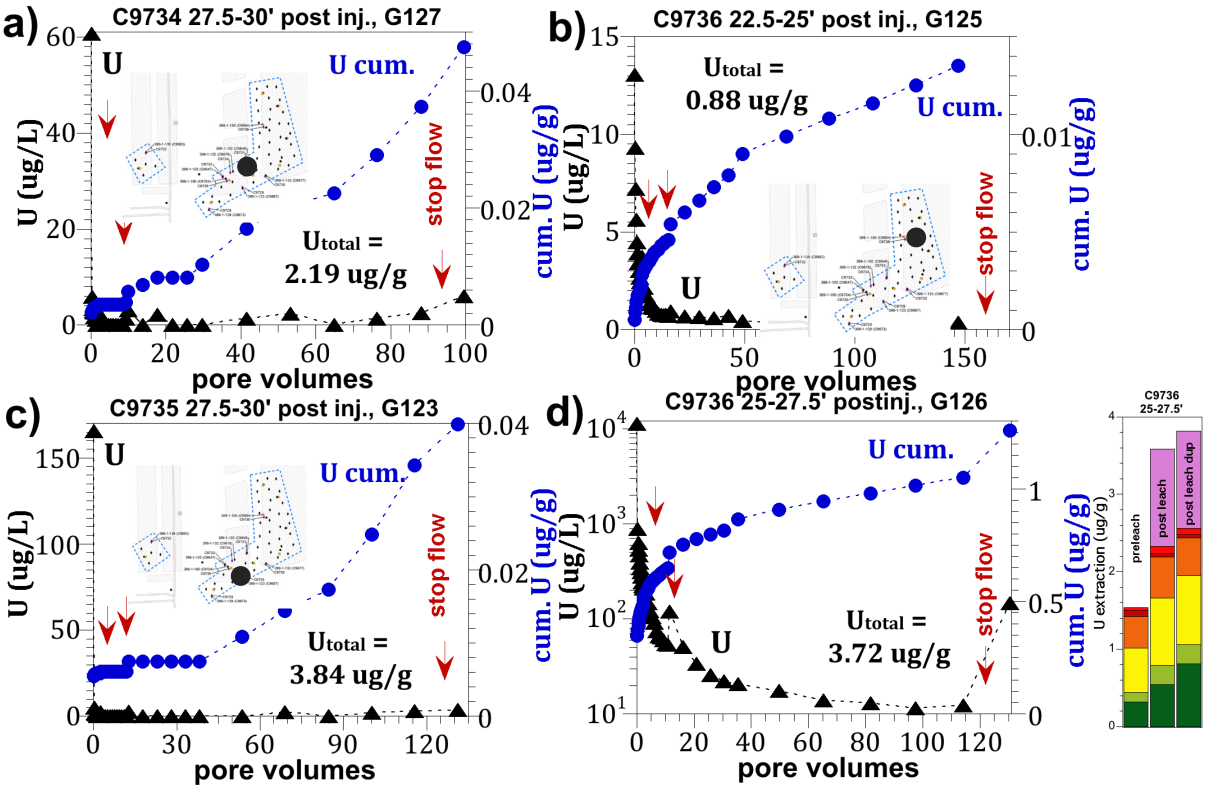

Figure 4.30. 1-D leach of post-injection sediments from C9734 (a), C9735(c), and C9736 (b and d), which do not have nearby pre-injection boreholes. Pre- and post-leach sequential extractions for C9736 at 25 ft shown in (e). Borehole locations are shown in (a, b, and c). Note that the U concentration (Y-axis) scales differ. The pink bar in the post leach extractions is the leached U mass.

The maximum aqueous specific conductance of post-injection sediments in 1-D leach experiments varied from 468 to 2280 µS/cm (mean 1307 ± 586 µS/cm, Appendix D) for these sediment samples taken 6 months after injection. The specific conductance of the field injection solution (based on median skid concentrations) was 11,510 µS/cm, which originally contained approximately 70 mM PO_4 and 61 mM bicarbonate. In a laboratory study of polyphosphate stability, the 960 mM total PO_4 solution had a specific conductance of 155,000 µS/cm, so the injected solution of 80 mM total PO_4 should have a specific conductance of 12,900 µS/cm. Based on the considerable decrease in the specific conductance of post-injection sediments, carbonate and phosphate precipitated and/or advected downgradient. Analysis of the aqueous pore water carbonate (Table 4.5) for eight post-injection sediments showed <0.5 to 66 g/L carbonate, which also indicates the high carbonate in the injection water precipitated and/or advected downgradient.

4.3.2 Uranium Leached Mass and Release Rate in 1-D Columns

Comparing all pre- to post-injection leach experiments, there was a 58.9 ± 53.2% decrease in uranium leaching, as defined from the fraction leached to total uranium for each leach experiment. Of the 10 pre-/post-injection pairs, 9 pairs showed a decrease in uranium leaching for the post-injection experiment, and one pair showed an increase (C9729 at 30 ft, Figure 4.31). The change in uranium leaching was dependent on the amount of phosphate (if any) delivered to that location, as measured by solid phase extracted phosphate and aqueous phosphate in the first few effluent samples of each leach experiment. Of 13 post-injection sediments in which leach experiments were conducted, 10 received high phosphate (see Section 4.5) and, as a result, had a large decrease in uranium leaching compared to pre-injection sediments. Based on extractable phosphate (extraction 5 in Section 4.5), while most locations showed higher PO_4 in post injection sediments relative to pre-injection paired sediments, C9729 at 30 ft, C9736 at 22.5 ft and 25 ft showed low post-injection extractable PO_4 (Figure 4.51e). In addition, there was low measured aqueous phosphate in C9729 at 30 ft, C9736 at 22.5 ft and 25 ft. These locations that showed low measured solid and/or aqueous phosphate showed higher uranium leaching.

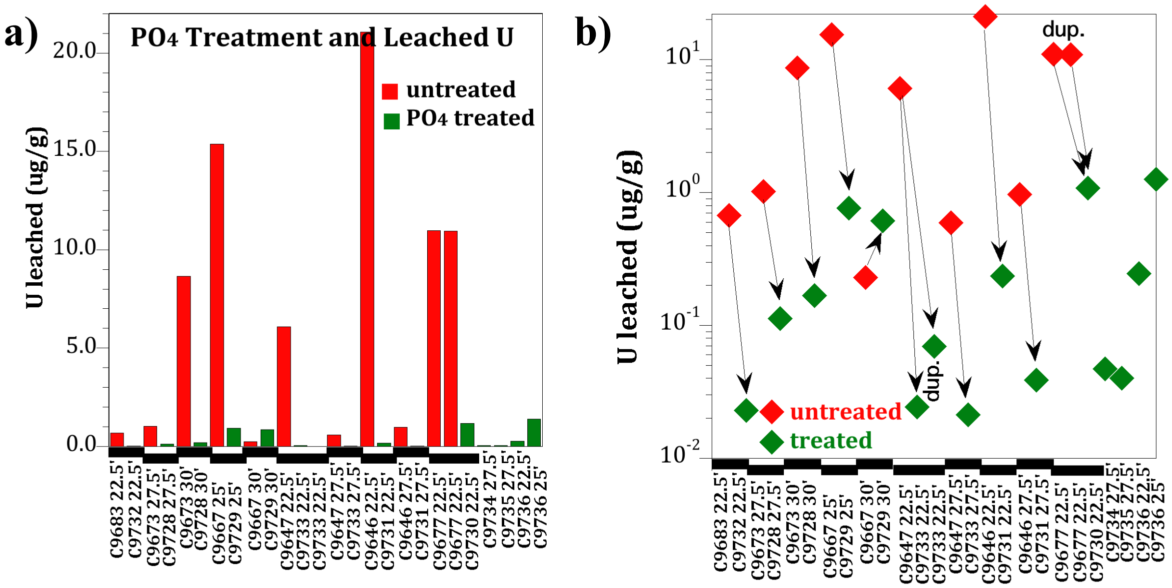

Figure 4.31. Change in pre- to post-injection uranium leaching in 1-D column experiments, as shown by uranium mass leached in experiments: (a) linear scale, and (b) log scale with untreated (red) and phosphate-treated (green) sediments.

All 2-month-long column experiments included stop-flow events at ~2, 10, and 100 pore volumes that were selected to quantify the uranium release rate from sediments predominantly from adsorbed uranium at 2 pore volumes, high-solubility uranium minerals at 10 pore volumes, and low-solubility uranium minerals at 100 pore volumes, respectively. In general, the rate of release of uranium from sediments was one to three orders of magnitude higher for untreated sediments (red symbols, Figure 4.32a) compared to -the phosphate-treated sediments (green symbols, Figure 4.32a, pre- and post-injection sediment pairs have the same symbol but different colors). Even for untreated sediments, release rates varied over three orders of magnitude, as sediments ranged in total uranium from 0.3 to 136 µg/g. For untreated sediments, the uranium release rate at 2 pore volumes was 2 to 5 times greater than the release rate at 10 pore volumes, which was an order of magnitude greater than the uranium release rate at 100 pore volumes.

There was a different trend for post-injection sediments, where the uranium release rate at 2 and 10 pore volumes was about the same, and there was a 2 to 4 times decrease in release rate by 100 pore volumes. These results are consistent with the most mobile uranium (i.e., aqueous and adsorbed uranium) significantly decreasing as a result of the phosphate treatment as shown by sequential extractions (Figure 4.17a and b). Natural uranium is in equilibrium with sediment minerals, so there is generally little net dissolution of natural U from minerals. In contrast, anthropogenic uranium that has been in contact with sediment minerals for only decades may not be in equilibrium, and, as such, some uranium minerals are slowly dissolving leading to a higher U release rate from sediment. The uranium release rates for these

300-FF-5 Area untreated vadose zone sediments, most of which contain anthropogenic uranium (Figure 4.32a), were one to two orders of magnitude greater than for uranium in 200 Area contaminated vadose zone sediments under the B, S, and T complexes (Truex et al. 2017), most of which are at low U concentration close to natural uranium concentration (Figure 4.32b), with the exception of C9487 at 58 ft (black squares) which is 200 µg/g. In contrast, after 300-FF-5 Area sediments received phosphate treatment, the U release rate decreased two to three orders of magnitude (green symbols in Figure 4.32a compared to pre-injection sediments in red symbols).

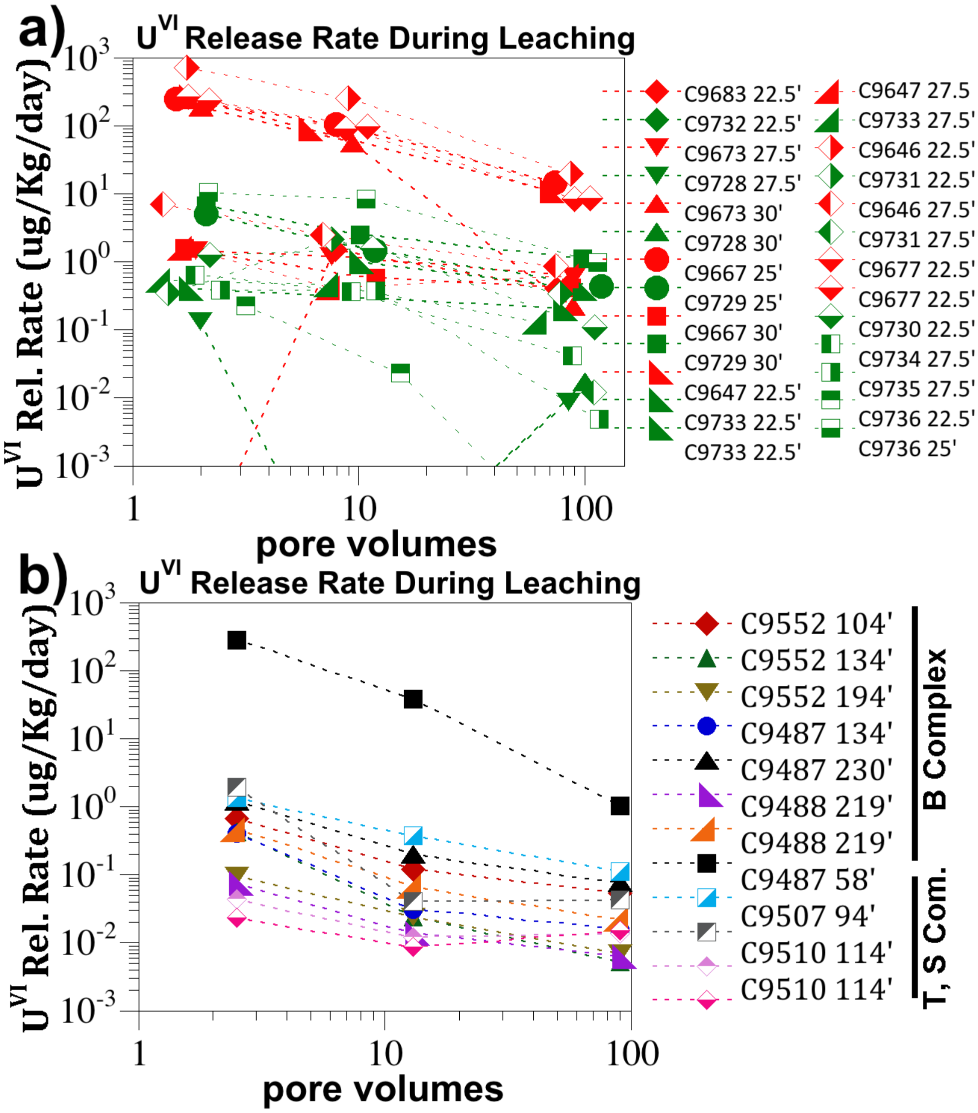

Figure 4.32. Uranium release rate calculated from stop-flow events in 1-D columns for (a) 300-FF-5 Area vadose zone sediments, and (b) 200 Area vadose zone sediments. In (a), red symbols are pre-injection boreholes and green symbols are post-injection boreholes.

4.4 Uranium Solid Phase Characterization

Different solid phase characterization techniques used to identify the uranium precipitate composition, morphology, and oxidation state in pre- and post-injection sediments included (a) 2-D elemental mapping by μ-XRF), (b) μ-XANES, (c) μ-EXAFS (a-c at the APS) and (d) 2-D elemental mapping by scanning electron microscope with energy dispersive spectroscopy detector (SEM-EDS). The 2-D elemental mapping by μ-XRF at APS included analysis of U, Cu, Fe, Ca, Ti, Bi, and Zn. Spectra of lower energy elements of interest (P and Si) could not be obtained due to limitations with radioactive samples at APS. As a result, additional 2-D elemental mapping was conducted by SEM-EDS for P, Si, O, Na, Al, K, Fe, and Cu; however, U was below the detection limit. At APS, XANES spectra at selected point locations of uranium precipitates was conducted to quantify the uranium oxidation state via comparison with U^{IV}, U^{VI} mineral standards. Then, at APS, EXAFS spectra at selected point locations were used to quantify the nearest element to U and crystal structure via comparison to U^{IV}, U^{VI} mineral standards. Natural uranium in Hanford formation sediments is generally associated with silt and clay size fractions (Um et al. 2009), as aqueous and adsorbed Ca-uranyl-carbonate complexes (see Section 2.0), in secondary precipitates (e.g., uranophane and Na-boltwoodite), and co-precipitated in calcium carbonate phases (Catalano and Brown Jr., 2004; Liu et al. 2006; Um et al. 2009; Wang et al. 2005). Researchers previously used the following techniques to identify solid phases, generally with at least three of these methods combined to confirm U phases: XRF, X-ray absorption-spectroscopy (XAS; XANES and EXAFS, μ- and bulk), fluorescence spectroscopy (including time-resolved laser-induced fluorescence spectroscopy), XRD (μ- and bulk), SEM-EDS, transmission electron microscopy, EMP analysis, and acid digestion.

In the 300 Area NPP and sediments beneath the NPP, U has been identified as metatorbernite [$Cu(UO_2)_2(PO_4)_2 \cdot 8H_2O$], uranophane [$Ca(UO_2)_2(HSiO_4)_2 \cdot 5H_2O$], disordered uranyl carbonate, and U adsorbed to muscovite (Arai et al. 2007; McKinley et al. 2007) following disposal of approximately 50 tons of Cu and 30 tons of U to the NPP (Gerber 1993). In addition, SEM-EDS indicated that particles were cemented with C-, Al-, and Si-rich coatings on quartz, albite grains, and additional CuO coatings (Arai et al. 2007; McKinley et al. 2007). Laser ablation inductively coupled plasma mass spectrometry (ICP-MS) confirmed the strong association of Cu and U on the surface of larger particles (Peng et al. 2012). Previous solid phase characterization was conducted on sediments from directly below the NPP, with the majority of characterization data for sediments collected after the second excavation in 2001-2002 from shallow depths. For example, Arai et al. (2007) characterized a sediment sample from 4.00 ft depth while Catalano et al. (2006) characterized sediments from up to 12.1 ft (3.7 m) depth. These samples had 140 to 3310 μg/g of U (Catalano et al. 2006; Arai et al. 2007).

Pre-and post-injection sediment samples from borehole pairs C9667/C9729 and C9673/C9728 from depths of 25 and 30 ft, respectively, were further characterized via XAS, XRF, and SEM-EDS. Table 4.6 summarizes the total U, Cu, Fe, and Ca extracted from these boreholes in sequential extractions and measured inorganic carbon. Figure 4.33 shows the U, Cu, Fe, and Ca extracted in each operationally defined step of the extractions. Due to the relatively low concentration of U in these samples, micro techniques were utilized to collect data on particles with the greatest U signal (Table 4.6).

Table 4.6. Summary of total Cu, Fe, and Ca extracted in sequential liquid extractions.

Sample ID[(a)] Depth (ft)	U (μg/g)	Cu (μg/g)	Fe (μg/g)	Ca (μg/g)	P[(b)] (μg/g)	Inorganic C
G3, C9667, 25 ft	94	782	20,671	5980	121	--
G4, C9729, 25 ft	48	762	13,235	7657	347	--
G5, C9673, 30 ft	56	518	21,232	6996	107	< 0.01
G6, C9728, 30 ft	136	463	23,294	9464	465	< 0.01

(a) Sample ID represents Lab ID, borehole ID, and depth (ft).
(b) From sequential extraction 5.

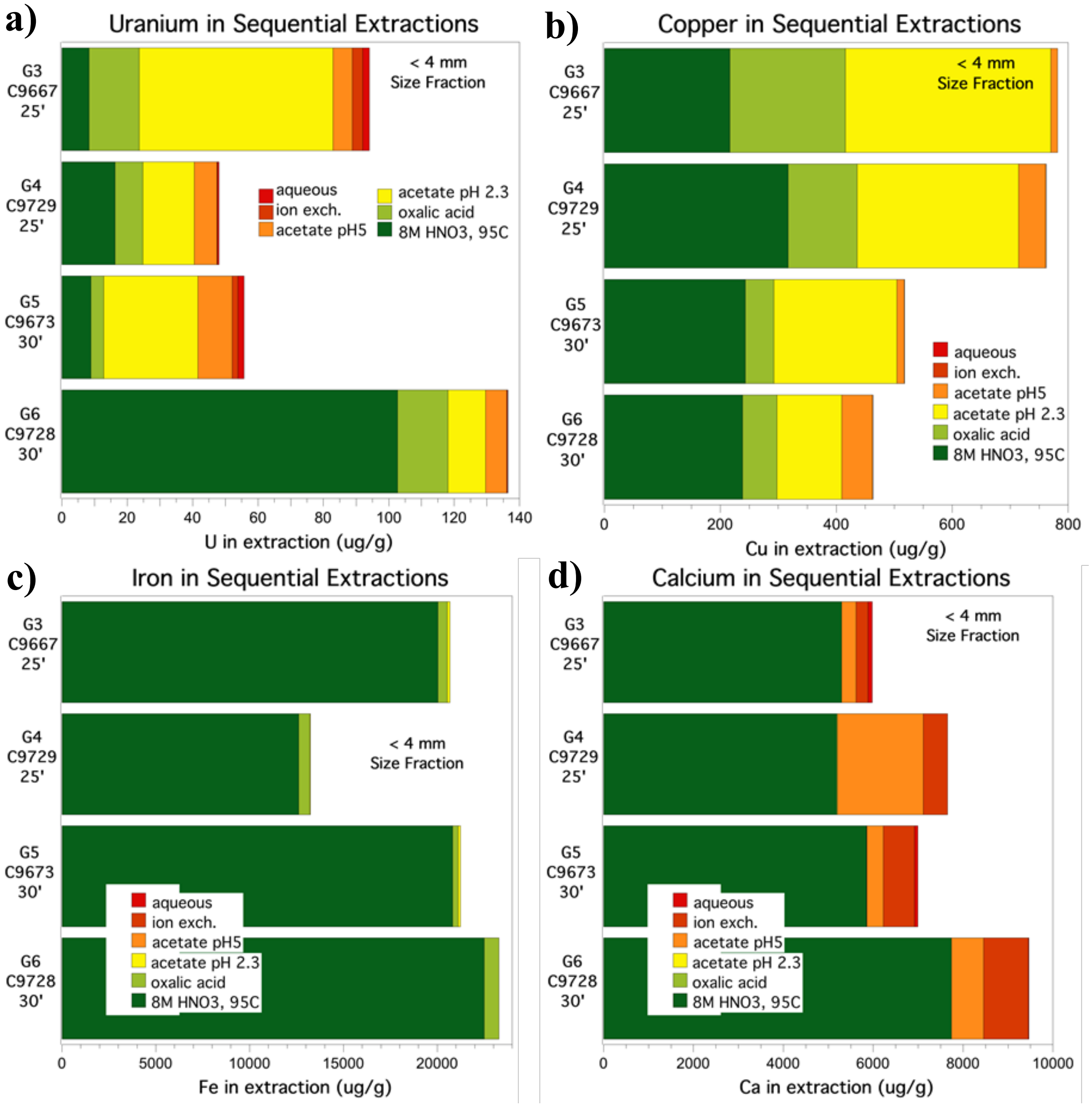

Figure 4.33. Sequential liquid extractions of pre- (G3 C9667 and G5 C9673) and post-injection (G4 C9729 and G6 C9728) sediment pairs showing uranium (a), copper (b), iron (c), and calcium (d). Note that results not shown for Ca for extraction 4 due to Ca used in extraction solution.

4.4.1 Major Elements Associated with U in Pre- and Post-Treatment Sediments

For one pre-injection sediment (C9673, 30 ft depth), uranium is commonly associated with the following elements: Cu, Fe, Ca, as well as trace metals (e.g., Bi, Ti, and Zn) based on 2-D µ-XRF mapping depicted in Figure 4.34 to Figure 4.37. However, correlation is highly dependent on the particles and some U particles are not correlated with any of the elements measured via µ-XRF (Fe, Cu, Bi, Mn, Ca, Ti, Zn, Zr, Sr, Y; e.g., particle 4 in Figure 4.35). These particles may be discrete uranium particles (e.g., U metal or UO_2) or U associated with lighter elements (e.g.., P or Si). Elements with low energies (i.e., Si, P) could not be detected on the 20-ID-B, C beamline at the APS due to limitations in changing beam energies with radioactive samples. Therefore, identification of autunite [$Ca(UO_2)_2(PO_4)_2 \cdot 10\text{-}12H_2O$] or apatite

[$Ca_{10}(PO_4)_6(OH)_2$] was not possible with the μ-XRF data, but P and Si 2-D mapping was measured on these same thin sections by SEM-EDS (Section 4.43).

Figure 4.34 to Figure 4.36 are representative maps of the sediments analyzed by μ-XRF at APS with additional maps shown in Appendix E. For pre-injection sediments from C9673 at 30 to 32.5 ft depth, the areas of high uranium indicated with circles 1 – 4 are co-located with high copper (Figure 4.34a and b). The uranium particles shown with circles 3 and 4 represent areas with potentially more Cu than U based on the intensity of signal. Iron, bismuth, and zinc are also co-located with small uranium particles (1-4) at more trace levels. The exceptions are for Bi in particle 2 and Fe and Bi in particle 4, where stronger signals were observed (Figure 4.34a, d, e, and g). Further, the uranium particles shown with circles 1-3 are not correlated with calcium or titanium while particle 4 shows some correlation. It is possible that Bi was disposed of in the 300 Area as the bismuth phosphate separations process was tested at the pilot scale in the 321, 325, and 3706 buildings nearby beginning in 1944 (Gerber 1993). However, Bi has not been previously identified in correlation with U phases in these sediments and an inventory of Bi releases to the area was not available at this time.

For the pre-/post-treatment pair C9667/C9729 at 25 ft depth (Figure 4.35 and Figure 4.36, respectively), uranium was also primarily associated with Cu and Fe in mapping, with some particles being associated with Cu, Fe, and Bi (particles 1 and 2 in both maps) while others were primarily Cu and U (particle 3 in both maps) or primarily Fe/Bi and U (particle 1 in both maps). However, significant differences between pre- and post-treated U solid phases were not distinguishable through μ-XRF. Further, similar phases were observed as compared to the pre-treated sample, Figure 4.34, although there was a greater abundance of Cu as compared to Fe/Bi. In addition, small U particles (Figure 4.35, labeled with a 4) were observed in the other pre-treated map (C9667, G3) without a strong U correlation to any other elements analyzed, suggesting either discrete U particles or association with lighter elements that were not measurable (e.g., Si and P).The correlation between uranium and other elements from the μ-XRF data shows a strong linear correlation between uranium and copper, bismuth, and zinc, and weak correlations between uranium and calcium and titanium (Figure 4.38). For these comparisons, lower uranium signals were not included in this analysis and the full correlation plots are shown in the Appendix E. Element correlation plots illustrate good correlations between uranium and copper ($R^2 = 0.57$), iron ($R^2 = 0.70$), bismuth ($R^2 = 0.79$), titanium ($R^2 = 0.78$), and zinc ($R^2 = 0.63$).

Calcium is also observed in correlation with U or surrounding particles (Figure 4.37) in both pre- and post-treatment samples, as shown in sample C9667 (pre-treatment), highlighted areas 1-3 (Figure 4.37a and b), and in sample C9729 (post-treatment) circles 1 and 2 (Figure 4.37c and d) and with circles 1, 3, 5 and 6 (Figure 4.37e and f). Areas of high uranium without calcium have also been identified (Figure 4.37, circles 1-2 in a and b; circles 1-2 in c and d, and circles 1, 3, 5, and 6 in e and f). In general, more Ca was observed in C9667/C9729 (G3/G4) sediment thin sections as compared to C9673/C9728 (G5/G6) sediments (see additional maps in Appendix E). Sequential extractions also showed an increase in Ca with treatment based on slightly higher Ca In the total extractions and final extraction phase between these sample pairs with slightly greater Ca in pre- and post-treated pairs, C9673/C9728 (G5/G6) (Table 4.6), which may be due to precipitation of Ca from porewaters and river water infiltration in the 6 months following injections. The element correlation plots suggest that U is strongly associated with mineral phases containing Cu and Fe as well as trace elements with a lesser correlation with Ca.

Previous research showed that in natural Hanford formation sediments, calcite averages at 1.9 ± 1.7 wt.% (Xie et al. 2003), but inorganic carbon analysis on 11 sediments in this study showed 10 with < 0.01% and one sample at 0.04% inorganic carbon, so a significant amount of the calcite may have been dissolved by the historical disposal of acidic waste. In addition, very little calcium was extracted in the two acetate extractions (Figure 4.33), which are designed to dissolve calcite, and most of the calcium was extracted in extraction 6. These results suggest that Ca may be directly or indirectly associated with U in pre- or post-treatment sediment thin sections investigated at APS as it may be associated with secondary coatings formed after waste release (e.g., apatite or calcite, particle 1, Figure 4.37c-d) or as U phases formed during remediation injection (e.g., autunite, particle 1, Figure 4.37a-b).

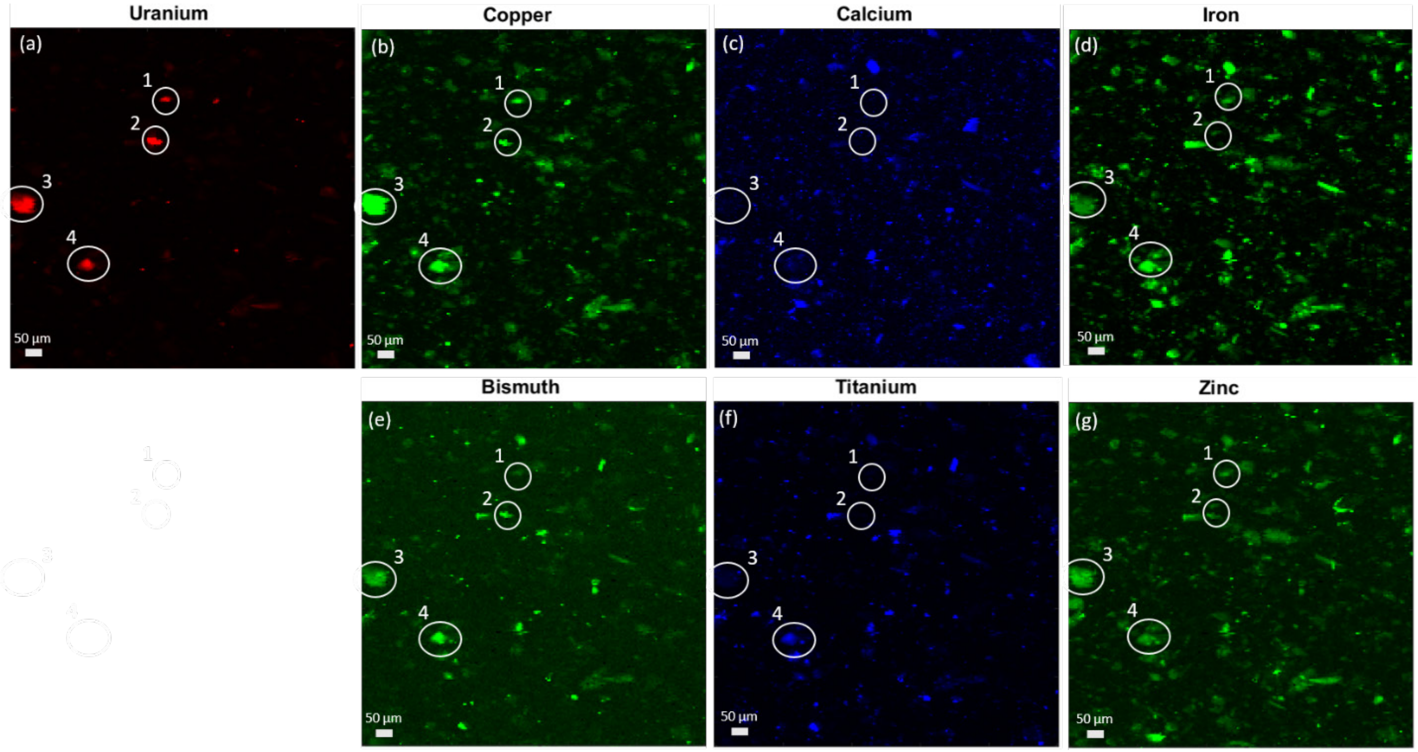

Figure 4.34. 2-D µ-X-ray fluorescence mapping of pre-treatment C9673, 30 ft depth (G5, point 4) showing elemental maps of (a) U, (b) Cu, (c) Ca, (d) Fe, (e) Bi, (f) Ti, and (g) Zn with the scale shown by the white bar in the bottom left corner. Data shown is FIO.

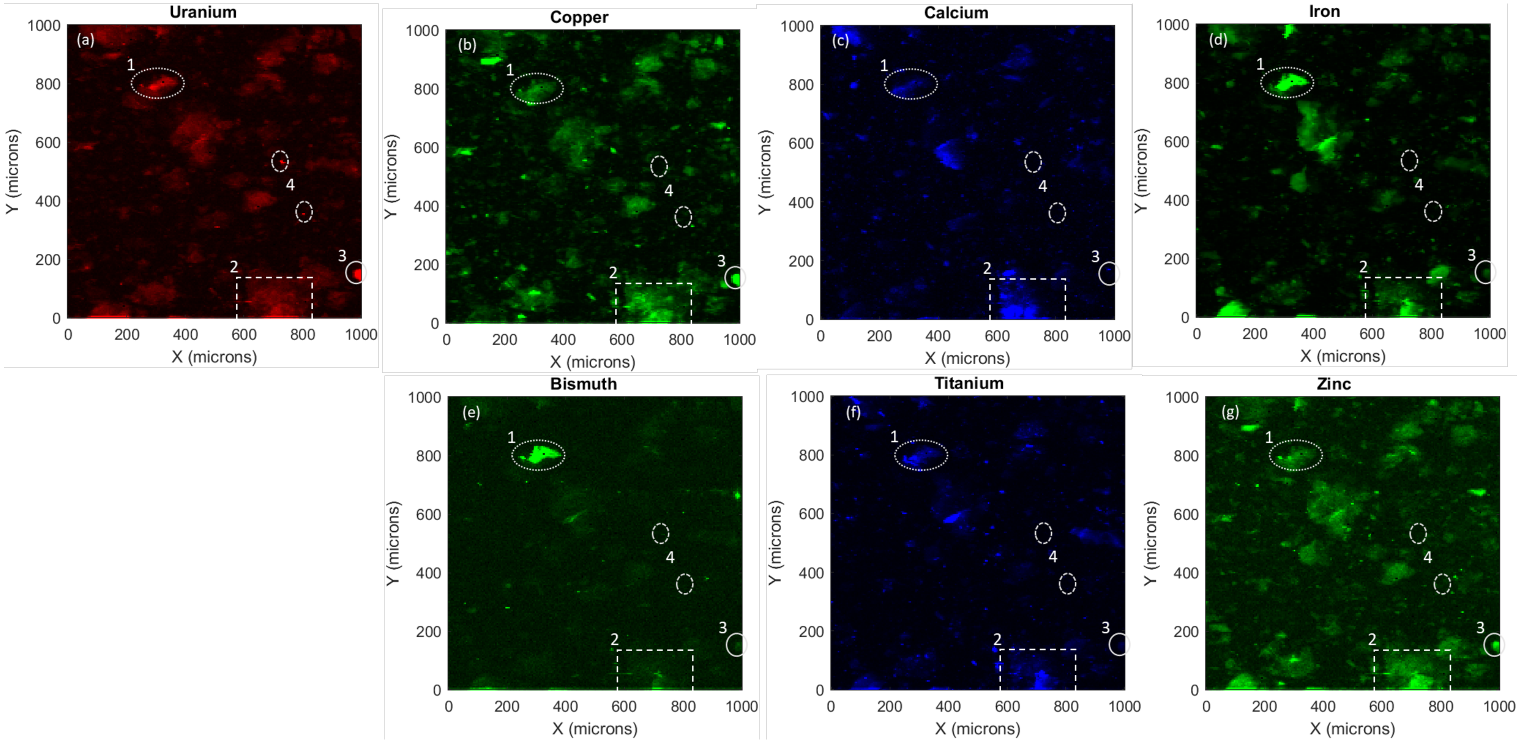

Figure 4.35. 2-D µ-X-ray fluorescence mapping of pre-treatment C9667, 25 ft depth (G3, point 2) showing elemental maps of (a) U, (b) Cu, (c) Ca, (d) Fe, (e) Bi, (f) Ti, and (g) Zn with the scale shown by the x- and y-axes in microns. Data shown is FIO.

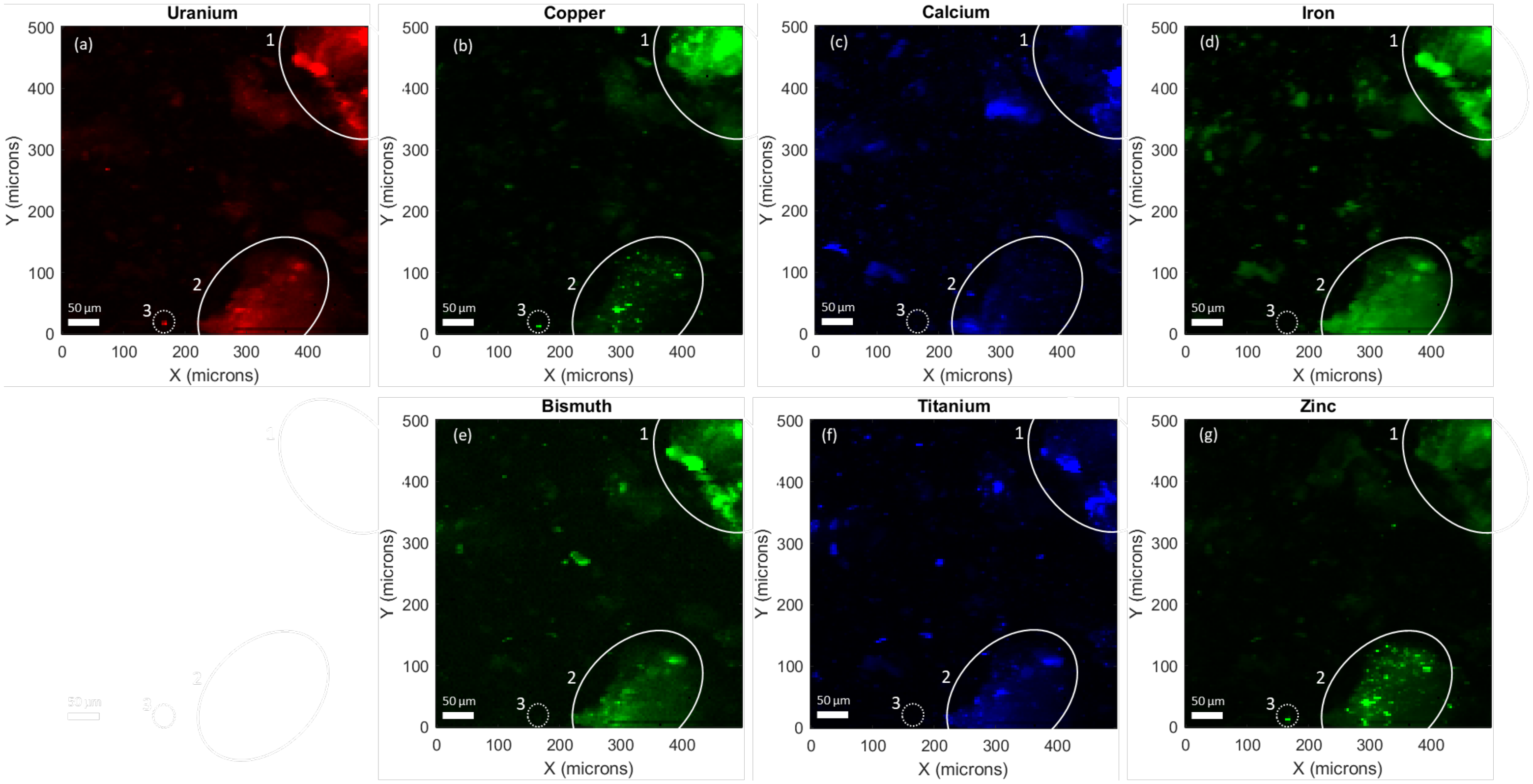

Figure 4.36. 2-D µ-X-ray fluorescence mapping of post-treatment C9729, 25 ft depth (G4, point 2)] showing elemental maps of (a) U, (b) Cu, (c) Ca, (d) Fe, (e) Bi, (f) Ti, and (g) Zn with the scale shown by the x- and y-axes in microns. Data shown is FIO.

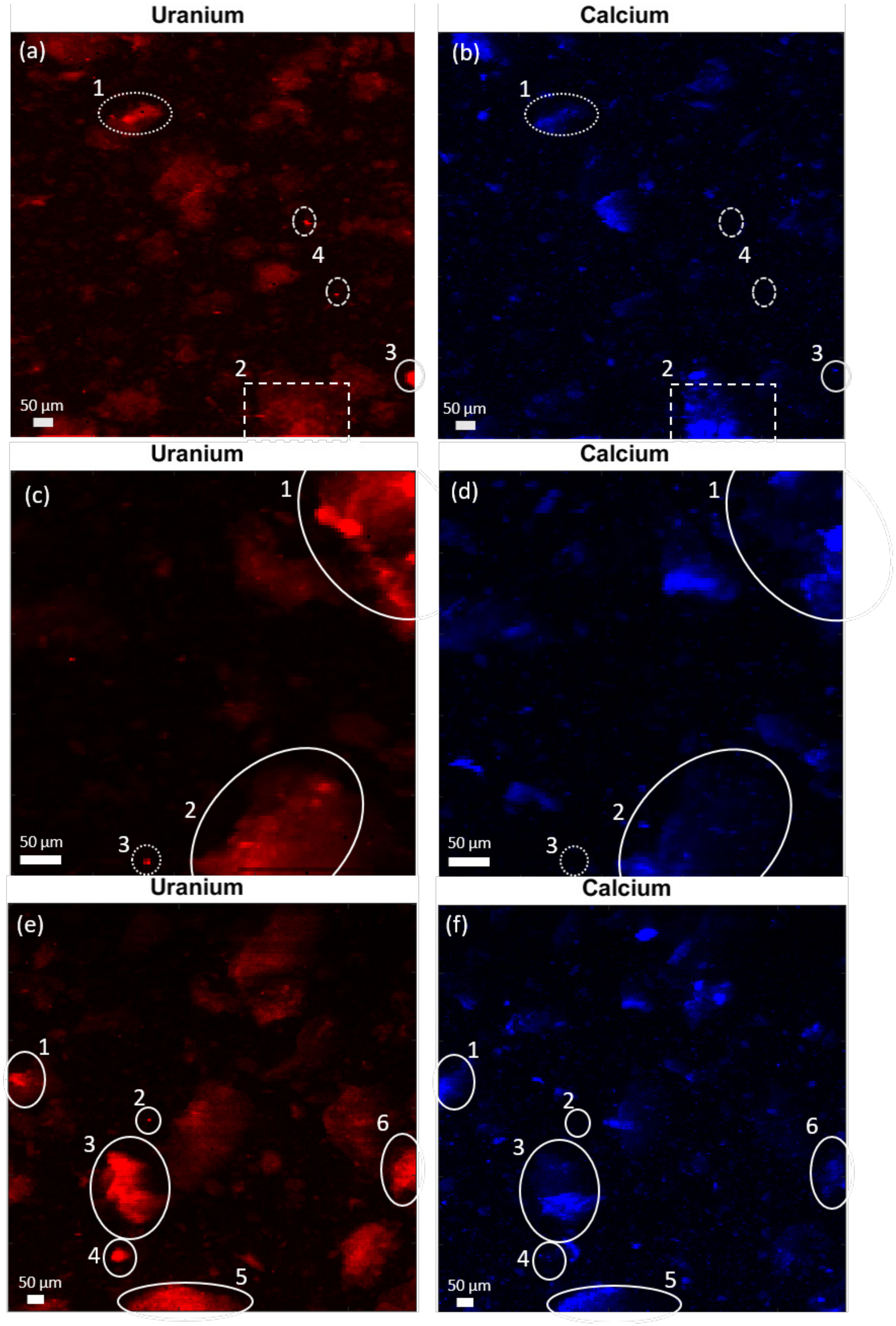

Figure 4.37. 2-D µ-X-ray fluorescence mapping of samples showing U (red) and Ca (blue) for (a-b) pre-injection C9667, 25 ft depth (G3, point 2) and (c-d) post-injection C9729, 25 ft depth (G4, point 2), and (e-f) post-injection C9729 25 ft depth (G4, point 4) with the scale shown by the white bar in the bottle left corner of each image. Data shown is FIO.

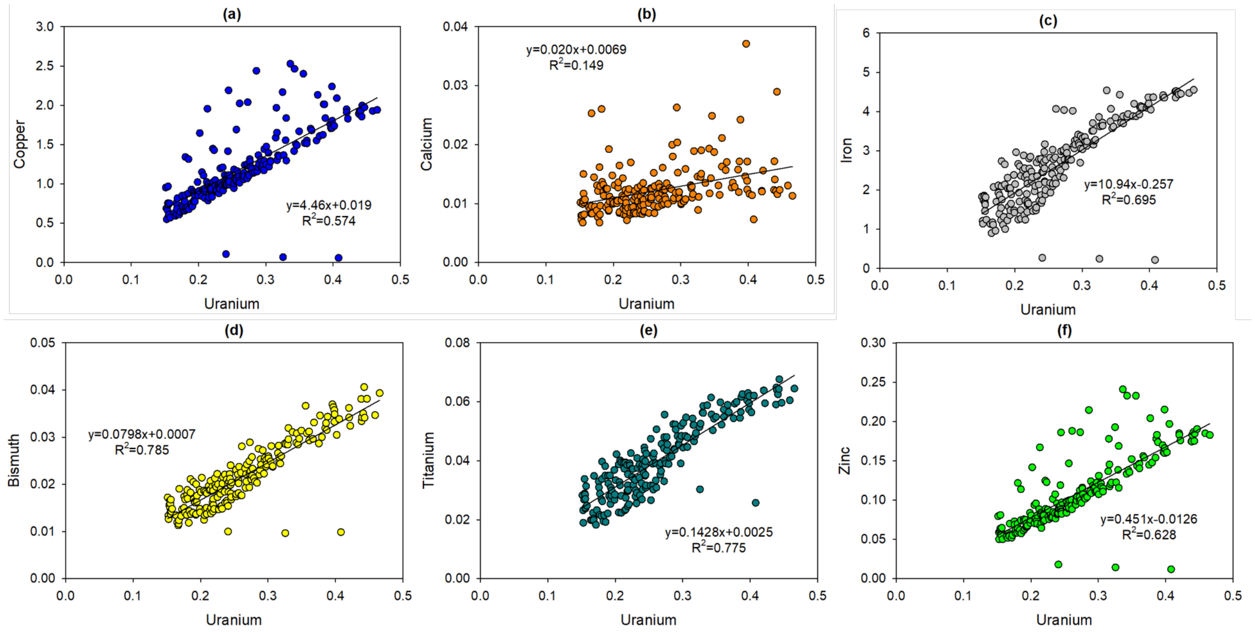

Figure 4.38. Correlation plots of 2-D elemental mapping by µ-XRF of C9673 pre-treatment (sample G3, point 2) comparing uranium (x-axis) with (a) copper, (b) calcium, (c) iron, (d) bismuth, (e) titanium, and (f) zinc where the x- and y-axis represent the counts observed by the detector which correlate with concentration. Data shown is FIO.

4.4.2 µ-XANES and µ-EXAFS Analysis of U Minerals in Sediments

The X-ray absorption spectroscopy data presented in this section are based on the measured absorption for the U L_{III} edge which occurs at X-ray energies > 17,166 eV. The µ-XANES data is shown as *normalized absorption* or re-scaled so that the rise associated with the edge or energy jump due to X-ray absorption and excitation of U atoms is 1.0. This normalization step is conducted in order to allow for direct comparison of spectra from different samples and standards. The XANES region is broadly defined as the region 30-50 eV above the energy jump (Calvin 2013). In order to show the EXAFS oscillations, a smooth background function is drawn through the data to subtract gradual trends associated with background absorptions, $\chi(E)$. Then, the results are manipulated in order to present as $\chi(k)$. The χ factor represents the probability of an absorption of an X-ray by a U atom and is shown in terms of energy (E) and wavenumber (k). The normalized energy spectra are converted to k based on simplified Eqs. (4.1) and (4.2) (Calvin 2013). The final $\chi(k)$ or *EXAFS equation* is shown in Eq. (4.3) and represents corrections for multiple interactions that may occur in real samples (e.g., multiple scattering events with nearby atoms, including direct and indirect scatters, phase shifts of the photoelectron wave, isotropic spreading of the spherical photoelectron waves, and thermal disorder, among others). Further, µ-EXAFS data are shown in terms of a *k-weighted χ(k)* as this weighting is used to create a more uniform amplitude and de-emphasize the XANES region as consistent background subtraction is difficult to achieve in this region. For comparison, the µ-EXAFS data are also shown as a Fourier transform in *R-space* in order to combine multiple sine waves.

$$k = \frac{2\pi}{h}\sqrt{2m_e(E - E_0)} \tag{4.1}$$

where h = Plank's constant, m_e = electron mass, E = incident photon energy, E_0 = energy to remove the photoelectron from the absorbing atom:

$$\chi(k) = f(k)\cos(2kD) \tag{4.2}$$

where f(k) = proportionality constant for the possibility of scattering and D = distance between absorbing and scattering atoms:

$$\chi(k) = S_0{}^2 \sum_i N_i \frac{f_i(k)}{kD_i{}^2} e^{-\frac{2D_i}{\lambda(k)}} e^{-2k^2\sigma_i{}^2} \sin(2kD_i + \delta_i(k)) \tag{4.3}$$

where S_0 = amplitude reduction factor, N_i = degeneracy factor, σ_i = mean square radial displacement factor (variance in D due to disorder), $\lambda(k)$ = mean free path of a photoelectron.

The μ-XANES analysis of pre- and post-treated sediments shows that U is primarily present as U^{VI} (Table 4.7, only one fit included UO_2 standard with 2.8 ± 4.8% for a point analysis within pre-treatment, C9673, G5 sediment), similar to results from previous research prior to phosphate injection in the 300 Area (Arai et al. 2007; Catalano et al. 2006). Linear combination fitting (LCF) for both normalized energy and k-space correlated most strongly with torbernite and Na-boltwoodite in pre- and post-treated sediments (Figure 4.39, Table 4.8, k-space results not shown). These fits are based on allowing a maximum of three reference species to fit with sample spectra from sediment thin sections based on analysis of standard minerals (autunite, torbernite, Na-boltwoodite, uranyl carbonate, and uranium dioxide) prepared as pressed powders. The best fits are shown in Table 4.5 based on statistics (χ^2), although fits that included a subtraction of a reference mineral were not included because, while these mathematical fits are better statistically, they are not appropriate to describe the real system. Further, although fit statistics are acceptable and the top fits by statistics are generally consistent, the fits do not necessarily represent unique solutions due to the similarity of reference spectra as confirmed by previous research (Catalano et al. 2006). In addition, the spectra are also not always great fits visually (Figure 4.39), and a sufficient number of spectra could not be collected to confirm statistical differences in pre- and post-treated samples over the time allotted at APS.

Autunite group spectra are similar and may be indistinguishable via EXAFS (e.g., meta-autunite versus metatorbernite) (Catalano and Brown Jr. 2004; Catalano et al. 2006). Table 4.8 summarizes interatomic distances and coordination numbers for major autunite group minerals, confirming the similarities in mineral structure (Locock and Burns 2003; Makarov and Ivanov 1960; Ross et al. 1964). Table 4.9 summarizes previous fits by Catalano and Brown Jr. (2004) for meta-autunite and metatorbernite, further highlighting that their reference minerals could not be differentiated by EXAFS. In addition, a previous torbernite spectra could not be identified in literature, although the spectra collected for our reference mineral is missing characteristic features previously observed for metatorbernite. Further, although distances are sufficiently different for Cu versus Ca in mineral species, the spectra collected in this research are not adequate for fitting past the first shell (U-O) and do not represent a statistically significant number of measurements. Therefore, these results cannot differentiate between meta-autunite and metatorbernite and are inconclusive as to whether (a) autunite species formed or (b) additional uranium phosphate species are present in post-treated sediments. However, a visual comparison of EXAFS spectra for samples and standards suggests some correlation with Na-boltwoodite and autunite group minerals (Figure 4.40 and Figure 4.41).

Table 4.7. LCF results for the best fits for each µ-XANES spectra collected in pre- (*white*) and post-injection (*gray*) samples at multiple points. Data shown is FIO.

Mineral	C9667 25 ft (G3, pt 1)	C9729 25 ft (G4, pt 1)	C9729 25 ft (G4, pt 2)	C9673 30 ft (G5, pt 1)	C9673 30 ft (G5, pt 2)	C9728 30 ft (G6, pt 1)	C9728 30 ft (G6, pt 2)	C9728 30 ft (G6, pt 3)
Autunite	-	-	-	-	-	-	0.53 ± 0.11	-
Torbernite	0.80 ± 0.05	0.50 ± 0.08	0.33 ± 0.06	0.32 ± 0.02	0.80 ± 0.05	0.92 ± 0.01	0.38 ± 0.07	0.92 ± 0.12
Uranium dioxide	-	-	-	0.03 ± 0.05	-	-	-	-
Boltwoodite	0.20 ± 0.05	0.50 ± 0.07	0.67 ± 0.06	0.66 ± 0.02	0.20 ± 0.05	-	-	0.06 ± 0.11
Uranyl carbonate	-	-	-	-	-	0.08 ± 0.01	0.08 ± 0.03	0.02 ± 0.01
χ^2	0.004	0.006	0.006	0.002	0.004	0.004	0.009	0.002

Note: If initial best fit included a subtraction of any reference mineral, it was excluded, and the next best fit is shown.

Table 4.8. Mineral structures for autunite group minerals (Locock and Burns 2003; Makarov and Ivanov 1960; Ross et al. 1964).

	Meta-autunite		Autunite		Metatorbernite		Torbernite	
	$Ca(UO_2)_2(PO_4)_2 \cdot 6H_2O$		$Ca(UO_2PO_4)_2 \cdot 10\text{-}12H_2O$		$Cu(UO_2)_2(PO_4)_2 \cdot 8H_2O$		$Cu(UO_2)_2(PO_4)_2 \cdot 8\text{-}12H_2O$	
	Distance (Å)	CN	Distance (Å)	CN	Distance (Å)	CN	Distance (Å)	CN
U-U	3.048	6	2.88	6	2.88	6	2.88	6
U-O	3.432	4, 9, 12	3.264	7, 8	3.264	4, 8	3.264	7, 8
U-P	2.4	4	2.232	4	2.232	4	2.232	4
U-Ca	3.048	10	2.88	6	-	-	-	-
U-H_2O	3.6	8	-	-	-	-	-	-
U-Cu	-	-	-	-	2.808	6	2.808	6

Table 4.9. Comparison of previous fits for meta-autunite and metatorbernite reference minerals via EXAFS (Catalano and Brown Jr. 2004) with the error on the last digit shown in parenthesis for EXAFS fitting.

	Meta-autunite			Metatorbernite		
Shell	N	R (Å) - EXAFS	R (Å) - XRD	N	R (Å) - EXAFS	R (Å) - XRD
O_{ax}	2	1.774(6)	1.789	2	1.768(4)	1.81
O_{eq}	4	2.277(6)	2.28	4	2.284(4)	2.3
P	4	3.59(2)	3.6	4	3.59(2)	3.59
MS(a)	8	3.71(2)	3.71	8	3.72(4)	3.7
MS(a)	4	3.81(b)	3.81	4	3.76(12)	3.8
U	4	5.21(11)	5.24	4	5.23(5)	5.24

(a) MS = multiple scatters

(b) No error reported on this parameter as it was fixed during EXAFS fitting.

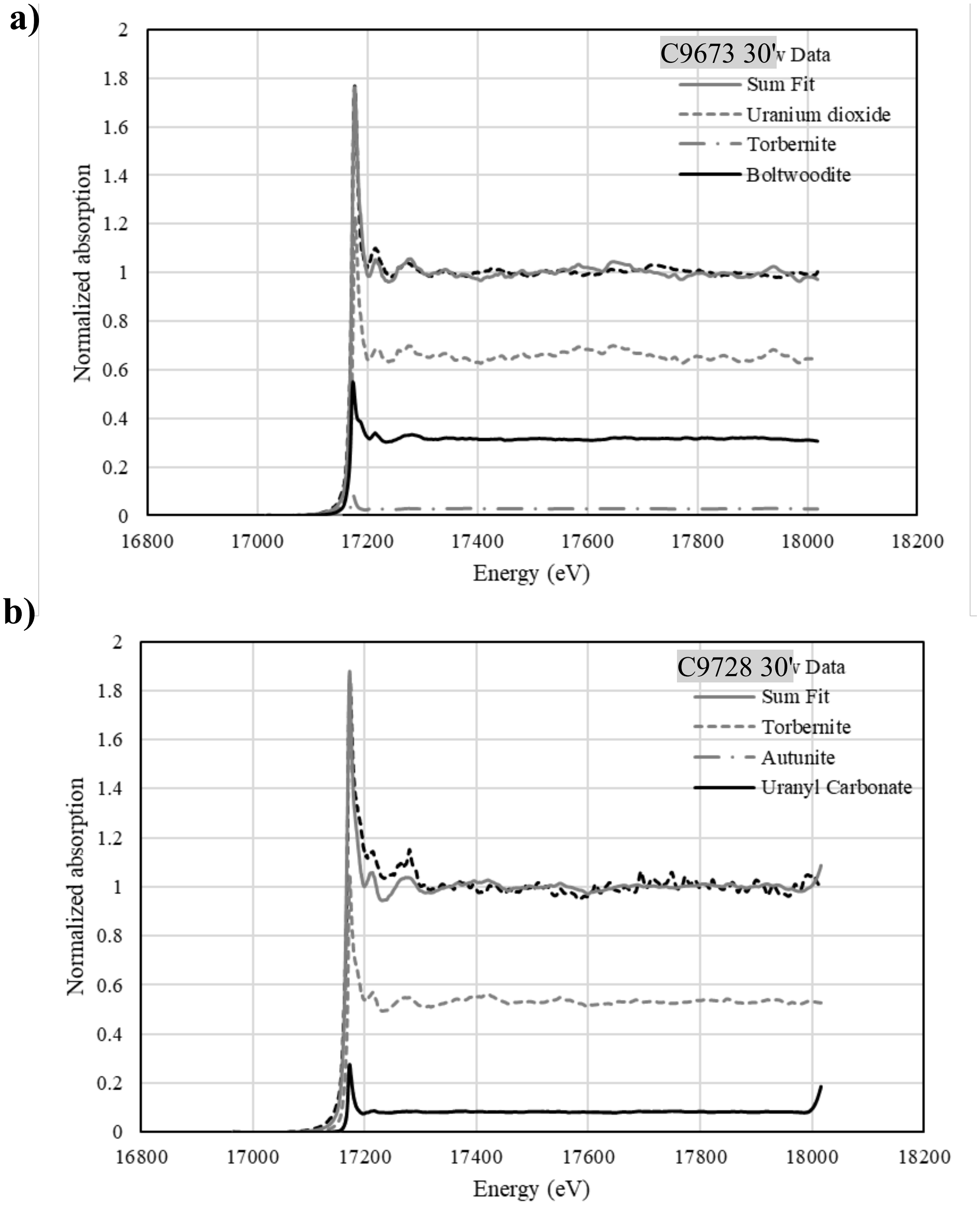

Figure 4.39. Comparison of best fits for LCF for μ-XANES spectra for samples (a) C9673 30 ft depth, G5, point 1, pre-treatment and (b) C9728 30 ft depth, G6, point 2, post-treatment. Data shown is FIO.

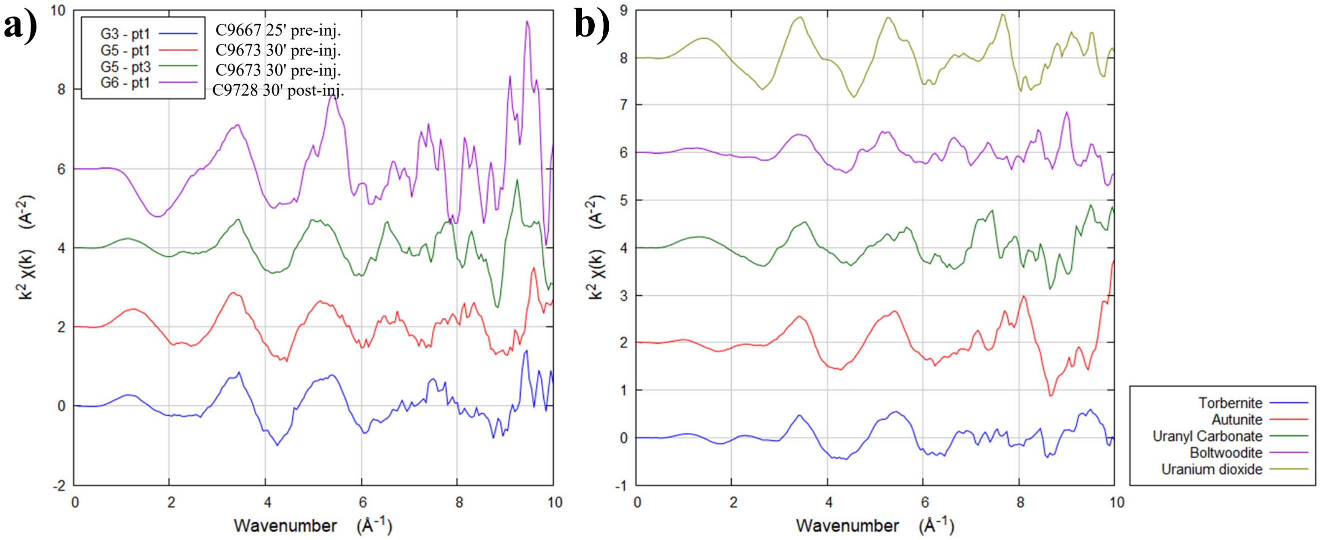

Figure 4.40. μ-EXAFS k^2-weighted spectra collected for samples (a) and reference minerals (b). Data shown is FIO.

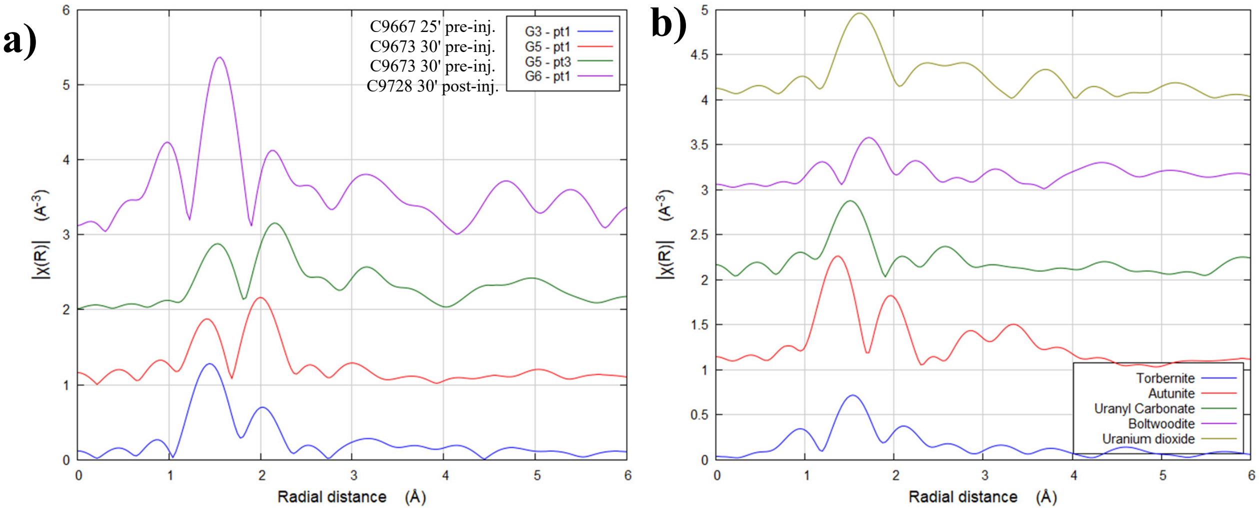

Figure 4.41. μ-EXAFS Fourier transformed to R-space for samples (a) and reference minerals (b). Data shown is FIO.

4.4.3 Major Elements Identified via SEM-EDS

SEM-EDS was used to quantify phosphorus and other elements in pre-injection sample C9667 25 ft (G3) and post-injection sample C9729 25 ft (G4). Elements that were identified included P, Ca, Mg, Al, Si, O, K, Ti, Fe, Cu, but not U, as it was present at concentrations below the detection limit of the EDS detector. Therefore, U cannot be correlated with potential Ca-phosphate precipitates identified by elemental mapping. For the C9667 25 ft depth pre-injection sample, 2-D EDS scans of elements at seven locations did find one grain with Ca and P only (i.e., likely apatite), and many locations that contained Cu correlated with O and not correlated with Ca (Figure 4.42). In contrast to the pre-injection sample, SEM-EDS analysis of the post-injection sample from borehole C9729 25 ft (G4) showed significant Ca-P association in 6 of 11 locations in which the 2-D elemental analysis was conducted. In one particle from C9729 25 ft (Figure 4.42), most of the P is associated with Ca and O, with two locations showing Ca-Cu-P association.

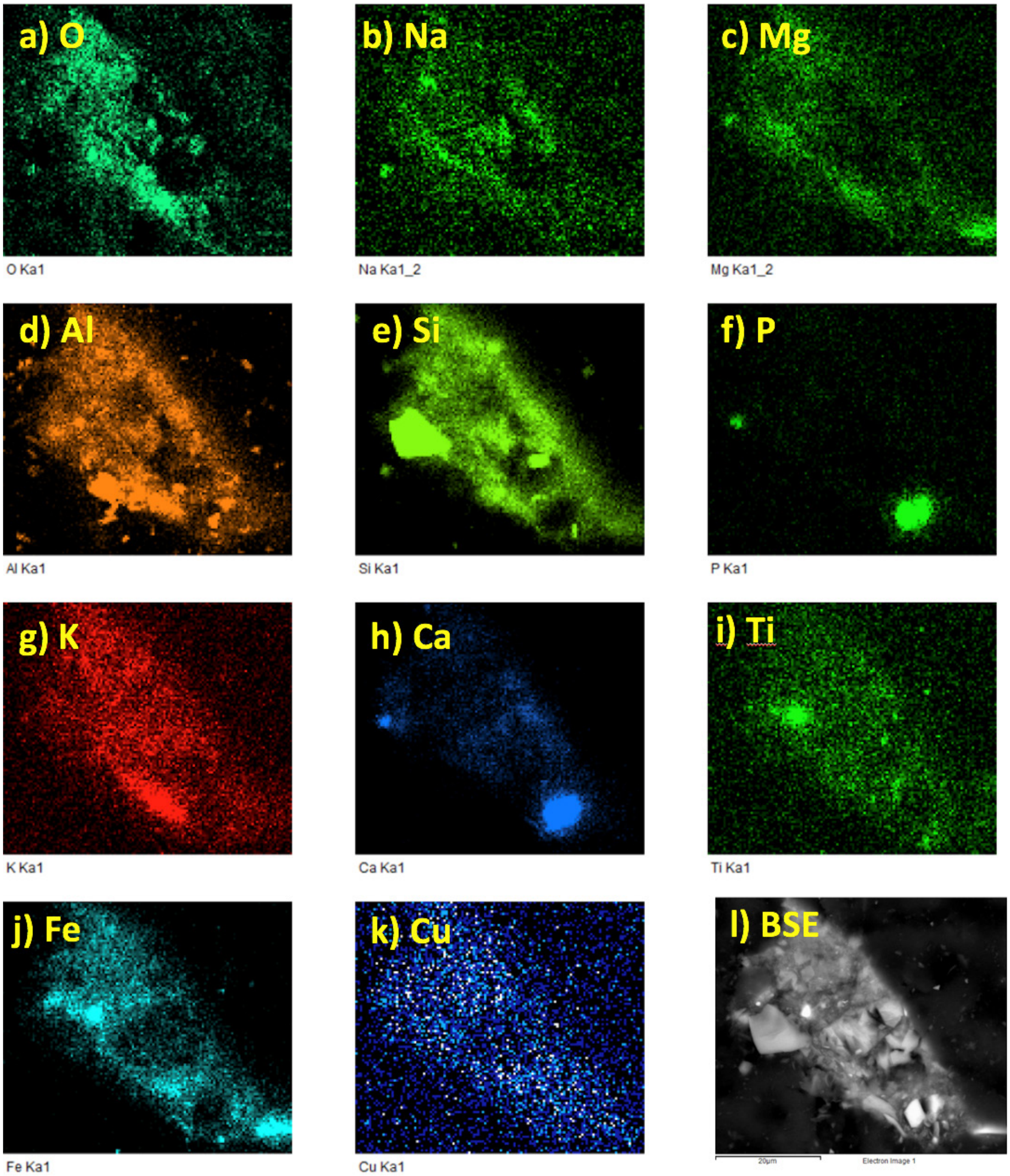

Figure 4.42. 2-D elemental maps of elements by SEM-EDS of pre-injection sediment C9667 25 ft (G3) showing elements (a-k) and electron backscatter (l). Data shown is FIO.

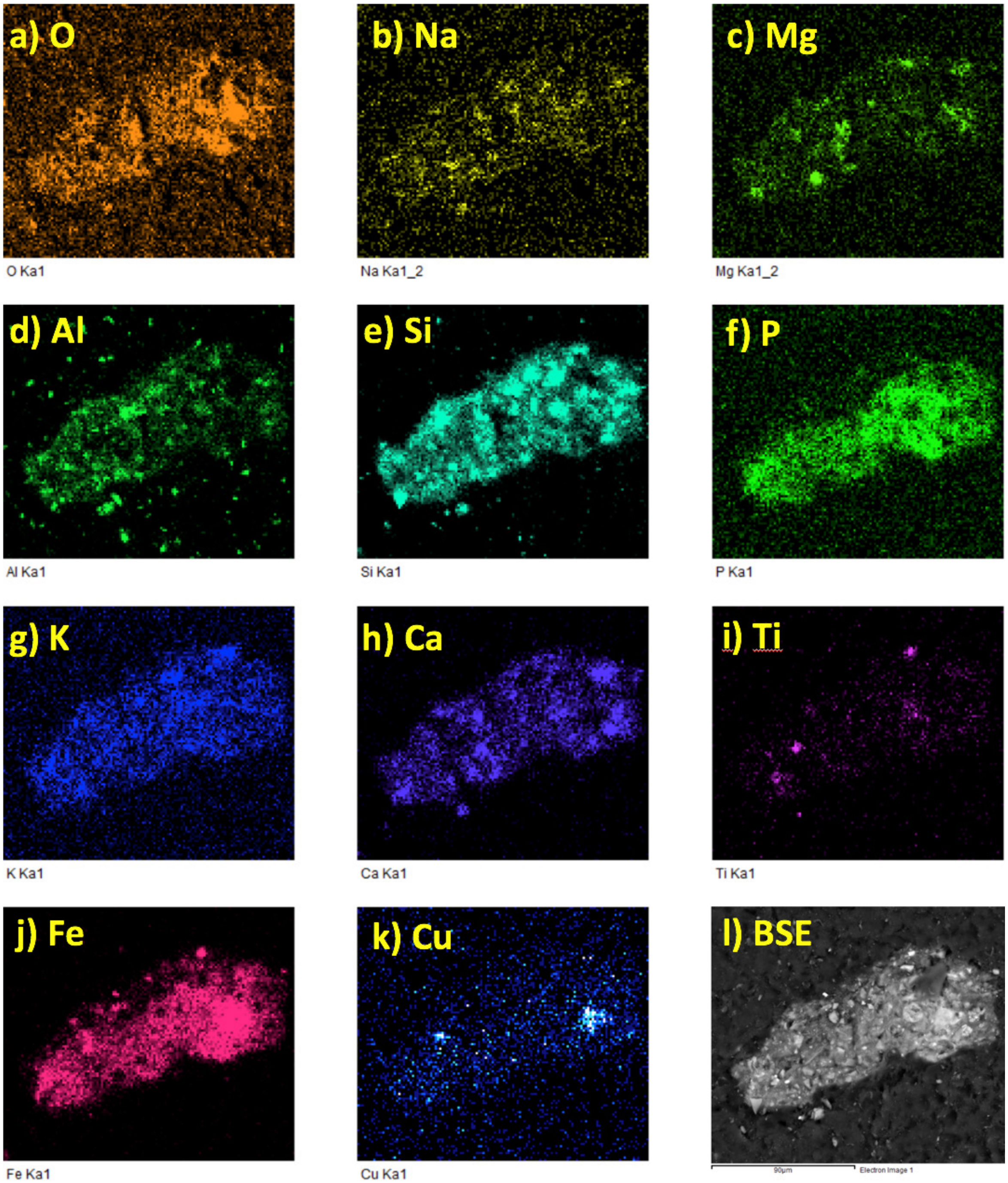

Figure 4.43. Scanning electron microscope 2-D map of elements using SEM-EDS of post-injection sediment C9729 25 ft showing elements (a-k) and electron backscatter (l). Data shown is FIO.

4.4.4 Predicted Precipitates based on Geochemical Equilibrium Modeling

Geochemical modeling was used to predict potential U sequestration mechanisms, including whether the conditions favored precipitation of apatite and autunite, in order to inform on the phases expected during and after injection as well as to complement the observations from solid phase characterization. Previous studies have identified multiple mechanisms that may decrease uranium mobility (i) apatite precipitation that can structurally incorporate U, (ii) autunite mineral group precipitation (e.g. $Ca(UO_2)_2(PO_4)_2$•10-12H_2O), (iii) aqueous uranium sorption to precipitated apatite, and (iv) apatite coating of existing uranium surface phases, as described in detail in Section 1.0 (Wellman et al. 2005, 2006, 2007, 2008a-c; Mehta et al. 2016; Lammers et al. 2017). While these models cannot predict U incorporation or co-precipitation with and coating by apatite, they can inform on the phases that are thermodynamically favorable to precipitate in the subsurface. Due to the differences in delivered versus targeted components in solutions, models were run under variable conditions (Appendix F, Table F.1 – comparison of major components of targeted versus delivered solutions). Because this modeling was not NQA-1 qualified, all information presented in this section is FIO.

The potential precipitation of apatite and autunite were investigated via GWB modeling. It shows that apatite precipitation is favored at pH 6.5 to 8 with the injection solution (i.e., 87 mM PO_4, 61 mM CO_3, Figure 4.44a), with autunite favored at pH < 6.5. These results are similar to precipitates reported by Mehta et al. (2016). For one of the U sequestration mechanisms (i.e., autunite precipitation), equilibrium speciation modeling in GWB investigated the thermodynamic favorability of uranyl phosphate species formation in conditions ranging from the injection solution to natural groundwater (model input in F.1, Table F.2 and Table F.3, with additional discussion on thermodynamic constants for uranium in Table F.6 and Table F.7). Sequential extractions, 1000-h carbonate extraction, and 1-D leach experiments described elsewhere in Section 4.0 show the functional measure of the change in uranium mobility as a result of polyphosphate treatment by a combination of these mechanisms. In general, adsorbed U (to sediment and apatite) decreased [i.e., mechanism (ii) is likely small in sediments 6 months after injection], apatite was shown to precipitate by extractions and SEM work [Section 4.4.4, so mechanism (iii) may contribute], and autunite precipitation was not identified [mechanism (i), previous section]. Over time, the contribution of mechanisms may change as autunite may precipitate in the differing geochemical conditions, and upgradient U migrating into the apatite-laden zone with low ionic strength groundwater may adsorb to apatite.

The polyphosphate injection solution contained approximately 87 mM PO_4 and 61 mM bicarbonate [i.e. PO_4/HCO_3 ratio of 1.4, Log(ratio) = 0.146]. Under the injection solution conditions with a high bicarbonate concentration, simulations indicate that uranyl carbonate minerals [e.g., andersonite, $Na_2Ca(UO_2)(CO_3)_3$•6H_2O, and grimselite, $K_3Na(UO_2)(CO_3)_3$•H_2O)] are the most likely to form (Figure 4.42b; Appendix F, Figure F.2). It should be noted that andersonite solubility is considerably lower than calcite, so precipitation of andersonite would decrease U leaching. By 6 months, the specific conductance of the pore water (based on 1-D column leach in post-injection sediment samples) had decreased significantly (Table 4.5), as well as aqueous inorganic carbon, which decreased to 52.5 to 837 mg/L (Table 4.5) in 1:1 DI H_2O to sediment suspensions. Solid phase carbonate analysis of post injection sediments further indicates that significant precipitation of carbonates did not occur (Table 4.4); hence, carbonate likely advected downgradient and decreased to near natural groundwater conditions (Table 4.5, both within measurement detection limits, Section 4.2.3). Phosphate remains in the immediate area due to precipitation (e.g., hydroxyapatite) and sorption as shown by the significant increase in solid phase phosphorus (Section 4.5) where it is likely to slowly dissolve or desorb back into solution. Pore water bicarbonate in cores (6 months after injection) are near natural groundwater and river water concentrations (i.e., approximately 22 and 52 times less bicarbonate compared to phosphate).

Under the low (i.e., close to natural groundwater) bicarbonate conditions (i.e., PO_4/HCO_3 ratio of >20) reached by 6 months, uranium is favored to precipitate as autunite group minerals (Figure 4.42b). This trend is consistent with previous modeling and the hypothesis that apatite acts as a source for additional autunite formation (Wellman et al. 2008a). Moreover, at pH 7.5, the autunite saturation index is 3 orders of magnitude greater than andersonite/grimselite, and at pH 7.0, the autunite saturation index is 5 orders of magnitude greater, confirming high favorability for autunite precipitation. Therefore, as high-solubility U precipitates, such as uranophane and Na-boltwoodite, dissolve with time (Figure 4.21), it is hypothesized that autunite will form and/or U will sorb to apatite in the long term and/or can be incorporated into Ca-PO_4 precipitates (Mehta et al., 2016).

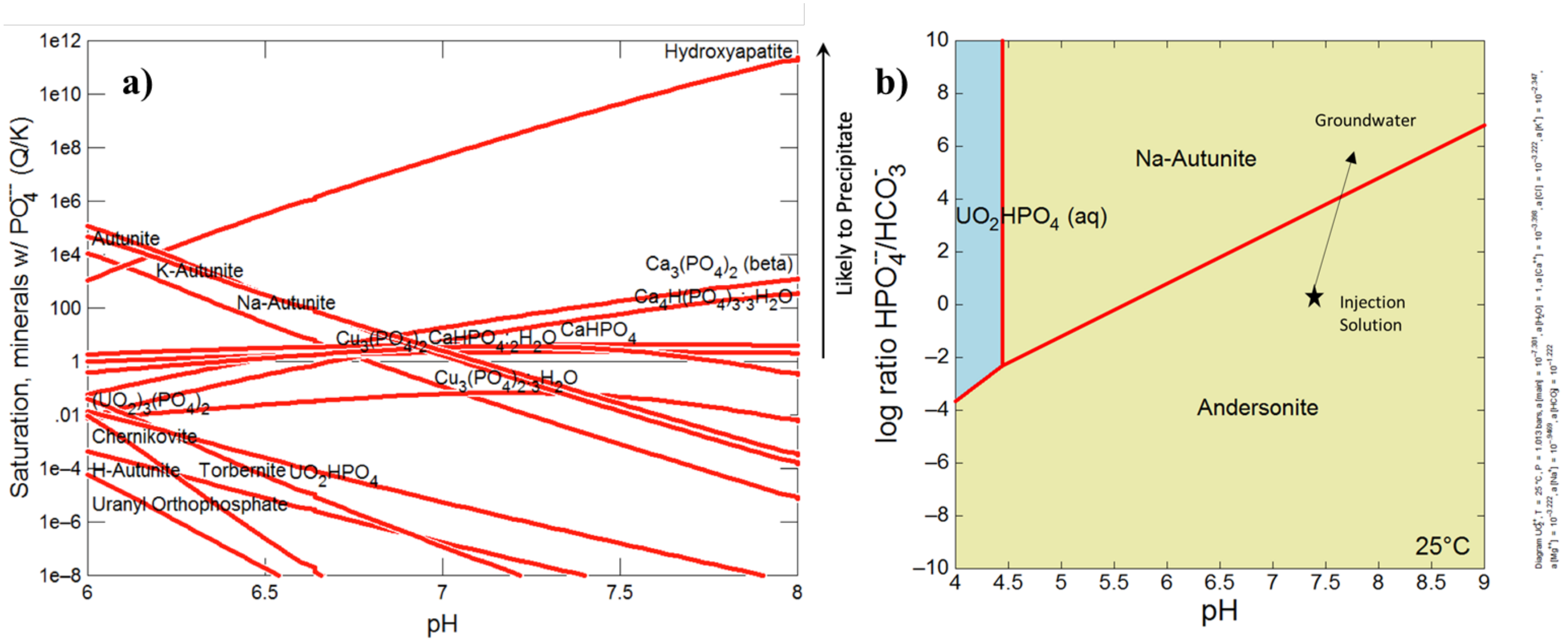

Figure 4.44. Geochemical equilibrium simulations of (a) polyphosphate injection solution showing all phosphate precipitates with the black arrow indicating the region where precipitation is favored (SI > 1), and (b) major U species predicted in delivered (actual) injection solution over a range of HPO_4^{2-} to HCO_3^- ratio with respect to pH. The star represents the injection conditions (i.e., delivered polyphosphate solution) where andersonite precipitation is favored, and the solid line and arrow shows that over time, autunite precipitation is favored. Data shown is FIO.

Additional geochemical equilibrium modeling was conducted to investigate the thermodynamic favorability of two different autunite mineral group minerals: autunite ($Ca(UO_2)_2(PO_4)_2$•10-12H_2O) and torbernite ($Cu(UO_2)_2(PO_4)_2$•8-12H_2O). Torbernite has previously been identified in NPP sediments (pre-injection, see Section 2.0, Arai et al. 2007) and there are high copper concentrations in the 300-FF-5 sediments from waste disposal (see Figure 4.56). Data from average Ca, Cu, and P in all extractions shows significantly greater Ca to Cu in aqueous, adsorbed, low- and high-solubility precipitates (Table 4.10), whereas high Cu in extraction 5 is highly unlikely to dissolve and be available to form torbernite. Simulations were conducted at different Ca/Cu ratios and results are presented in terms of the saturation index (SI) where a higher value indicates a greater likelihood of precipitation (assuming geochemical equilibrium, SI > 1.0 identifies saturation with respect to each mineral phase). In these simulations, torbernite is favored over autunite if significantly more Cu than Ca is present in the aqueous phase and the pH decreases below 6.5 (Figure 4.45). Moreover, because torbernite is not favorable until Ca:Cu molar ratios are < 1.7 (Cu:Ca 0.58) and environmentally available Cu in extractions 1-4 are significantly lower than this value, it is highly unlikely that torbernite would form in this system. In addition, previously precipitated torbernite phases are unlikely to dissolve during and after polyphosphate injections due to their low solubility (similar to the targeted autunite phases, see Figure 4.20).

In addition, the potential change in pH as a result of phosphate precipitation was investigated experimentally (Section 4.2.4) as well as through simulations (this section). Precipitation of apatite and autunite in a batch reactor in the absence of sediment or any pH buffering precipitate (i.e., calcite) or dissolved carbonate shows that the pH can decrease from 7.7 to 6.5 to 7.0 (Figure 4.21c). It should be noted that significant calcite precipitation is not expected in this system based on measured inorganic carbon analysis (Table 4.4). Simulations conducted using a geochemical equilibrium model in PHREEQC show that the pH of the system will decrease as apatite precipitates depending on the amount of calcite to buffer the system (Appendix F, Table F.4 and Table F.5). At field scale, groundwater monitoring conducted by CHPRC using field dataloggers shows that the pH dropped in only 1 of 24 wells (399-1-23) monitored during injection, confirming that it is highly unlikely that additional torbernite will form in this system. Therefore, if autunite can be differentiated from torbernite species in future analysis, it could be shown that new uranyl phosphate species could be forming in this system as torbernite likely formed under the acidic conditions of historical waste disposal and would no longer be favored in this system. However, the current solid phase characterization results cannot differentiate between autunite and torbernite species (Section 4.4).

Table 4.10. Ratio of Cu/Ca extracted from pre-injection sediments with sequential extractions.

Extraction	Ca (ug/g)	Cu (ug/g)	P (ug/g)	Ca/Cu (ug/ug)	Ca/Cu (mol/mol)
Aqueous, extr. 1	97.2 ± 10.3	< 0.1 (MDL)	< 0.5 (MDL)	>1000[(a)]	>1600[(a)]
Adsorbed, extr. 2	594 ± 184	0.559 ± 0.067	< 0.1 (MDL)	950 ± 2460	1550 ± 4020
pH 5 acetate, 3	364 ± 310	5.69 ± 7.69	2.50 ± 2.11	54.7 ± 40.0	89.4 ± 65.5
pH 2.3 acetate, 4	300 ± 257	113 ± 165	8.08 ± 9.23	1.36 ± 0.730	2.23 ± 1.19
Oxalate, extr. 5	6.85 ± 11.1	49.1 ± 60.3	115 ± 21.7	0.044 ± 0.027	0.073 ± 0.045
HNO_3, extr. 6	5860 ± 390	165 ± 178	1160 ± 152	35.8 ± 34.8	58.6 ± 56.9

(a) Ratio based on Cu MDL

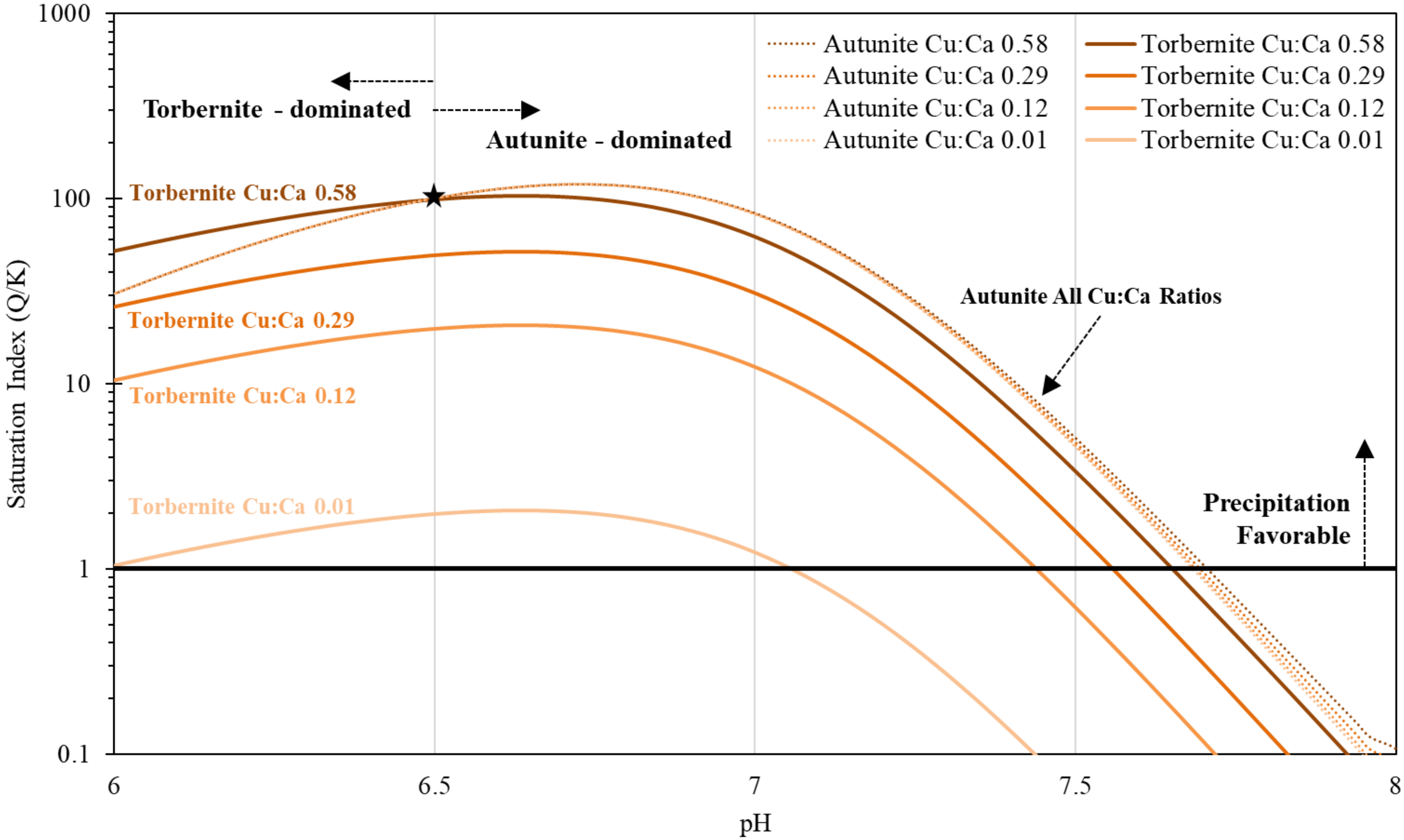

Figure 4.45. Saturation indices (as Q/K) for autunite (*dotted lines*) and torbernite (*solid lines*) for simulated Hanford Site groundwater with remediation solution components with Cu varied, each series represents the Cu:Ca ratio by mass as predicted by GWB, the *star* highlights the transition between torbernite and autunite as the most favorable phase for precipitation. A saturation index > 1.0, indicates that precipitation is favorable. Data shown in FIO.

4.5 Phosphate in Sediments

Phosphate extractions were conducted on pre- and post-injection sediments (Section 3.3) that consisted of a 0.1 mol/L nitric acid dissolution of surface phases for 15 min, to maximize dissolution of freshly precipitated phosphate phases on mineral grains and minimize dissolution of natural phosphate in the sediment. In addition, phosphorus was measured in the sequential liquid extractions (Section 3.5). Results of the phosphate extraction in pre- and post-injection pairs (Figure 4.46 through Figure 4.49) show small increases in some post-injection sediments, and large PO_4 increase at a few depths.

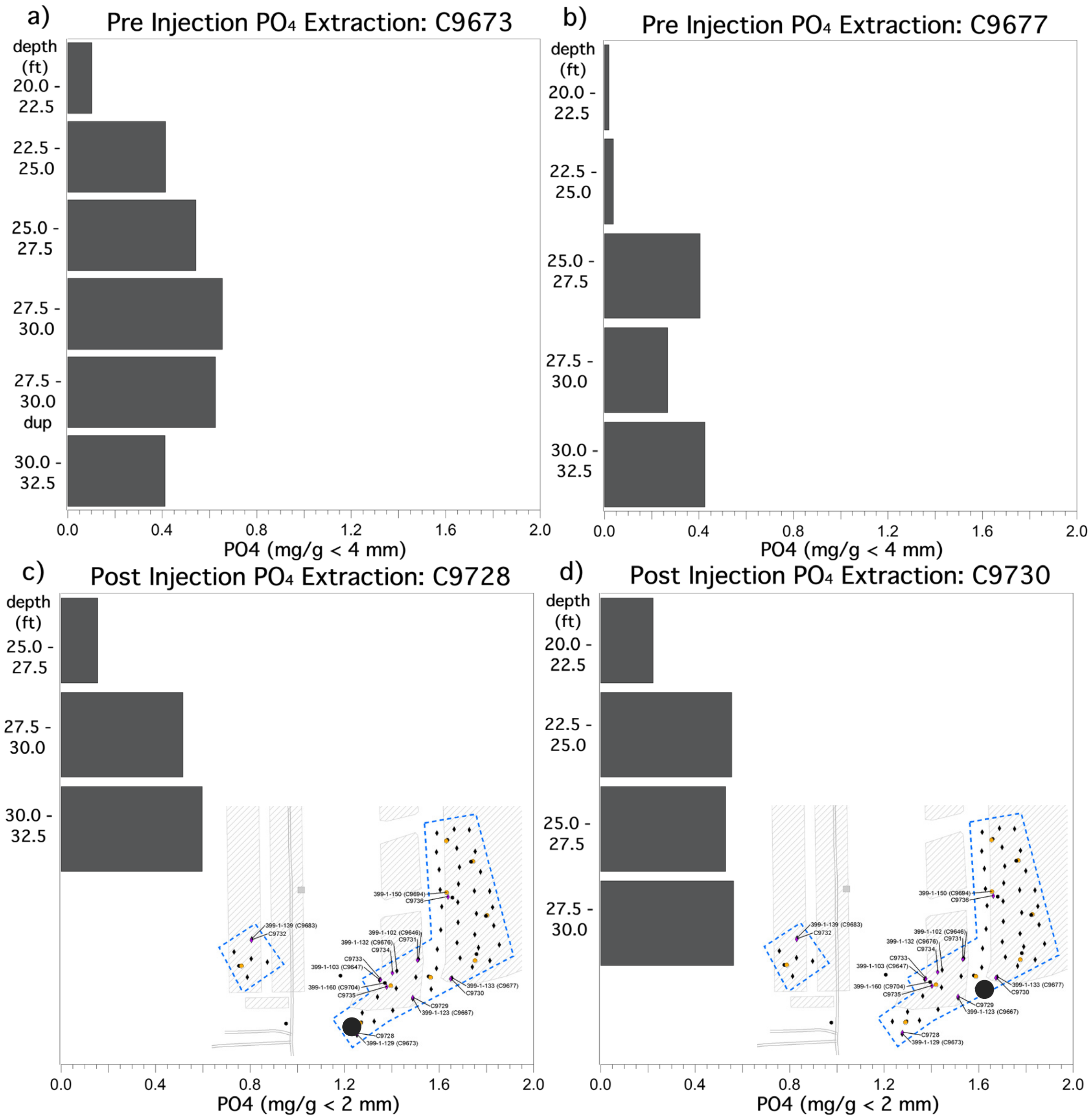

Figure 4.46. Phosphate extractions in pre-/post-injection sediment borehole pairs C9673 (a) and C9728 (c), and pair C9677 (b) and C9730 (d). Locations of boreholes are shown in (c) and (d).

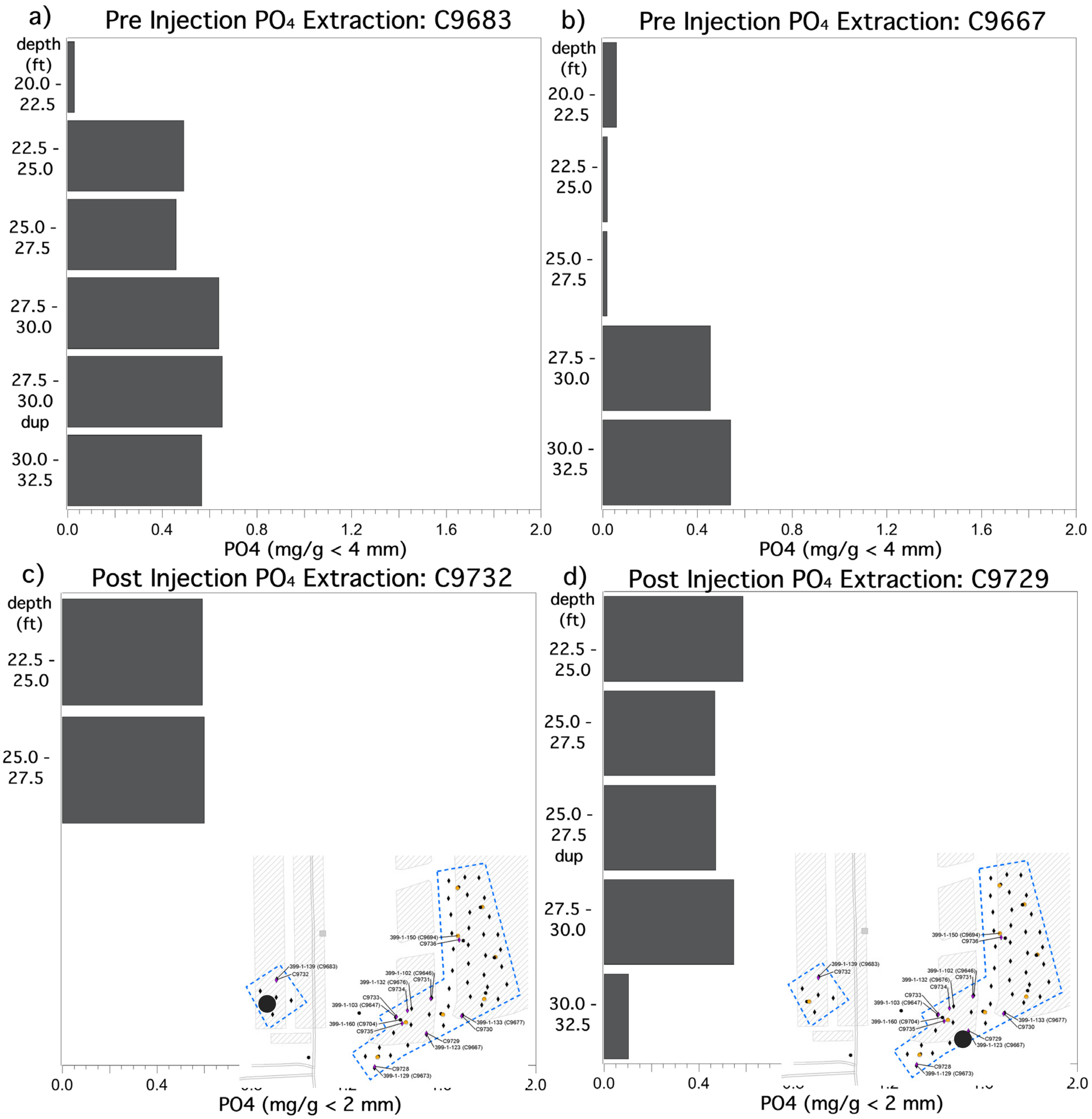

Figure 4.47. Phosphate extractions in pre-/post-injection sediment borehole pairs C96783 (a) and C9732 (c), and pair C9667 (b) and C9729 (d). Locations of boreholes are shown in (c) and (d).

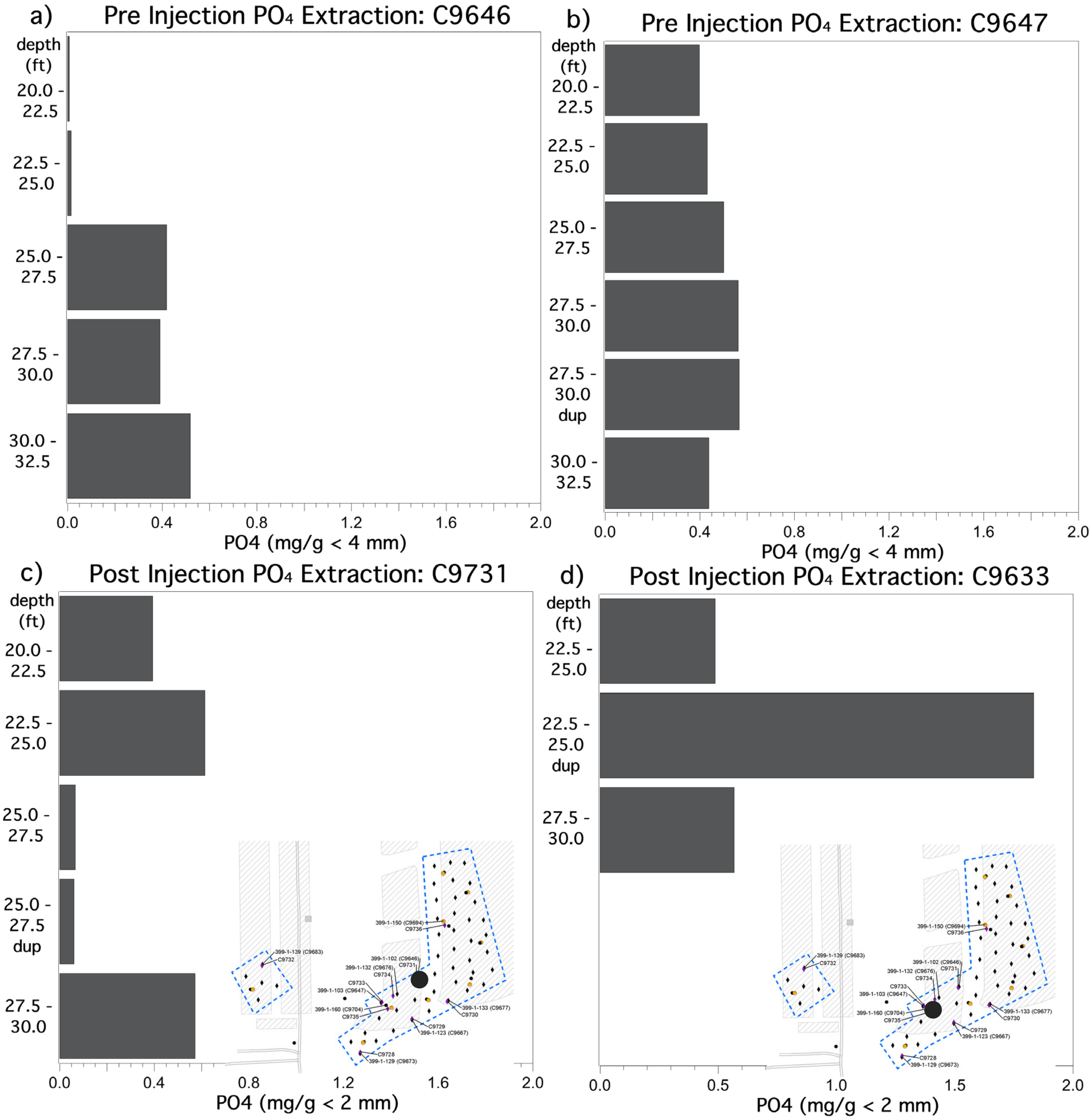

Figure 4.48. Phosphate extractions in pre-/post-injection sediment borehole pairs C96746 (a) and C9731 (c), and pair C9647 (b) and C9733 (d). Locations of boreholes are shown in (c) and (d).

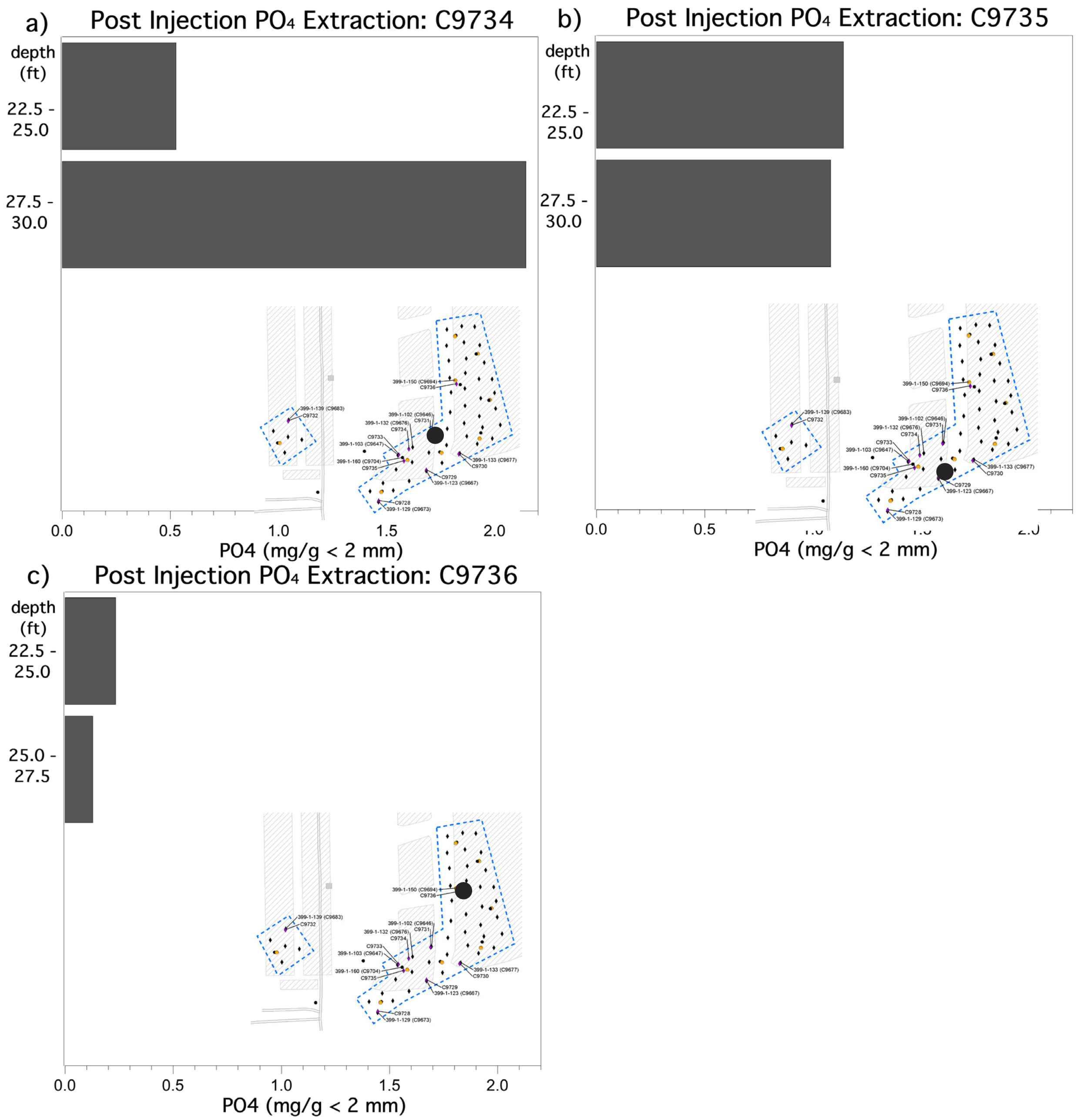

Figure 4.49. Phosphate extractions in post-injection, unpaired sediment boreholes C9734 (a), C9735 (b), and C9736 (c).

A comparison of pre-/post-injection borehole phosphate precipitate from the sequential extraction shows an increase in extractions 4, 5, and 6, although the magnitude of the increase is difficult to quantify on the log scale (Figure 4.50a and b). Pre-injection sequential analyses of P in extractions 1 (aqueous) and 2 (adsorbed) were all less than detection limits, so a direct comparison of pre- to post-injection analysis for these extractions is not possible although post results being above detection limits suggests an increase. For extraction 3, half of the pre-injection samples were below detection limits. For the remaining samples, the average gain in phosphate for extraction 3 was 118 ± 97.8 µg P/g. Extractions 4, 5, and 6, and the separate phosphate extraction are shown in detail in Figure 4.50 and Figure 4.51, respectively.

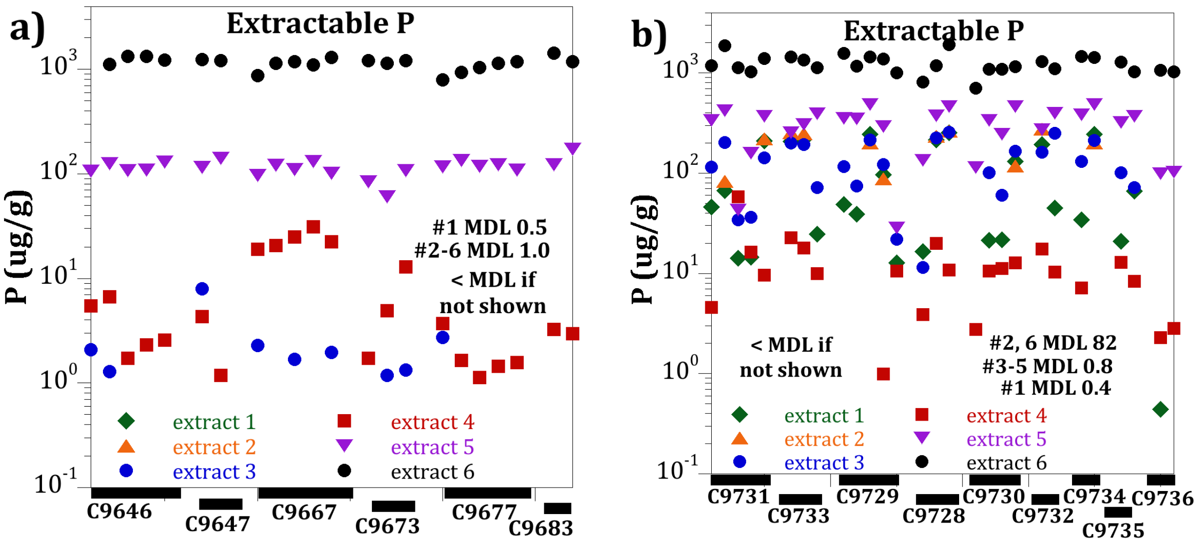

Figure 4.50. Sequential extraction phosphorus for (a) pre-injection sediments, and (b) post-injection sediments.

The separate 0.5 M HNO_3 phosphate extraction showed that post-injection boreholes had an average of 67 µg/g more phosphate (reported as P, equivalent to 205 µg/g as PO_4), which varies widely between sediments (Figure 4.51a and b). Sequential extraction 4 shows, on average, a 2.4 µg/g P gain (i.e., nearly no gain), with only slightly fewer sediment pairs showing a loss compared to sediments showing a P gain (Figure 4.51c and d). Sequential extraction 5 showed a consistent P gain in nearly all sediments, averaging 183 µg/g (Figure 4.51e and f, equivalent to 561 µg/g as PO_4), or about 3 times more than the 0.5 M HNO_3 extraction. Finally, sequential extraction 6 showed an average P gain of 123 µg/g (Figure 4.51g and h, equivalent to 377 µg/g as PO_4), with about a third of the sediments showing a loss.

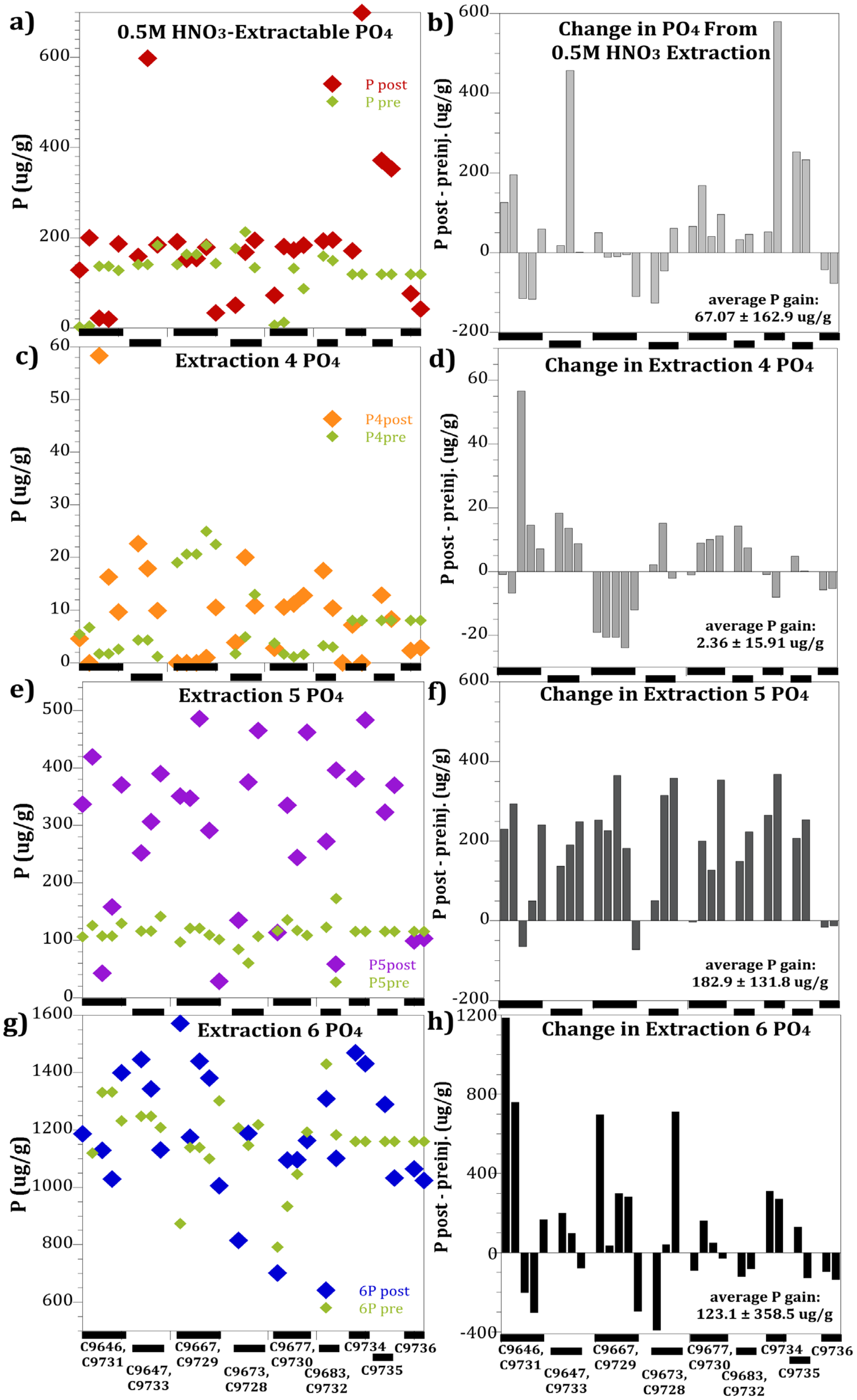

Figure 4.51. Extractable phosphate precipitate in sediments shown by (a, b) 0.5 M HNO_3 extraction, (c, d) acetic acid extraction (extraction 4), (e, f) NH_3-oxalate extraction (extraction 5), and (g, h) 8 M HNO_3 extraction (extraction 6). Concentrations are reported as P in ug/g.

Because injection was conducted at two different intervals (screens at 16 to 21 ft depth and 26 to 31 ft depth), there may be a depth-associated phosphate distribution due to release occurring only through screened areas of the wells. However, results from the phosphate extraction and sequential extraction 5 with depth show little trend (Figure 4.52). In addition, there should be a decrease in phosphate with distance from the injection well, as the injected polyphosphate solution sorbs and precipitates over time. Most post-injection borehole samples, however, are within 3.28 ft (1 m) of the injection well (Table 3.2) and showed a wide range of phosphate concentrations (Figure 4.53). Conversely, post-injection samples at 10 to 25 ft distance from injection wells do show a decreasing phosphate concentration with distance trend providing some correlation with expectations.

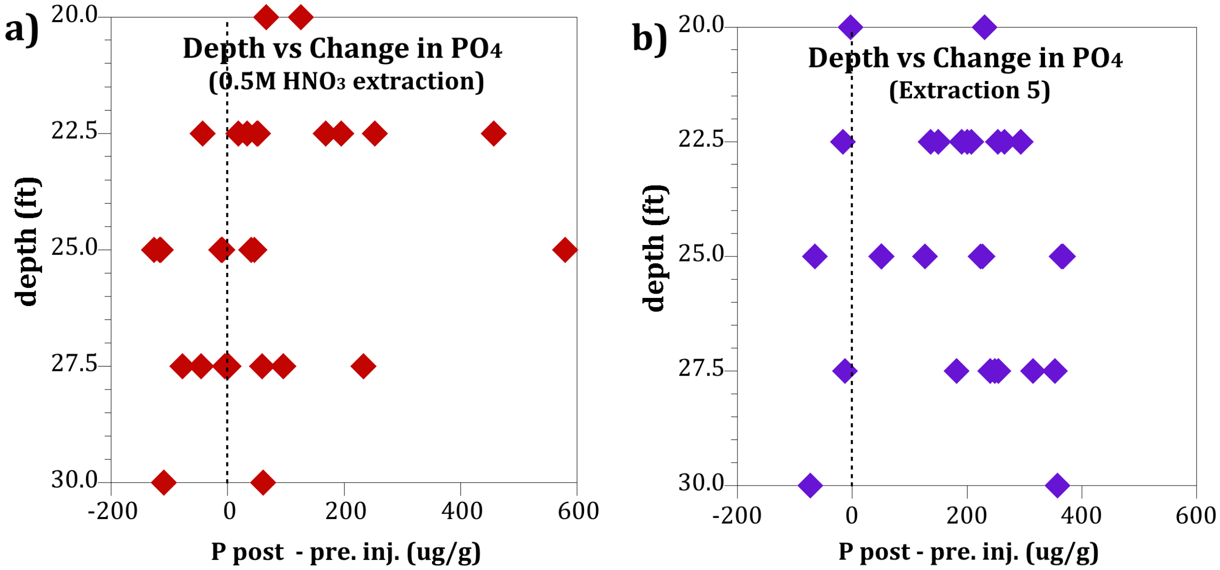

Figure 4.52. Phosphate in post-injection wells minus pre-injection concentrations for pairs 1 m apart, based on (a) 0.5 M HNO_3extraction, and (b) sequential extraction 5.

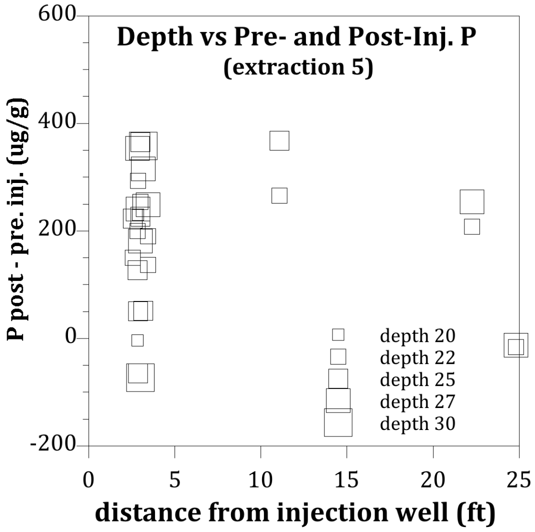

Figure 4.53. Change in phosphate in post-injection sediments with distance from the injection well.

4.6 Metals in Sequential Extractions as Indicators of Co-Contaminants and Solid Phase Changes

4.6.1 Major Cations

Calcium, magnesium, sodium, and potassium are present in aqueous solution and adsorbed or exchanged to minerals in natural Hanford groundwater. For some extractions, specific cations are not reportable due to their high concentration in the extraction solutions, which includes Mg in extraction 2 [$Mg(NO_3)_2$], Na in extraction 3 [Na-acetate], and Ca in extraction 4 [$Ca(NO_3)_2$]. With the injection of the Na,K-polyphosphate solution, significant Na^+ and K^+ is injected, which will displace adsorbed ions. In addition, eventual precipitation of phosphates will consume Ca^{2+} and Mg^{2+}. Therefore, it is expected that aqueous and adsorbed Na and K will increase, and Ca and Mg will decrease. There may be additional changes in extracted metals for extractions 3 through 6, based on dissolution or precipitation of different phases. The aqueous calcium in post-injection cores averaged 4.6 times less than in pre-injection cores, likely reflecting precipitation with phosphate. The aqueous magnesium also decreased 2.5 times in post- versus pre-injection cores (Figure 4.54). There were no significant changes in extractions 3 through 6 (i.e., precipitates) for calcium and magnesium. As expected, the aqueous and adsorbed concentrations of Na and K increased significantly (about 5 times) due to the Na,K-polyphosphate injection (Figure 4.55). The K in extractions 3, 4, and 5 also consistently increased.

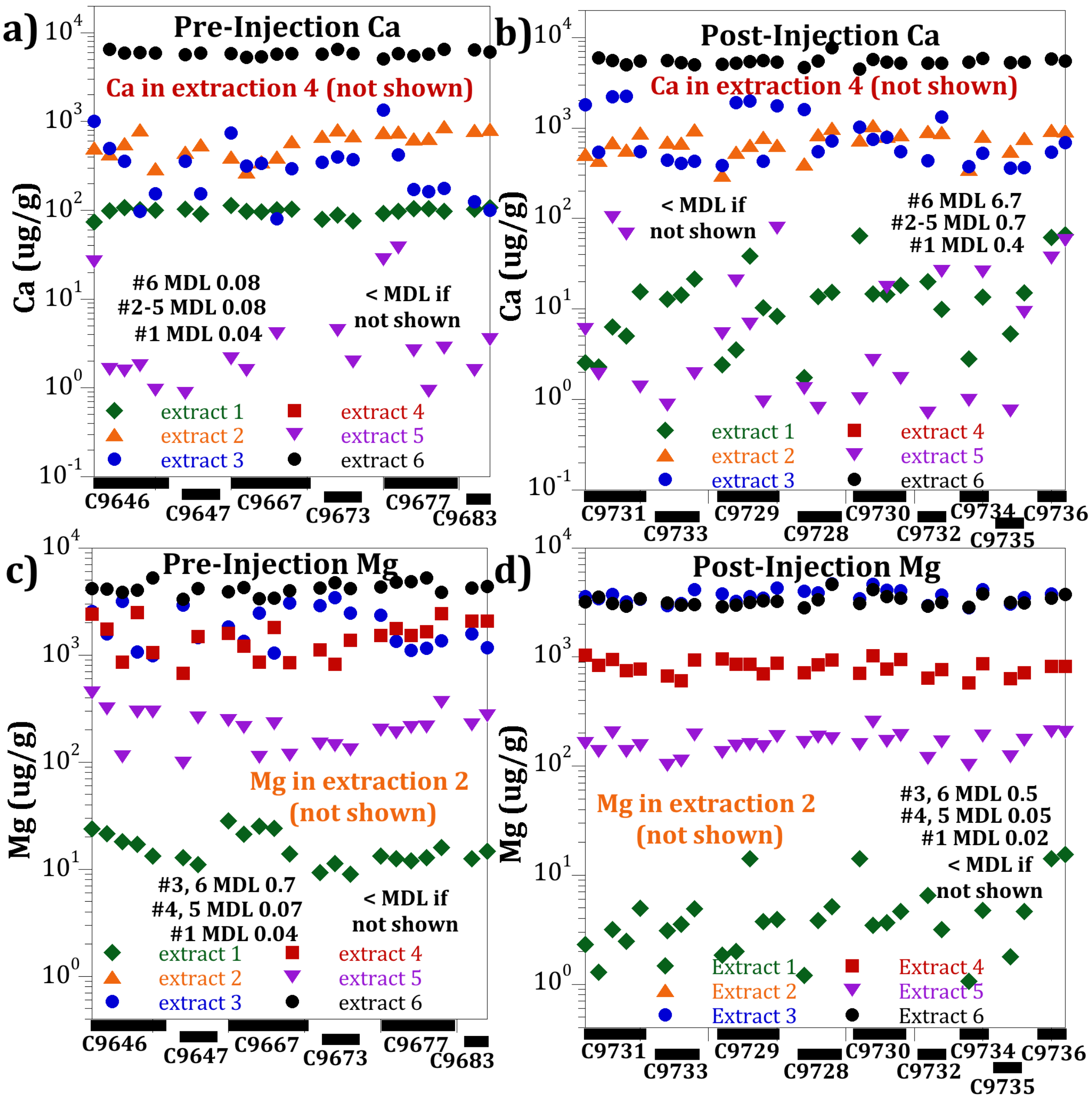

Figure 4.54. Sequential extraction of pre- and post-injection cores with Ca (a, b) and Mg (c, d) analysis.

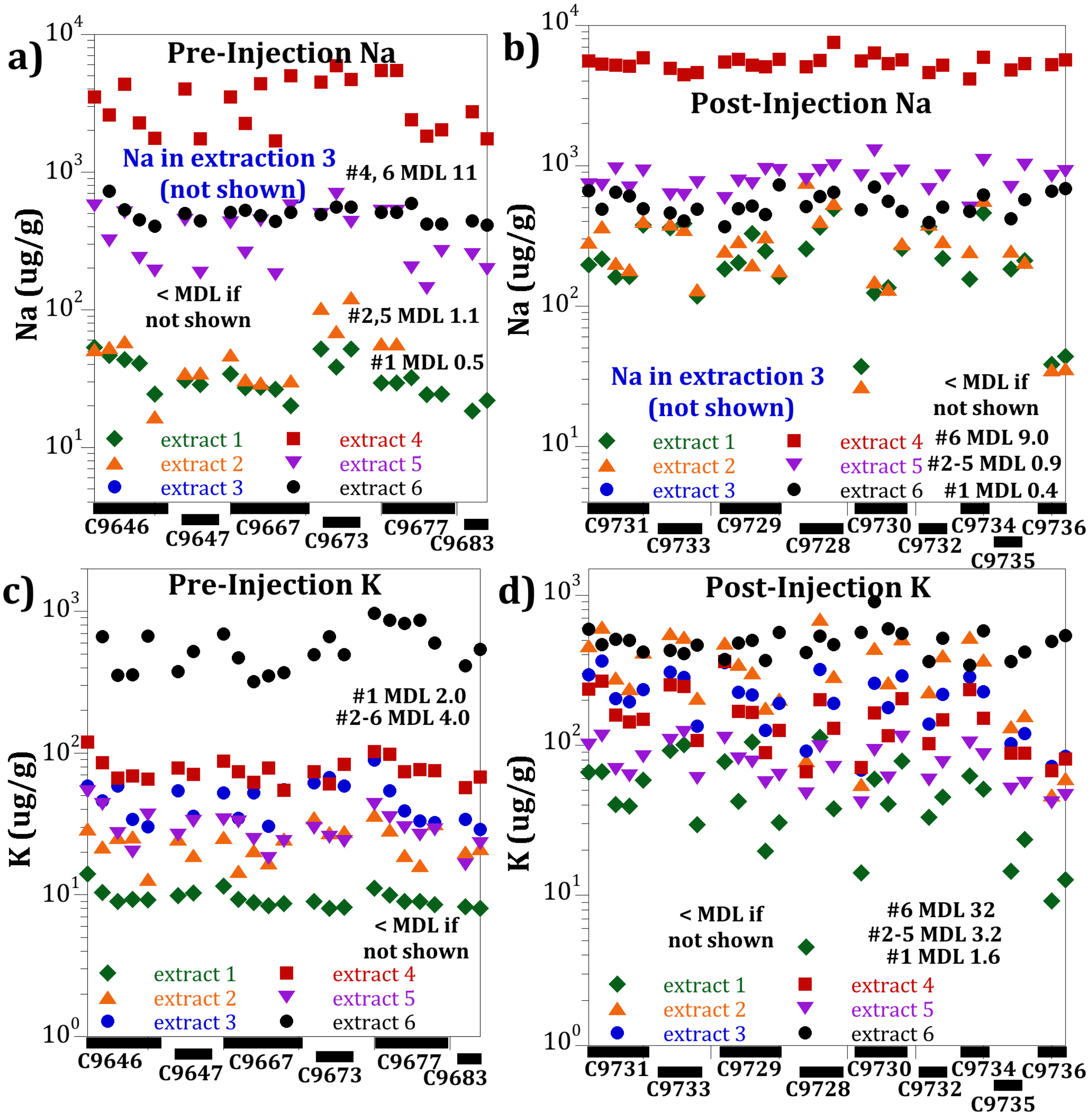

Figure 4.55. Sequential extraction of pre- and post-injection cores with Na (a, b) and K (c, d) analysis.

4.6.2 Copper

Copper is known to be present in the NPP and SPP waste (Catalano et al. 2006). In the NPP, 50 tons of Cu were disposed of along with 30 tons of U (Gerber 1993; see Section 2.0 for additional co-contaminants). Pre-injection copper extracted from sediments shows low (below MDL) aqueous copper, and low concentrations of adsorbed copper, but significantly greater concentrations of copper in one or more solid phases extracted in pre-injection sediments (Figure 4.56a). Significant copper is in extractions 4, 5, and 6. Copper-uranyl-phosphates (torbernite, metatorbernite) have also been previously identified in 300 Area sediments (Arai et al. 2007). Torbernite is a low-solubility mineral that can be dissolved in the 8 mol/L nitric acid (extraction 6, Figure 4.22a). The ratio of copper to uranium in extractions from sediments with values ranging from 0.5 to 250 shows that copper is primarily in excess to uranium, so it is likely present as $Cu_2(PO_4)OH$ or other copper precipitates (Figure 4.56c). The post-injection extracted copper (Figure 4.56b) was higher in extraction 3 and lower in extractions 1 and 2 (aqueous and adsorbed), implying precipitation of a Cu-phosphate.

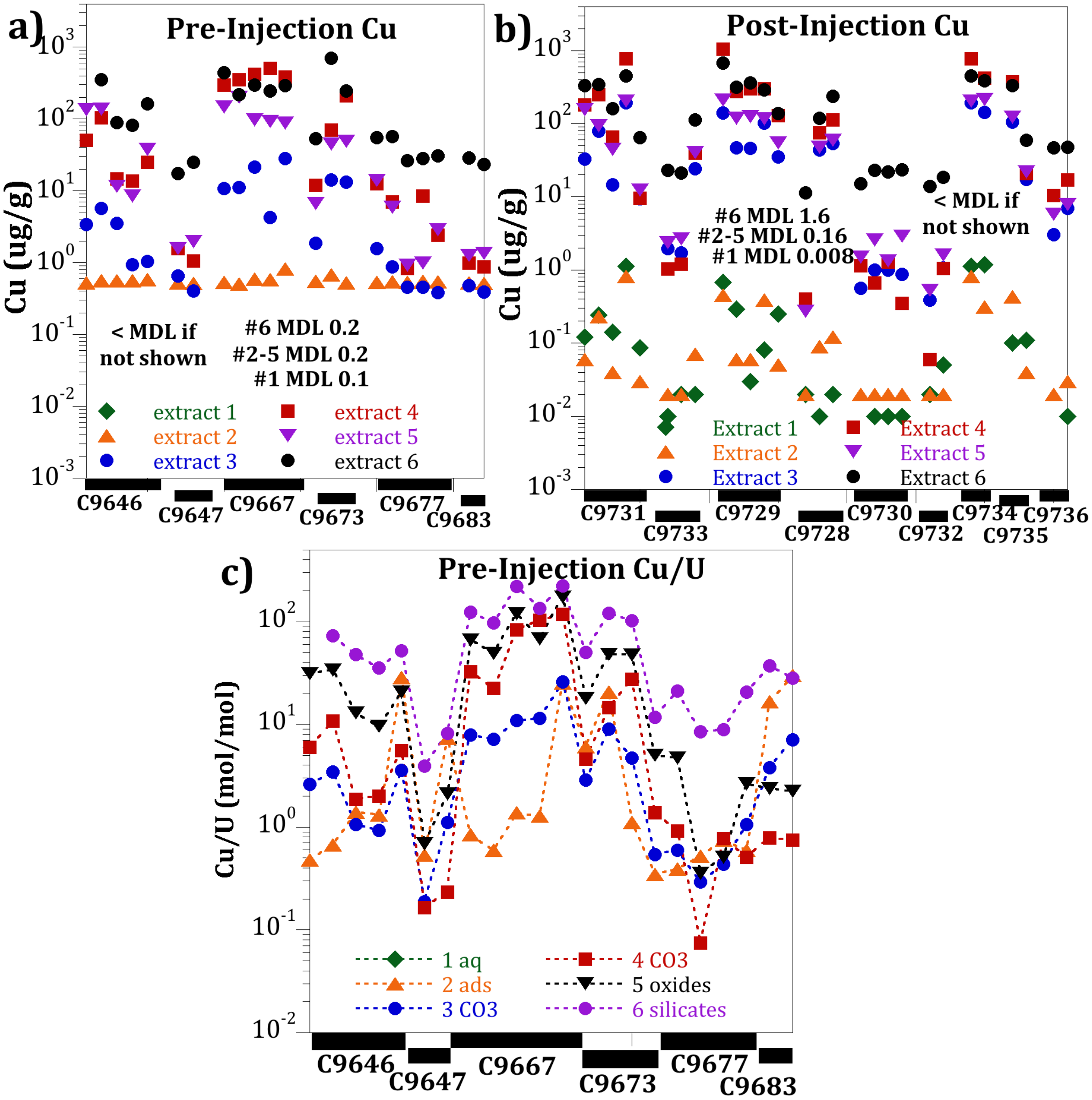

Figure 4.56. Sequential extraction of pre- and post-injection cores with copper analysis (a, b), and the ratio of copper/uranium in extractions (c).

4.6.3 Iron and Manganese

Iron and manganese oxides can be redox reactive, which can influence uranium oxidation state (and mobility). In addition, uranium can incorporate into precipitating Fe/Mn oxides. As NPP and SPP acidic waste was disposed, calcite, clays, iron oxides, and other minerals would dissolve to some extent (Szecsody et al. 2013), and as the pH was neutralized by these reactions, iron oxides would precipitate, and possibly incorporate some uranium. Sequential extractions of iron in pre- and post-injection samples show that moderate iron concentrations are removed from sediments in extraction 3 (pH 5 acetate) and extraction 4 (pH 2.3 acetic acid), both of which have been shown to dissolve Fe oxides (Figure 4.57a and b; Chao and Zao 1983). Pre- and post-injection iron in extractions 3 through 6 are unchanged. The high iron concentrations in extraction 6 are likely from mafic minerals such as fayalite (Fe_2SiO_4).

Manganese is another redox-reactive transition metal, similar to iron, although it is typically present in lower aqueous and adsorbed concentrations. The post-injection sediments showed lower aqueous Mn^{2+} concentrations (extraction 1) compared with pre-injection sediments, and thus may have been displaced by the K^+ and Na^+ in the injection solution (Figure 4.57c and d). Extraction 3 (pH 5 acetate) increased from pre- to post-injection sediments, indicating Mn precipitated (Mn^{3+} can substitute into apatite).

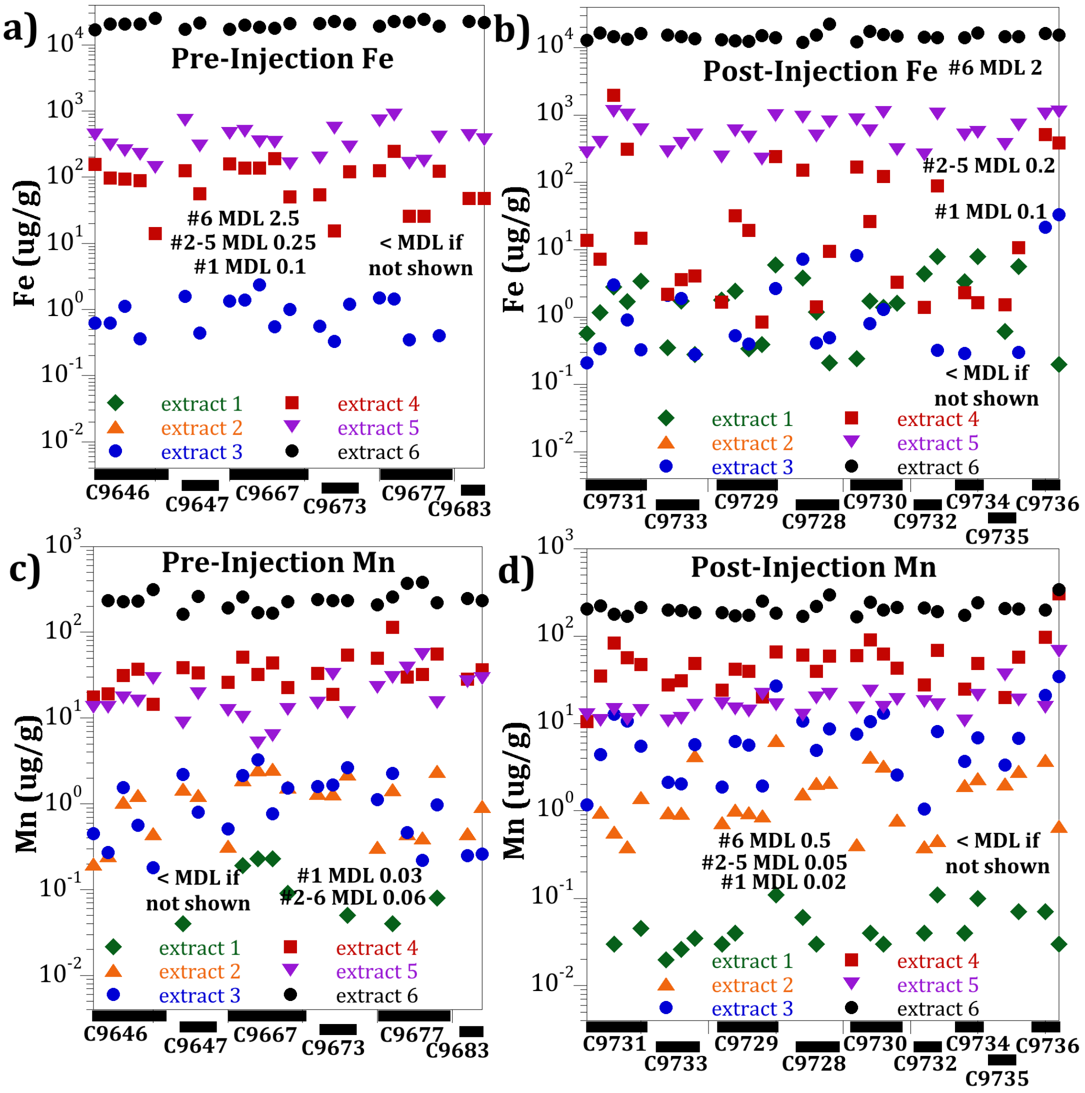

Figure 4.57. Sequential extraction of pre- and post-injection cores with iron analysis (a, b) and manganese analysis (c, d).

4.6.4 Silica and Aluminum

Although silica and aluminum are in many natural minerals, from 2:1 and 1:1 clays (Si:Al ratio) to minerals that contain only silica (i.e., quartz, SiO_2), to Al-only minerals (e.g., gibbsite $Al(OH)_3$, boehmite [AlO(OH)], diaspore [AlO(OH)]), bauxite, and other metal oxides. Elemental analysis (i.e., digestion) of 40 different Hanford formation samples shows SiO_2 weight percent ranging from 64% to 82%, and Al_2O_3 weight percent ranging from 12% to 16% (Xie et al. 2003), so Al is not found in excess of Si in natural Hanford formation sediments. However, in the NPP, 2000 tons of sodium aluminate was co-disposed with 30 tons of uranium (see Section 2.0 for additional co-contaminants; Wang et al. 2005; Gerber 1993).

In pre- and post-injection sediments, aqueous and adsorbed Si was largely unchanged, as were extractions 4 to 6 (Figure 4.58a and b). The post-injection Si in extraction 3 (pH 5 acetate) increased, indicating precipitation. For Al, there was little change between pre- and post-injection samples for all extractions, although aqueous and adsorbed concentrations were less than detection limits. The extractable Al in extraction 6 was significantly greater than Si in extraction 6, which likely reflects anthropogenic disposed Al (Figure 4.58c and d). In one pre-injection borehole (C9677), the aluminum concentration decreased by an order of magnitude with depth in a similar pattern to Cu (Figure 4.56a), possibly indicating Al and Cu precipitation at shallower depth.

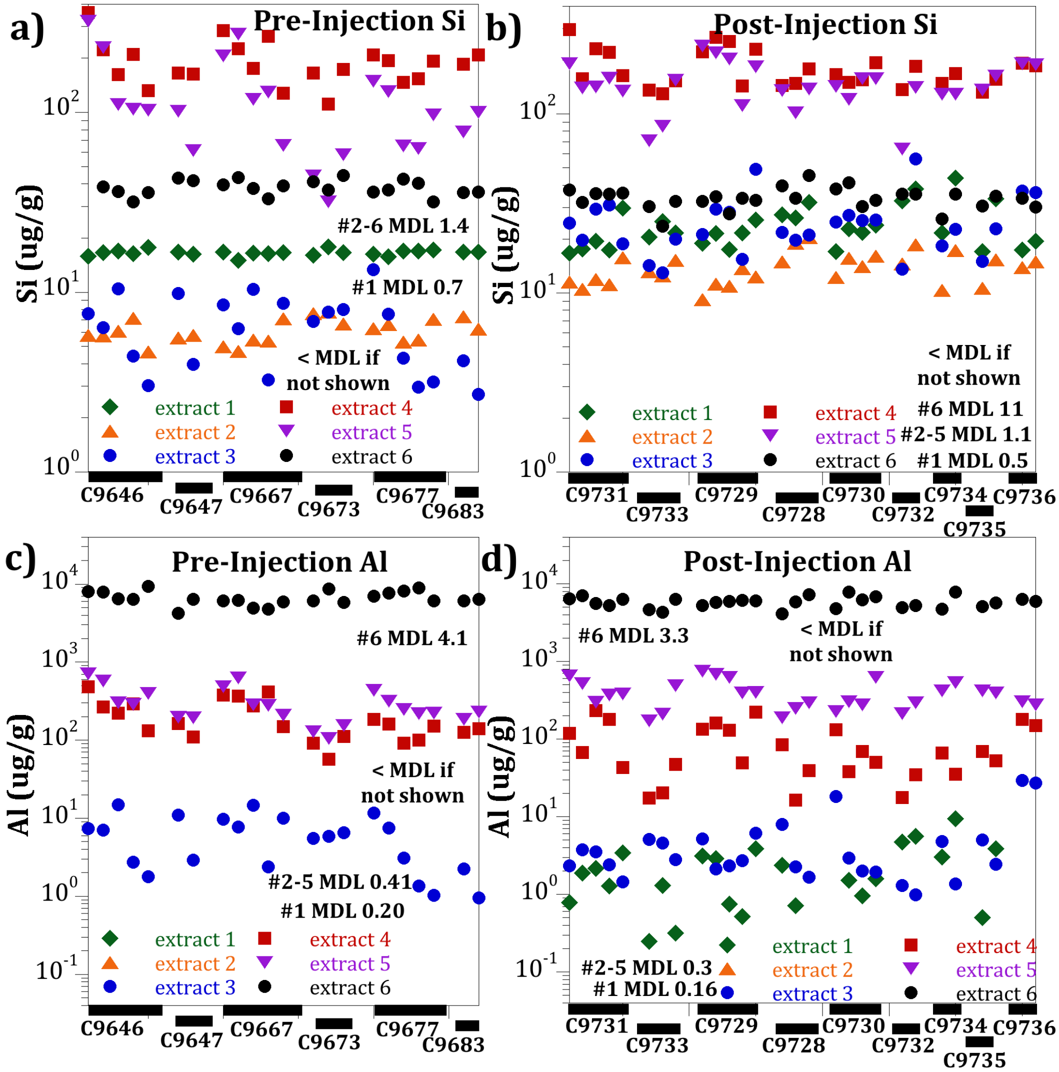

Figure 4.58. Sequential extraction of pre- and post-injection cores with Si analysis (a, b) and Al analysis (c, d).

4.6.5 Strontium and Sulfur

Although some Sr extraction data are below detection limits (Figure 4.59a and b), it was expected that aqueous and adsorbed Sr would decrease and precipitate in apatite, similar to Ca behavior (Figure 4.54a and b). Aqueous sulfur (most likely present as sulfate in the oxic water) is present in Hanford groundwater at 67 mg/L (natural, see artificial groundwater formula, Table 3.3) and also due to its presence in waste (from sulfuric acid, H_2SO_4). Post-injection sediments showed that aqueous sulfur was unchanged, but adsorbed sulfur decreased (Figure 4.59c and d) relative to pre-injection sediments. Sulfur in extractions 4 and 6 also decreased in post-injection sediments.

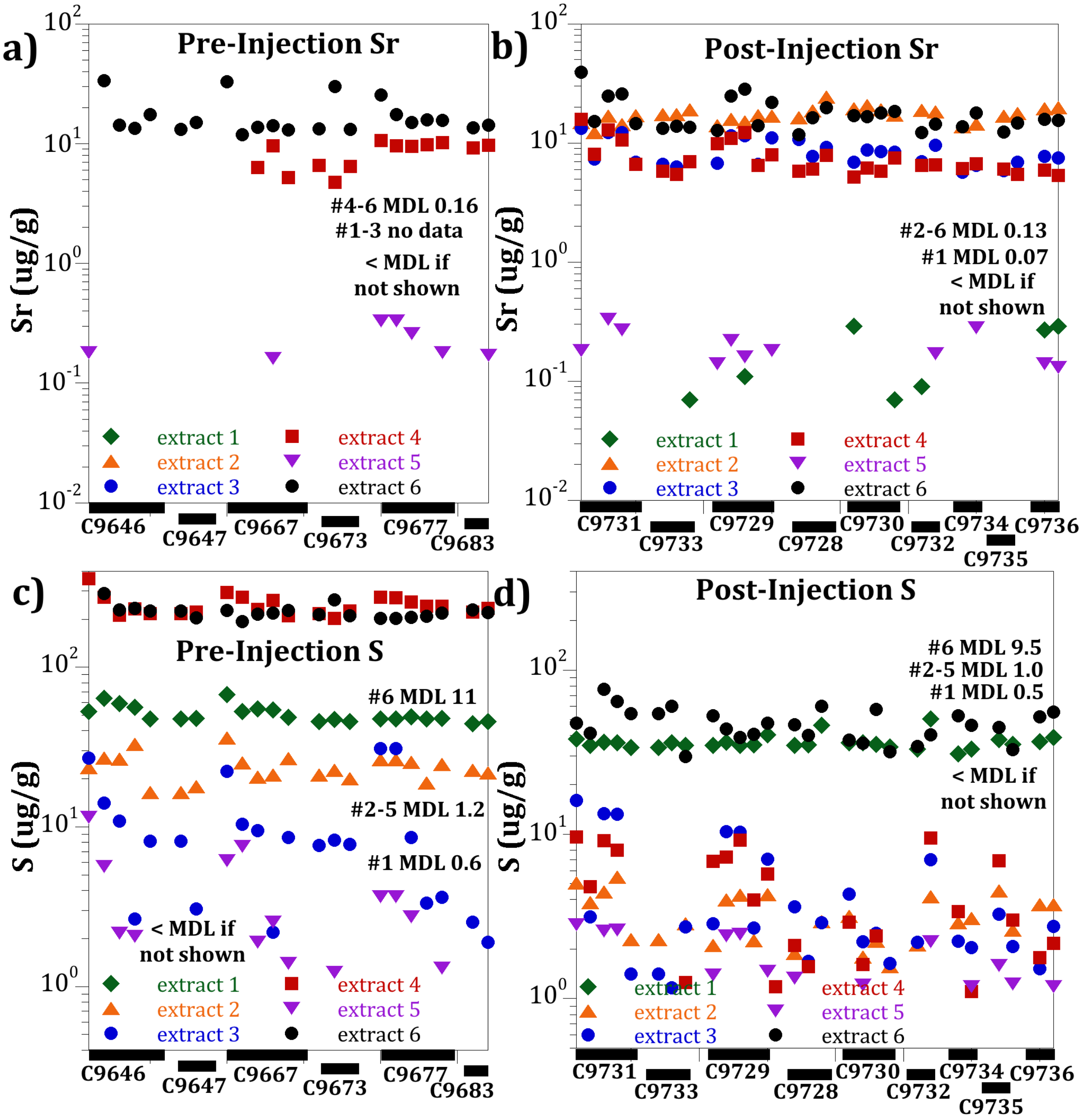

Figure 4.59. Sequential extraction of pre- and post-injection cores with Sr analysis (a, b) and S analysis (c, d).

4.6.6 Trace Metals Ti, V, As, Be, and Pb

Several trace metals were analyzed by ICP-OES and ICP-MS in sequential extraction liquids. Although trace metals were not the focus of this study, some of the trace metal analysis is useful for indicating the presence of possible U-containing precipitates or providing indications of waste co-contaminants. However, data is incomplete as concentrations of some trace metals in extractions were lower than the MDL. For example, titanium is present in trace precipitates as titanomagnetite and other oxides that can be associated with uranium. There was no change in pre- and post-injection extractions 5 and 6, with limited results for extractions 1 through 4 (Figure 4.60a and b). Vanadium is another trace metal that is typically present as vanadate that can form low-solubility uranium minerals (carnotite, tyuyamunite). Vanadium in pre- and post-injection extractions 5 and 6 is unchanged (Figure 4.60c and d).

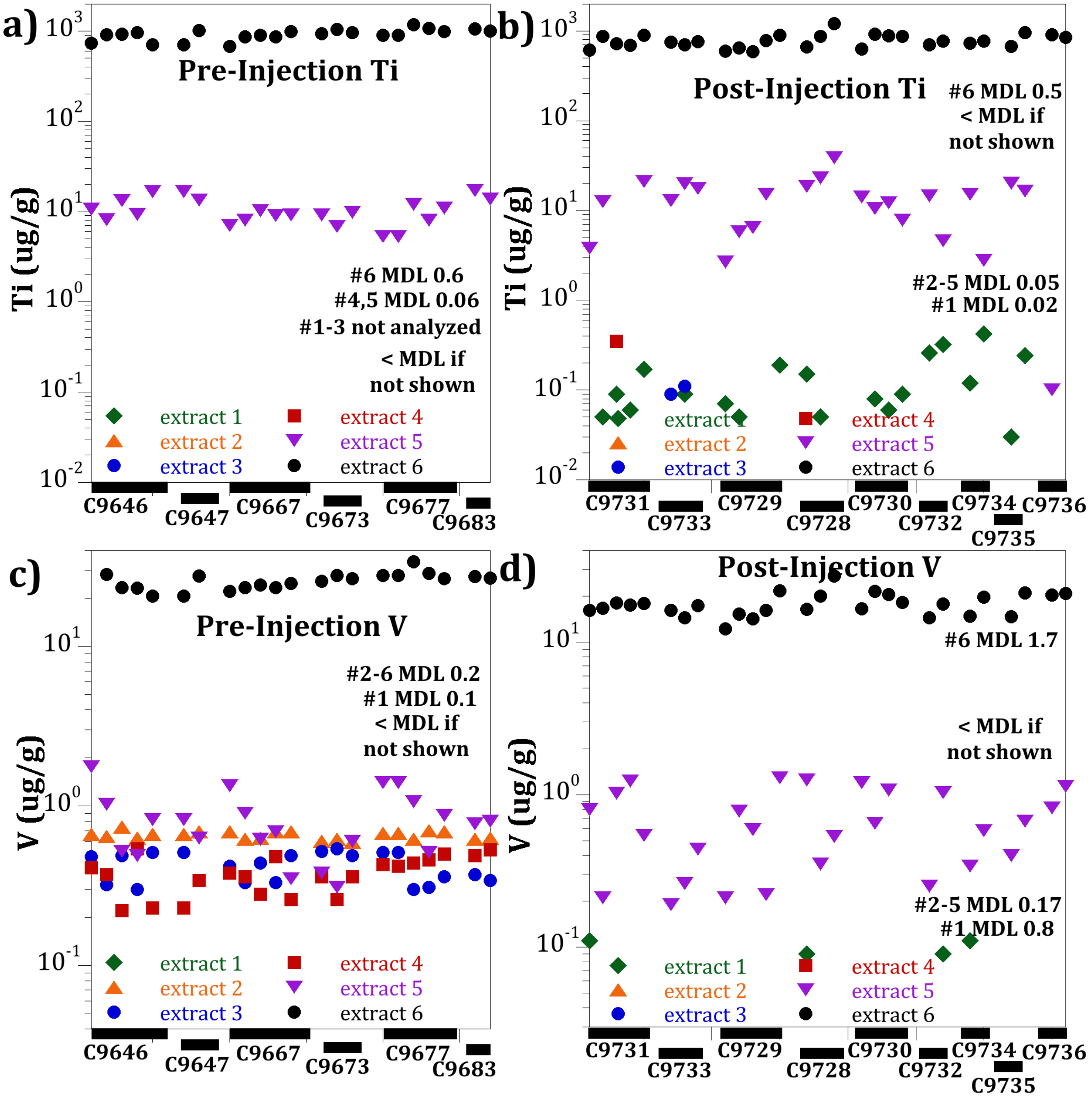

Figure 4.60. Sequential extraction of pre- and post-injection cores with Ti analysis (a, b) and V analysis (c, d).

Arsenic is a trace metal that can substitute in Fe oxides, which can incorporate uranium. Arsenic can also be present in aqueous solution as an oxyanion arsenate (AsO_4^{3-}) in an oxic environment or arsenite (AsO_3^{3-}) in a reducing environment. There is insufficient pre-injection data to compare to post-injection extractions (Figure 4.61), but post-injection sediments contain low adsorbed As, and in precipitates that were dissolved in extractions 3 and 4.

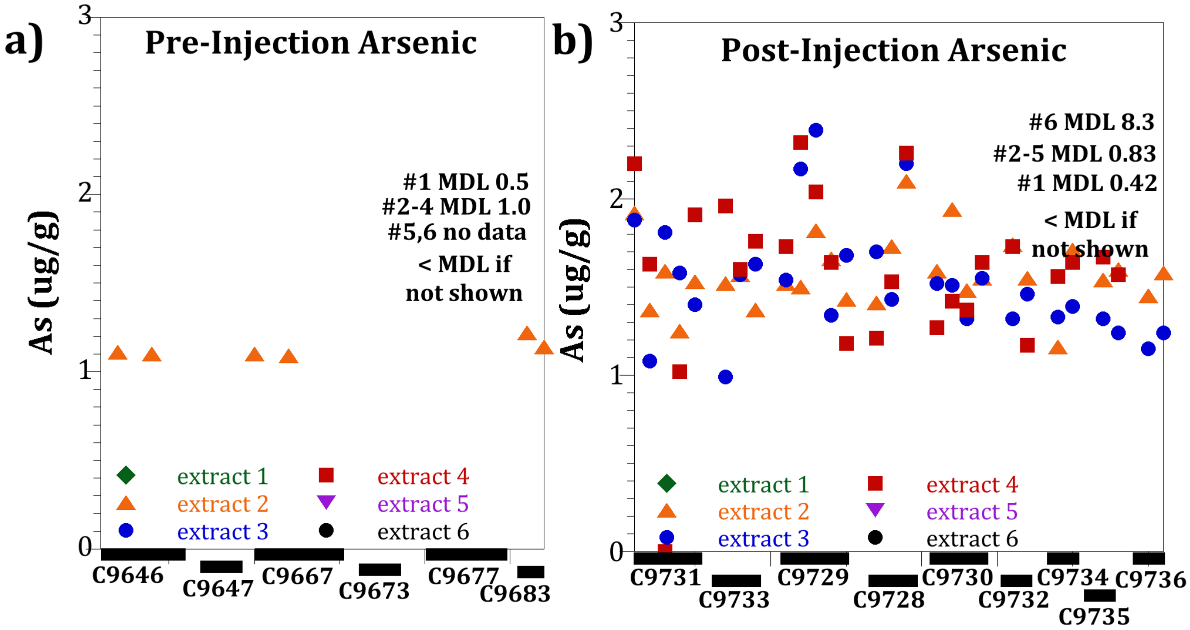

Figure 4.61. Arsenic in sequential extraction of pre-injection sediments (a) and post-injection sediments (b).

Beryllium is a trace metal present naturally in Hanford sediments, but may also be present as a co-contaminant in U waste (i.e., Be is used in U shielding). Limited Be data in sediment extractions show low concentrations present in precipitates (Figure 4.62a and b) and indicate that Be is not migrating. Lead is also a trace metal present naturally in Hanford sediments and can also be an indicator of waste (i.e., lead is also used for shielding). Lead is present only in low concentrations (Figure 4.62c and d). Although both Be and Pb data are limited, the fact that the concentrations vary little between 15 different boreholes indicates it is likely natural, as a waste co-contaminant would result in spatial variability in concentrations.

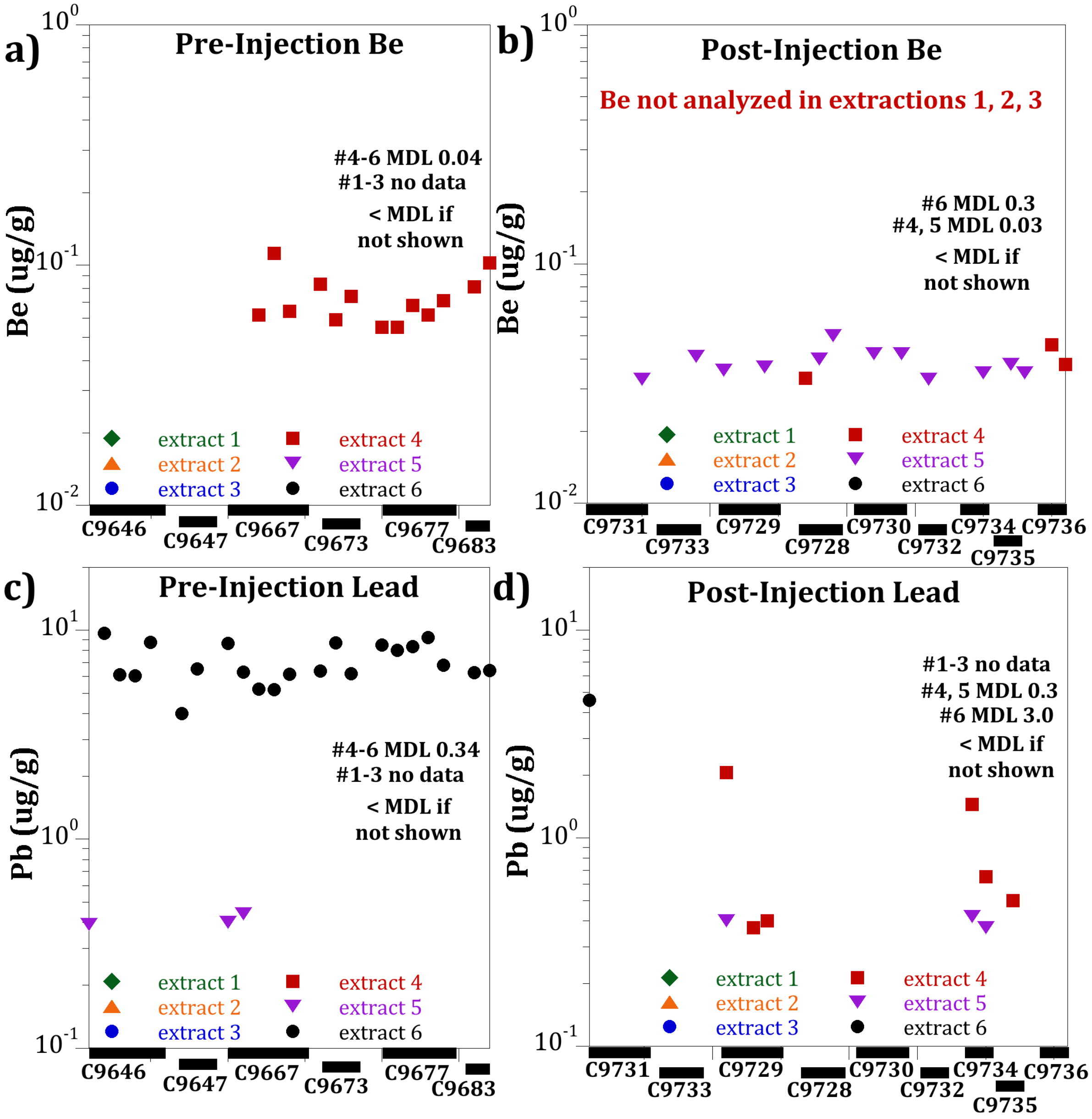

Figure 4.62. Sequential extraction of pre- and post-injection cores with Be analysis (a, b) and Pb analysis (c, d).

5.0 Discussion

The purpose of the 300-FF-5 Stage B injection of a ~87 mM polyphosphate solution into 48 wells was to decrease the mobility of uranium in contaminated sediments in the PRZ and shallow groundwater. This study was initiated to quantify differences in solubility and leachability of uranium between pre- and post-PO_4-treated vadose zone sediments. Four different types of analyses were conducted that included analysis of uranium in (a) a carbonate solution extraction from sediment over 1000 h, (b) six sequential liquid extractions from sediment over a week, (c) leaching from sediment in 1-D column experiments over 2 months, and (d) solid phase identification of uranium minerals and other minerals that influence uranium mobility (i.e., apatite). Additional extractions were conducted to evaluate the phosphate precipitate formation in sediments. Metals were also analyzed in sequential liquid extractions as indicators of (a) injection delivery, (b) co-contaminant movement, and (c) changes in solid phases.

Although results of this study do show a significant and consistent decrease in uranium leaching in nearly all sediments, because sediment samples were taken from a 20 to 32 ft depth at approximately 6 months after injection, it is difficult to evaluate phosphate injection extent and uranium leaching from the upper screened interval (i.e., 16 to 21 ft). The areal extent of uranium mobility change given that sediment samples are taken 3 to 21 ft from injection wells is evaluated given that the 48 injection wells are spaced less than 25 ft apart. For a complete evaluation of uranium leachability at field scale, results from this study should be combined with (a) well injection analysis (i.e., volume and concentration injected into each well); (b) adjacent and downgradient monitoring well groundwater sampling (i.e., specific conductivity, phosphate, Na, K, and U analysis showing injection and resulting change in U mobility); and (c) cross-borehole electrical resistivity tomography measurements showing spatial extent of injection solution injection into sediment from upper and lower screened interval injections in three cross-borehole clusters.

5.1 Phosphate Delivery to the Subsurface

The injected polyphosphate solution with 87 mM total PO_4 (composition described in Section 3.5) initially precipitates as amorphous monocalcium phosphate ($Ca(H_2PO_4)_2$, Ca:P = 0.5), and over weeks to months as hydroxyapatite ($Ca_{10}(PO_4)_6(OH)_2$ or other apatite group minerals, Ca:P = 1.67 and autunite ($Ca(UO_2)_2(PO_4)_2 \cdot XH_2O$) (Sumner 1999). Because co-contaminants in the 300-FF-5 Area subsurface include copper and phosphate (Wellman et al. 2008a-c), and torbernite ($Cu(UO_2)_2(PO_4)_2 \bullet 8\text{-}10H_2O$) has previously been identified (Arai et al. 2007), extractable phosphate in pre-injection sediments was subtracted from extractable phosphate in post-injection sediments (from the paired borehole and depth) to quantify the mass of aqueous, adsorbed, and solid phase phosphate precipitated as a result of the injections.

There was low (< 2 mg/L) to high (1000 mg/L) aqueous phosphate measured in post-injection pore water during leaching and no aqueous phosphate measured in pre-injection pore water as shown by extraction 1. Measurements of precipitated phosphate as a result of the polyphosphate injection were shown by two different extractions, which averaged P gain of 67.1 ± 163 µg/g (Figure 4.51b, 0.5 mol/L HNO_3 extraction, or 206 µg/g as PO_4) and 183 ± 132 µg/g (extraction 5, 0.1 mol/L NH_3 oxalate, 0.1 mol/L oxalic acid extraction, or 561 µg/g as PO_4), as shown in Figure 5.1a. There is P in natural minerals, so the sum of all P precipitates (i.e., extractions 3 through 6) is large, although the average increase from pre- to post-injection sediments was 433 ± 687 µg/g as P (1329 µg/g as PO_4, Figure 5.1b).

Although the well injection screens are at 16 to 21 ft depth and 26 to 31 ft depth, phosphate extractions showed little trend with depth (Figure 5.2) with samples within a 3.61 ft (1.1 m) distance from the injection well. However, post injection samples from approximately six months after injection at a 10 to 25 ft distance from injection wells do show a trend of decreasing phosphate concentration with distance.

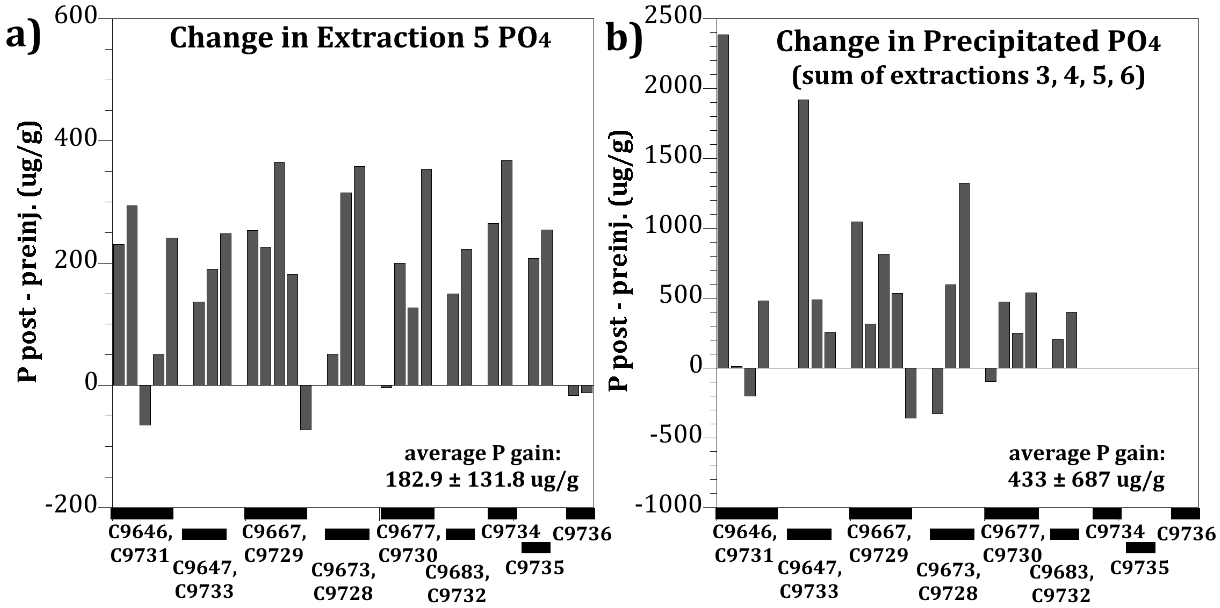

Figure 5.1. Measurement of precipitated phosphate by (a) phosphate extraction (0.5 mol/L nitric acid extraction, 15 min), and (b) extraction 5 (0.1 mol/L NH_3 oxalate, 0.1 mol/L oxalic acid extraction for 1.0 h).

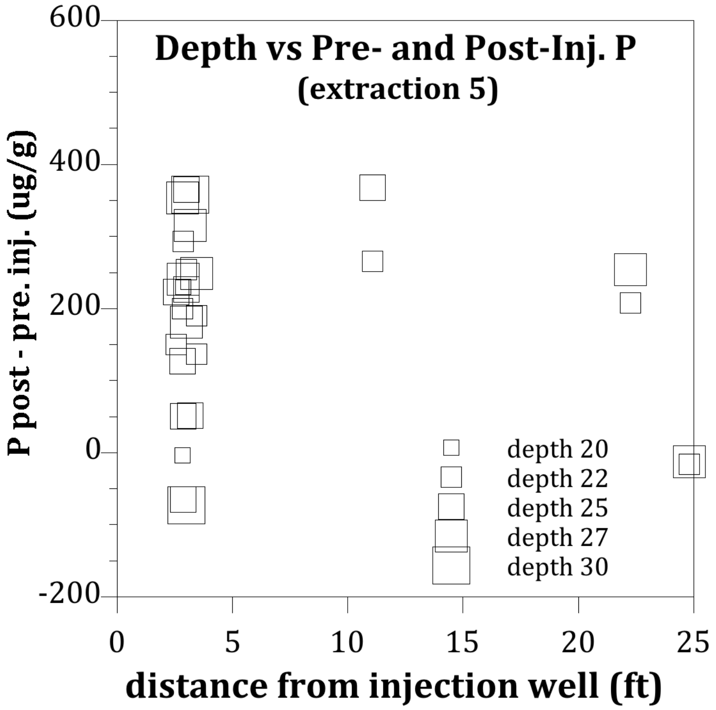

Figure 5.2. Phosphate in post-injection sediments with distance from the injection well as compared by the depth with squares of increasing size with increasing depth.

5.2 Change in Uranium Mobility from Polyphosphate Injections

The change in uranium mobility was quantified in (a) 24 1-D leach experiments (10 pre, 14 post, and 2 duplicates), (b) 44 carbonate solution extractions of uranium from sediment over 1000 h (19 pre, 25 post, and 6 duplicates), and (c) six sequential liquid extractions of uranium from 44 sediment samples (19 pre, 25 post, and 6 duplicates) over a week. The 1-D leach experiments were conducted with pre- and post-injection sediments to measure the change in uranium mobility (i.e., uranium mass and concentration released) as a result of the field-injected phosphate treatment and to measure the rate of uranium release from the sediment. There was a 58.9 ± 53.2% decrease in uranium leaching, as defined from the fraction leached to total uranium for each leach experiment (Figure 5.3a). Of the 20 pre-/post-injection samples or 10 pairs, 9 pairs showed a decrease in uranium leaching for the post-injection experiment, and 1 pair showed an increase. The change in uranium leaching was dependent on the amount of phosphate (if any) delivered to that location, defined by aqueous phosphate in the first few effluent samples of each leach experiment. Of 13 post-injection sediments analyzed in which leach experiments were conducted, 10 received high phosphate (see Section 4.5) and as a result had a large decrease in uranium leaching compared to pre-injection sediments. In contrast, three post-injection sediments showed low phosphate (one sediment) or no detectable aqueous or precipitated phosphate (two sediments), and as a result, there was little decrease in uranium leaching. It is possible that the three locations were low in phosphate due to (a) advection away prior to precipitation or (b) little phosphate delivery to this location.

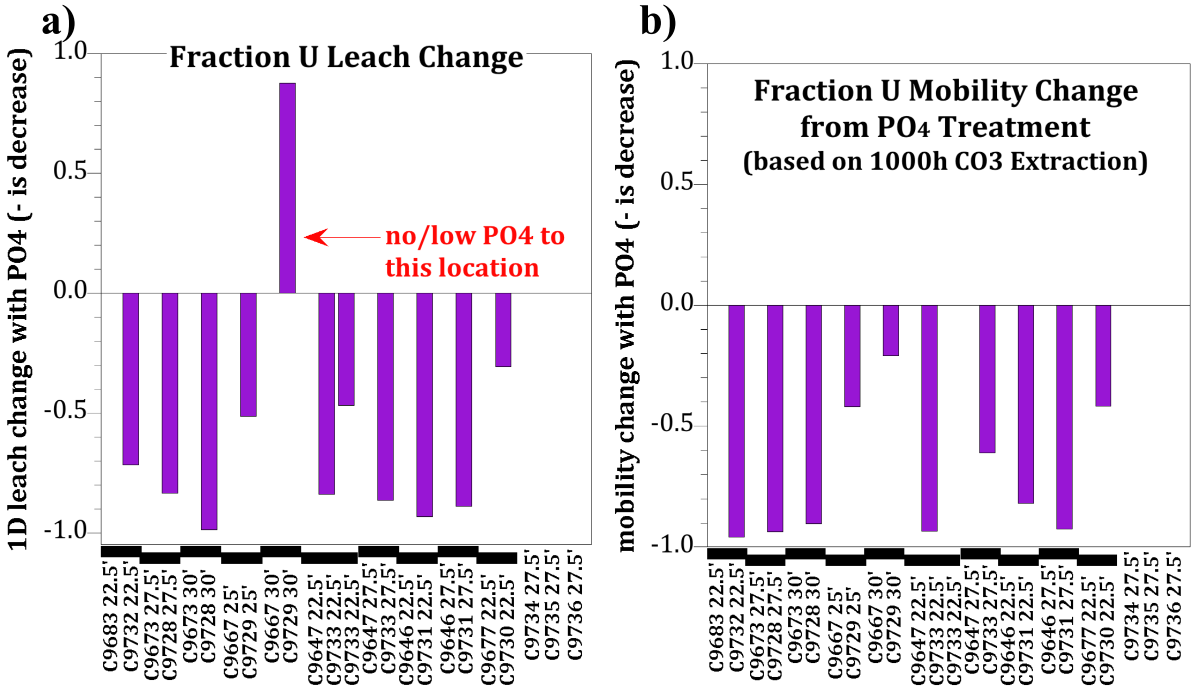

Figure 5.3. Change in uranium mobility as shown in (a) column leach experiments and (b) 1000-h carbonate extractions on 10 pre- and post-injection pairs of sediments selected for the 1-D leach studies.

The comparison of the fraction labile uranium (1000-h batch extraction) for each of the 19 pairs shows that the mobile fraction uranium for pre-injection (i.e., untreated) sediments is 0.425 ± 0.096, and for post-injection samples is 0.156 ± 0.143, or an average of 63% less mobile U as a result of the polyphosphate treatment, based on results of this 1000-h carbonate batch extraction (Figure 5.3b).

For sequential liquid extractions of 19 pre- and post-injection pairs of sediments from six borehole pairs, post-injection samples had less mobile uranium and a greater fraction of low-solubility uranium precipitates. More specifically, aqueous and adsorbed uranium (extractions 1 and 2, highly mobile U fraction) decreased from 6.7% to 3.4% of the total extracted U, acetate/acetic acid extractable U (extractions 3 and 4, soluble U precipitates) decreased from 58.6% to 37.2%, and the oxalate/nitric acid extractable U (extractions 5 and 6, low-solubility U precipitates) increased from 36.8% to 54.3%. Separate batch experiments showed that uranophane, Na-boltwoodite, and U substituted calcite are high-solubility U minerals and autunite and torbernite are low-solubility minerals that are dissolved in extraction 6 (nitric acid), which is consistent with the increase in the U in extraction 6 post-injection.

A comparison of both the changes in uranium sequential extractions shows that there is a loss in the aqueous and adsorbed uranium (red) and in extraction 4 for nearly all sediment pairs, both in terms of uranium concentration (Figure 5.4a) and in fraction U of total (Figure 5.4b). There is a corresponding increase in extraction 6 for most sediments. It is also evident from the U concentration graph that the loss in extraction 4 is greater than the gain in extraction 6, due to the post-injection sediments having on average 19.9 µg/g less U than pre-injection sediments and spatial variability. The sum of the average change in each of the 19 pairs of extractions shows a net loss of 18.2 µg/g, which is mainly in extraction 4.

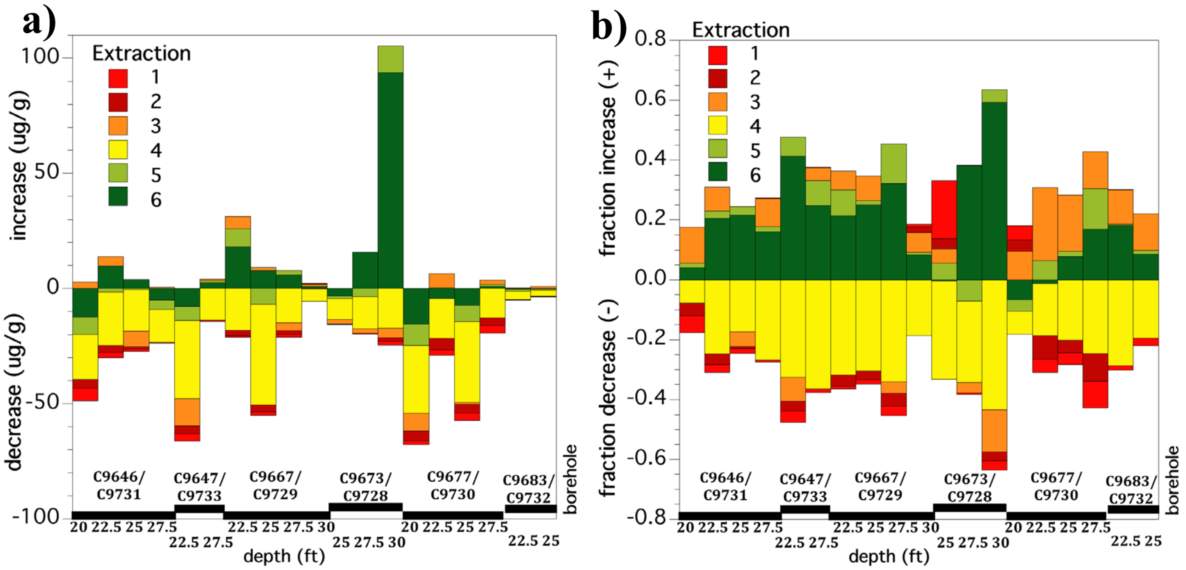

Figure 5.4. Change in uranium sequential extracted from 19 pairs of sediments, as shown in (a) U concentration (µg/g), and (b) fraction of total extracted uranium.

As noted in Section 4.0, because pre-injection boreholes are injection wells, and most post-injection boreholes are located within 3.61 ft (1.1 m), some decrease in aqueous and adsorbed U may be caused by advection during injection, although aqueous U in the polyphosphate solution will precipitate (Mehta et al. 2016; Szecsody et al. 2012). The 19% decrease in extraction 4 (acetic acid pH 2.3) from pre- to post-injection samples indicates one or more phases that contain uranium are decreasing due to the polyphosphate injection solution. Batch experiments showed that the moderate-solubility hydrous U silicates, uranophane and Na-boltwoodite, and U substituted in calcite, are somewhat soluble in the polyphosphate solution (and are removed in sequential extractions 3 and 4). Inorganic carbon analysis of five pre-/post-sediment pairs indicates very low inorganic carbon in all samples (< 0.01%), which indicates U-carbonates are likely present at low concentrations and U in extractions 3 and 4 is more likely hydrous U silicates (uranophane and Na-boltwoodite). However, the 0.01% carbon detection limit (8.33 x

10^{-6} mol C/g) is still higher than the highest uranium concentration in the sediment (i.e., 136 µg U/g is 5.71 x 10^{-7} mol U/g), so U could still be present as U carbonates as well as hydrous silicates.

The total uranium extracted in pre-injection sediments averaged 52.21 ± 26.93 µg/g (minimum 10.28, maximum 94.08 µg/g), whereas the total uranium extracted in post-injection sediment (most of which was from pre-/post-borehole pairs, so within 1 m) averaged 33.98 ± 31.68 µg/g (minimum 2.99, maximum 136.4 µg/g). Some of the variability in total U (but not the trend) was caused by differences in the grain size distribution between pre- and post-injection sediments (even at less than 3.61 ft apart), because finer grained sediments have greater surface area, and thus adsorb and precipitate more uranium (Figure 5.5).

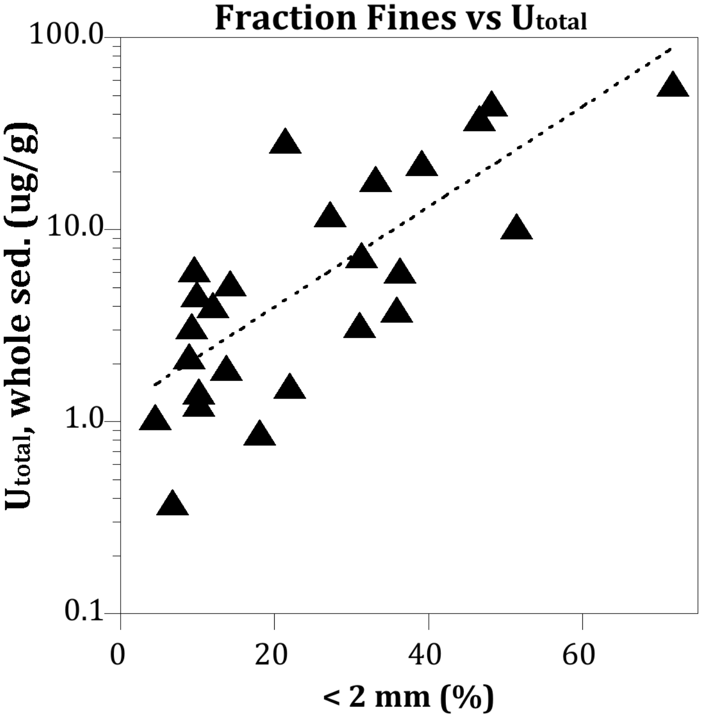

Figure 5.5. Correlation between the non-gravel (i.e., sand, silt, clay) fraction in sediments to the total uranium concentration.

The total U in post-injection sediments was 33.2 ± 50.8% smaller than pre-injection sediments, or 19.9 µg/g in the 19 pre- and post-injection sediment pairs. This is consistent with extraction 4 showing an average decrease of 18.6 µg/g from pre- to post-injection samples (Figure 5.4a). Therefore, the trend of less U in post-injection samples may be caused by dissolution of U-carbonates and hydrous silicates from the post-injection locations at less than 3.61 ft (1.1 m) from the injection well, which likely precipitated with the injected phosphate at a greater radial distance and/or depth from injection wells. These results confirm that the polyphosphate injection solution did not advect mobile and other labile uranium out of the injection area (leaving only immobile U in extraction 6), as extraction 6 (8 M HNO_3) from pre- to post-injection samples in 19 pre/post pairs increased on average from 11.1 ± 6.9 to 15.7 ± 23.3 µg/g also indicating some in situ transformation of U to less mobile phases.

In a previous laboratory study of polyphosphate treatment of 300 Area sediments, a complete mass balance of uranium was possible (Szecsody et al. 2012) as untreated and PO_4-treatments were conducted on the same sediment, and changes in U phases in the sediment and in the effluent was measured. In that study, the average of 20 1-D leach experiments with the same sediment showed that untreated sediments leached 7.9 ± 1.8% of the total extracted uranium in the first 7.5 pore volumes, whereas polyphosphate-treated sediments leached 0.13 ± 0.06% of the total extracted uranium in the first 7.5 pore volumes (including leaching during polyphosphate treatment).

5.3 Uranium Solid Phases in Pre- and Post-Injection Sediments

Two pairs of pre- and post-injection sediments analyzed by multiple solid phase techniques (2-D elemental maps by μ-XRF, 2-D elemental maps by SEM-EDS, XANES, EXAFS) showed that uranium was primarily associated with Cu, and to a lesser extent Fe and Ca. The copper association is consistent with previous studies where metatorbernite ($Cu(UO_2)_2(PO_4)_2•8H_2O$) has been identified in the NPP sediments (Arai et al. 2007). Additional calcium in surrounding particles was also near U precipitates, which is consistent with apatite precipitation on sediment surfaces. Unfortunately, P and Si could not be mapped with uranium at the APS beamline, but were identified separately by SEM at PNNL, which has higher detection limits for uranium. Elements that were identified by SEM-EDS included P, Ca, Mg, Al, Si, O, K, Ti, Fe, Cu, but not U, as it was present at concentrations below the detection limit of the EDS detector.

For the pre-injection sample C9667 at 25 ft depth, Ca associated with P only and not Cu (i.e., likely apatite) and was identified in one of seven locations in which 2-D SEM-EDS scans were made. In contrast, for the post-injection sample C9729 at 25 ft depth, significant Ca-P association (i.e., apatite) in 6 of 11 locations in which the 2-D elemental analysis was conducted. Copper was identified in multiple locations, both associated with P and in other locations with O (oxygen). Therefore, SEM-EDS data did show an increase in $Ca-PO_4$ (likely apatite) in the post-injection sample, which is consistent with the formation of apatite that can coat existing uranium solid phases. The μ-XANES showed that uranium is primarily in the +6 valence state in both pre- and post-injection sediments, which is consistent with previous studies of NPP sediments prior to remediation injection (Arai et al. 2007; Catalano et al. 2006). The μ-EXAFS spectra for identified uranium minerals in sediments that were compared with potential reference spectra (autunite, torbernite, boltwoodite, uranyl carbonate, and uranium dioxide) most strongly correlated with torbernite and boltwoodite in pre- and post-injection sediments. Because autunite group spectra are similar (i.e., autunite and torbernite), torbernite and autunite phases cannot be effectively differentiated and EXAFS fits are inconclusive as to whether additional uranium phosphate species are in post-injection sediments relative to pre-injection sediments. Further, because correlations between the Ca-phosphate precipitates identified in SEM-EDS and uranium could not be positively identified, it was inconclusive whether autunite group minerals formed in post-injection sediments. However, select locations analyzed via μ-XRF at APS showed correlation of Ca and U as well as Ca phases nearby U which may be associated with Ca-phosphate, although results were also inconclusive as to whether there was an increase in these phases following treatment. Geochemical equilibrium simulations indicated that uranium-carbonate should precipitate initially given the polyphosphate injection solution of 70 mM PO_4 and 61 mM CO_3, but autunite should form at later times as bicarbonate advects downgradient. The aqueous carbonate (Table 4.5) and specific conductance of post-injection sediment pore water taken 6 months after injection indicates that the aqueous bicarbonate concentration is near natural groundwater concentration, and under these conditions, autunite should form (Figure 4.42).

5.4 Uranium Release Mass and Rate in Untreated and PO_4-Treated Sediments

The 2-month-long, 1-D leach experiments included stop-flow events that were selected to quantify the uranium release rate from sediments predominantly from adsorbed uranium (at 2 pore volumes), high-solubility uranium minerals (at 10 pore volumes), and low-solubility uranium minerals (at 100 pore volumes). As shown in Section 4.3.2, the rate of release of uranium from sediments was one to three orders of magnitude higher for untreated sediments (red symbols, Figure 5.6a) compared to the phosphate-treated sediments (green symbols, Figure 5.6a). Uncontaminated Hanford sediments have < 2 µg/g total extractable uranium, low leachable uranium (< 0.2 µg/g), and slow release rates, as uranium phases are in equilibrium with pore water. In contrast, anthropogenic uranium released into sediments over the past few decades may not be in equilibrium, so generally have higher total extractable uranium, higher leachable uranium, and faster uranium release rates. As a result, there is a general correlation between uranium release mass and the release rate, as shown in Figure 5.6b over a range in uranium leached mass that covers four orders of magnitude. In comparison, untreated 300-FF-5 Area vadose zone sediments (red symbols, Figure 5.6a) had uranium leached mass and release rates (Figure 5.6a) as high as the most contaminated 200 Area sediments (C9487, 58 ft depth with 39.8 µg/g total U). In contrast, phosphate-treated 300-FF-5 Area vadose zone sediments (green symbols, Figure 5.6a) showed leached uranium mass and rates similar to uncontaminated or low-U contaminated 200 Area vadose zone and aquifer sediments (Figure 5.6b, from Truex et al. 2017 and Szecsody et al. 2017).

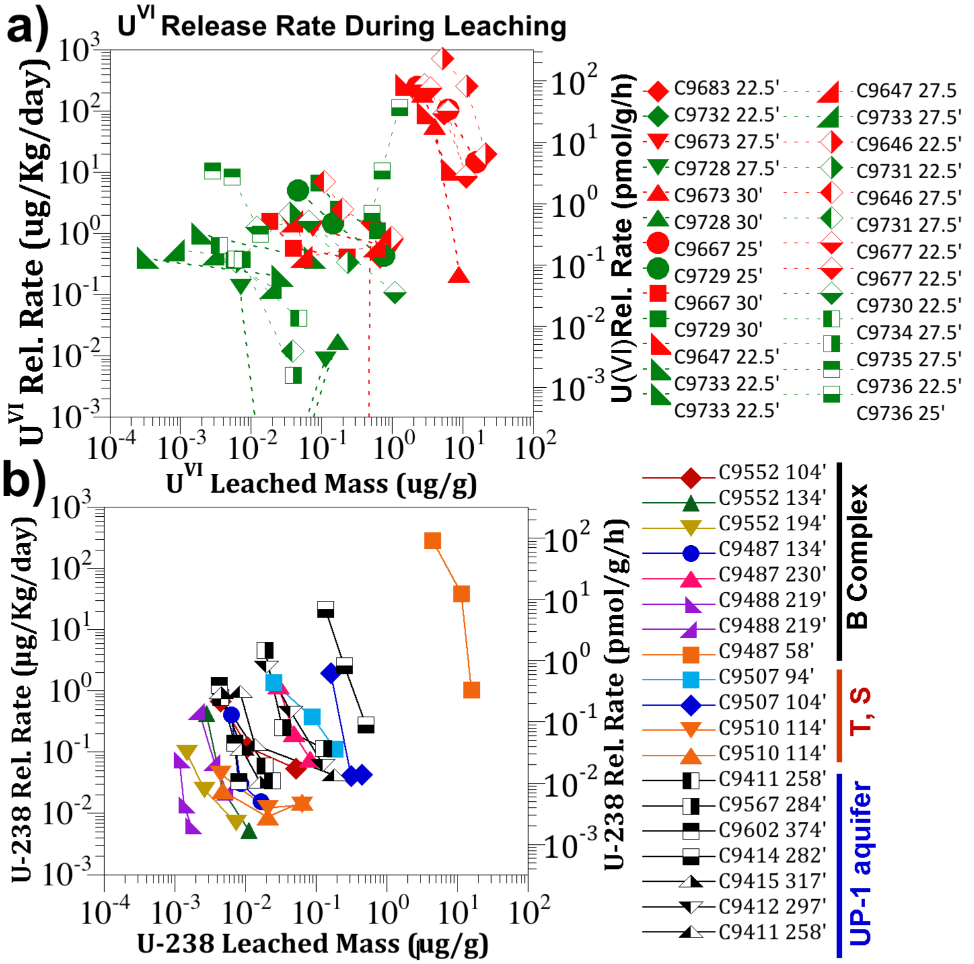

Figure 5.6. Correlation between uranium release mass and release rate for (a) 300-FF-5 sediments with pre-injection wells as red symbols and the post-injection wells as green symbols, and (b) 200 Area vadose zone and aquifer sediments.

The correlation between addition of phosphate and the decrease in the uranium release rate has previously been seen in a laboratory study of phosphate treatment of sediments from a former uranium milling operation in Rifle, Colorado (Figure 5.7, Szecsody et al. 2016, Moore et al., 2016). In that case, the column experiments were packed with uranium contaminated sediments and additional uranium was injected at 32 to 383 µg/L into the column in order to evaluate phosphate as both a permeable reactive barrier and for source area treatment. In this manner, it was shown that leaching of U decreased and uptake of U increased with phosphate treatment.

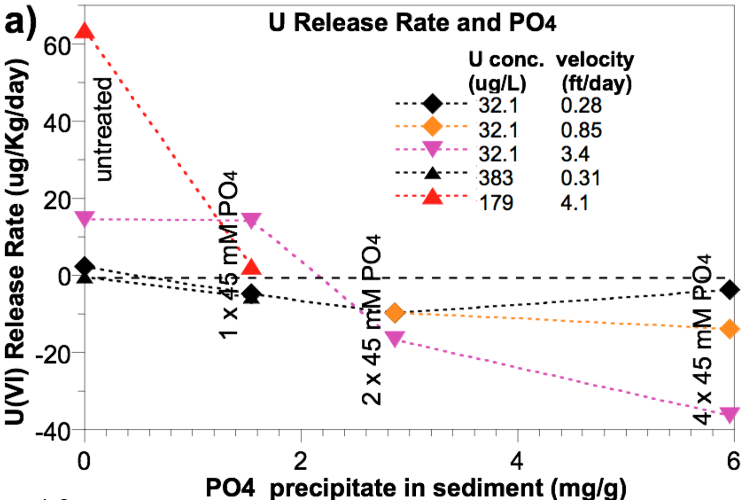

Figure 5.7. Example from Rifle, CO, sediments of the correlation of phosphate precipitated in sediment to the uranium release rate (Szecsody et al. 2016).

5.5 Correlation of Phosphate Treatment to Uranium Mobility

As described in the introduction (Section 1.0), previous laboratory-scale studies have identified multiple mechanisms that decrease uranium mobility: (a) precipitation of a low-solubility uranium-phosphate mineral (autunite); (b) precipitation of a Ca-phosphate mineral (apatite) that coats existing uranium phases (i.e., U in calcite, U in Fe-oxides), reducing uranium leaching; (c) structural incorporation of U with apatite; and (d) aqueous Ca-U-carbonate species adsorption onto apatite (Wellman et al. 2006, 2008a-c). This geochemical system is complicated, given that there are multiple uranium phases present in sediments and multiple mechanisms that cause a change in uranium mobility (from phosphate treatment). However, even with that complexity, there is a correlation of phosphate treatment and the reduction in uranium leaching or mobility, based on different experiments.

The 1-D leach columns are an idealized representation of pore water flow through contaminated sediments, and there is a good correlation between aqueous phosphate in 1-D effluent samples and the change in the fraction of uranium leached from the sediments (Figure 5.8a, $R^2 = 0.65$). More importantly, there is also a correlation between *precipitated* phosphate in the post-injection sediments and the change in the fraction of uranium leached from the sediments (Figure 5.8c, $R^2 = 0.88$). Both correlations show that the sediments with the highest phosphate precipitate concentration (based on sequential extraction 5) had the lowest fraction of uranium released from the sediment. One post-injection sediment (C9729, 30 ft depth) that had only a low aqueous phosphate increase and no solid phosphate increase (upper left point in Figure 5.8a and b) leached a high fraction of uranium compared to the paired, untreated sediment (C9667, 30 ft depth). Although these two sediments are in boreholes 3.61 ft (1.1 m) apart, the fraction of fines (i.e., < 2 mm) differed significantly, with 31.3% for the untreated sediment and 51.4% for the sediment with low phosphate treatment. As shown earlier (Figure 5.5), because the post-injection sediment had a higher proportion of fines, it also had a higher uranium concentration (10.4 µg/g) compared to the untreated sediment (7.4 µg/g). Finally, a fair correlation also exists between the precipitated phosphate extracted in post-injection sediments and the "mobile uranium" extracted from sediments in the 1000-h carbonate batch experiments (Figure 5.8c, $R^2 = 0.39$).

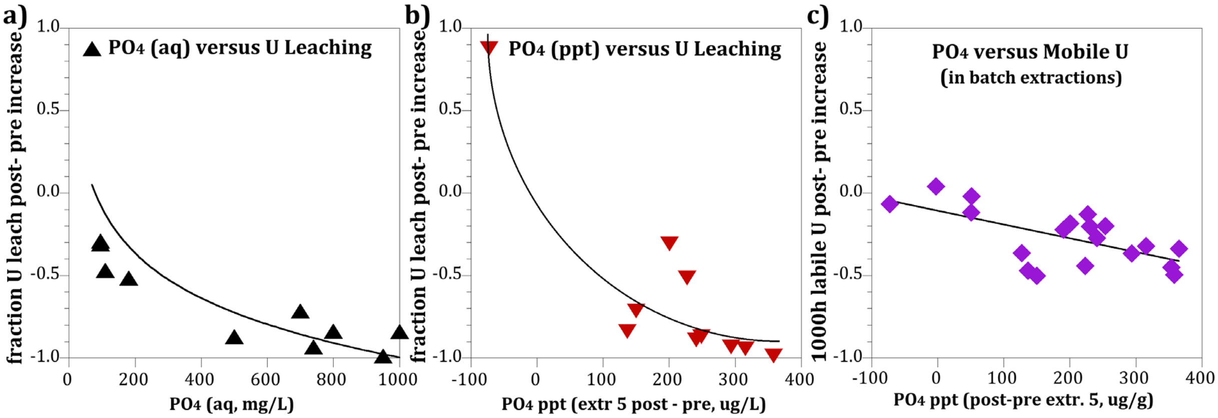

Figure 5.8. Correlation of phosphate treatment to a change in uranium mobility: (a) aqueous phosphate and 1-D column fraction U leached, (b) phosphate precipitate and 1-D column fraction U leached, and (c) phosphate precipitate and labile uranium as defined by the 1000-h carbonate extraction.

A correlation between the mass loading of phosphate and the decrease in uranium leaching has been previously observed in uranium-contaminated sediments from Rifle, Colorado (Szecsody et al. 2016). The comparison of the leached uranium in untreated sediment (Figure 5.9a, red triangles) to three different phosphate treatments shows higher phosphate loading results in less uranium leached. In these experiments, the uranium-contaminated sediment (with 2.2 µg/g total U) in each column was injected with additional uranium in the influent water simulating field scale upgradient uranium migrating into the uranium-contaminated sediment. Calculation of the net uranium leached from the sediment (i.e., total effluent uranium minus influent uranium) shows that high-phosphate treatments are sequestering some uranium in the influent (Figure 5.9b) along with leaching less uranium from the contaminated sediment.

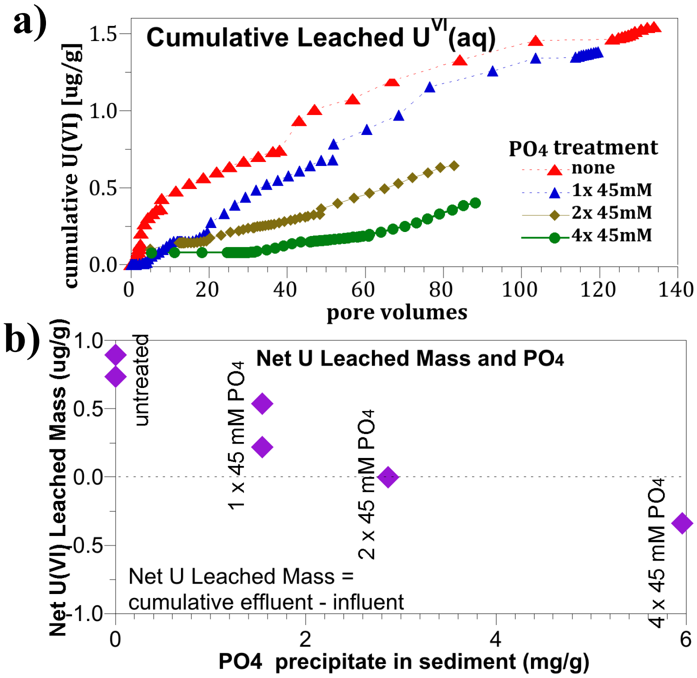

Figure 5.9. Example from Rifle, CO, sediments showing (a) decrease in cumulative leached U in 1-D columns with higher PO_4 loading, and (b) correlation of the measured phosphate precipitate to net leached uranium.

Phosphate extractions show that a significant mass of apatite does precipitate from the polyphosphate injection into sediments, and geochemical modeling indicates that apatite is favored to precipitate over pH 6.5 to 8 in a wide range of carbonate concentration. Uranium extractions show that post-injection sediments have a significant decrease in aqueous and adsorbed uranium, and high-solubility U precipitates (extraction 4), and a large increase in low solubility precipitates (extraction 6). Given the previously reported mechanisms that decrease uranium mobility (i.e., autunite precipitation, apatite coating of existing U surface phases, aqueous U adsorption onto apatite, Section 1.0), extraction results are consistent with apatite coating of existing U surface phases, autunite precipitation, or possibly other U phases (carbonates) coprecipitating with apatite, but not an increase in adsorbed U (as extractions showed a decrease in adsorbed U). Geochemical modeling showed that under the initial injection solution conditions (i.e., PO_4 and CO_3 concentrations), U carbonates andersonite and grimselite rather than autunite are favored to precipitate. In contrast, geochemical modeling of measured pore water and solid phase carbonate and phosphate in post-injection sediments taken six months after injection show that autunite is favored to precipitate. Although some aspects of the combination of mechanisms that decreases mobility have been identified, more importantly, the decrease in U mobility has been measured in field sediments by different methods.

6.0 Conclusions

The purpose of this study was to evaluate the change in uranium mobility in the periodically rewetted zone of the unconfined aquifer of the 300-FF-5 operable unit as a result of the Stage B polyphosphate injections. Pre-injection sediments were collected during drilling of injection wells, and post-injection sediments were collected approximately 6 months after the 48 wells were injected with the polyphosphate solution. These 300 Area sediments are beneath or near the former NPP, which has previously been shown to contain metatorbernite [$Cu(UO_2)_2(PO_4)_2{\bullet}8H_2O$] and uranophane [$Ca(UO_2)_2(HSiO_4)_2{\bullet}5H_2O$], along with aqueous and adsorbed uranium. A total of 30 tons of U was disposed of in the NPP, along with 50 tons of Cu, 800 tons of nitrate, 900 tons of nitric acid, 800 tons of NaOH, and 2000 tons of sodium aluminate (Gerber 1993; Wang et al. 2005; Arai et al. 2007). Infiltration of the acidic water from the NPP dissolved some to all of the natural calcite (and U substituted in calcite) in sediments.

Previous laboratory-scale studies have identified multiple mechanisms that decrease uranium mobility with polyphosphate injection: (a) precipitation of a low-solubility uranium-phosphate mineral (autunite); (b) precipitation of a Ca-phosphate mineral (apatite) that can structurally incorporate U, (c) precipitation of Ca-phosphate that coats existing uranium phases (i.e., U in calcite, U in Fe-oxides), reducing uranium leaching; and (d) aqueous Ca-U-carbonate species adsorption onto apatite (Wellman et al. 2006, 2008a-c, Mehta et al. 2016, Lammers et al. 2017). Given the significant amount of apatite precipitation, other U phases such as carbonates could also coprecipitate with apatite. To quantify differences in solubility and leachability of uranium between pre- and post-PO_4-treated sediments, four different types of analyses were conducted, which included analysis of uranium in (a) a carbonate solution extraction from sediment over 1000 h, (b) six sequential liquid extractions from sediment over a week, (c) leaching from sediment in 1-D column experiments over 2 months, and (d) solid phase analysis of uranium and other minerals. Additional extractions were conducted to evaluate the phosphate precipitate in sediments. Metals were analyzed in sequential extractions as indicators of (a) amendment injection delivery, (b) co-contaminant movement, and (c) changes in solid phases.

The following bullets summarize the major conclusions from these experiments:

- A comparison of 19 post-injection sediments that were collected within 3.61 ft (1.1 m) of pre-injection sediments showed *a consistent increase in phosphate precipitates in the post-injection sediments when compared to pre-injection sediments at the same depth*, averaging 183 ± 132 µg/g (as P).

- Uranium mobility measured in *26 1-D leach experiments showed a 58.9 ± 53.2% decrease in uranium leaching*, as defined from the fraction leached to total uranium for each leach experiment. Of the 10 pre-/post-injection pairs, 9 pairs showed a decrease in uranium leaching for the post injection experiment, and 1 pair showed an increase. One post-injection sediment that had low aqueous phosphate and two had no detectable aqueous phosphate (and little precipitated phosphate), and, as a result, there was little decrease in uranium leaching in the sediments that received limited phosphate treatment. Therefore, there is a general trend of increasing measured phosphate precipitate to measured decrease in uranium leaching. These experiments also showed that the *uranium release rates were one to three orders of magnitude less in post-injection* sediments relative to pre-injection sediments.

- The mobile uranium fraction for pre-injection (i.e., untreated) sediments is 0.425 ± 0.096, and for post-injection samples is 0.156 ± 0.143, or *an average of 63% less mobile U as a result of the polyphosphate treatment* based on carbonate extractions of 42 sediments including 19 pre-/post-injection pairs. There was also a general trend of measured phosphate precipitate to the change in pre- to post-injection measured extracted uranium ($R^2 = 0.88$).

- *Six sequential extractions showed that the most mobile uranium (i.e., aqueous and adsorbed) decreased from 6.7% to 3.4% (of the total extracted U), high-solubility U minerals decreased from 58.6% to 37.2%, and low-solubility U minerals increased from 36.8% to 54.3% as a result of the phosphate injections* with comparison of 19 pre- and post-injection sediments. The total uranium extracted in pre-injection sediments (52.2 ± 26.3 µg/g) was greater than the total uranium in post injection sediments (34.0 ± 31.7 µg/g) by 19.9 µg/g, or consistent with the 18.6 µg/g decrease in high-solubility U mineral extraction fraction. The decrease in adsorbed U for post injection sediments indicates that the contribution of one of the sequestration mechanisms (U adsorption to apatite) is likely small in these samples taken 6 months after injection. Aqueous U adsorption to apatite may contribute to a greater extent over time as upgradient uranium in low ionic strength groundwater migrates into the apatite-treated area although carbonate complexation will likely play an important role.

- It is hypothesized that the decrease in the high-solubility U minerals from pre- to post-injection sediments (58.6% to 37.2%) was due to dissolution of uranophane or Na-boltwoodite. This theory is based on separate batch experiments which showed that uranophane, Na-boltwoodite, and U-substituted calcite are high-solubility U minerals (solubilized in extractions 1-4) and autunite and torbernite are low-solubility minerals (solubilized in extractions 5 and 6) based on the operationally defined sequential extractions.

- Phosphate extractions show that a significant mass of apatite does precipitate from the polyphosphate solution injection into sediments (and confirmed by speciation modeling). This indicates that the large increase in low-solubility U minerals (extraction 6) may be due to (a) precipitation of autunite, (b) apatite coating existing U surface phases, or (c) other U phases (i.e., U carbonates) coprecipitating with apatite.

- Solid phase analysis conducted using 2-D elemental mapping by µ-XRF and SEM-EDS, µ-XANES, and µ-EXAFS showed that (a) *nearly all uranium was in the +6 valence state* (from XANES), as expected; (b) *uranium was strongly associated with Cu in pre- and post-treatment sediments in µ-XRF*, consistent with previous identifications of metatorbernite ($Cu(UO_2)_2(PO_4)_2 \cdot 8H_2O$) in NPP sediments (Arai et al. 2007); (c) U was also associated with Fe and Ca in pre- and post-injection sediments (µ-XRF); and (d) *significant phosphate precipitates were identified by SEM-EDS in post-injection sediments*. However, it was inconclusive whether additional uranium phosphate species (e.g., autunite group minerals) were formed in post-injection sediments relative to pre-injection sediments.

- Geochemical equilibrium simulations indicated that (a) apatite is favored to precipitate over pH 6.5 to 8 in injection solutions, (b) uranium carbonates should precipitate initially given the polyphosphate injection solution of 87 mM PO_4 and 61 mM HCO_3, and (c) autunite group minerals may precipitate as bicarbonate returns to natural conditions.

The comparison of pre- and post-injection sediments at the 300-FF-5 Stage B polyphosphate injection site showed a consistent trend of decreasing mobile uranium (60%) due to the injected phosphate, as defined by 1-D column leach experiments, a separate 1000-h uranium batch extraction, solid phase analysis, and with a series of six liquid extractions, although the specific mechanisms leading to the decrease in mobility are not directly identified.

7.0 Quality Assurance

This work was performed in accordance with the PNNL Nuclear Quality Assurance Program (NQAP). The NQAP complies with U.S. Department of Energy Order 414.1D, *Quality Assurance*. The NQAP uses NQA-1-2012, *Quality Assurance Requirements for Nuclear Facility Applications*, as its consensus standard and NQA-1-2012 Subpart, 4.2.1 as the basis for its graded approach to quality.

This work used PNNL's Environmental Sciences Laboratory (ESL) for chemical analyses. The ESL operates under a dedicated QA plan that complies with the *Hanford Analytical Services Quality Assurance Requirements Document* (HASQARD; DOE/RL-96-68), Rev. 3. ESL implements HASQARD through *Conducting Analytical Work in Support of Regulatory Programs* (CAWSRP). Data quality objectives established in CAWSRP were generated in accordance with HASQARD requirements. Chemical analyses of testing samples and materials were conducted under the ESL QA Plan.

QA reviews of data and analyses were conducted for this work in accordance with the QA plan. There were no reportable QA issues with the data included in this report.

8.0 References

Arai Y, M Marcus, N Tamura, J Davis, and J Zachara. 2007. “Spectroscopic evidence for uranium bearing precipitates in vadose zone sediments at the Hanford 300-Area site.” *Environmental Science & Technology* 41:4633-4639.

ASME NQA-1-2012, *Quality Assurance Requirements for Nuclear Facility Applications*. The American Society of Mechanical Engineers, New York, NY.

ASTM D6913-04, *Standard Test Methods for Particle-Size Distribution (Gradation) of Soils Using Sieve Analysis*, ASTM International, West Conshohocken, PA.

Berthouex PM and LC Brown. 1994. *Multiple Paired Comparisons of k Averages*, in *Statistics for Environmental Engineers*. CRC Press, Boca Raton, FL. p. 123-128.

Brina R and AG Miller. 1992. “Direct detection of trace levels of uranium by laser induced kinetic phosphorimetry.” *Analytical Chemistry* 64(13):1413-1418.

Calvin S. 2013. *XAFS for Everyone*. CRC Press, Boca Raton, FL.

Catalano JG and GE Brown, Jr. 2004. “Analysis of uranyl-bearing phases by EXAFS spectroscopy: Interferences, multiple scattering, accuracy of structural parameters, and spectral differences.” *American Mineralogist* 89(7):1004-10021.

Catalano J, J McKinley, J Zachara, S Heald, S Smith, and G Brown, Jr. 2006. “Changes in uranium speciation through a depth sequence of contaminated Hanford sediments.” *Environmental Science & Technology* 40:2517-2524.

Chao T and L Zhou. 1983. “Extraction techniques for selective dissolution of amorphous iron oxides from soils and sediments.” *Soil Science Society of America Journal* 47(2):225-232.

DOE Order 414.1D, *Quality Assurance*. U.S. Department of Energy, Washington, D.C.

Gerber MS. 1993. *Multiple Missions: The 300 Area in Hanford Site History*. WHC-MR-0440, Westinghouse Hanford Company, Richland, WA.

Gleyzes C, S Tellier, and M Astruc. 2002. “Fractionation studies of trace elements in contaminated soils and sediments: a review of sequential extraction procedures.” *Trends in Analytical Chemistry* 21(6 - 7):451-467.

Gorman-Lewis D, PC Burns, and JB Fein. 2008. “Review of uranyl mineral solubility measurements.” *The Journal of Chemical Thermodynamics* 40(3):335-352.

Gorman-Lewis D, T Shvareva, K-A Kubatko, PC Burns, DM Wellman, B McNamara, JES Szymanowski, A Navrotsky, and JB Fein. 2009. “Thermodynamic properties of autunite, uranyl hydrogen phosphate, and uranyl orthophosphate from solubility and calorimetric measurements.” *Environmental Science and Technology* 43(19):7416-7422.

Guillamont R, T Fanghanel, I Grenthe, V Neck, D Palmer, and MH Rand. 2003. “Update on the chemical thermodynamics of uranium, neptunium, plutonium, americium, and technetium.” *Chemical Thermodynamics* 5:959.

Hall G, J Vaive, R Beer, and N Hoashi. 1996. “Selective leaches revisited, with emphasis on the amorphous Fe oxyhydroxide phase extraction.” *Journal of Geochemical Exploration* 56:59-78.

Kohler M, DP Curtis, DE Meece, and JA Davis. 2004. “Methods for estimating adsorbed uranium (VI) and distribution coefficients of contaminated sediments.” *Environmental Science and Technology* 38:240-247.

Lammers L, H Rasmussen, D Adilman, J deLemos, P Zeeb, D Larson, and A Quicksall. 2017. “Groundwater uranium stabilization by a metastable hydroxyapatite.” *Applied Geochemistry* 84:105-113.

Langmuir D. 1997. *Aqueous Environmental Geochemistry*. R McConnin, ETP Harrison, J Conte, and T Pisciotti (eds.). Prentice Hall, Upper Saddle River, NJ.

Larner B, A Seen, and A Townsend. 2006. “Comparative study of optimized BCR sequential extraction scheme and acid leaching of elements in certified reference material NIST 2711.” *Analytica Chimica Acta* 556:444-449.

Last GV, M Snyder, Z Wang, O Qafoku, JR Stephenson, RE Clayton, and BD Williams. 2016. *Analytical Data Report for Sediment Samples Collected from 300-FF-5: Boreholes C9580, C9581, and C9582*. PNNL-25420, Pacific Northwest National Laboratory, Richland, WA.

Liu C, JM Zachara, W Yantasee, PD Majors, and JP McKinley. 2006. “Microscopic reactive diffusion of uranium in the contaminated sediments at Hanford, United States.” *Water Resources Research* 42:1-15.

Locock AJ and PC Burns. 2003. “Crystal structures and synthesis of the copper-dominant members of the autunite and meta-autunite groups: torbernite, zeunerite, metatorbernite, and metazeunerite.” *The Canadian Mineralogist* 41(2): 489-502.

Makarov ES and VI Ivanov. 1960. “The crystal structure of meta-autunite $Ca(UO_2)_2(PO_4)_2$-$6H_2O$. Conference Proceedings: *Doklady Akad. NAuk SSR* 132.

McKinley JP, JM Zachara, J Wan, DE McCready, and SM Heald. 2007. “Geochemical controls on contaminant uranium in vadose Hanford formation sediments at the 200 area and 300 area, Hanford site Washington.” *Vadose Zone Journal* 6(4):1004-1017.

Mehta S. 2017. “Geochemical evaluation of uranium sequestration from field-scale infiltration and injection of polyphosphate solutions in contaminated Hanford sediments.” *Applied Geochemistry* 84:133-153.

Mehta VS, F Mailot, Z Wang, JG Catalono, and DE Giammar. 2016. “Effect of reaction pathway on the extent and mechanism of uranium(VI) immobilization with calcium and phosphate.” *Environmental Science and Technology* 50:3128-3136.

Moore R, JE Szecsody, M Rigali, V Vermeul, and JR Luellen. 2016. “Assessment of a hydroxyapatite permeable reactive barrier to remediate uranium at the Old Rifle Site, Colorado.” 16193. *Proceedings from the Waste Management Symposia*. SAND – 2016-0995C. Sandia National Laboratories, Albuquerque, NM.

Mossop K and C Davison. 2003. “Comparison of original and modified BCR sequential extraction procedures for the fractionation of copper, iron, lead, manganese, and zinc in soils and sediments.” *Analytica Chimica Acta* 478:111-118.

Peng S, Q Hu, RP Ewing, C Liu, and JM Zachara. 2012. “Quantitative 3-D elemental mapping by LA-ICP-MS of a basaltic clast from the Hanford 300 Area, Washington, USA.” *Environmental Science and Technology* 46(4):2025-2032.

Qafoku NP, CC Ainsworth, JE Szecsody, and OS Qafoku. 2004. “Transport-controlled kinetics of dissolution and precipitation in the sediments under alkaline and saline conditions.” *Geochimica et Cosmochimica Acta* 68(14):2981-2995.

Ravel B and M Newville. 2005. ATHENA, ARTEMIS, HEPHAESTUS: data analysis for x-ray absorption spectroscopy using IFEFFIT. *Journal of Synchrotron Radiation* 12(4):537-541.

Ross M, HT Evans Jr., and DE Appleman. 1964. “Studies of the torbernite minerals (II): The crystal structure of meta-torbernite.” *American Mineralogist: Journal of Earth and Planetary Materials* 49(11-12): 1603-1621.

Serne RJ, BN Bjornstad, HT Schaef, BA Williams, DC Lanigan, DG Horton, RE Clayton, AV Mitroshkov, VL LeGore, MJ O’Hara, CF Brown, KE Parker, IV Kutnyakov, JN Serne, GV Last, SC Smith, CW Lindenmeier, JM Zachara, and DB Burke. 2002. *Characterization of Vadose Zone Sediment: Uncontaminated RCRA Borehole Core Samples and Composite Samples*. PNNL-13757-1, Pacific Northwest National Laboratory, Richland, WA.

Serne RJ, BN Bjornstad, DC Lanigan, GW Gee, CW Lindenmeier, RE Clayton, VL LeGore, MJ O’Hara, CF Brown, GV Last, IV Kutnyakov, DS Burke, TC Wilson, and BA Williams. 2008. *Characterization of vadose zone sediment: Borehole 299-W12-19 [SX-115] in the S-SX waste management area*. PNNL-13757-2, Rev 1.0, Pacific Northwest National Laboratory, Richland, WA.

Shi Z, C Liu, J Zachara, Z Wang, and B Deng. 2009. “Inhibition Effect of Secondary Phosphate Mineral Precipitation on Uranium Release from Contaminated Sediments.” *Environmental Science and Technology* 43:8344–8349.

Sumner ME. 2000. *Handbook of Soil Science*. CRC Press, Boca Raton, FL.

Sutherland R and F Tack. 2002. “Determination of Al, Cu, Fe, Mn, Pb, and Zn in certified reference materials using the optimized BCR sequential extraction procedure.” *Analytica Chimica Acta* 454:249-257.

Szecsody JE, KJ Cantrell, KM Kruupka, CT Resch, MD Williams, and JS Fruchter. 1998. *Uranium mobility during in situ redox manipulation of the 100 Areas of the Hanford Site*. PNNL-12048. Pacific Northewst National Laboratory, Richland, WA.

Szecsody JE, D Jansik, JP McKinley, and N Hess. 2014. “Influence of alkaline waste on technetium mobility in Hanford formation sediments.” *Journal of Environmental Radioactivity* 135:147-160.

Szecsody J, M Truex, N Qafoku, D Wellman, T Resch, and L Zhong. 2013. “Influence of acidic and alkaline co-contaminants on uranium migration in vadose zone sediments.” *Journal of Contaminant Hydrology* 151:155-175.

Szecsody J, M Truex, N Qafoku, and T Resch. 2019. “Persistence of Chromate Reduction in Natural Oxic Aquifer Sediments: Role of Abiotic and Biotic Reactions.” *Chemosphere* 676: 482-492.

Szecsody JE, VR Vermeul, JS Fruchter, MD Williams, ML Rockhold, NP Qafoku, and JL Phillips. 2010. *Hanford 100-N area in situ apatite and phosphate emplacement by groundwater and jet injection: Geochemical and physical core analysis*. PNNL-19524. Pacific Northwest National Laboratory, Richland, WA.

Szecsody J, L Zhong, M Oostrom, VR Vermeul, JS Fruchter, and MD Williams. 2012. *Use of Polyphosphate to Decrease Uranium Leaching in Hanford 300 Area Smear Zone Sediment*. PNNL-21733, Pacific Northwest National Laboratory, Richland, WA.

Szecsody J, L Zhong, V Vermeul, J McKinley, M Bowden, M Williams, and E Eisenhauer. 2016a. “Laboratory study of the influence of $scCO_2$ injection on metals migration, precipitation, and microbial growth.” *International Journal of Greenhouse Gas Control* 47:71-85. http://dx.doi.org/10.1016/j.ijggc.2016.01.029

Szecsody J, R Moore, M Rigali, V Vermeul, and J Luellen. 2016b. *Use of a Ca-citrate-phosphate solution to form hydroxyapatite for uranium stabilization of Old Rifle sediments: Laboratory proof of principle studies*. PNNL-25303. Pacific Northwest National Laboratory, Richland, WA.

Szecsody J, M Rockhold, M Oostrom, R Moore, C Burns, M Williams, L Zhong, J Fruchter, J McKinley, V Vermeul, M Covert, T Wietsma, A Breshears, and B Garcia. 2009. *Sequestration of Sr-90 Subsurface Contamination in the Hanford 100-N Area by Surface Infiltration of a Ca-Citrate-Phosphate Solution*. PNNL-18303, Pacific Northwest National Laboratory, Richland, WA.

Szecsody J, M Truex, B Lee, C Strickland, J Moran, M Snyder, C Resch, L Zhong, B Gartman, D Saunders, S Baum, I Leavy, J Horner, B Williams, B Christiansen, E McElroy, M Nims, R Clayton, and D Appriou. 2017. *Geochemical, Microbial, and Physical Characterization of 200-DV-1 Operable Unit B-Complex Cores from Boreholes C9552, C9487, and C9488 on the Hanford Site Central Plateau*. PNNL-26266, Pacific Northwest National Laboratory, Richland, WA.

Truex M, J Szecsody, N Qafoku, C Strickland, J Moran, B Lee, M Snyder, A Lawter, C Resch, B Gartman, L Zhong, M Nims, D Saunders, B Williams, J Horner, I Leavy, S Baum, B Christiansen, R Clayton, E McElroy, D Appriou, K Tyrell, and M Striluk. 2017. *Contaminant Attenuation And Transport Characterization of 200-DV-1 Operable Unit Sediment Samples*. PNNL-26208, Pacific Northwest National Laboratory, Richland, WA.

Um W, ZM Wang, RJ Serne, BD Williams, CF Brown, CJ Dodge, AJ Francis. 2009. “Uranium phases in contaminated sediments below Hanford’s U tank farm.” *Environmental Science and Technology* 43(12):4280-4286.

Vermeul VR, DP Mendoza, BN Bjornstad, DR Newcomer, BG Fritz, ML Rockhold, JS Fruchter, DM Wellman, RD Mackley, and MD Williams. 2009. *300 Area Uranium Stabilization through Polyphosphate Injection: Final Report*. PNNL-18529, Pacific Northwest National Laboratory, Richland, WA.

Waite TD, JA Davis, TE Payne, GA Waychunas, and N Xu. 1994. “Uranium (VI) adsorption to ferrihydrite: Application of a surface complexation model.” *Geochimica et Cosmochimica Acta* 58(24): 5465-5478.

Wang Z, J Zachara, W Yantasee, P Gassman, C Liu, and A Joly. 2005. “Cryogenic laser induced fluorescence characterization of U(VI) in Hanford vadose zone pore waters.” *Environmental Science and Technology* 38:5591-5597.

Wellman DM, JG Catalano, JP Icenhower, and AP Gamerdinger. 2005. “Synthesis and characterization of sodium meta-autunite, Na[UO_2PO_4]•$3H_2O$.” *Radiochimica Acta* 93:393-399.

Wellman DM, EM Pierce, DH Bacon, M Oostrom, KM Gunderson, SM Webb, CC Bovaird, EA Cordova, ET Clayton, KE Parker, RM Ermi, SR Baum, VR Vermeul, and JS Fruchter. 2008a. *300 Area Treatability Test: Laboratory Development of Polyphosphate Remediation Technology for in Situ Treatment of Uranium Contamination in the Vadose Zone and Capillary Fringe*. PNNL-17818, Pacific Northwest National Laboratory, Richland, WA.

Wellman DM, JN Glovack, K Parker, EL Richards, and EM Pierce. 2008b. “Sequestration and Retention of Uranium(VI) in the Presence of Hydroxylapatite under Dynamic Geochemical Conditions.” *Environmental Chemistry* 5(1):40-50.

Wellman, DM, JS Fruchter, VR Vermeul, and MD Williams. 2008c. *Challenges Associated with Apatite Remediation of Uranium in the 300 Area Aquifer*. PNNL-17480, Pacific Northwest National Laboratory, Richland, WA.

Wellman DM, JP Icenhower, and AT Owen. 2006. “Comparative Analysis of Soluble Phosphate Amendments for the Remediation of Heavy Metal Contaminants: Effect on Sediment Hydraulic Conductivity.” *Environmental Chemistry* 3:219–224.

Xie YL, CJ Murray, GV Last, and RD Mackley. 2003. *Mineralogical and bulk-rock geochemical signatures of Ringold and Hanford Formation sediments*. PNNL-14202, Pacific Northwest National Laboratory, Richland, WA.

Zachara J, C Liu, C Brown, S Kelly, J Christensen, J McKinley, J Davis, J Serne, E Dresel, and W Um. 2007. *A Site-Wide Perspective on Uranium Geochemistry at the Hanford Site*. PNNL-17031, Pacific Northwest National Laboratory, Richland, WA.

Appendix A – Uranium Sequential Extraction Data

Table A.1. Uranium sequential extraction data for pre- and post-injection boreholes for the whole sediment size fraction.

Borehole	Depth (ft)	Extract 1 (µg/g)	Extract 2 (µg/g)	Extract 3 (µg/g)	Extract 4 (µg/g)	Extract 5 (µg/g)	Extract 6 (µg/g)	Sum (µg/g)	1000h Co$_3$ (µg/g)	Extract 1 fraction	Extract 2 fraction	Extract 3 fraction	Extract 4 fraction	Extract 5 fraction	Extract 6 fraction
C9646 pre	20 - 22.5	2.57	1.87	2.23	14.65	7.42	12.83	41.56	15.28	0.0619	0.0449	0.0537	0.352	0.179	0.309
C9731 post	20 - 22.5	0.0397	0.0270	1.293	2.04	1.44	2.60	7.44	1.24	0.0053	0.0036	0.174	0.275	0.193	0.350
C9646 pre	22.5 - 25	1.22	1.44	2.92	16.87	7.07	8.53	38.05	16.95	0.032	0.0377	0.0767	0.444	0.186	0.224
C9731 post	22.5 - 25	0.0323	4.29E-03	0.978	1.23	1.31	2.68	6.23	0.503	0.0052	0.0007	0.157	0.197	0.210	0.430
C9646 pre	25 - 27.5	0.509	0.488	4.07	9.66	1.09	2.29	18.11	6.11	0.0281	0.0269	0.225	0.533	0.060	0.126
C9646 pre dup	25 - 27.5	0.297	0.522	1.24	8.43	1.09	2.82	14.40	6.87	0.0206	0.0363	0.086	0.585	0.076	0.196
C9731 post	25 - 27.5	0.0549	0.0950	0.780	1.61	0.397	1.53	4.47	0.987	0.0123	0.0213	0.1745	0.360	0.089	0.343
C9731 post dup	25 - 27.5	0.0414	0.0664	0.844	1.26	0.365	1.25	3.82	0.877	0.0108	0.0174	0.221	0.329	0.0954	0.326
C9646 pre	27.5 - 30	0.0382	0.0109	0.153	2.42	0.965	1.67	5.26	1.54	0.0073	0.0021	0.0292	0.460	0.184	0.318
C9731 post	27.5 - 30	1.37E-03	9.94E-03	0.233	0.367	0.386	0.912	1.91	0.0411	0.0007	0.0052	0.1219	0.192	0.202	0.478
C9647 pre	22.5 - 25	2.25	2.60	9.34	25.4	6.16	11.9	57.7	29.0	0.039	0.0451	0.1619	0.440	0.107	0.207
C9733 post	22.5 - 25	1.13E-03	0.0171	0.119	0.165	0.244	0.890	1.44	0.0472	0.0008	0.0119	0.0828	0.115	0.170	0.620
C9733 post dup	22.5 - 25	2.59E-03	0.0139	0.103	0.172	0.230	0.724	1.24	0.0289	0.0021	0.0112	0.0825	0.138	0.185	0.581
C9647 pre	27.5 - 30	0.0601	0.0316	0.162	2.04	0.417	1.35	4.06	1.48	0.0148	0.0078	0.0399	0.502	0.103	0.333
C9733 post	27.5 - 30	4.44E-04	5.62E-04	0.157	0.211	0.283	0.412	1.06	0.151	0.0021	0.0112	0.0825	0.138	0.185	0.581
C9667 pre	22.5 - 25	0.593	1.44	3.10	20.7	5.02	8.04	38.9	12.7	0.0152	0.037	0.0797	0.533	0.129	0.206
C9729 post	22.5 - 25	0.0779	9.47E-03	1.94	2.93	2.94	5.73	13.62	1.75	0.0057	0.0007	0.142	0.215	0.216	0.421
C9667 pre	25 - 27.5	1.01	1.53	2.82	28.6	7.37	4.02	45.35	13.8	0.0222	0.0337	0.0621	0.631	0.163	0.089
C9729 post	25 - 27.5	0.0385	0.0225	0.686	1.54	0.841	1.60	4.73	0.834	0.0081	0.0047	0.145	0.326	0.178	0.338
C9729 post dup	25 - 27.5	5.62E-03	0.0141	0.620	1.45	0.789	1.63	4.50	0.717	0.0012	0.0031	0.138	0.321	0.175	0.361
C9667 pre	27.5 - 30	0.368	0.485	2.24	5.74	0.935	1.55	11.32	4.24	0.0325	0.0428	0.198	0.507	0.083	0.137
C9667 pre dup	27.5 - 30	0.370	0.514	0.427	5.61	1.56	2.09	10.57	4.35	0.0350	0.0486	0.0404	0.531	0.147	0.198
C9729 post	27.5 - 30	1.26E-03	2.37E-03	0.691	0.728	0.935	2.00	4.36	0.165	0.0003	0.0005	0.159	0.167	0.215	0.459
C9667 pre	30 - 32.5	0.0503	0.0379	1.29	3.84	0.596	1.55	7.36	2.31	0.0068	0.0051	0.175	0.522	0.081	0.210
C9729 post	30 - 32.5	0.166	0.252	2.52	3.51	0.930	3.06	10.43	2.59	0.0159	0.0241	0.242	0.336	0.089	0.293
C9673 pre	25 - 27.5	0.254	0.113	0.805	3.20	0.453	1.31	6.13	3.22	0.0415	0.0184	0.131	0.521	0.074	0.214
C9728 post	25 - 27.5	0.0852	0.0194	0.0651	0.0703	0.0469	0.0757	0.363	0.183	0.235	0.0535	0.180	0.194	0.129	0.209
C9673 pre	27.5 - 30	0.122	0.044	2.14	6.50	1.27	7.96	18.04	6.18	0.0068	0.0025	0.119	0.360	0.071	0.441
C9728 post	27.5 - 30	0.0129	0.0380	1.02	1.05	1.80	9.92	13.85	0.259	0.0011	0.0032	0.0848	0.087	0.000	0.823
C9673 pre	30 - 32.5	0.600	0.578	3.48	9.51	1.29	2.95	18.40	10.09	0.0326	0.0314	0.1889	0.517	0.070	0.160
C9728 post	30 - 32.5	7.71E-03	0.0668	1.39	2.44	3.30	21.93	29.13	1.55	0.0003	0.0023	0.0476	0.084	0.113	0.753
C9677 pre	20 - 22.5	0.656	1.30	2.50	7.77	2.38	4.04	18.64	8.11	0.0352	0.0697	0.134	0.417	0.128	0.217
C9730 post	20 - 22.5	0.205	0.259	0.560	0.827	0.219	0.366	2.44	1.16	0.084	0.1064	0.230	0.340	0.090	0.150
C9677 pre	22.5 - 25	1.08	2.05	2.13	11.15	1.82	3.94	22.18	9.81	0.0488	0.0922	0.0962	0.503	0.082	0.178
C9730 post	22.5 - 25	0.0187	0.0355	1.07	1.04	0.462	0.522	3.15	0.812	0.0059	0.0113	0.3406	0.330	0.147	0.166
C9677 pre	25 - 27.5	0.913	1.00	1.52	11.1	2.58	3.09	20.18	12.05	0.0452	0.0498	0.0755	0.548	0.128	0.153
C9677 pre dup	25 - 27.5	0.864	0.735	1.03	10.9	1.91	3.14	18.58	12.87	0.0465	0.0396	0.0555	0.587	0.103	0.169
C9730 post	25 - 27.5	9.26E-03	0.0175	0.498	0.657	0.277	0.438	1.90	0.443	0.0049	0.0092	0.2626	0.346	0.146	0.231
C9677 pre	27.5 - 30	0.839	0.887	0.349	4.58	1.05	1.44	9.14	4.62	0.0918	0.097	0.0382	0.501	0.115	0.157
C9730 post	27.5 - 30	3.25E-03	8.51E-03	0.344	0.543	0.530	0.692	2.12	0.119	0.0015	0.004	0.1622	0.256	0.250	0.327

Borehole	Depth (ft)	Extract 1 (µg/g)	Extract 2 (µg/g)	Extract 3 (µg/g)	Extract 4 (µg/g)	Extract 5 (µg/g)	Extract 6 (µg/g)	Sum (µg/g)	1000h Co_3 (µg/g)	Extract 1 fraction	Extract 2 fraction	Extract 3 fraction	Extract 4 fraction	Extract 5 fraction	Extract 6 fraction
C9683 pre	22.5 - 25	0.0531	0.0363	0.147	1.45	0.610	0.895	3.19	1.67	0.0166	0.0114	0.046	0.455	0.191	0.280
C9732 post	22.5 - 25	5.72E-04	5.03E-03	0.0612	0.0641	0.0748	0.177	0.383	0.0084	0.0015	0.0131	0.1599	0.168	0.196	0.462
C9683 pre	25 - 27.5	0.0532	0.0113	0.0362	0.776	0.400	0.549	1.83	0.970	0.0292	0.0062	0.0198	0.425	0.219	0.301
C9732 post	25 - 27.5	4.42E-03	6.69E-03	0.155	0.252	0.253	0.424	1.10	0.100	0.0040	0.0061	0.1418	0.230	0.231	0.387
C9734 post(a)	22.5 - 25	0.0692	0.0032	0.888	0.969	1.75	9.01	12.69	2.04	0.0055	0.0002	0.0700	0.0764	0.138	0.710
C9734 post(a)	27.5 - 30	3.82E-03	4.54E-03	0.172	0.287	0.643	1.08	2.195	0.0253	0.0017	0.0021	0.0785	0.131	0.293	0.494
C9735 post(a)	22.5 - 25	0.0256	7.37E-03	5.41	3.89	3.61	8.25	21.20	6.51	0.0012	0.0003	0.2553	0.184	0.170	0.389
C9735 post(a)	27.5 - 30	3.53E-03	4.38E-03	0.698	0.884	0.956	1.30	3.84	0.434	0.0009	0.0011	0.182	0.230	0.249	0.338
C9736 post(a)	22.5 - 25	0.0246	0.0564	0.301	0.277	0.065	0.151	0.875	0.378	0.0281	0.0645	0.344	0.316	0.0745	0.173
C9736 post(a)	25 - 27.5	0.0399	0.0802	0.405	0.573	0.126	0.314	1.54	0.499	0.0260	0.0521	0.2633	0.3727	0.0819	0.204

(a) Unpaired post injection sample

Appendix B – Grain Size Distributions

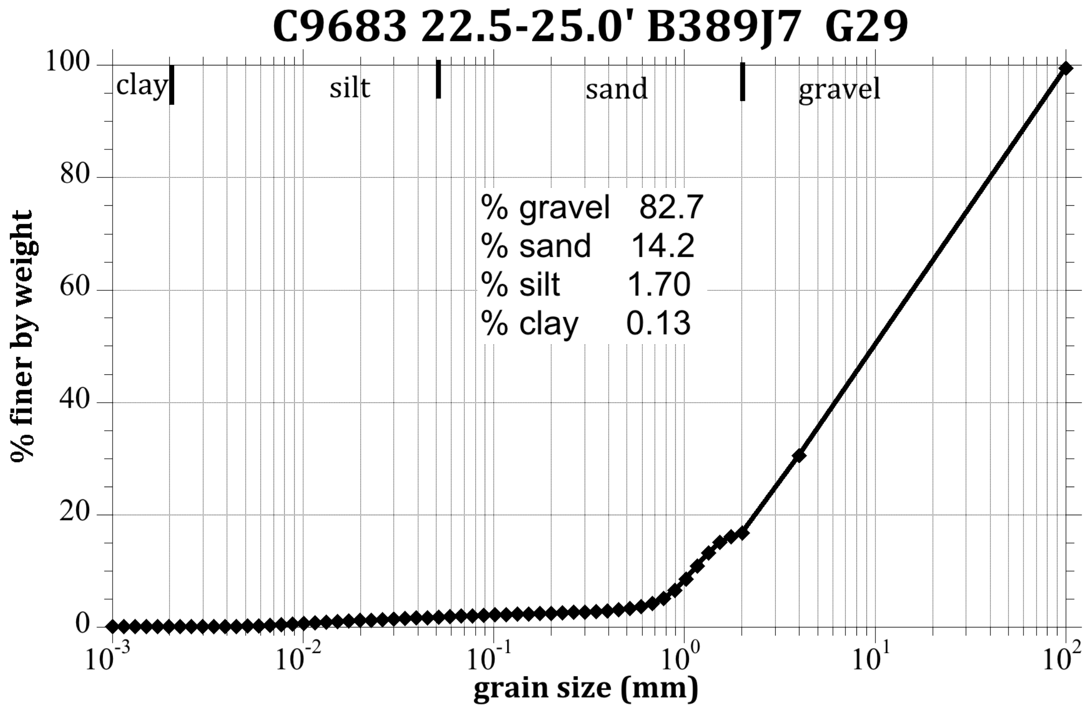

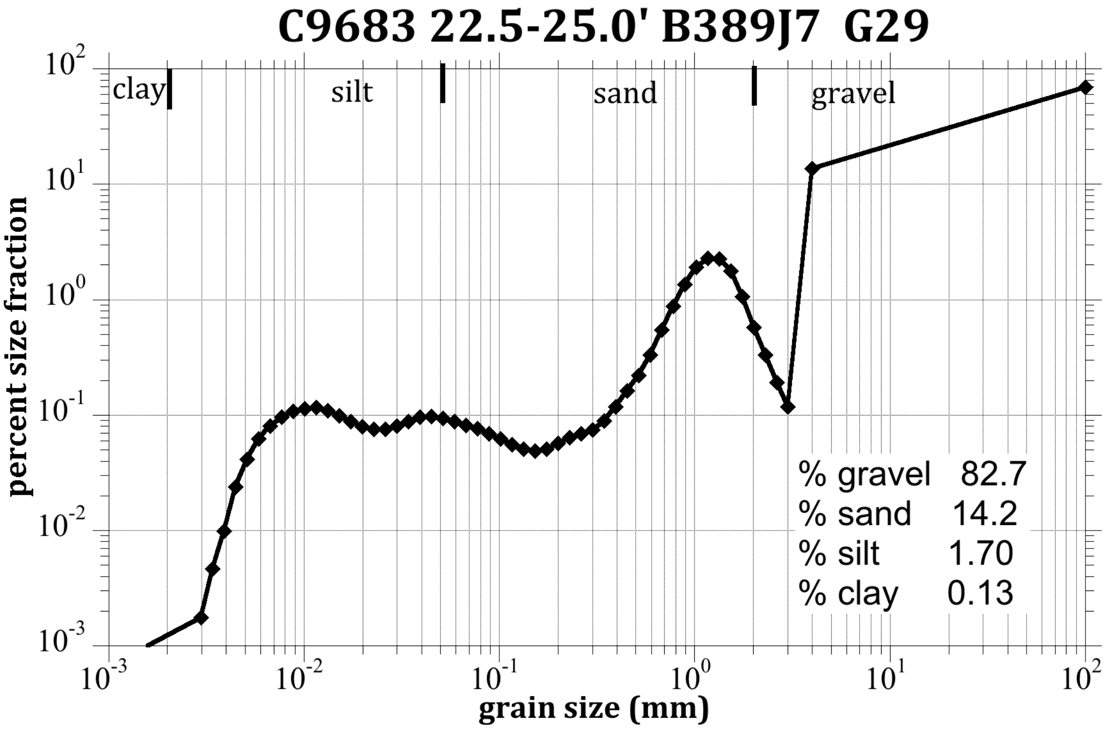

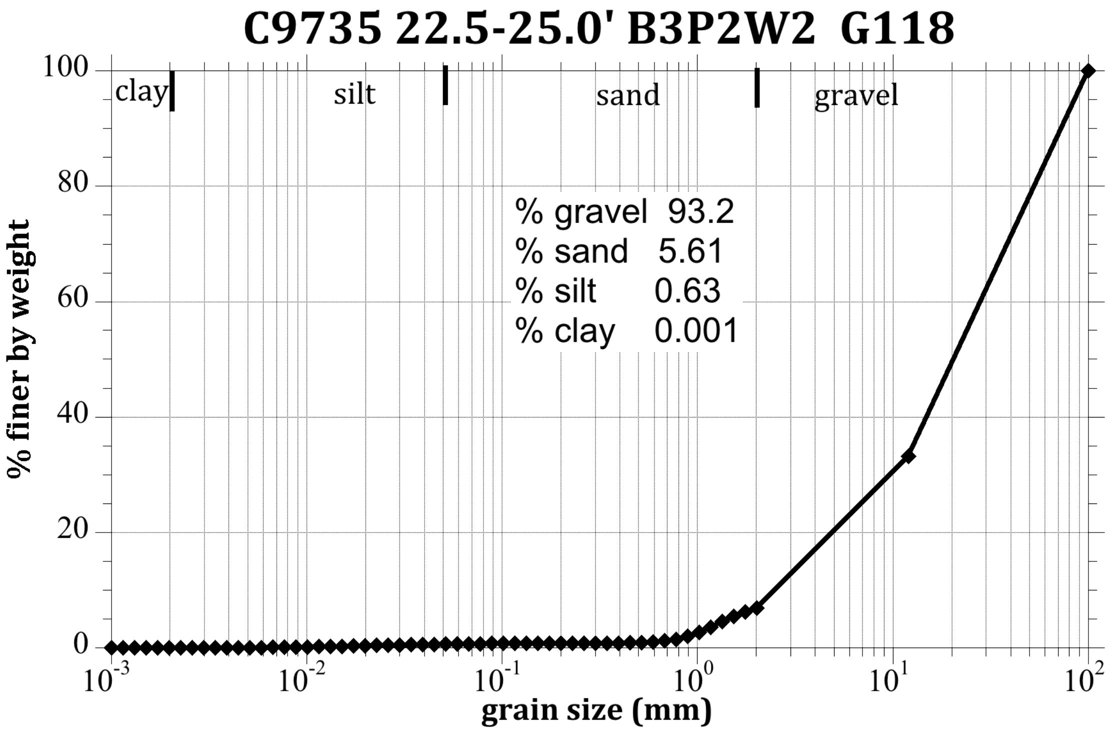
C9735 22.5-25.0' B3P2W2 G118
100
80
60
40
20
0
% finer by weight
clay
silt
sand
gravel
% gravel 93.2
% sand 5.61
% silt 0.63
% clay 0.001
10^{-3}
10^{-2}
10^{-1}
10^{0}
10^{1}
10^{2}
grain size (mm)

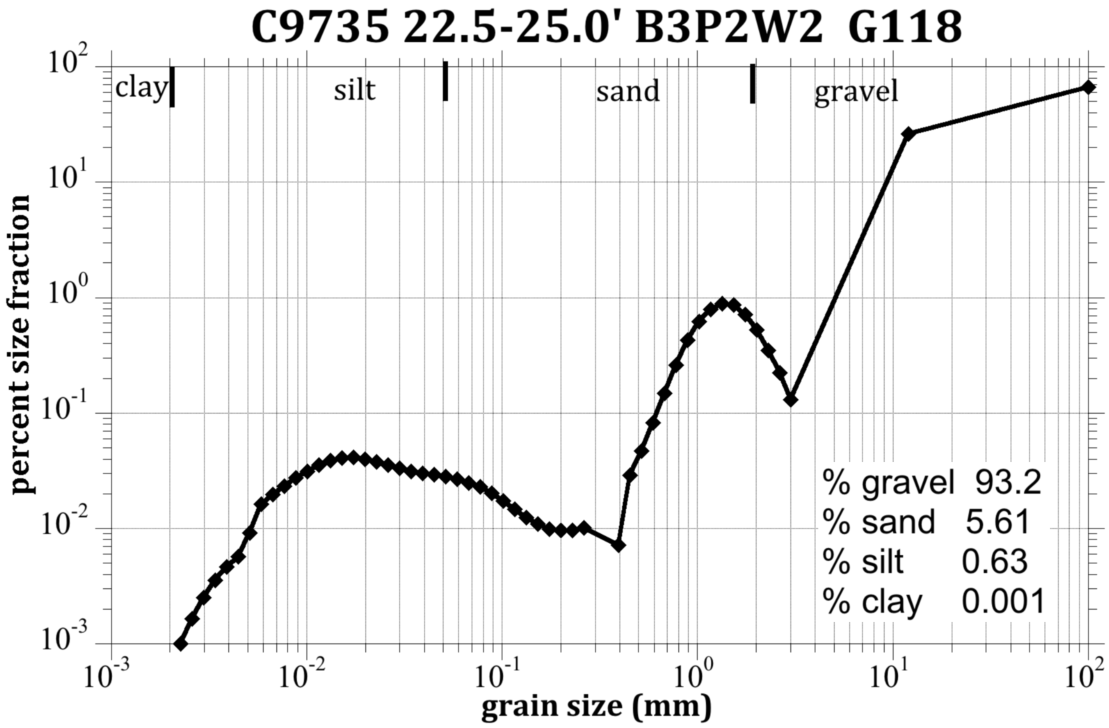
C9735 22.5-25.0' B3P2W2 G118
10^{2}
10^{1}
10^{0}
10^{-1}
10^{-2}
10^{-3}
percent size fraction
clay
silt
sand
gravel
% gravel 93.2
% sand 5.61
% silt 0.63
% clay 0.001
10^{-3}
10^{-2}
10^{-1}
10^{0}
10^{1}
10^{2}
grain size (mm)

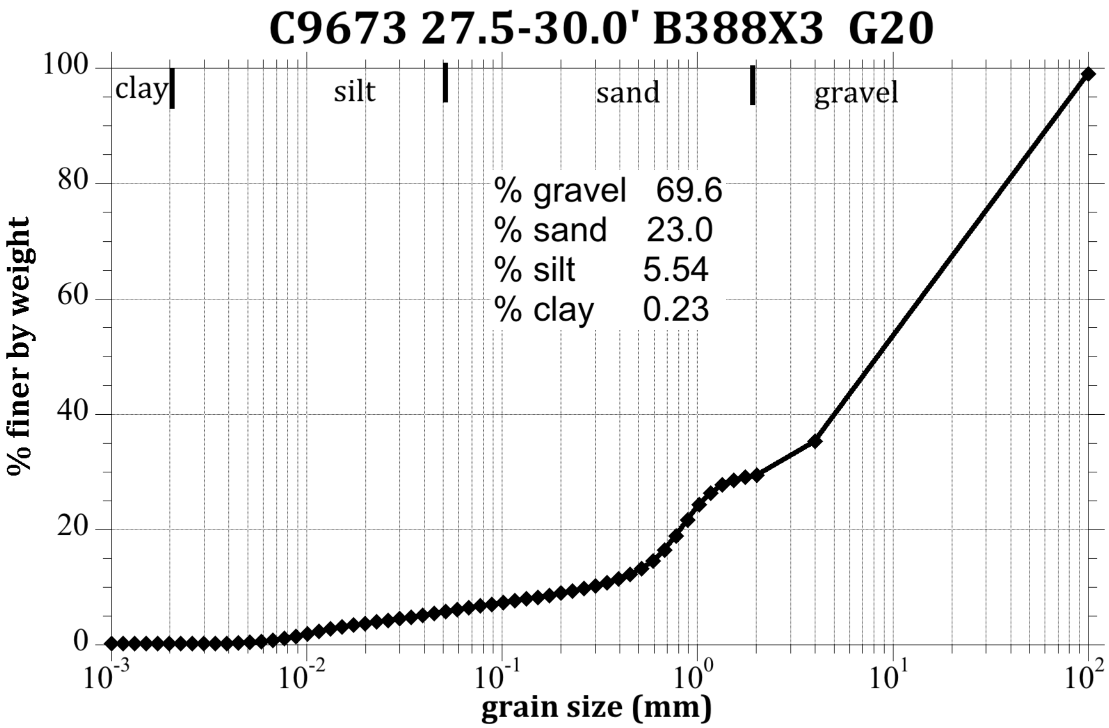
C9673 27.5-30.0' B388X3 G20
100
80
60
40
20
0
% finer by weight
clay
silt
sand
gravel
% gravel 69.6
% sand 23.0
% silt 5.54
% clay 0.23
10^{-3}
10^{-2}
10^{-1}
10^{0}
10^{1}
10^{2}
grain size (mm)

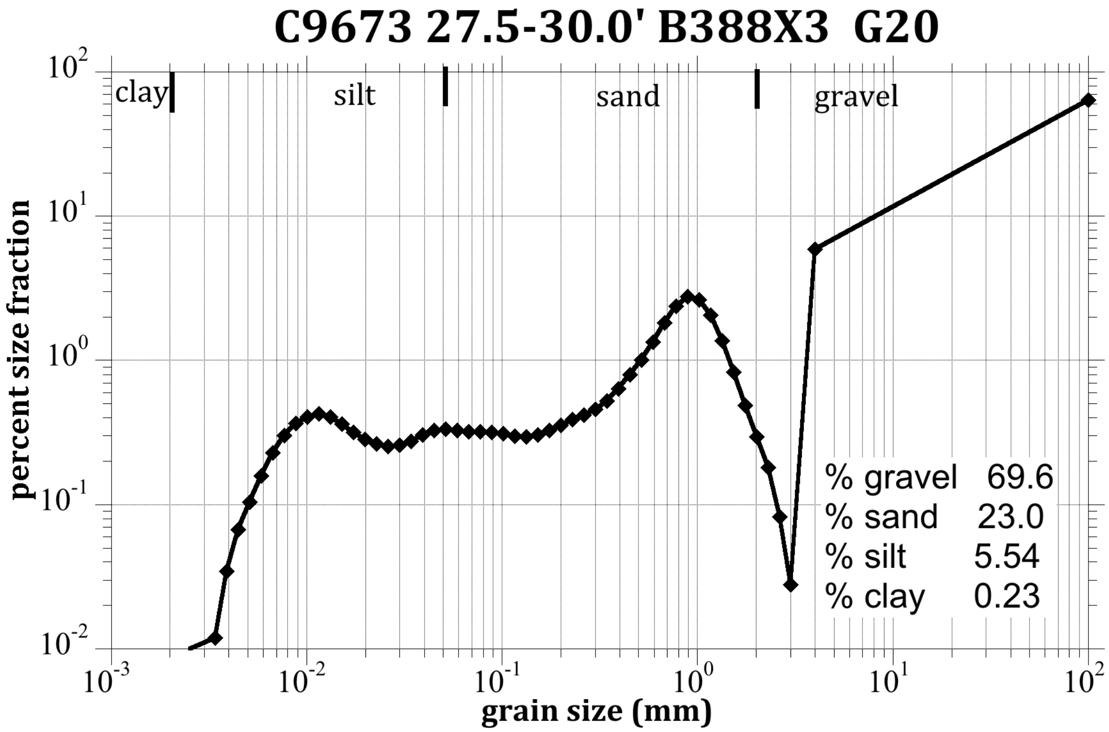
C9673 27.5-30.0' B388X3 G20
10^{2}
10^{1}
10^{0}
10^{-1}
10^{-2}
percent size fraction
clay
silt
sand
gravel
% gravel 69.6
% sand 23.0
% silt 5.54
% clay 0.23
10^{-3}
10^{-2}
10^{-1}
10^{0}
10^{1}
10^{2}
grain size (mm)

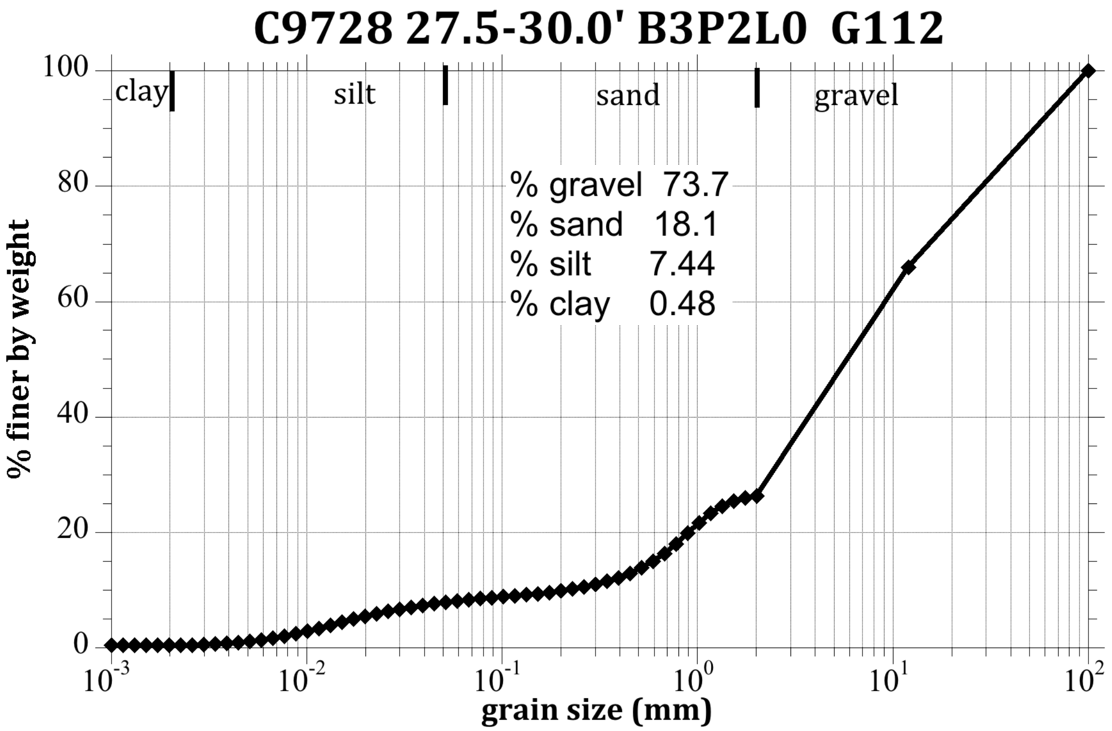
C9728 27.5-30.0' B3P2L0 G112
% finer by weight
100
80
60
40
20
0
clay
silt
sand
gravel
% gravel 73.7
% sand 18.1
% silt 7.44
% clay 0.48
10^{-3}
10^{-2}
10^{-1}
10^{0}
10^{1}
10^{2}
grain size (mm)

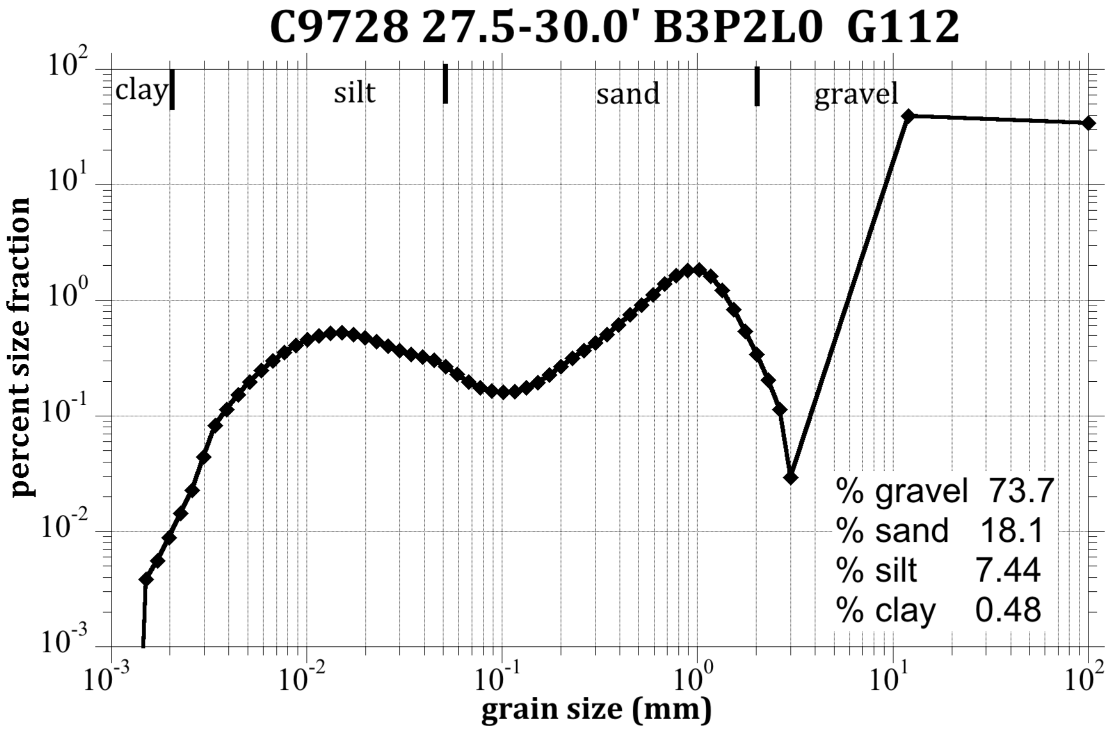
C9728 27.5-30.0' B3P2L0 G112
percent size fraction
10^{2}
10^{1}
10^{0}
10^{-1}
10^{-2}
10^{-3}
clay
silt
sand
gravel
% gravel 73.7
% sand 18.1
% silt 7.44
% clay 0.48
10^{-3}
10^{-2}
10^{-1}
10^{0}
10^{1}
10^{2}
grain size (mm)

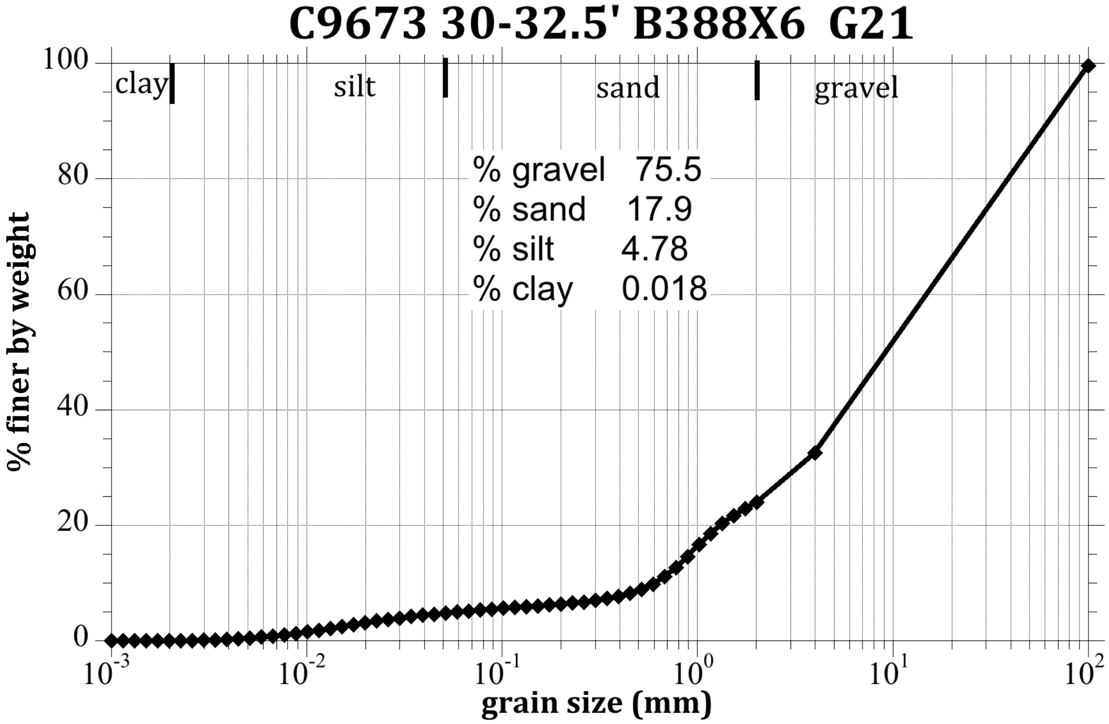
C9673 30-32.5' B388X6 G21
100
80
60
40
20
0
% finer by weight
clay
silt
sand
gravel
% gravel 75.5
% sand 17.9
% silt 4.78
% clay 0.018
10^{-3}
10^{-2}
10^{-1}
10^{0}
10^{1}
10^{2}
grain size (mm)

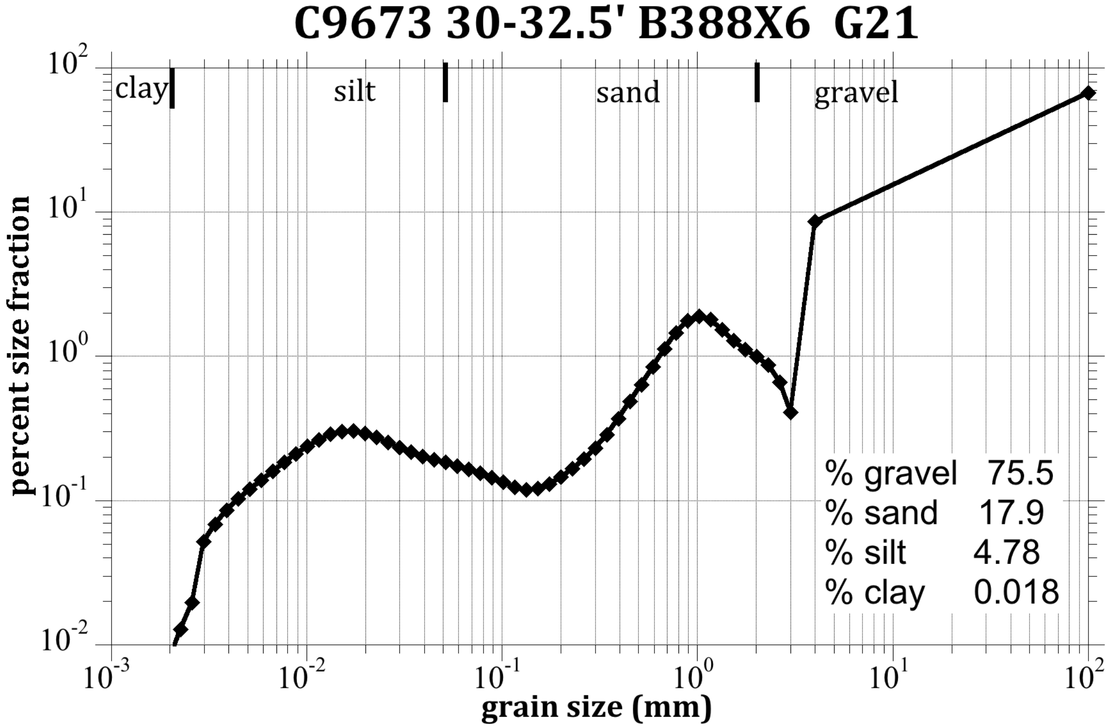
C9673 30-32.5' B388X6 G21
10^{2}
10^{1}
10^{0}
10^{-1}
10^{-2}
percent size fraction
clay
silt
sand
gravel
% gravel 75.5
% sand 17.9
% silt 4.78
% clay 0.018
10^{-3}
10^{-2}
10^{-1}
10^{0}
10^{1}
10^{2}
grain size (mm)

C9728 30.0-32.5' B3P2L4 G113

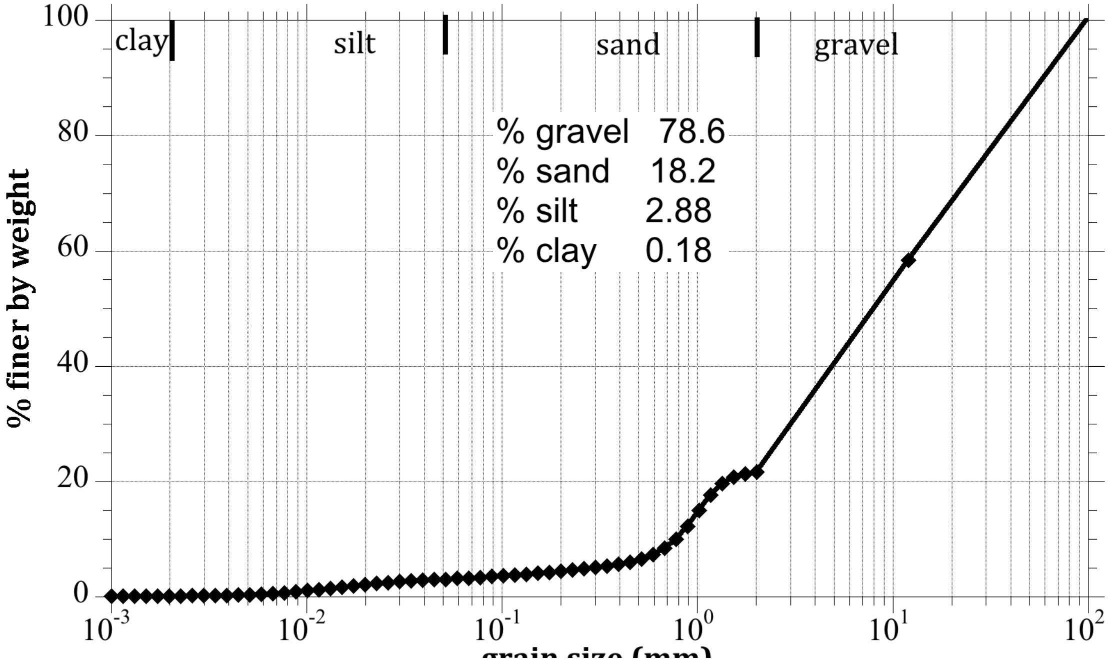

C9728 30.0-32.5' B3P2L4 G113

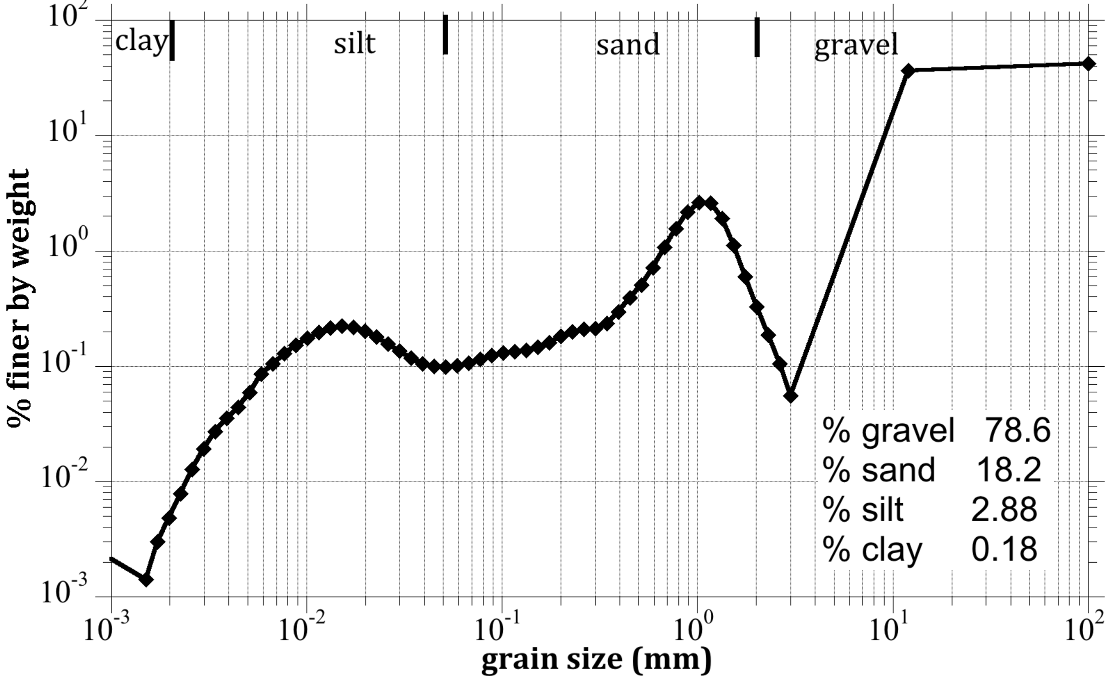

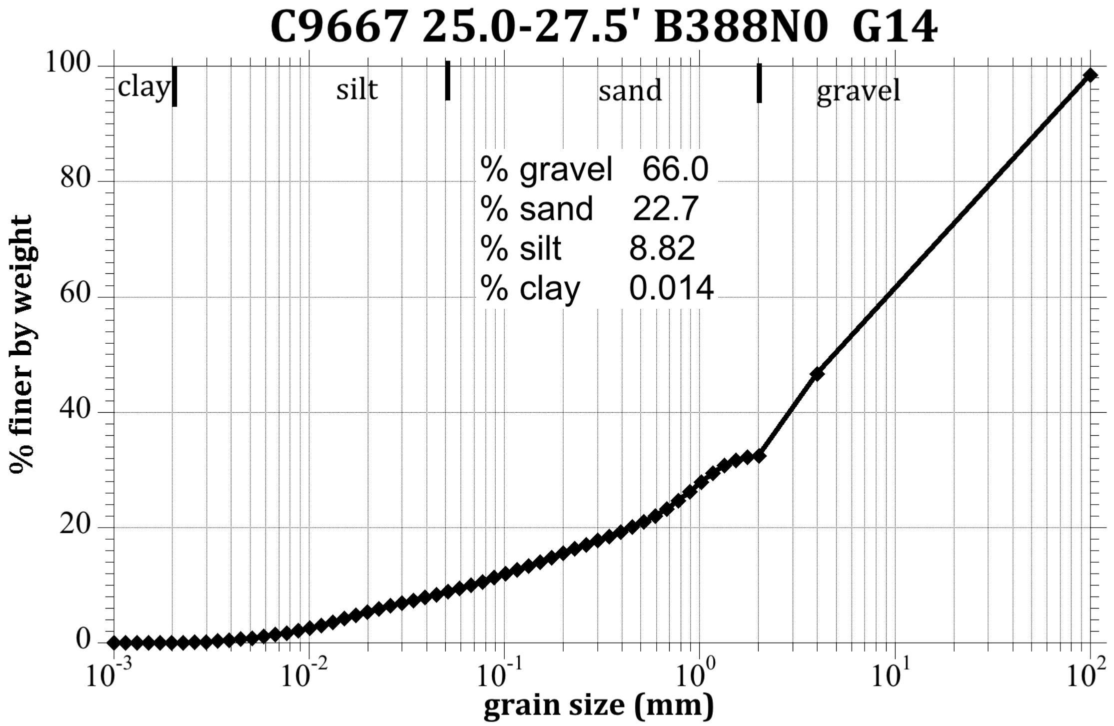
C9667 25.0-27.5' B388N0 G14
clay
silt
sand
gravel
% gravel 66.0
% sand 22.7
% silt 8.82
% clay 0.014
% finer by weight
100
80
60
40
20
0
10^{-3}
10^{-2}
10^{-1}
10^{0}
10^{1}
10^{2}
grain size (mm)

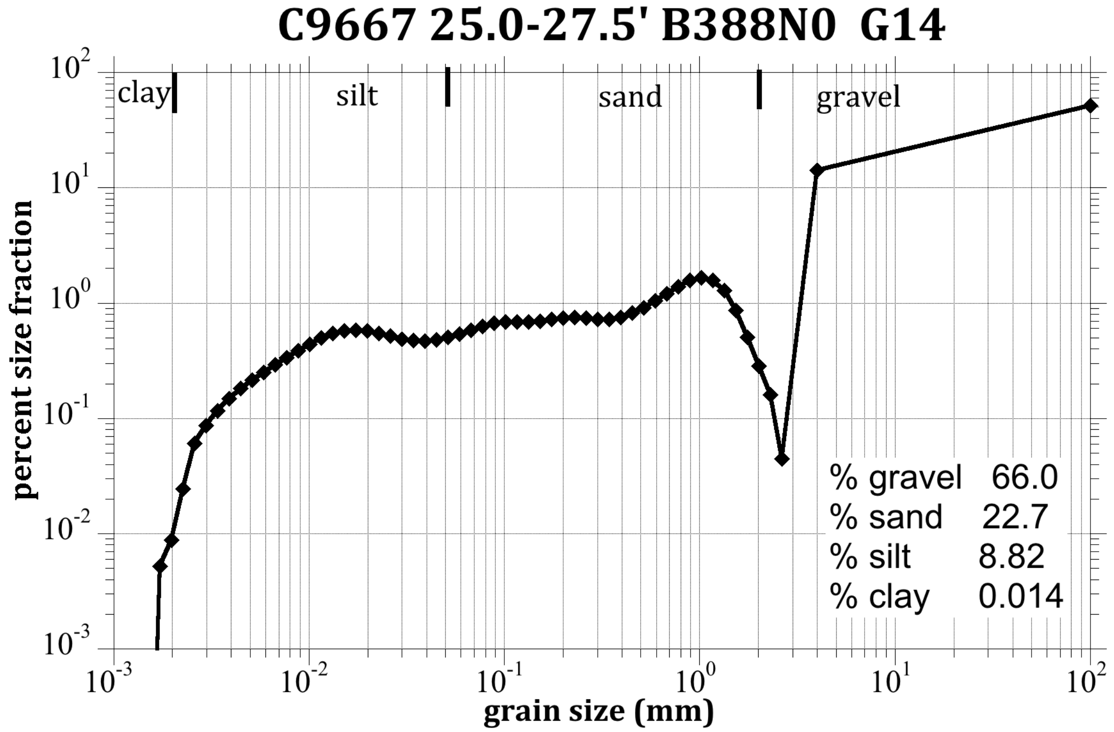
C9667 25.0-27.5' B388N0 G14
clay
silt
sand
gravel
% gravel 66.0
% sand 22.7
% silt 8.82
% clay 0.014
percent size fraction
10^{2}
10^{1}
10^{0}
10^{-1}
10^{-2}
10^{-3}
10^{-3}
10^{-2}
10^{-1}
10^{0}
10^{1}
10^{2}
grain size (mm)

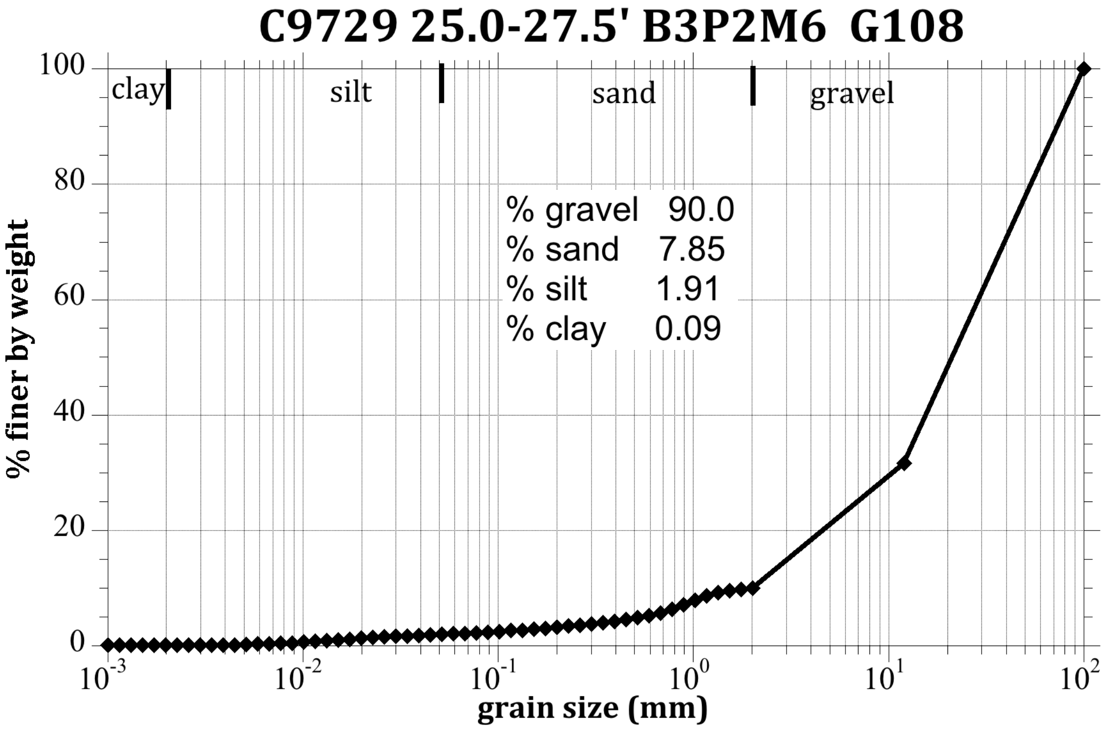
C9729 25.0-27.5' B3P2M6 G108
% finer by weight
grain size (mm)
clay
silt
sand
gravel
% gravel 90.0
% sand 7.85
% silt 1.91
% clay 0.09
0
20
40
60
80
100
10^{-3}
10^{-2}
10^{-1}
10^{0}
10^{1}
10^{2}

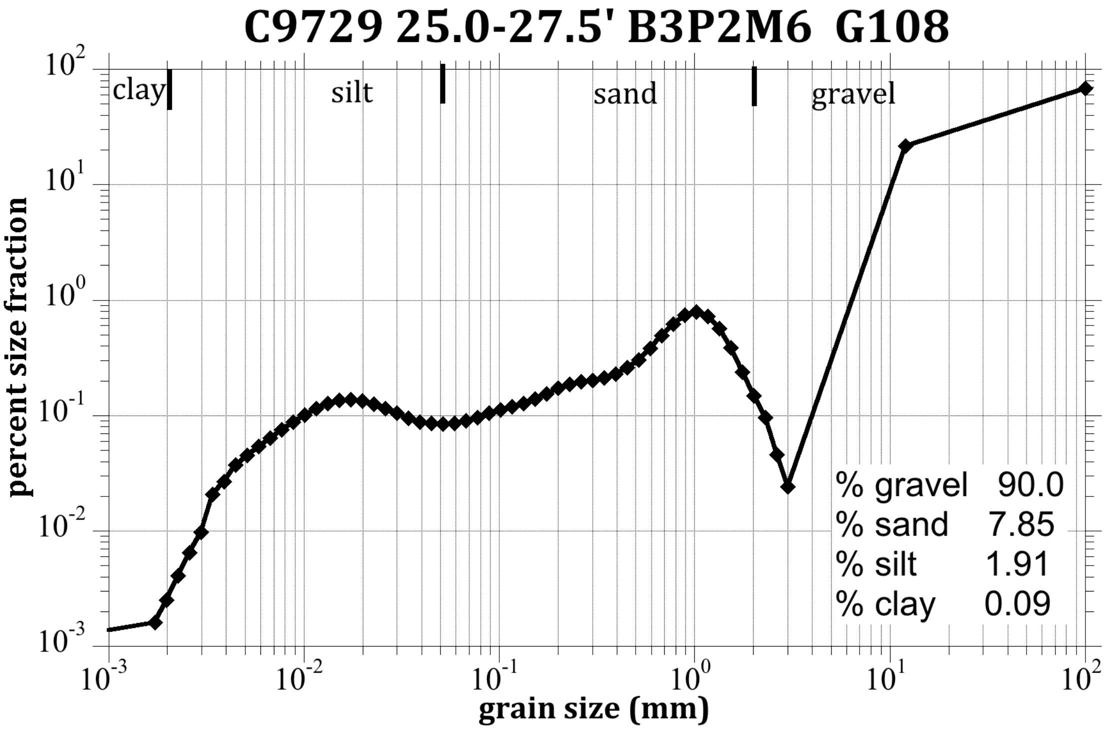
C9729 25.0-27.5' B3P2M6 G108
percent size fraction
grain size (mm)
clay
silt
sand
gravel
% gravel 90.0
% sand 7.85
% silt 1.91
% clay 0.09
10^{-3}
10^{-2}
10^{-1}
10^{0}
10^{1}
10^{2}

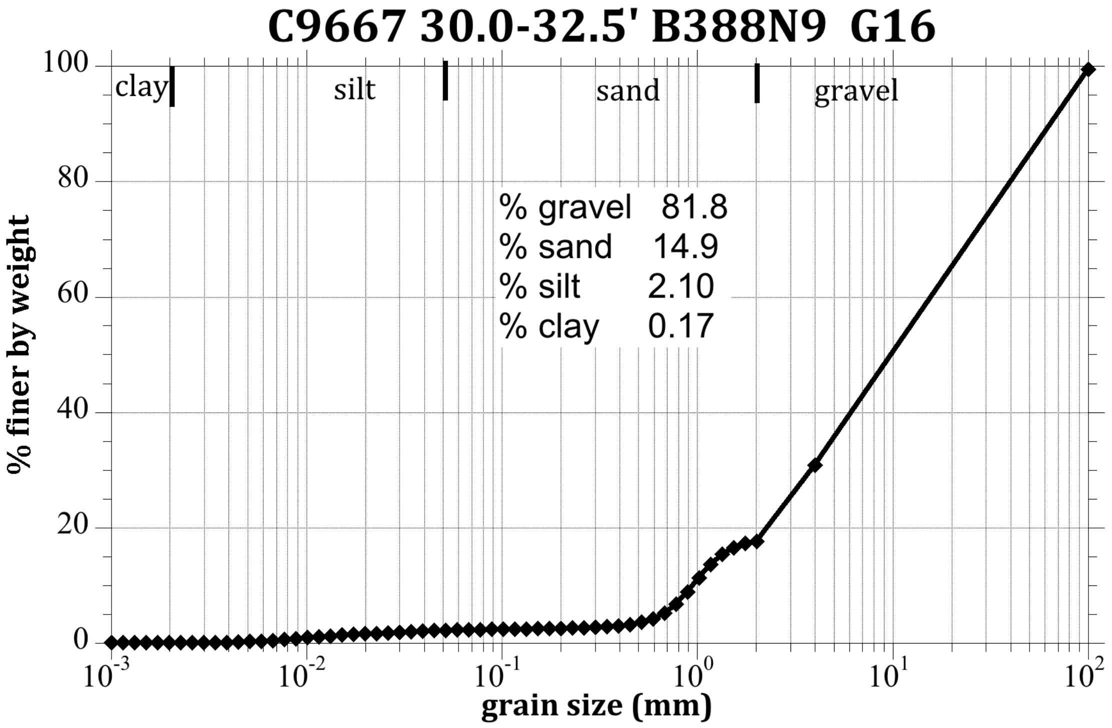
C9667 30.0-32.5' B388N9 G16

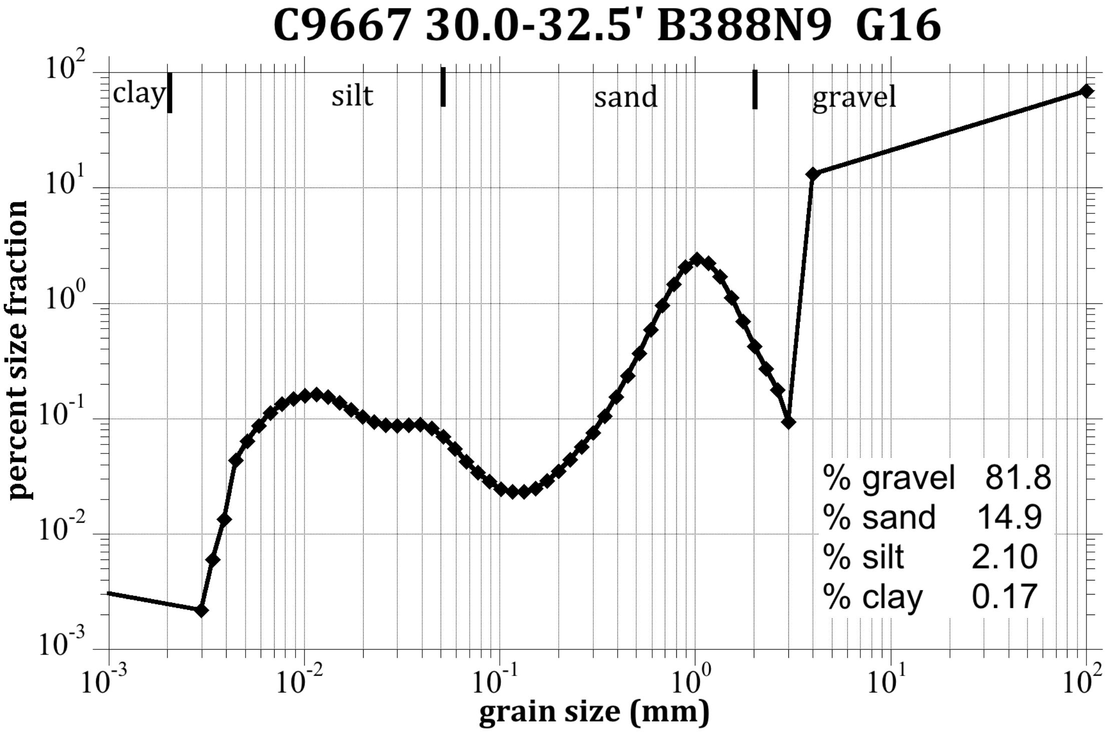
C9667 30.0-32.5' B388N9 G16

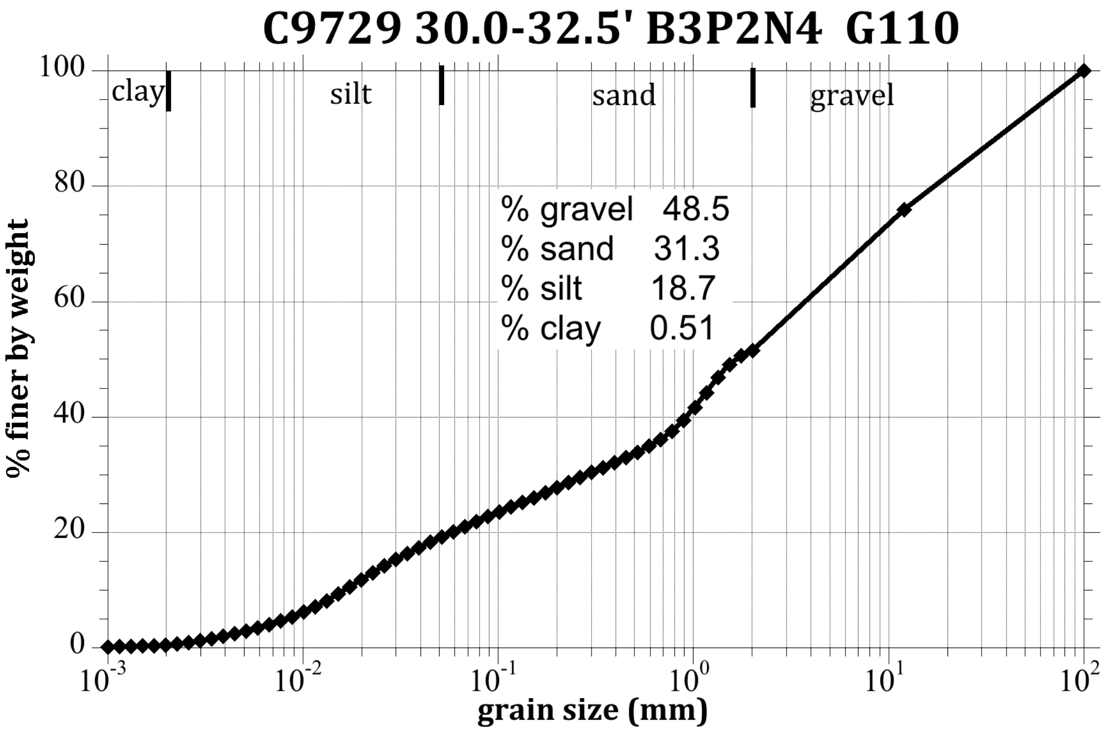
C9729 30.0-32.5' B3P2N4 G110
clay
silt
sand
gravel
% gravel 48.5
% sand 31.3
% silt 18.7
% clay 0.51
% finer by weight
100
80
60
40
20
0
10^{-3}
10^{-2}
10^{-1}
10^{0}
10^{1}
10^{2}
grain size (mm)

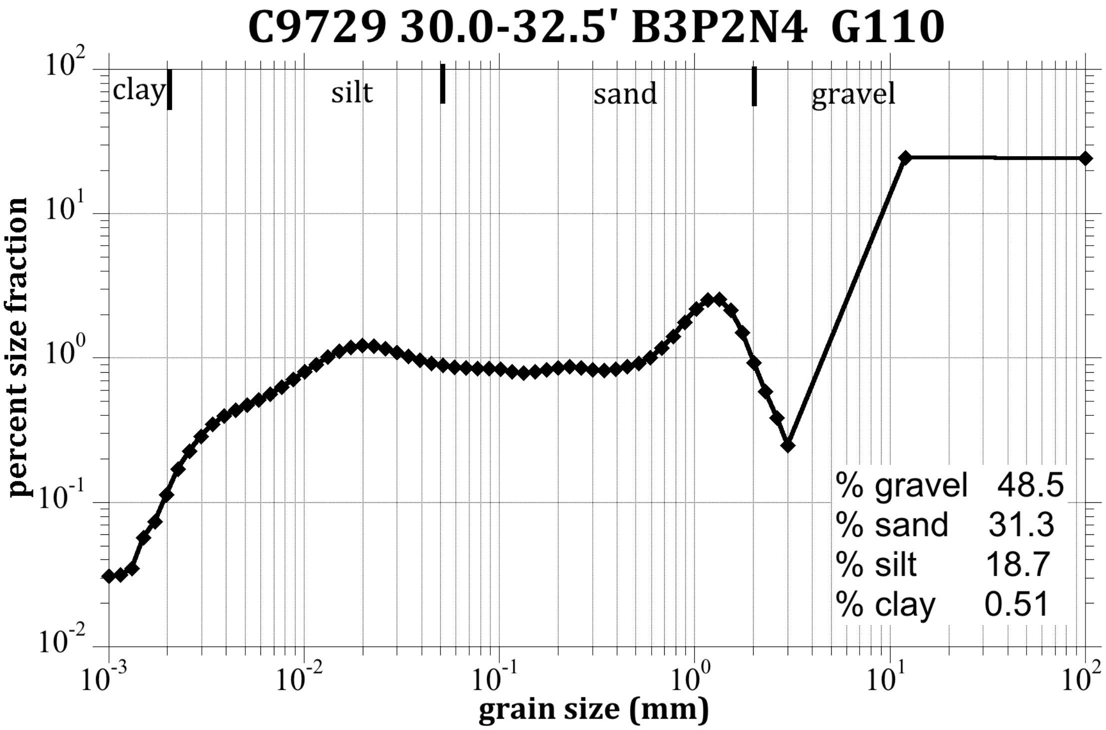
C9729 30.0-32.5' B3P2N4 G110
clay
silt
sand
gravel
% gravel 48.5
% sand 31.3
% silt 18.7
% clay 0.51
percent size fraction
10^{2}
10^{1}
10^{0}
10^{-1}
10^{-2}
10^{-3}
10^{-2}
10^{-1}
10^{0}
10^{1}
10^{2}
grain size (mm)

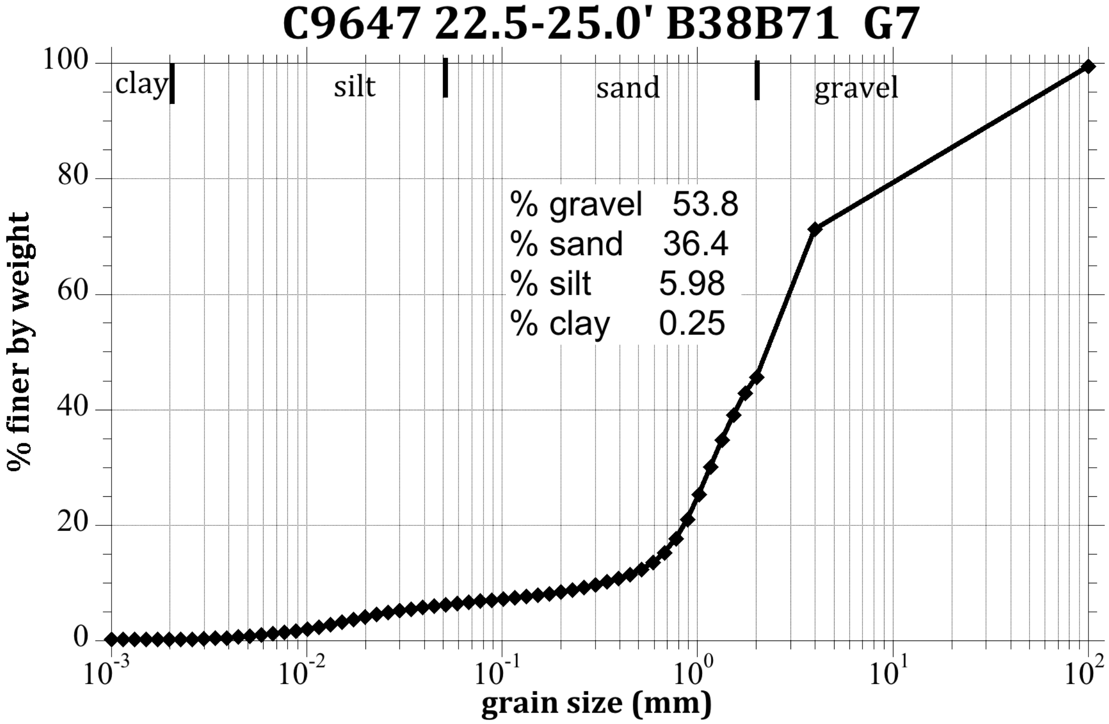

C9647 22.5-25.0' B38B71 G7

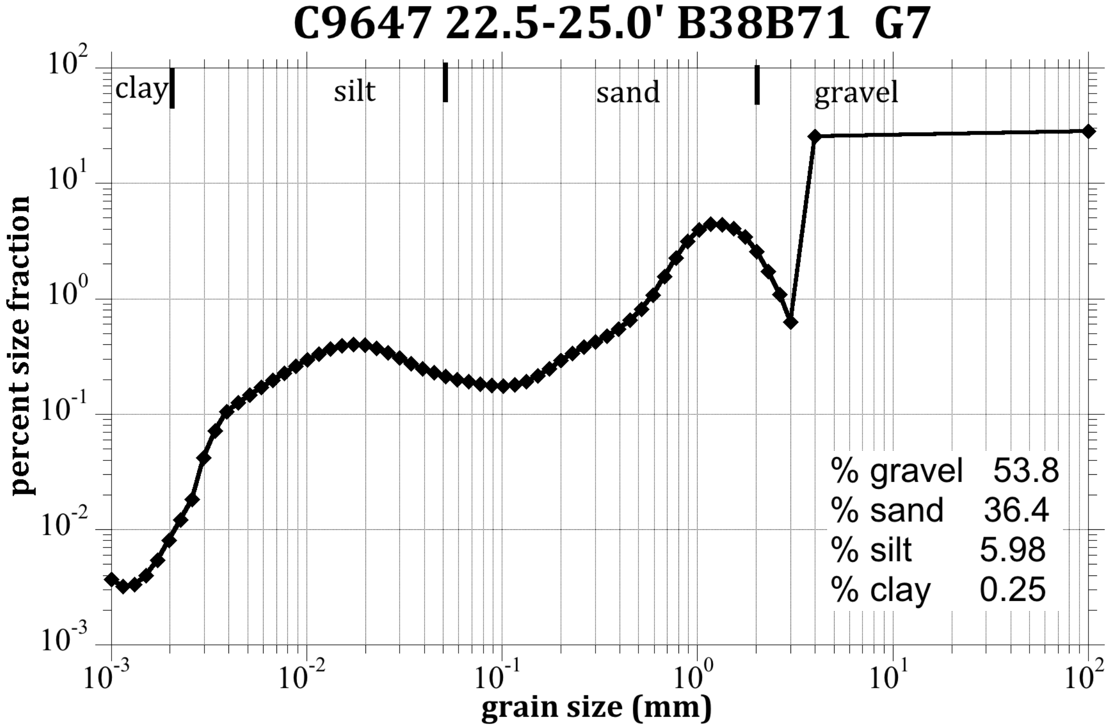

C9647 22.5-25.0' B38B71 G7

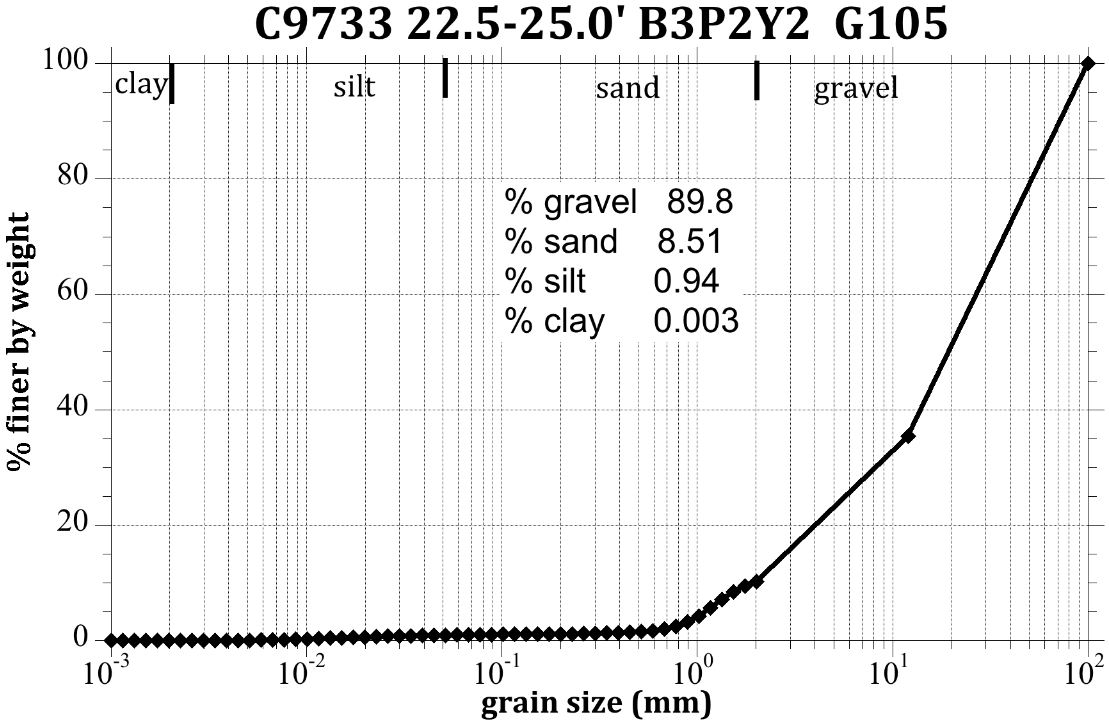
C9733 22.5-25.0' B3P2Y2 G105
clay
silt
sand
gravel
% gravel 89.8
% sand 8.51
% silt 0.94
% clay 0.003
% finer by weight
100
80
60
40
20
0
10^{-3}
10^{-2}
10^{-1}
10^{0}
10^{1}
10^{2}
grain size (mm)

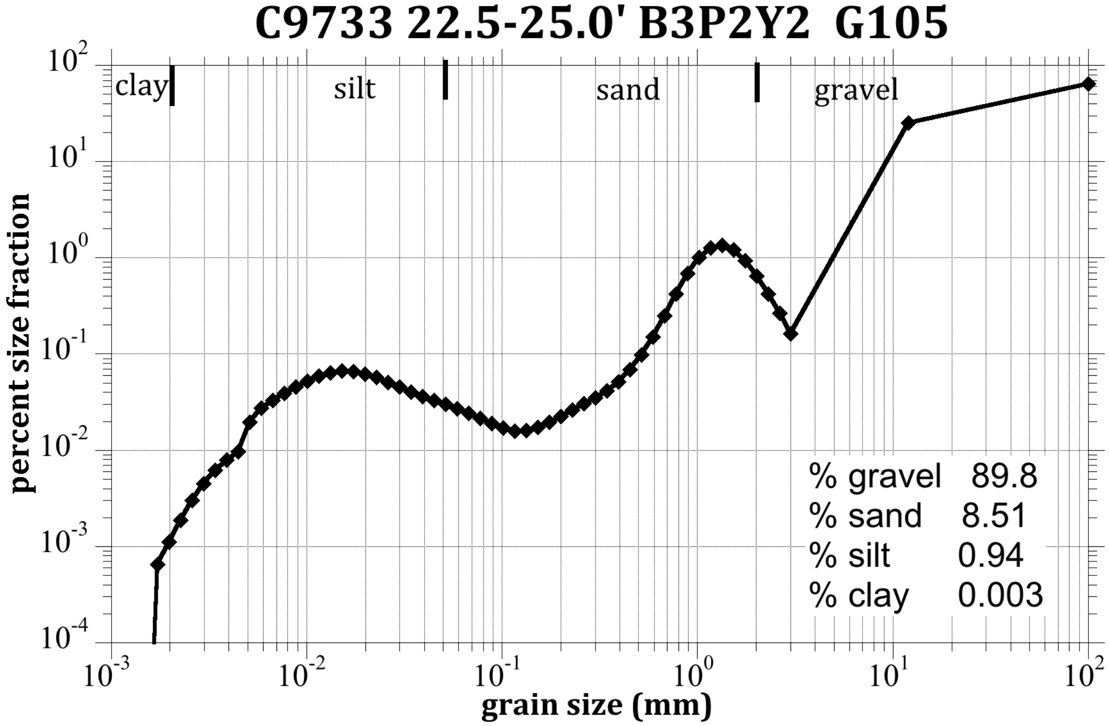
C9733 22.5-25.0' B3P2Y2 G105
clay
silt
sand
gravel
% gravel 89.8
% sand 8.51
% silt 0.94
% clay 0.003
percent size fraction
10^{2}
10^{1}
10^{0}
10^{-1}
10^{-2}
10^{-3}
10^{-4}
10^{-3}
10^{-2}
10^{-1}
10^{0}
10^{1}
10^{2}
grain size (mm)

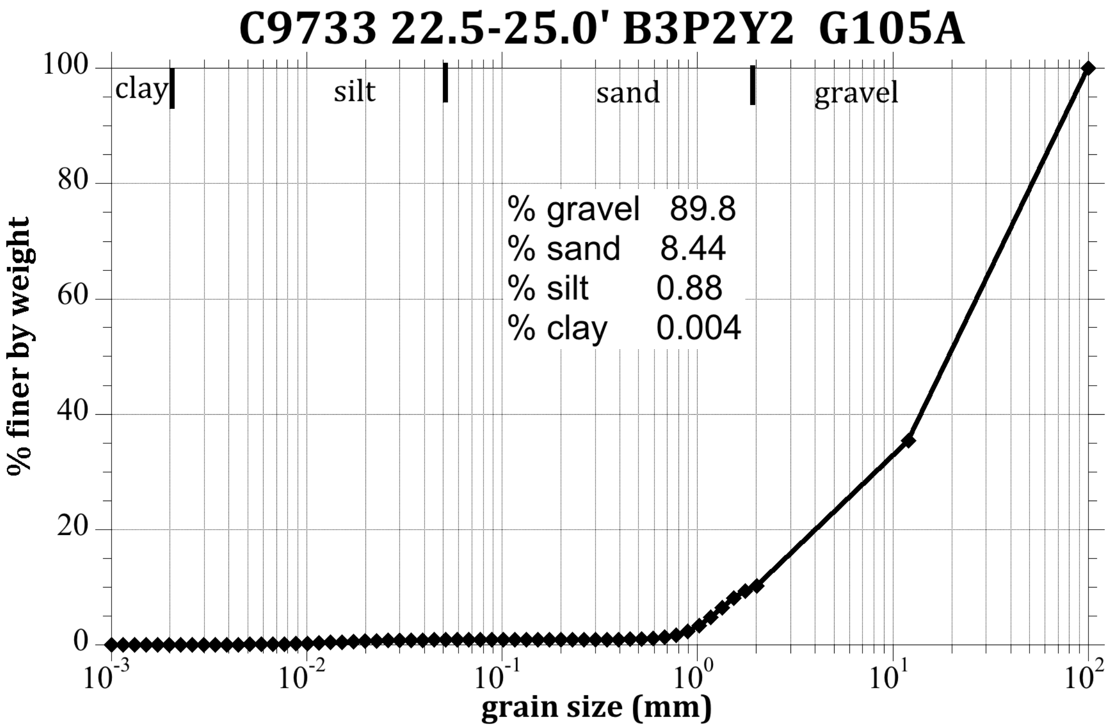
C9733 22.5-25.0' B3P2Y2 G105A
% finer by weight
grain size (mm)
clay
silt
sand
gravel
% gravel 89.8
% sand 8.44
% silt 0.88
% clay 0.004
100
80
60
40
20
0
10^{-3}
10^{-2}
10^{-1}
10^{0}
10^{1}
10^{2}

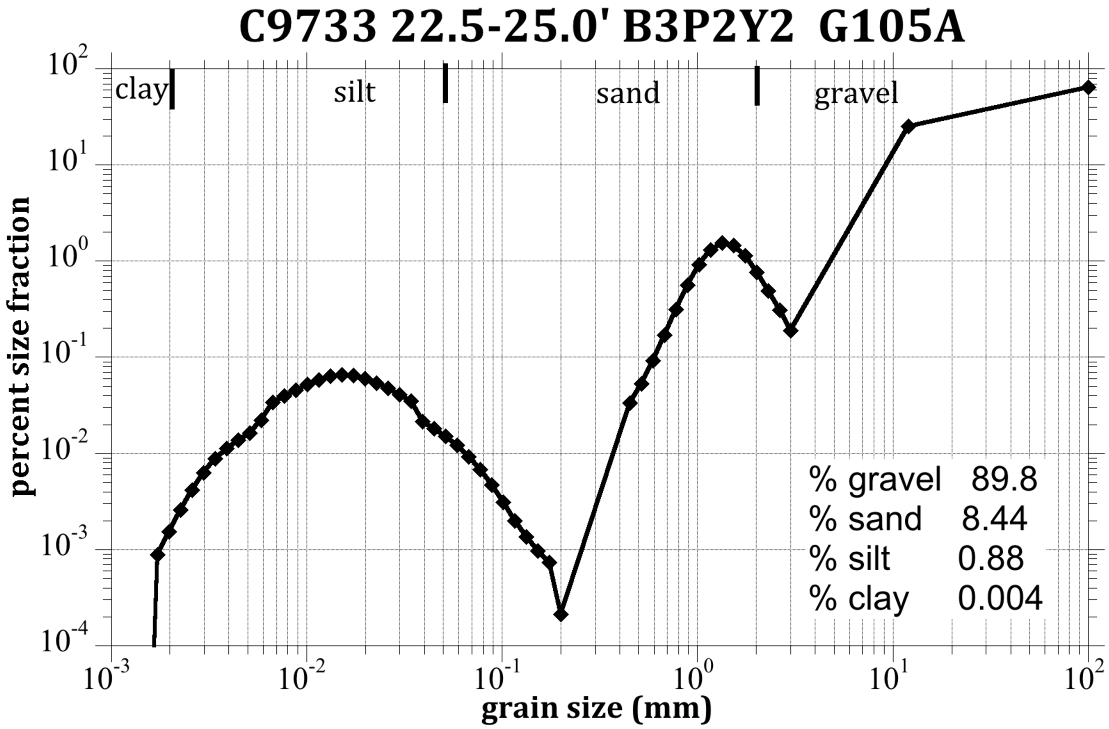
C9733 22.5-25.0' B3P2Y2 G105A
percent size fraction
grain size (mm)
clay
silt
sand
gravel
% gravel 89.8
% sand 8.44
% silt 0.88
% clay 0.004
10^{2}
10^{1}
10^{0}
10^{-1}
10^{-2}
10^{-3}
10^{-4}
10^{-3}
10^{-2}
10^{-1}
10^{0}
10^{1}
10^{2}

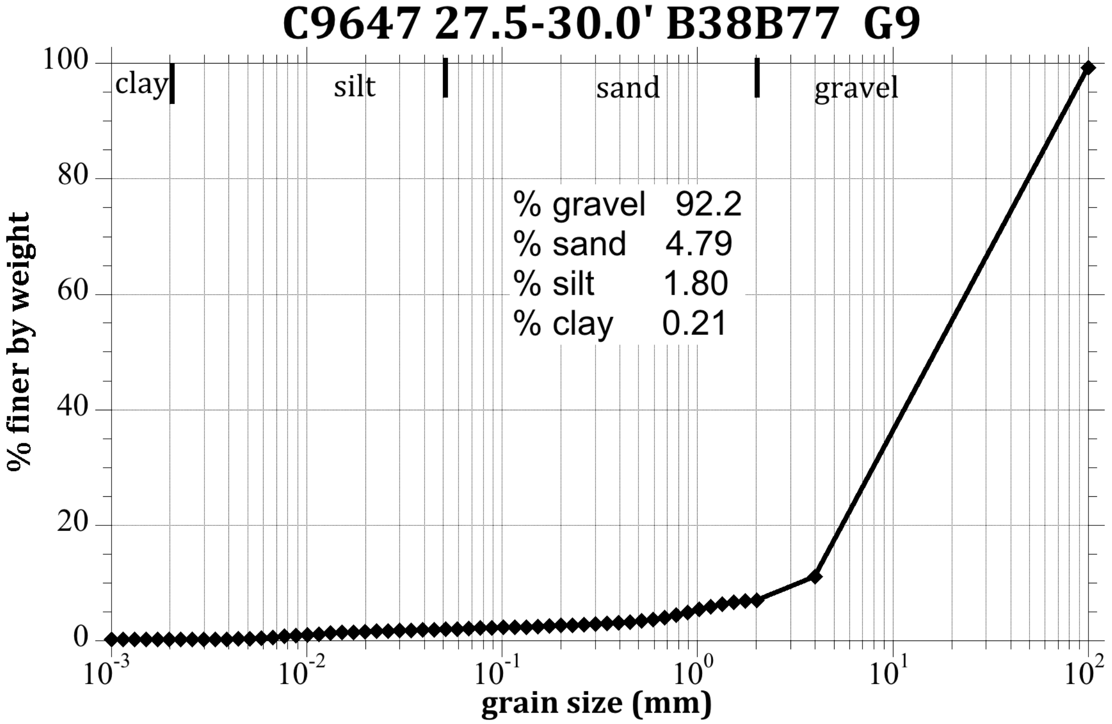
C9647 27.5-30.0' B38B77 G9
clay
silt
sand
gravel
% gravel 92.2
% sand 4.79
% silt 1.80
% clay 0.21
% finer by weight
0
20
40
60
80
100
10^{-3}
10^{-2}
10^{-1}
10^{0}
10^{1}
10^{2}
grain size (mm)

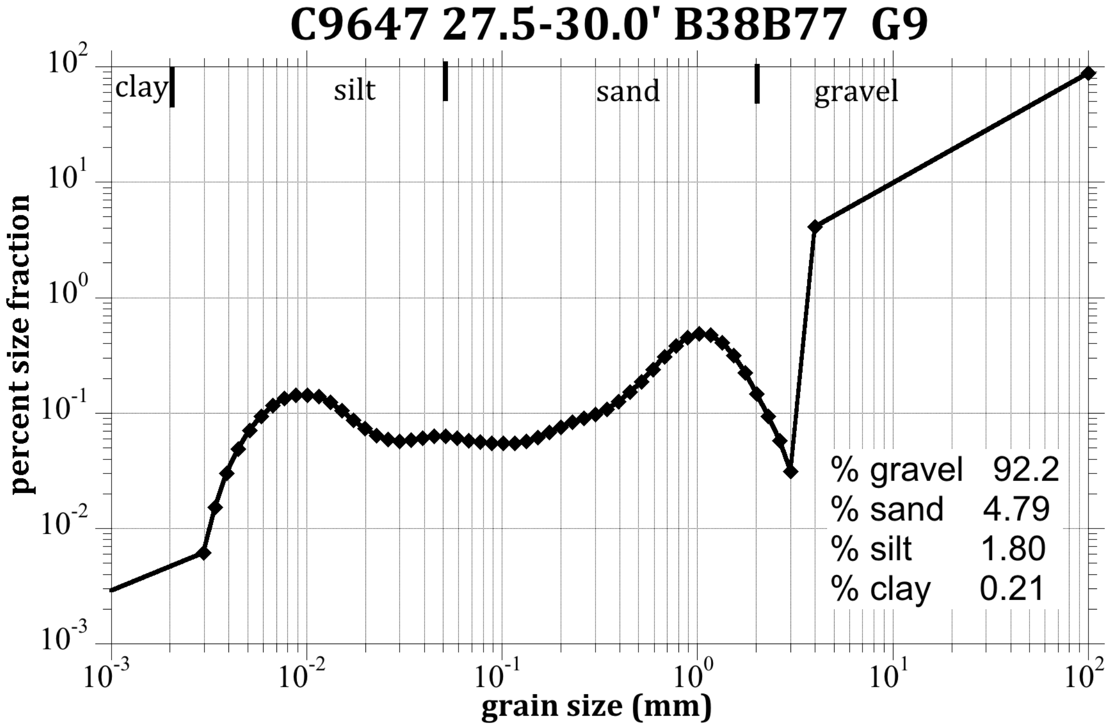
C9647 27.5-30.0' B38B77 G9
clay
silt
sand
gravel
% gravel 92.2
% sand 4.79
% silt 1.80
% clay 0.21
percent size fraction
10^{-3}
10^{-2}
10^{-1}
10^{0}
10^{1}
10^{2}
10^{-3}
10^{-2}
10^{-1}
10^{0}
10^{1}
10^{2}
grain size (mm)

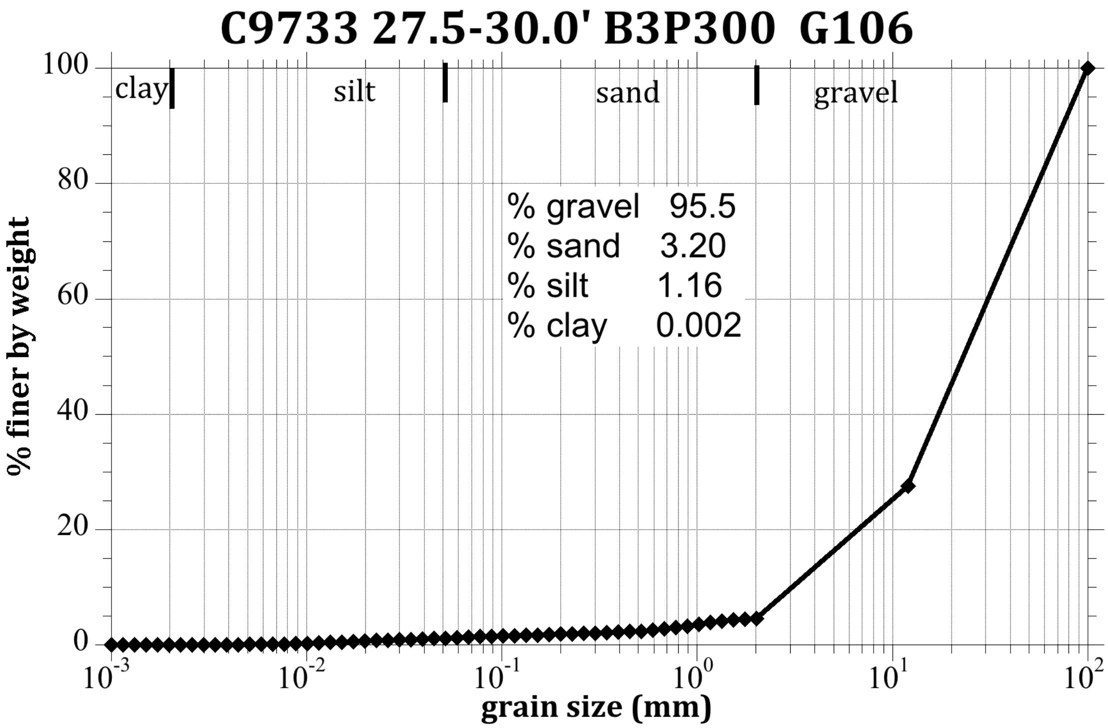
C9733 27.5-30.0' B3P300 G106
clay
silt
sand
gravel
% gravel 95.5
% sand 3.20
% silt 1.16
% clay 0.002
% finer by weight
0
20
40
60
80
100
10^{-3}
10^{-2}
10^{-1}
10^{0}
10^{1}
10^{2}
grain size (mm)

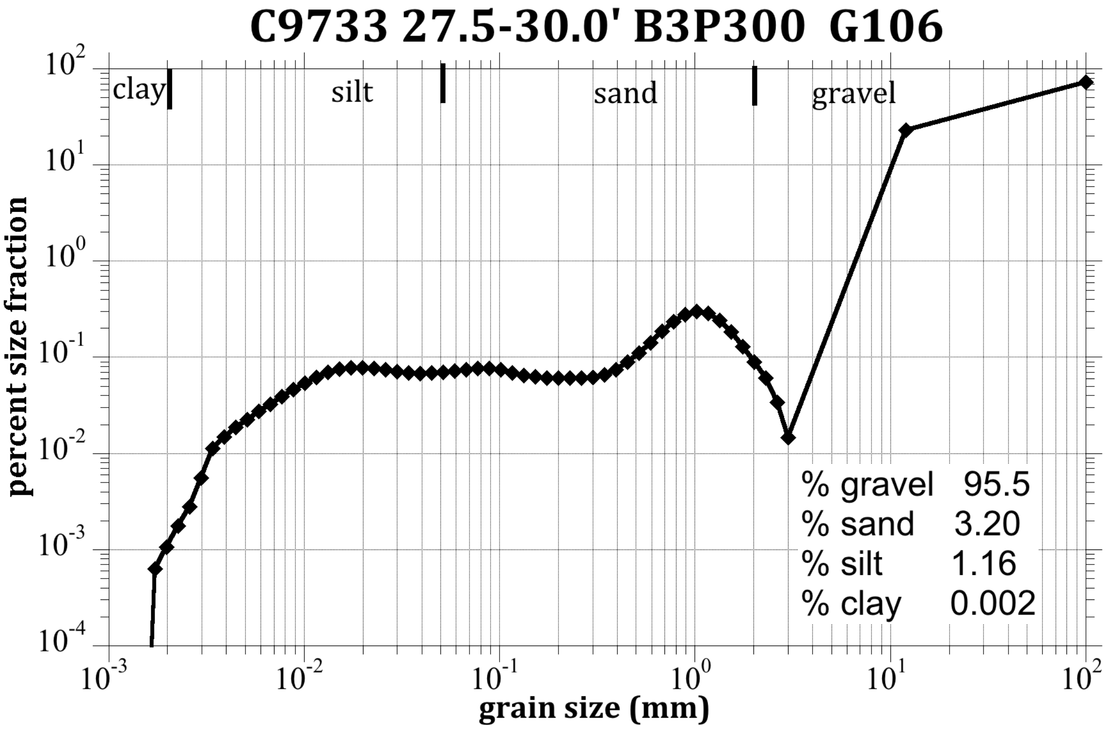
C9733 27.5-30.0' B3P300 G106
clay
silt
sand
gravel
% gravel 95.5
% sand 3.20
% silt 1.16
% clay 0.002
percent size fraction
10^{-4}
10^{-3}
10^{-2}
10^{-1}
10^{0}
10^{1}
10^{2}
10^{-3}
10^{-2}
10^{-1}
10^{0}
10^{1}
10^{2}
grain size (mm)

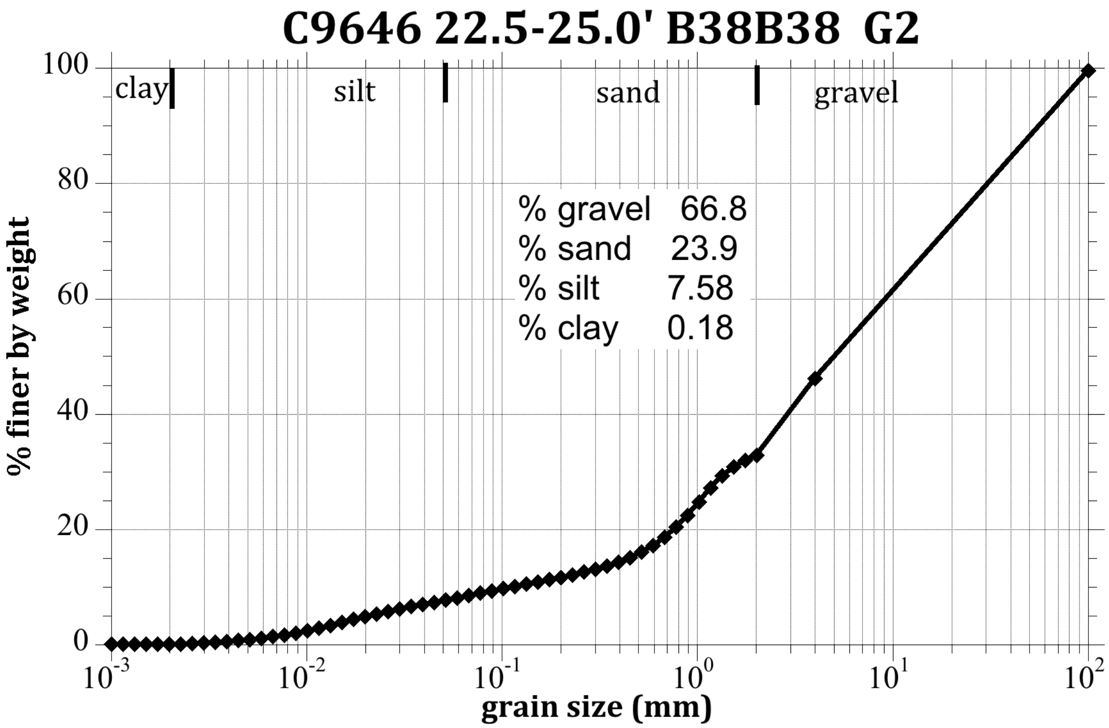
C9646 22.5-25.0' B38B38 G2
100
80
60
40
20
0
% finer by weight
clay
silt
sand
gravel
% gravel 66.8
% sand 23.9
% silt 7.58
% clay 0.18
10^{-3}
10^{-2}
10^{-1}
10^{0}
10^{1}
10^{2}
grain size (mm)

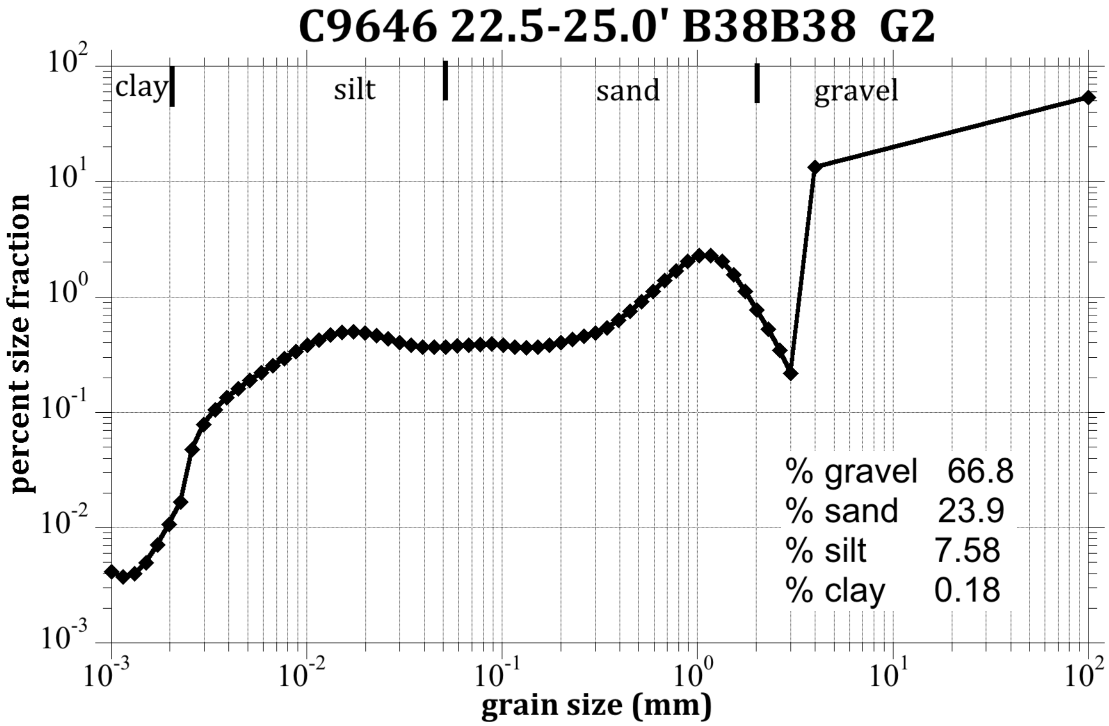
C9646 22.5-25.0' B38B38 G2
10^{2}
10^{1}
10^{0}
10^{-1}
10^{-2}
10^{-3}
percent size fraction
clay
silt
sand
gravel
% gravel 66.8
% sand 23.9
% silt 7.58
% clay 0.18
10^{-3}
10^{-2}
10^{-1}
10^{0}
10^{1}
10^{2}
grain size (mm)

C9731 24.0-26.0' B3P2T2 G101

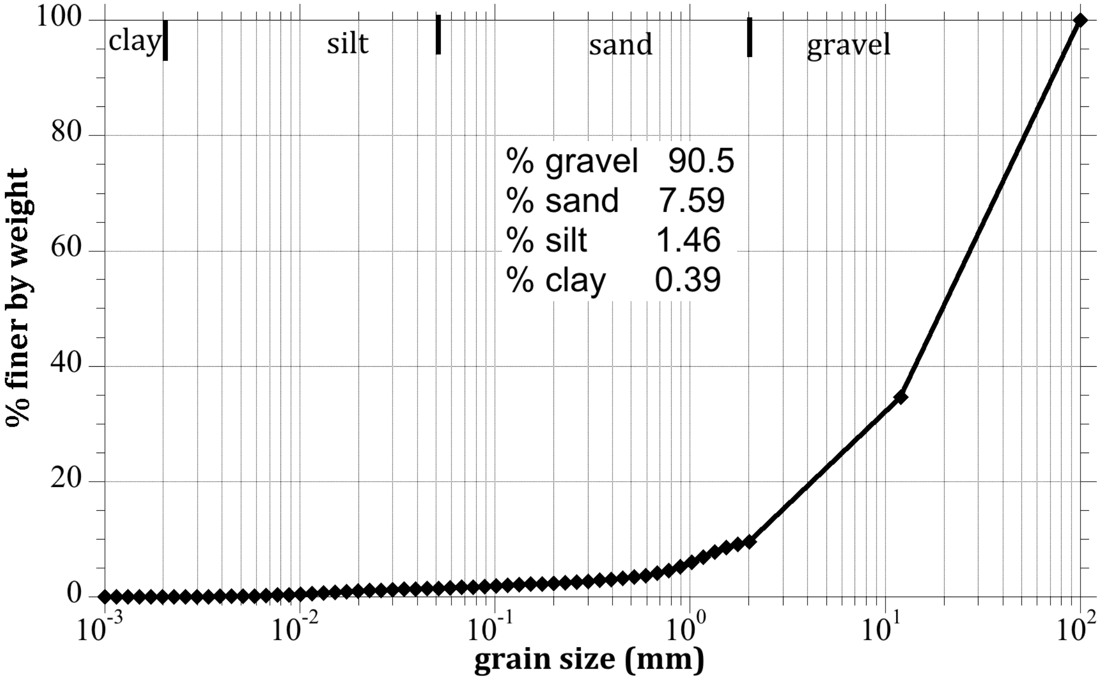

C9731 24.0-26.0' B3P2T2 G101

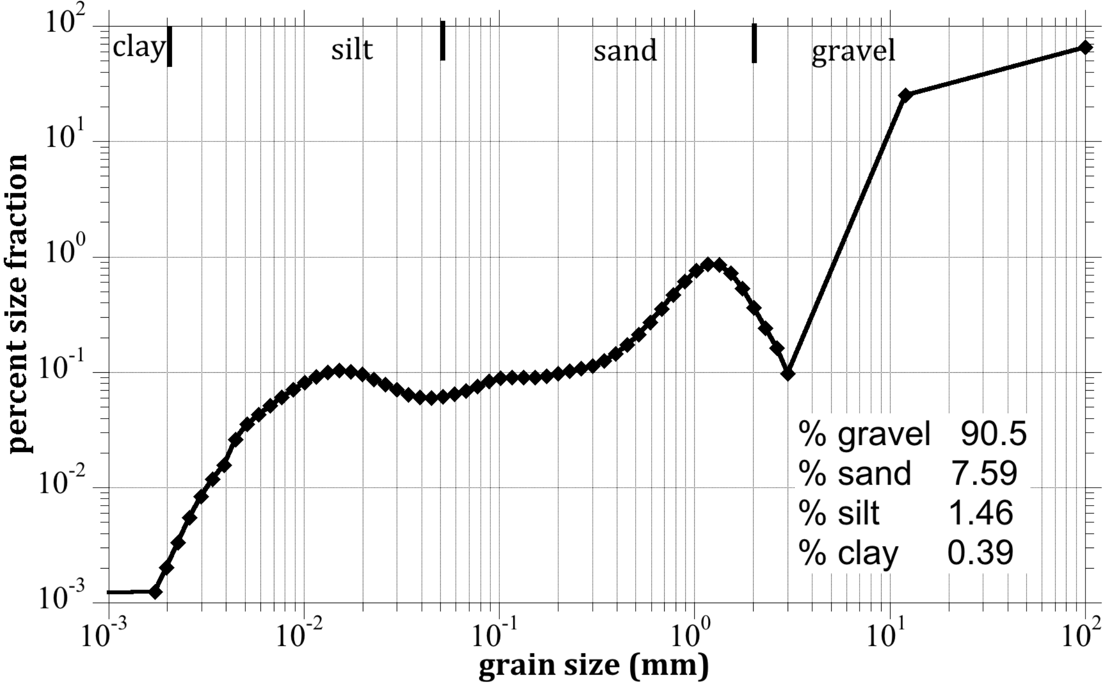

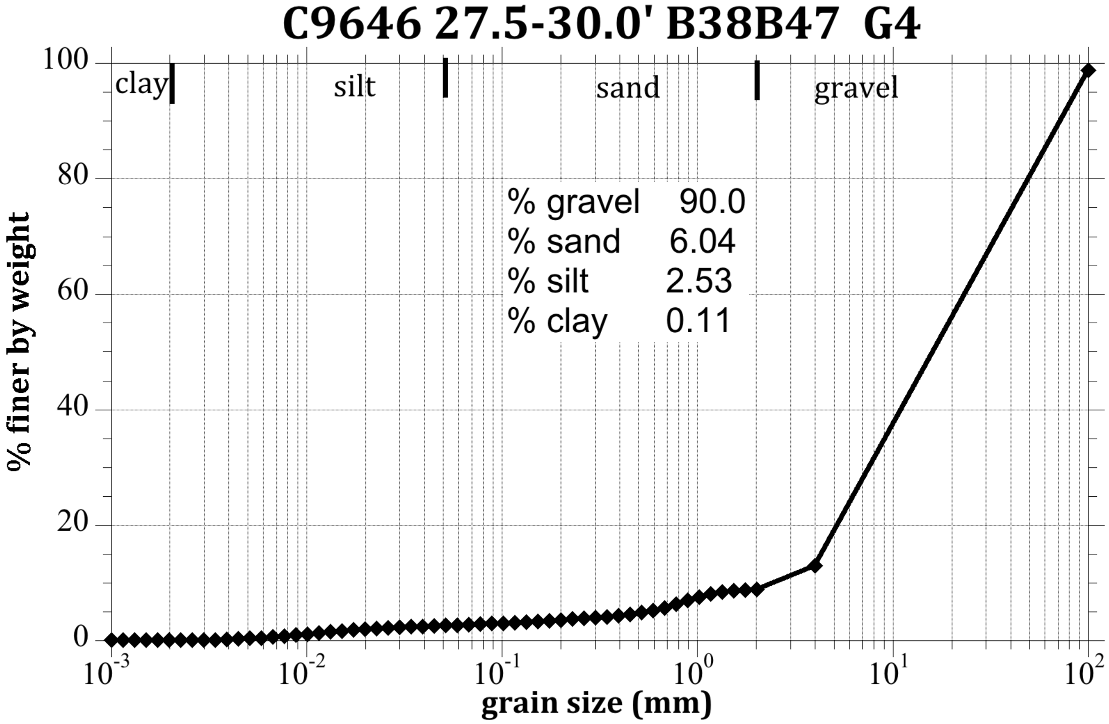
C9646 27.5-30.0' B38B47 G4
% finer by weight
0
20
40
60
80
100
clay
silt
sand
gravel
% gravel 90.0
% sand 6.04
% silt 2.53
% clay 0.11
10^{-3}
10^{-2}
10^{-1}
10^{0}
10^{1}
10^{2}
grain size (mm)

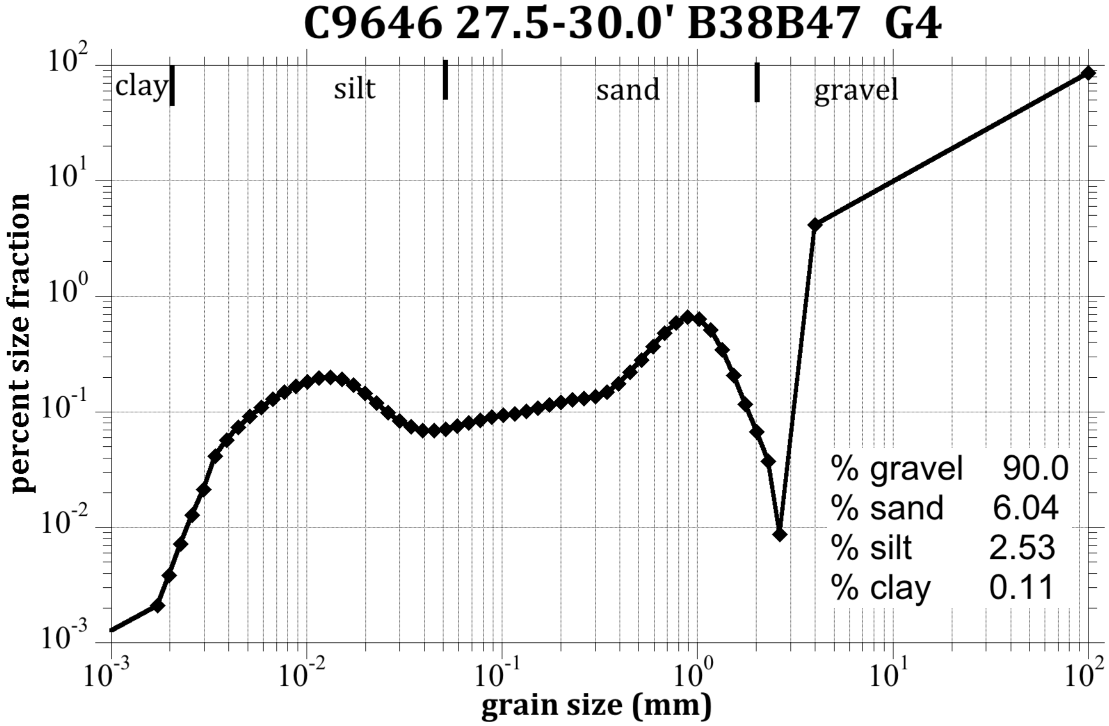
C9646 27.5-30.0' B38B47 G4
percent size fraction
10^{-3}
10^{-2}
10^{-1}
10^{0}
10^{1}
10^{2}
clay
silt
sand
gravel
% gravel 90.0
% sand 6.04
% silt 2.53
% clay 0.11
10^{-3}
10^{-2}
10^{-1}
10^{0}
10^{1}
10^{2}
grain size (mm)

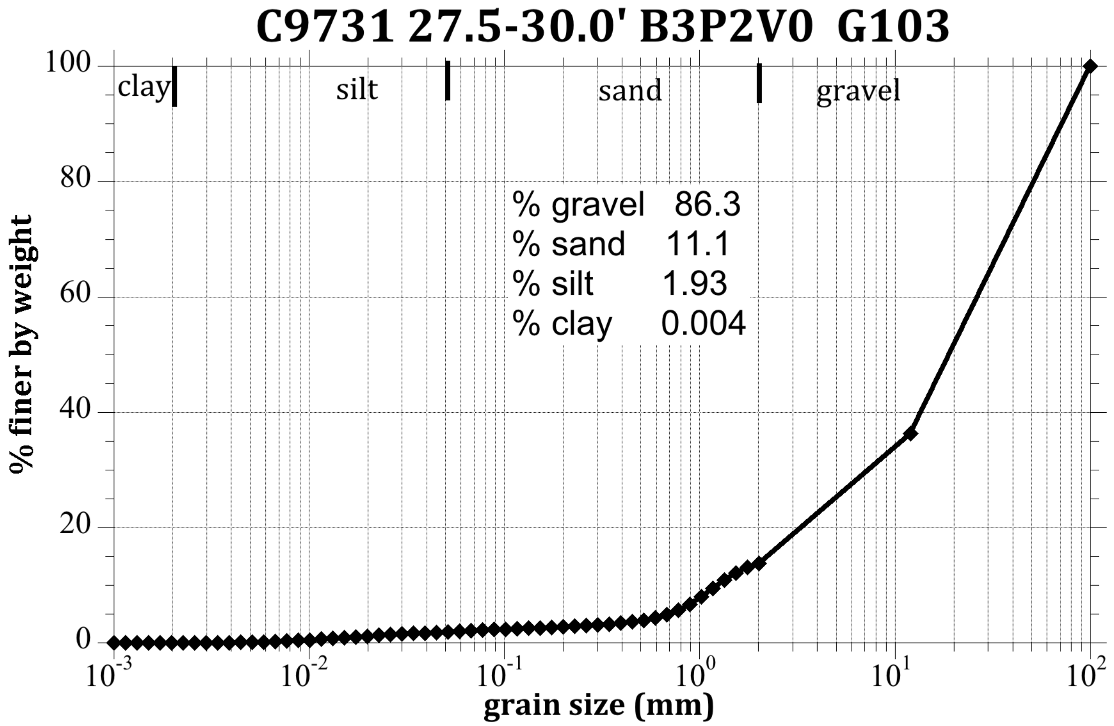
C9731 27.5-30.0' B3P2V0 G103
clay
silt
sand
gravel
% gravel 86.3
% sand 11.1
% silt 1.93
% clay 0.004
% finer by weight
0
20
40
60
80
100
10^{-3}
10^{-2}
10^{-1}
10^{0}
10^{1}
10^{2}
grain size (mm)

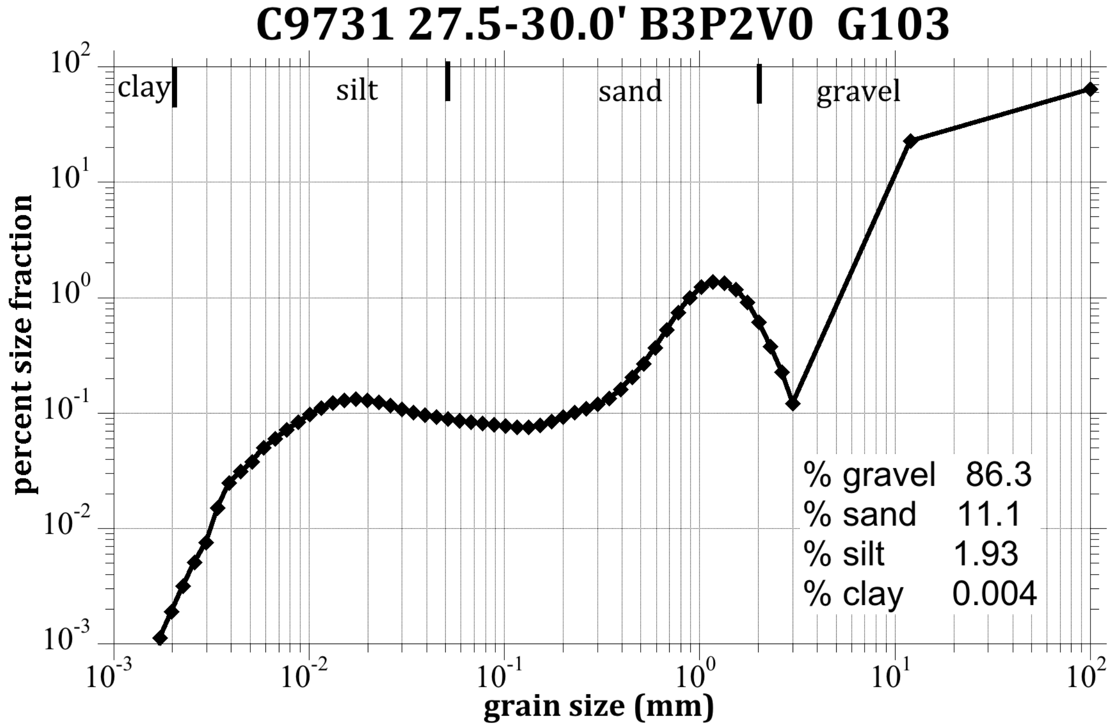
C9731 27.5-30.0' B3P2V0 G103
clay
silt
sand
gravel
% gravel 86.3
% sand 11.1
% silt 1.93
% clay 0.004
percent size fraction
10^{-3}
10^{-2}
10^{-1}
10^{0}
10^{1}
10^{2}
10^{-3}
10^{-2}
10^{-1}
10^{0}
10^{1}
10^{2}
grain size (mm)

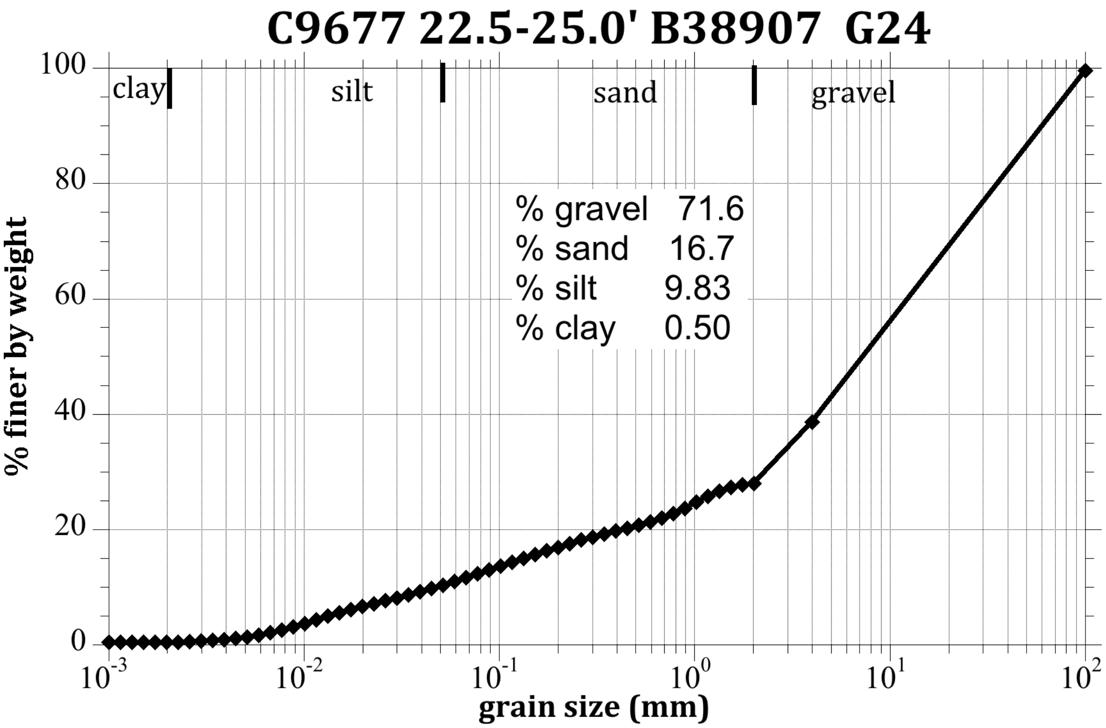
C9677 22.5-25.0' B38907 G24
% finer by weight
grain size (mm)
clay
silt
sand
gravel
% gravel 71.6
% sand 16.7
% silt 9.83
% clay 0.50
0
20
40
60
80
100
10^{-3}
10^{-2}
10^{-1}
10^{0}
10^{1}
10^{2}

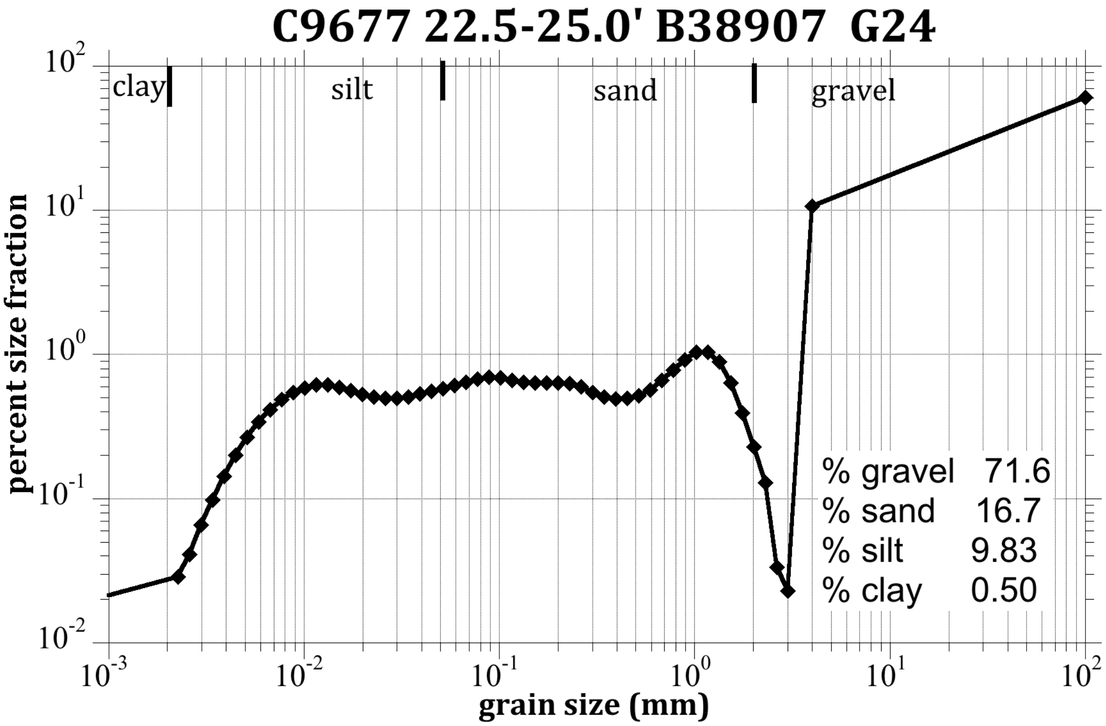
C9677 22.5-25.0' B38907 G24
percent size fraction
grain size (mm)
clay
silt
sand
gravel
% gravel 71.6
% sand 16.7
% silt 9.83
% clay 0.50
10^{-2}
10^{-1}
10^{0}
10^{1}
10^{2}
10^{-3}
10^{-2}
10^{-1}
10^{0}
10^{1}
10^{2}

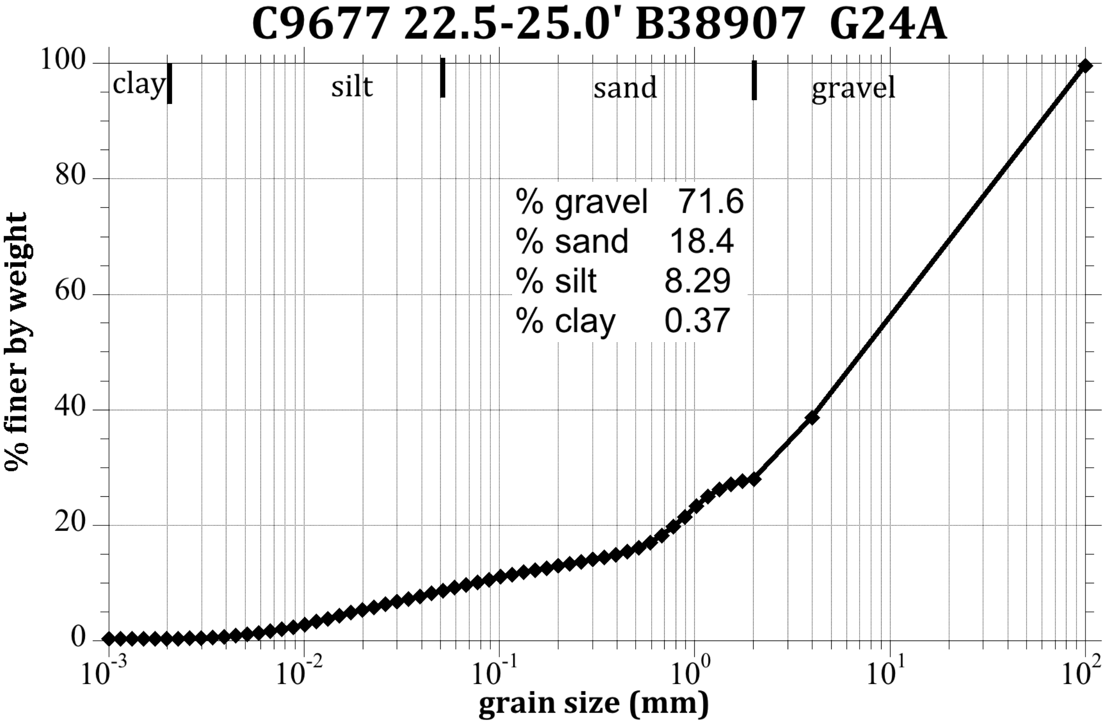
C9677 22.5-25.0' B38907 G24A
% finer by weight
grain size (mm)
clay
silt
sand
gravel
% gravel 71.6
% sand 18.4
% silt 8.29
% clay 0.37
0
20
40
60
80
100
10-3
10-2
10-1
100
101
102

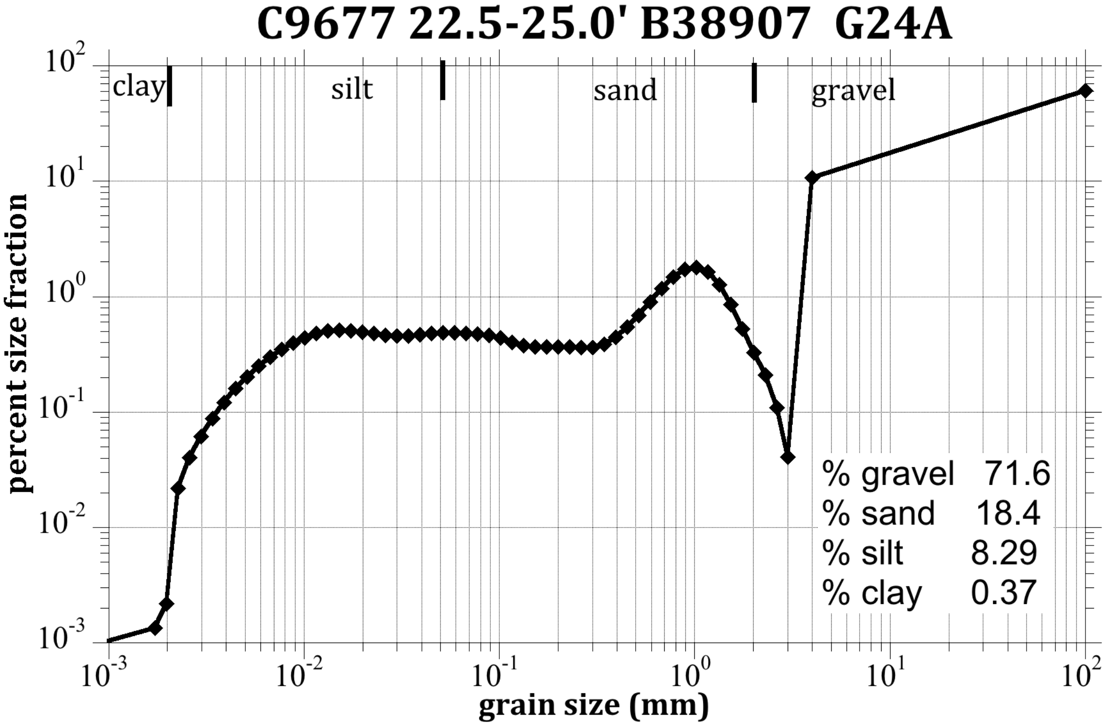
C9677 22.5-25.0' B38907 G24A
percent size fraction
grain size (mm)
clay
silt
sand
gravel
% gravel 71.6
% sand 18.4
% silt 8.29
% clay 0.37
10-3
10-2
10-1
100
101
102

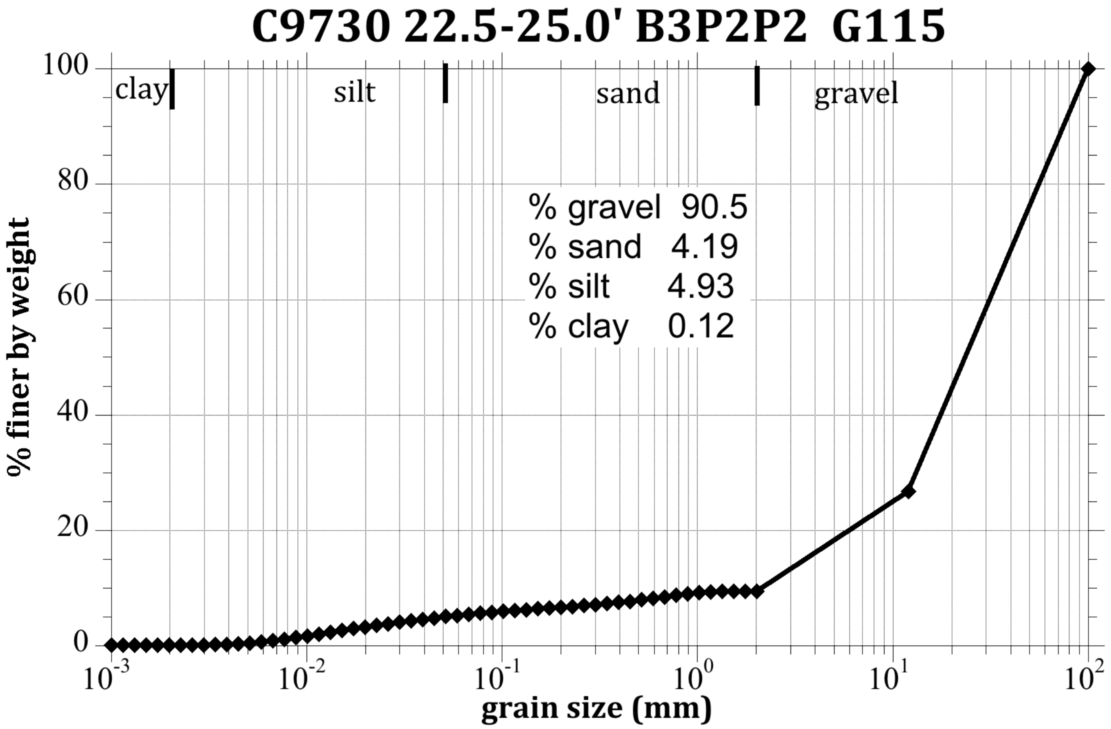
C9730 22.5-25.0' B3P2P2 G115
clay
silt
sand
gravel
% gravel 90.5
% sand 4.19
% silt 4.93
% clay 0.12
% finer by weight
0
20
40
60
80
100
10^{-3}
10^{-2}
10^{-1}
10^{0}
10^{1}
10^{2}
grain size (mm)

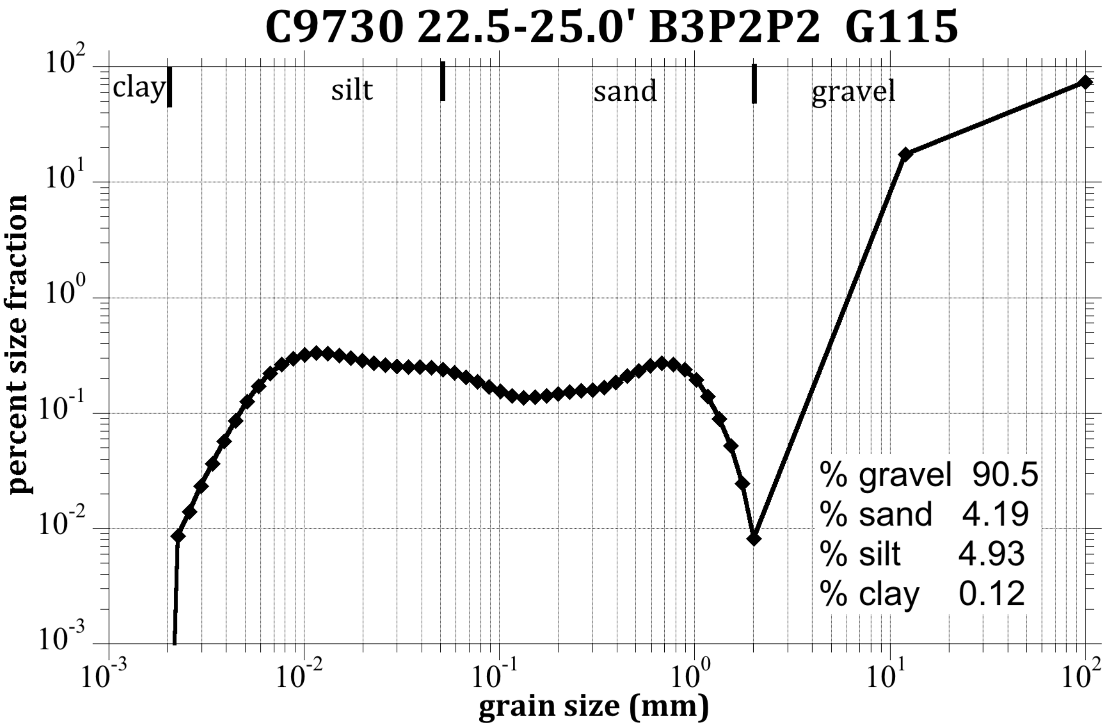
C9730 22.5-25.0' B3P2P2 G115
clay
silt
sand
gravel
% gravel 90.5
% sand 4.19
% silt 4.93
% clay 0.12
percent size fraction
10^{-3}
10^{-2}
10^{-1}
10^{0}
10^{1}
10^{2}
10^{-3}
10^{-2}
10^{-1}
10^{0}
10^{1}
10^{2}
grain size (mm)

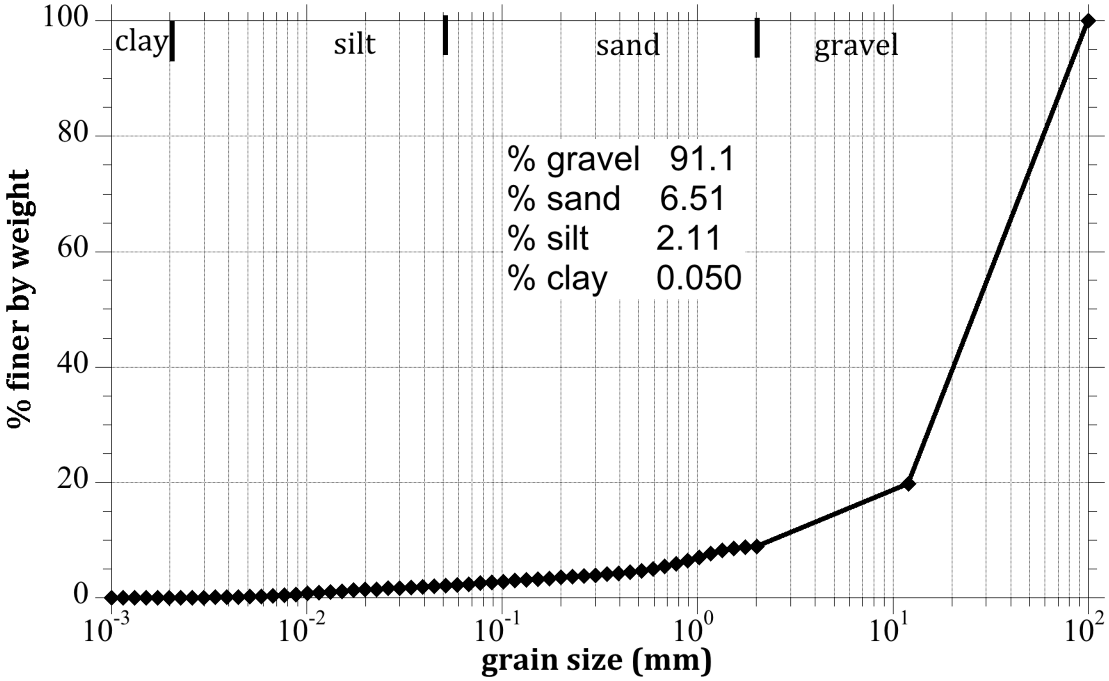

C9734 27.6-30.0' B3P320 G127

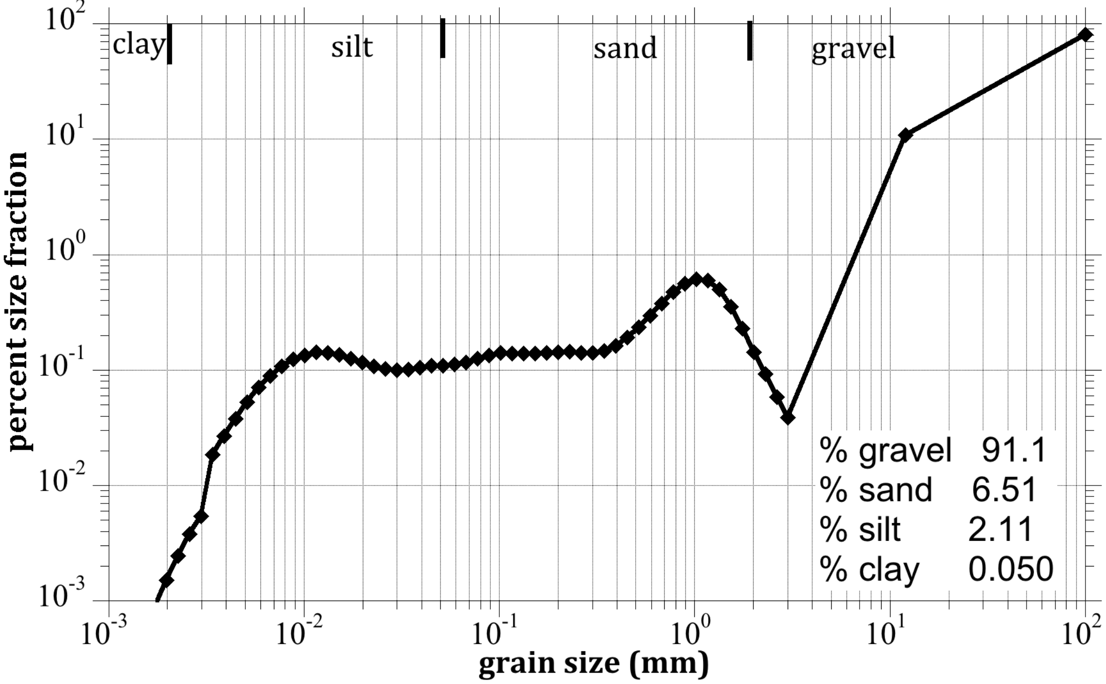

C9734 27.6-30.0' B3P320 G127

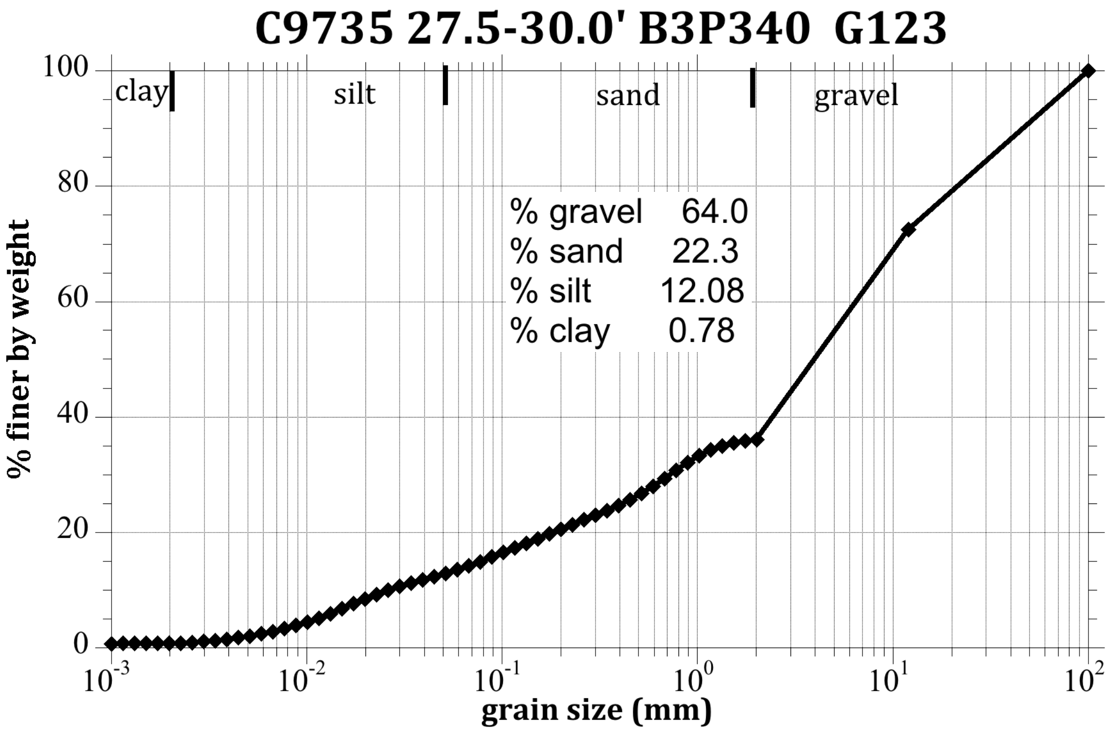
C9735 27.5-30.0' B3P340 G123
100
80
60
40
20
0
% finer by weight
clay
silt
sand
gravel
% gravel 64.0
% sand 22.3
% silt 12.08
% clay 0.78
10^{-3}
10^{-2}
10^{-1}
10^{0}
10^{1}
10^{2}
grain size (mm)

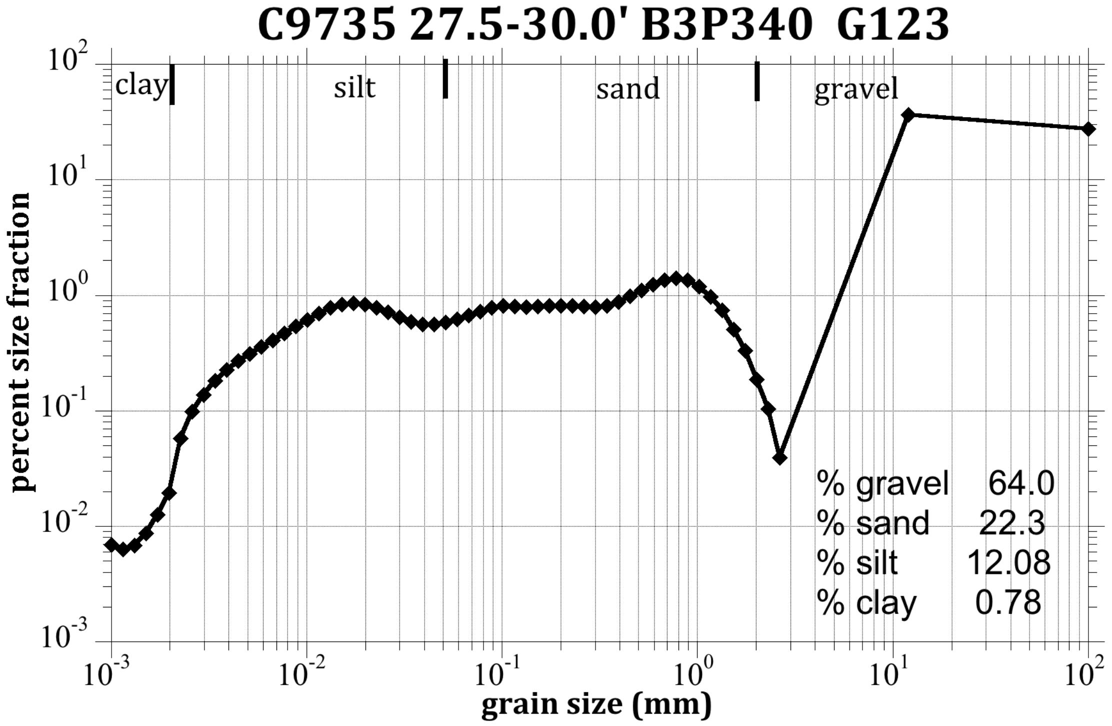
C9735 27.5-30.0' B3P340 G123
10^{2}
10^{1}
10^{0}
10^{-1}
10^{-2}
10^{-3}
percent size fraction
clay
silt
sand
gravel
% gravel 64.0
% sand 22.3
% silt 12.08
% clay 0.78
10^{-3}
10^{-2}
10^{-1}
10^{0}
10^{1}
10^{2}
grain size (mm)

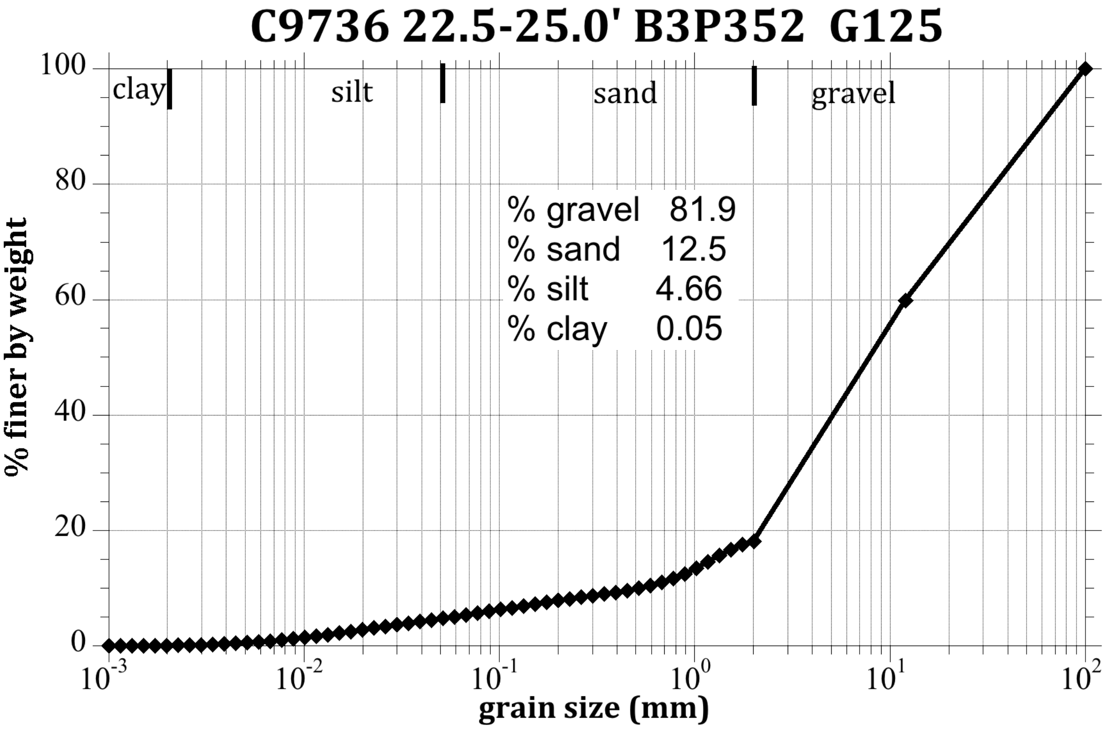
C9736 22.5-25.0' B3P352 G125
% finer by weight
grain size (mm)
clay
silt
sand
gravel
% gravel 81.9
% sand 12.5
% silt 4.66
% clay 0.05
0
20
40
60
80
100
10^-3
10^-2
10^-1
10^0
10^1
10^2

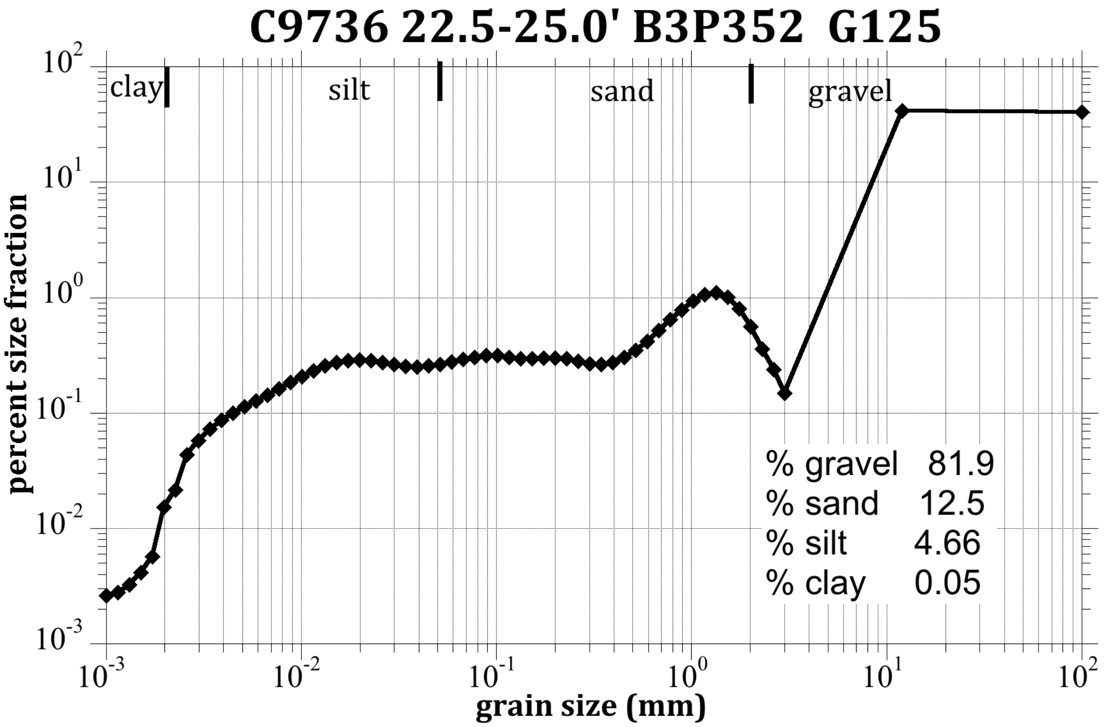
C9736 22.5-25.0' B3P352 G125
percent size fraction
grain size (mm)
clay
silt
sand
gravel
% gravel 81.9
% sand 12.5
% silt 4.66
% clay 0.05
10^-3
10^-2
10^-1
10^0
10^1
10^2
10^-3
10^-2
10^-1
10^0
10^1
10^2

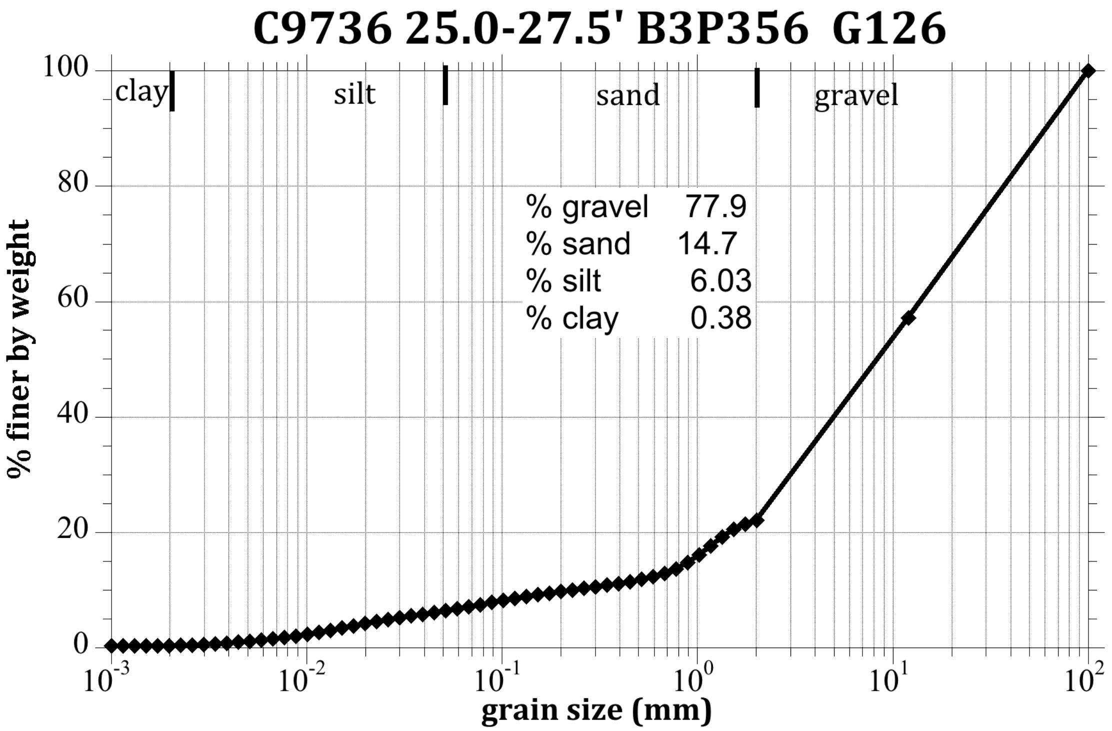
C9736 25.0-27.5' B3P356 G126
clay
silt
sand
gravel
% gravel 77.9
% sand 14.7
% silt 6.03
% clay 0.38
% finer by weight
100
80
60
40
20
0
10^{-3}
10^{-2}
10^{-1}
10^{0}
10^{1}
10^{2}
grain size (mm)

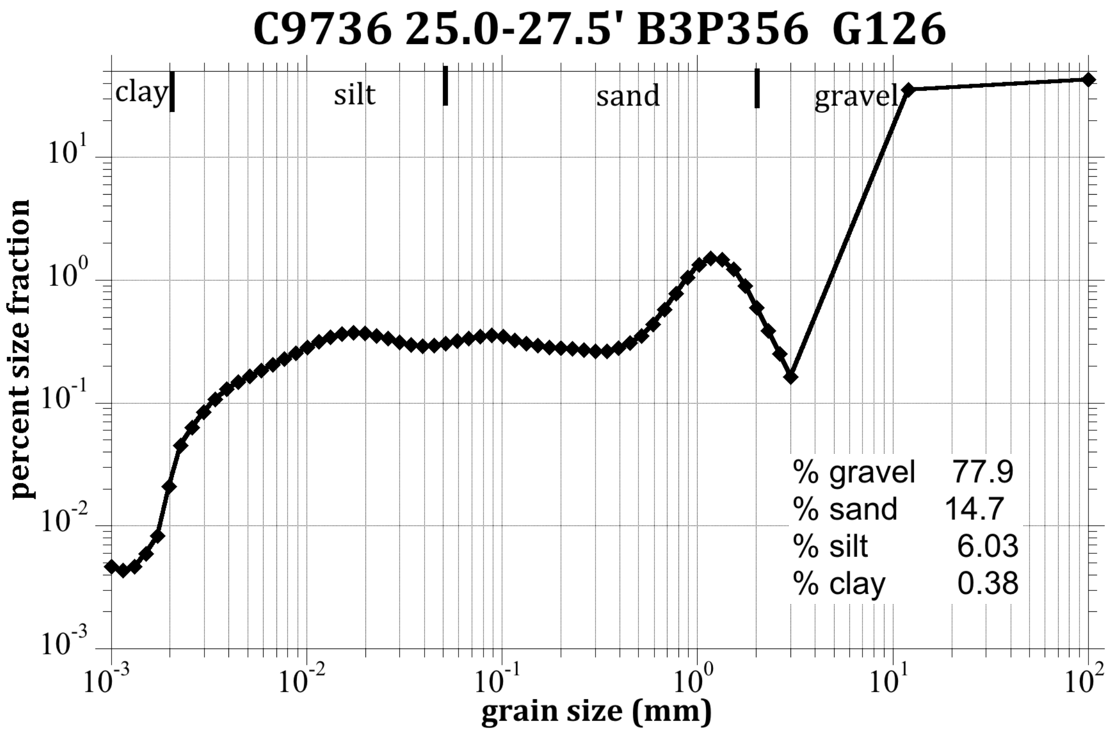
C9736 25.0-27.5' B3P356 G126
clay
silt
sand
gravel
% gravel 77.9
% sand 14.7
% silt 6.03
% clay 0.38
percent size fraction
10^{1}
10^{0}
10^{-1}
10^{-2}
10^{-3}
10^{-3}
10^{-2}
10^{-1}
10^{0}
10^{1}
10^{2}
grain size (mm)

Appendix C – 1-D Column Physical and Transport Parameters

Table C.1. 1-D Leach Column Parameters

PNNL #	Borehole	Start Depth (ft)	End Depth (ft)	HEIS #	Column Diameter (cm)	Column Length (cm)	Dry Bulk Density (g/cm^3)	Porosity (cm^3/cm^3)	Dry Sed. (g)	Pore Volume (mL)	Flow Rate (mL/min)	Residence Time (h/pore vol)	Bromide Rf
G29	C9683	22.5	25	B389J7	2.36	30.48	1.631	0.460	217.46	61.27	0.435	2.35	0.832
G118	C9732	22.5	25	B3P2W2	2.36	30.48	1.513	0.493	201.68	65.74	0.450	2.43	0.801
G20	C9673	27.5	30	B388X3	2.36	30.48	1.674	0.429	223.13	57.19	0.486	1.96	0.984
G112	C9728	27.5	30	B3P2L0	2.36	30.48	1.660	0.380	221.33	50.62	0.393	2.14	0.875
G21	C9673	30	32.5	B388X6	2.36	30.48	1.765	0.351	235.36	46.84	0.380	2.05	0.881
G113	C9728	30	32.5	B3P2L4	2.36	30.48	1.731	0.351	230.83	46.78	0.439	1.78	0.813
G14	C9667	25	27.5	B388NO	2.36	30.48	1.648	0.482	219.73	64.28	0.431	2.48	0.828
G108	C9729	25	27.5	B3P2M6	2.36	30.48	1.776	0.326	236.74	43.43	0.479	1.51	0.938
G16	C9667	30	32.5	B388N9	2.36	30.48	1.663	0.430	221.67	57.33	0.445	2.15	0.812
G110	C9729	30	32.5	B3P2N4	2.36	30.48	1.833	0.379	244.46	50.49	0.458	1.84	0.891
G7	C9647	22.5	25	B38B71	2.36	30.48	1.687	0.469	224.98	62.51	0.420	2.48	0.922
G105	C9733	22.5	25	B3P2Y2	2.36	30.48	1.646	0.447	219.52	59.64	0.432	2.30	0.890
G105A	C9733	22.5	25	B3P2Y2	2.36	30.48	1.630	0.402	217.31	53.66	0.474	1.89	0.781
G9	C9647	27.5	30	B38B77	2.36	30.48	1.707	0.438	227.54	58.33	0.480	2.02	0.850
G106	C9733	27.5	30	B3P300	2.36	30.48	1.617	0.419	215.62	55.90	0.317	2.94	1.125
G2	C9646	22.5	25	B38B38	2.36	30.48	1.695	0.446	226.01	59.44	0.475	2.08	0.890
G101	C9731	22.5	25	B3P2T2	2.36	30.48	1.636	0.471	218.16	62.84	0.451	2.32	0.725
G4	C9646	27.5	30	B38B47	2.36	30.48	1.131	0.503	150.84	67.07	0.460	2.43	0.734
G103	C9731	27.5	30	B3P2VO	2.36	30.48	1.761	0.359	234.77	47.86	0.487	1.64	0.843
G24	C9677	22.5	25	B38907	2.36	30.48	1.687	0.414	224.96	55.19	0.456	2.02	0.788
G24A dup	C9647	27.5	30	B38B77	2.36	30.48	1.695	0.363	225.99	48.43	0.474	1.70	0.887
G115	C9730	22.5	25	B3P2P2	2.36	30.48	1.592	0.353	212.267	47.09	0.483	1.62	0.875
G127	C9734	27.5	30	B3P320	2.36	30.48	1.570	0.449	209.35	59.90	0.488	2.04	0.797
G123	C9735	27.5	30	B3P340	2.36	30.48	1.768	0.331	235.76	44.18	0.473	1.56	0.902
G125	C9736	22.5	25	B3P352	2.36	30.48	1.823	0.268	243.02	35.74	0.483	1.22	1.127
G126	C9736	25	27.5	B3P356	2.36	30.48	1.878	0.328	250.41	43.66	0.459	1.59	1.078
						Average:	1.670	0.405	222.649	54.054	0.450	2.021	0.880
						Std dev:	0.138	0.061	18.430	8.127	0.039	0.386	0.104
						Maximum:	1.878	0.503	250.410	67.070	0.488	2.940	1.127
						Minimum:	1.131	0.268	150.840	35.740	0.317	1.220	0.725
						Skewness:	-2.314	-0.309	-2.311	-0.308	-1.891	0.148	1.107

Table C.2. 1-D Leach Experiment Stop Flow Calculated Release Rate and Measured Leached Mass.

						--------- at 1.9 pv ---------		--------- at 9.4 pv ---------		--------- at 92 pv ---------	
PNNL #	Borehole	Start Depth (ft)	End Depth (ft)	HEIS #	Pair	Release Rate (µg/kg/day)	Leached Mass (µg/g)	Release Rate (µg/kg/day)	Leached Mass (µg/g)	Release Rate (µg/kg/day)	Leached Mass (µg/g)
G29	C9683	22.5	25.0	B389J7	w/G118	-1.72E+01	0.4508	1.53E+00	0.4967	4.09E-01	0.6722
G118	C9732	22.5	25.0	B3P2W2	w/G29	-3.81E-03	0.0008	0.00E+00	0.0009	-3.13E-02	0.0229
G20	C9673	27.5	30.0	B388X3	w/G112	1.48E+00	0.0366	1.22E+00	0.0753	6.05E-01	1.023
G112	C9728	27.5	30.0	B3P2L0	w/G20	1.34E-01	0.0071	-4.19E-02	0.0179	8.67E-03	0.1123
G21	C9673	30	32.5	B388X6	w/G113	1.89E+02	2.661	5.60E+01	3.979	2.19E-01	8.659
G113	C9728	30	32.5	B3P2L4	w/G21	-2.87E-02	0.0075	-1.89E-02	0.0219	1.74E-02	0.1675
G14	C9667	25	27.5	B388NO	w/G108	2.50E+02	2.225	1.07E+02	6.171	1.47E+01	15.38
G108	C9729	25	27.5	B3P2M6	w/G14	5.14E+00	0.0457	1.49E+00	0.1425	4.39E-01	0.7611
G16	C9667	30	32.5	B388N9	w/G110	1.58E+00	0.0182	5.77E-01	0.0391	4.20E-01	0.2298
G110	C9729	30	32.5	B3P2N4	w/G16	6.80E+00	0.0916	2.52E+00	0.1707	1.12E+00	0.6108
G7	C9647	22.5	25.0	B38B71	w/G105	2.68E+02	1.380	9.24E+01	2.794	1.13E+01	6.075
G105	C9733	22.5	25.0	B3P2Y2	w/G7	4.11E-01	0.0003	0.00E+00	0.0006	2.06E-01	0.0243
G105A	C9733	22.5	25.0	B3P2Y2	w/G7	0.00E+00	0.0007	1.02E+00	0.0018	4.11E-01	0.0696
G9	C9647	27.5	30.0	B38B77	w/G106	1.59E+00	0.0432	4.19E-01	0.0587	6.22E-01	0.6248
G106	C9733	27.5	30.0	B3P300	w/G9	5.42E-01	0.0009	4.63E-01	0.0033	1.30E-01	0.0212
G2	C9646	22.5	25.0	B38B38	w/G101	7.20E+02	5.129	2.58E+02	11.25	1.98E+01	21.06
G101	C9731	22.5	25.0	B3P2T2	w/G2	3.48E-01	0.0061	2.18E+00	0.035	3.38E-01	0.2359
G4	C9646	27.5	30.0	B38B47	w/G103	7.11E+00	0.1075	2.51E+00	0.1947	8.77E-01	0.9656
G103	C9731	27.5	30.0	B3P2VO	w/G4	0.00E+00	0.0007	0.00E+00	0.0007	1.22E-02	0.0389
G24	C9677	22.5	25.0	B38907	w/G115	2.71E+02	2.868	9.16E+01	5.421	8.44E+00	10.96
G24A dup	C9677	22.5	30.0	B38B77	w/G115	2.36E+02	3.469	9.95E+01	6.057	8.74E+00	10.94
G115	C9730	22.5	25.0	B3P2P2	w/G24	1.28E+00	0.0122	1.59E+00	0.0654	1.10E-01	1.077
G127	C9734	27.5	30.0	B3P320	no pair	6.42E-01	0.0035	3.67E-01	0.0057	4.22E-02	0.0474
G123	C9735	27.5	30.0	B3P340	no pair	3.84E-01	0.0061	3.74E-01	0.0075	4.84E-03	0.0399
G125	C9736	22.5	25.0	B3P352	no pair	2.24E-01	0.0028	2.36E-02	0.0054	-2.13E-03	0.0135
G126	C9736	25	27.5	B3P356	no pair	1.06E+01	0.5184	8.57E+00	0.7167	9.84E-01	1.260

Appendix D – 1-D Leach Experiment Br, PO4, SpC, and pH Data

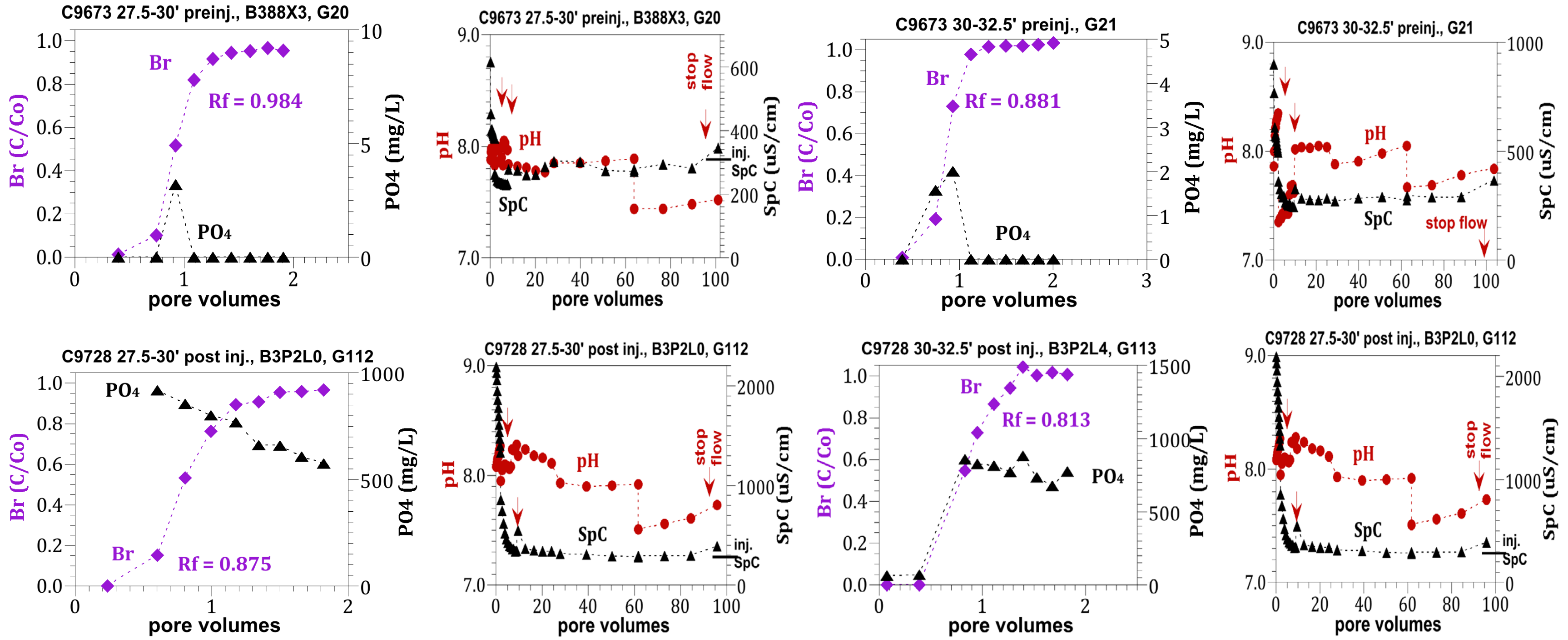

Figure D.1. Pre-and post-injection 1-D column experiment results for sediments in the southwest portion of Stage B injections showing Br, PO$_4$, SpC, and pH breakthrough. Pre-/post-injection pairs are C9673 (pre) and C9728 (post).

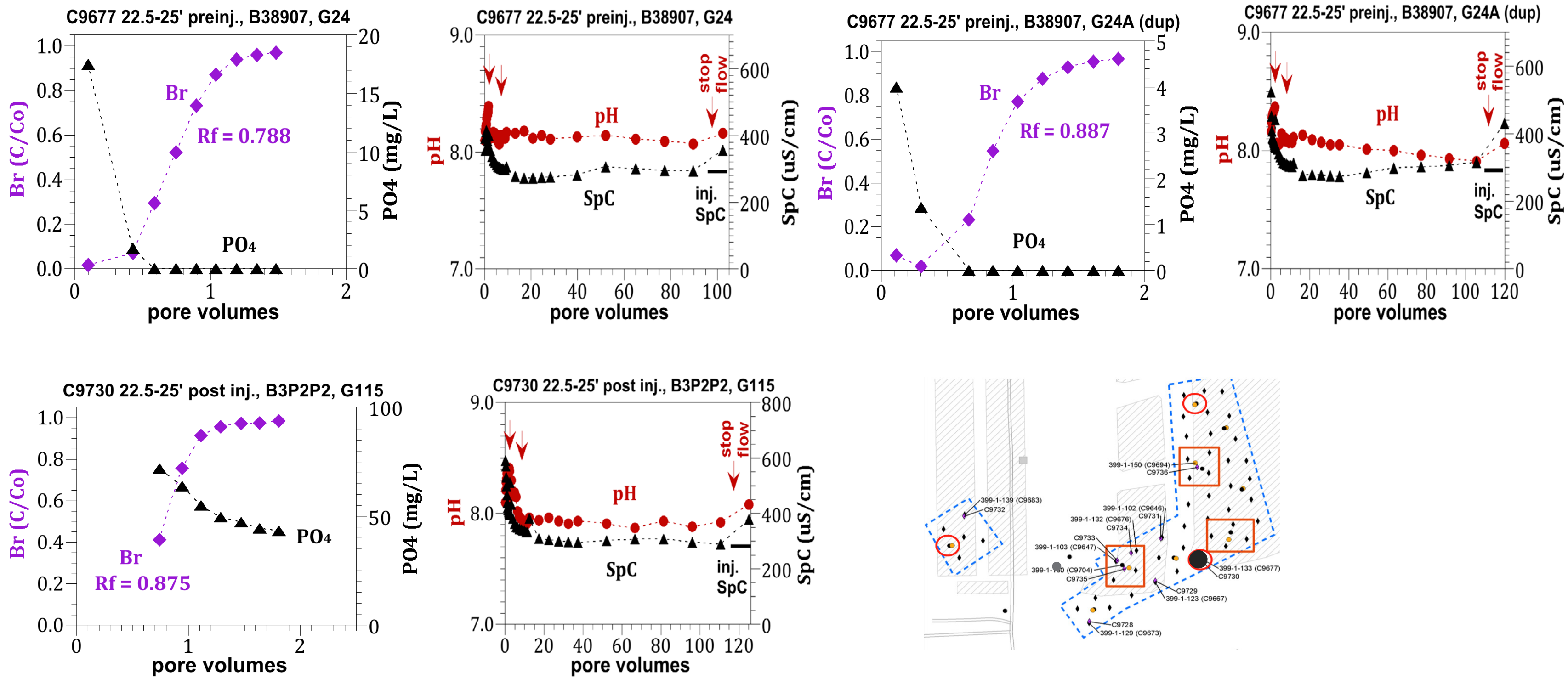

Figure D.2. Pre-and post-injection 1-D column experiment results for sediments in the south central portion of Stage B injections showing Br, PO4, SpC, and pH breakthrough. Pre-/post-injection pairs are C9677 (pre, duplicate experiments) and C97230 (post).

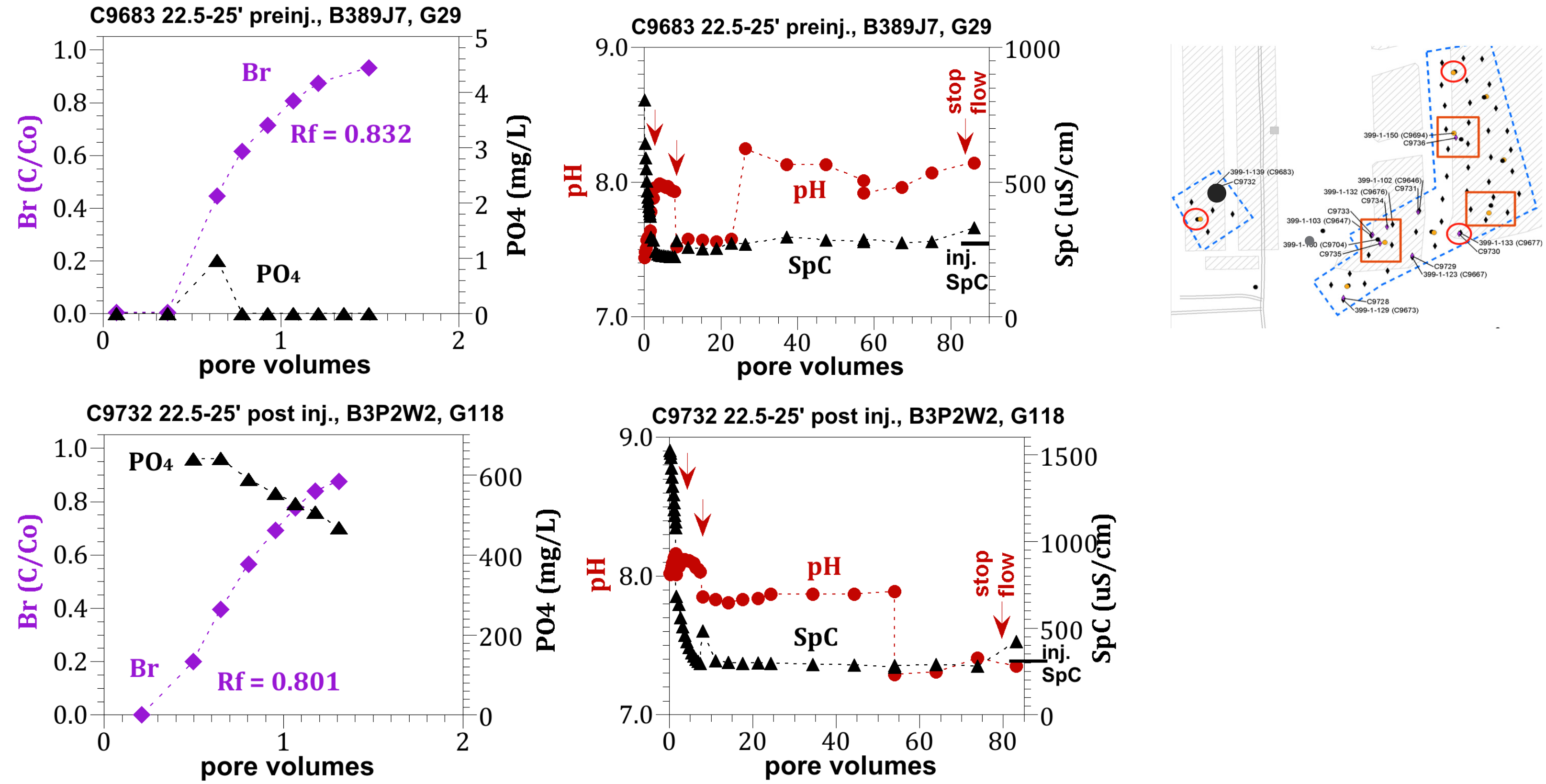

Figure D.3. Pre-and post-injection 1-D column experiment results for sediments in the west portion of Stage B injections (see map) showing Br, PO4, SpC, and pH breakthrough. Pre-/post-injection pairs are C9683 (pre, duplicate experiments) and C97232 (post).

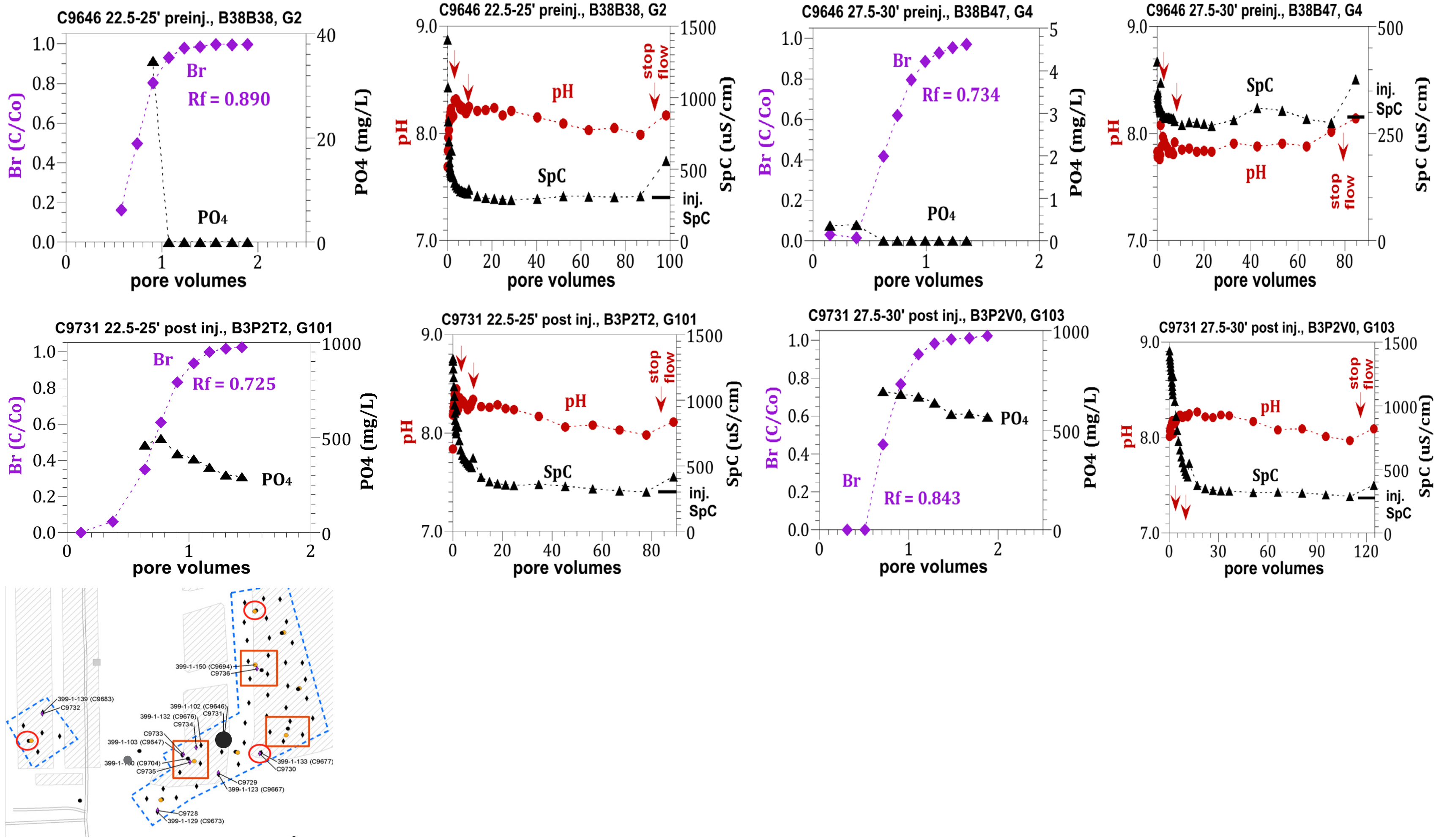

Figure D.4. Pre-and post-injection 1-D column experiment results for sediments in the central portion of Stage B injections (see map) showing Br, PO4, SpC, and pH breakthrough. Pre-/post-injection pairs are C9646 (pre, duplicate experiments) and C97231 (post).

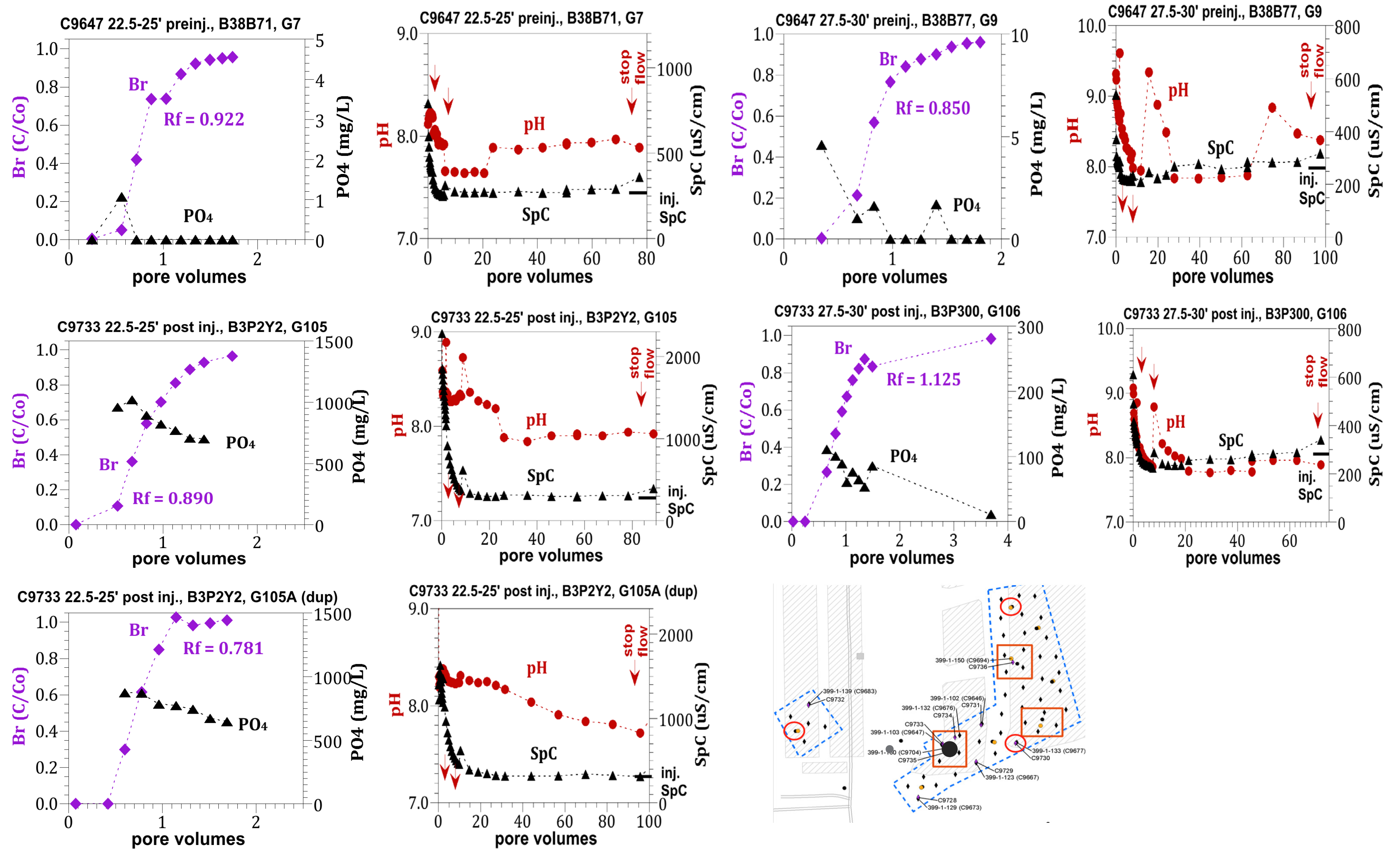

Figure D.5. Pre-and post-injection 1-D column experiment results for sediments in the southwest portion of Stage B injections (see map) showing Br, PO4, SpC, and pH breakthrough. Pre-/post-injection pairs are C9647 (pre, duplicate experiments) and C9733 (post).

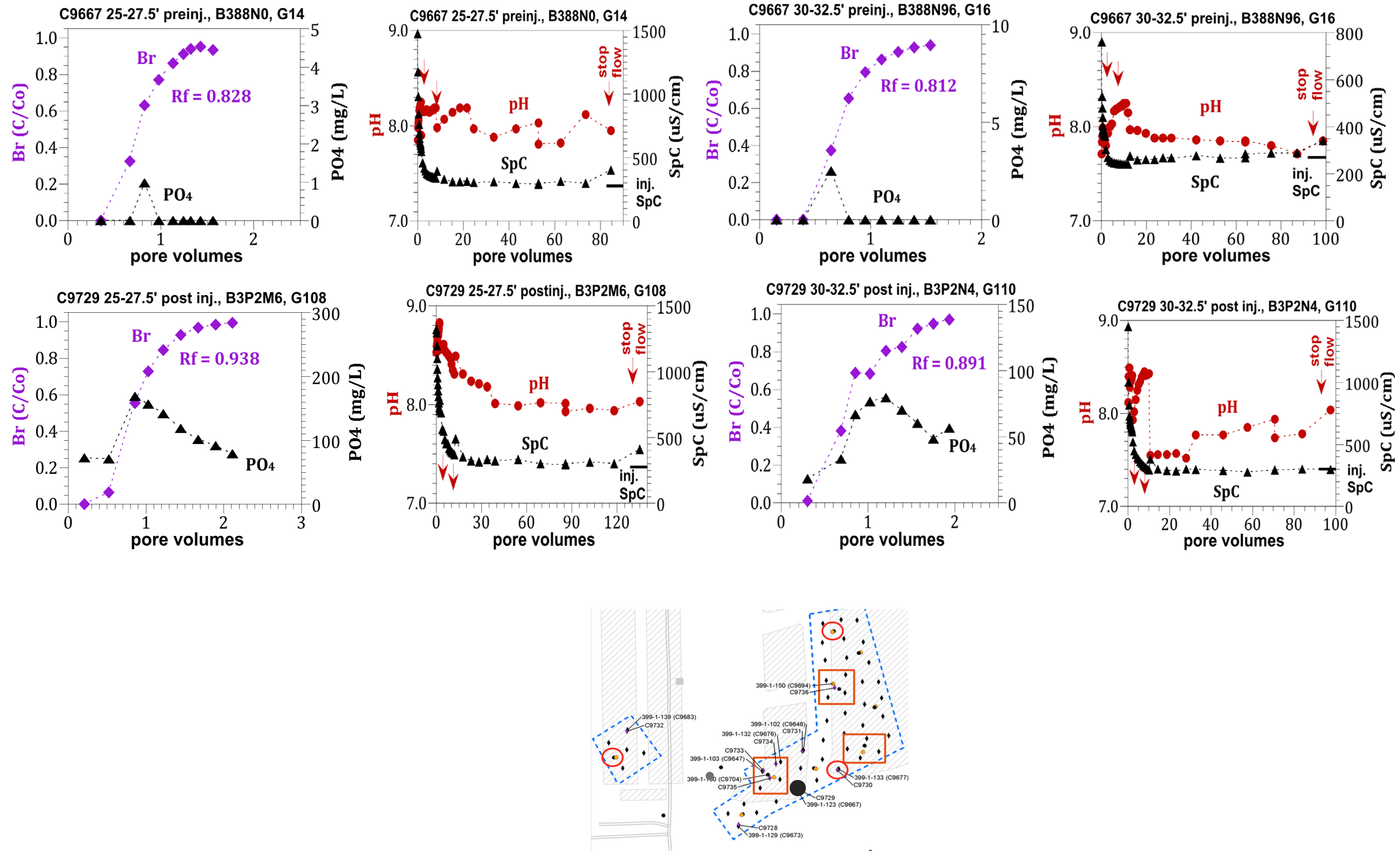

Figure D.6. Pre-and post-injection 1-D column experiment results for sediments in the south portion of Stage B injections (see map) showing Br, PO4, SpC, and pH breakthrough. Pre-/post-injection pairs are C9667 (pre, duplicate experiments) and C9729 (post).

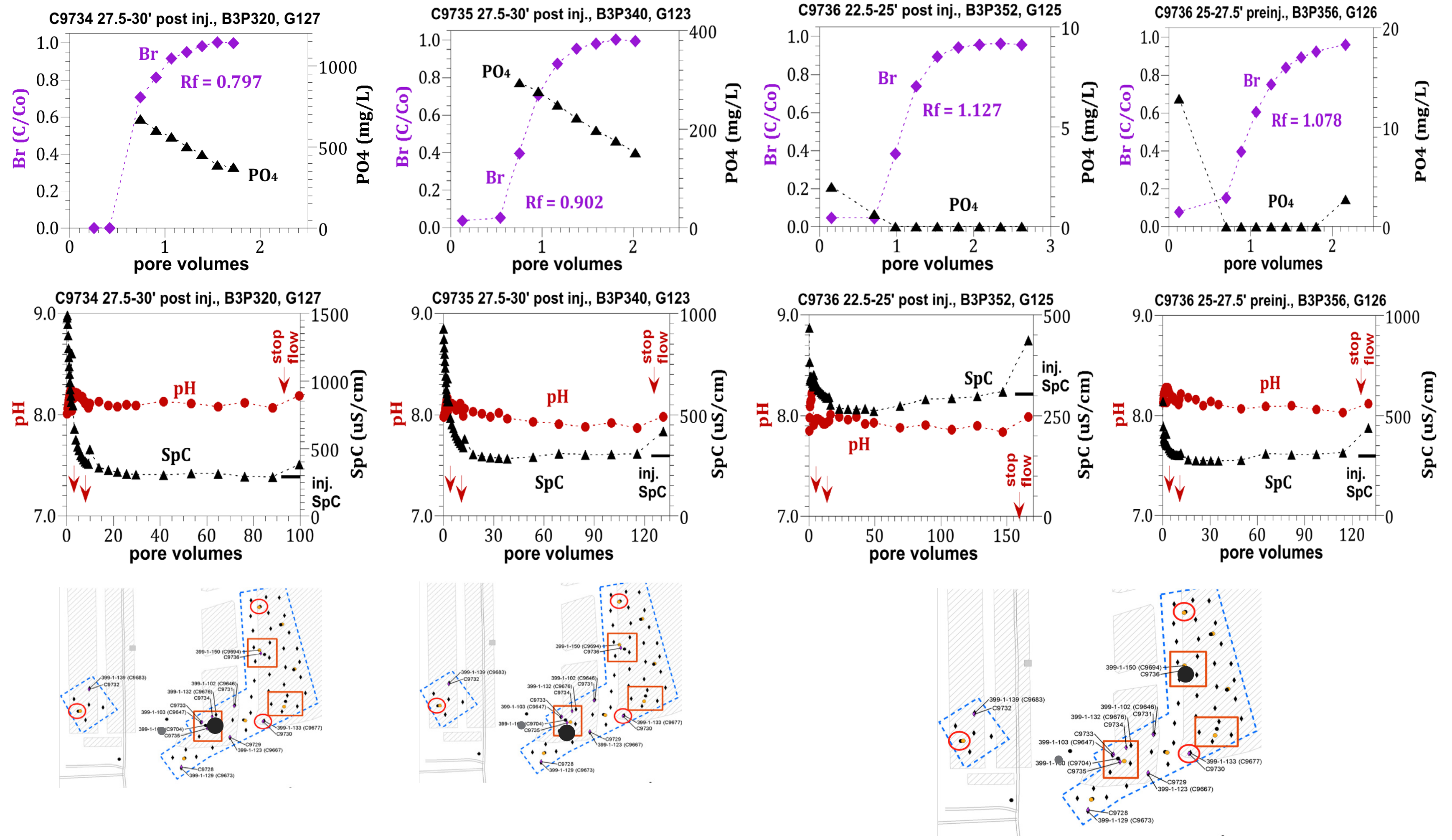

Figure D.7. Post-injection 1-D column experiment results for sediments in Stage B injections (see map) showing Br, PO4, SpC, and pH breakthrough. Post-injection boreholes C9734 and C9735 are near pre-injection borehole C9647. Post-injection borehole C9736 is near pre-injection borehole C9694.

Appendix E – Uranium Solid Phase Characterization

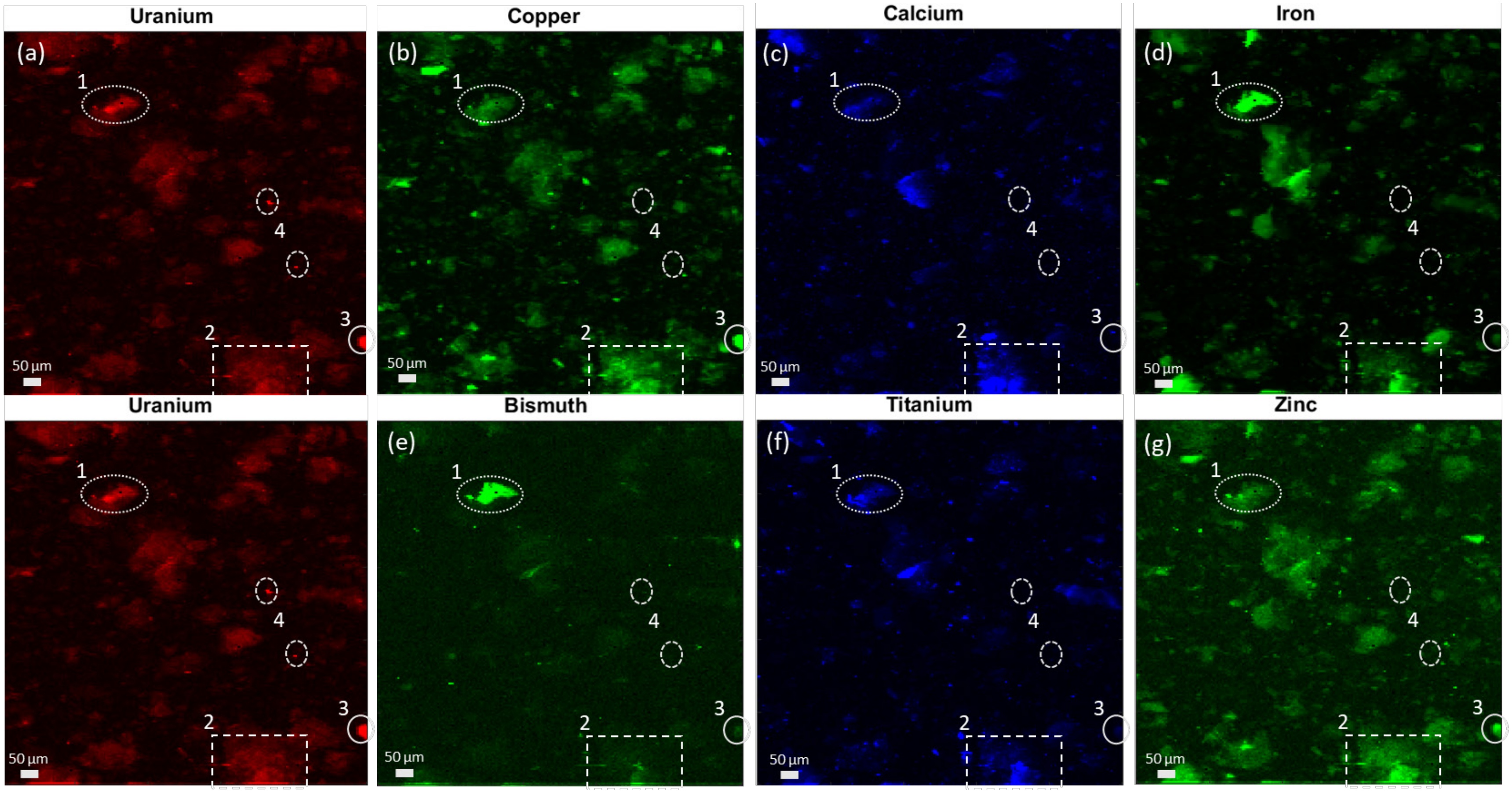

Figure E.1. µ-XRF elemental spectra of sample G3_pt2.001 for (a) uranium, (b) copper, (c) calcium, (d) iron, (e) bismuth, (f) titanium, (g) zinc. Areas of interest are highlighted with shapes 1-4. Circle 1 shows an area with high uranium that is collocated with all the elements shown (i.e., copper, calcium, iron, bismuth, titanium, and zinc). Square 2 also shows higher uranium present which is collocated with all the shown elements again but more strongly correlated with copper, calcium and zinc. Circle 3 shows a smaller uranium particle which also correlates with high copper and zinc. Circles 4 show two small uranium particles that do not correspond with any of the shown elements.

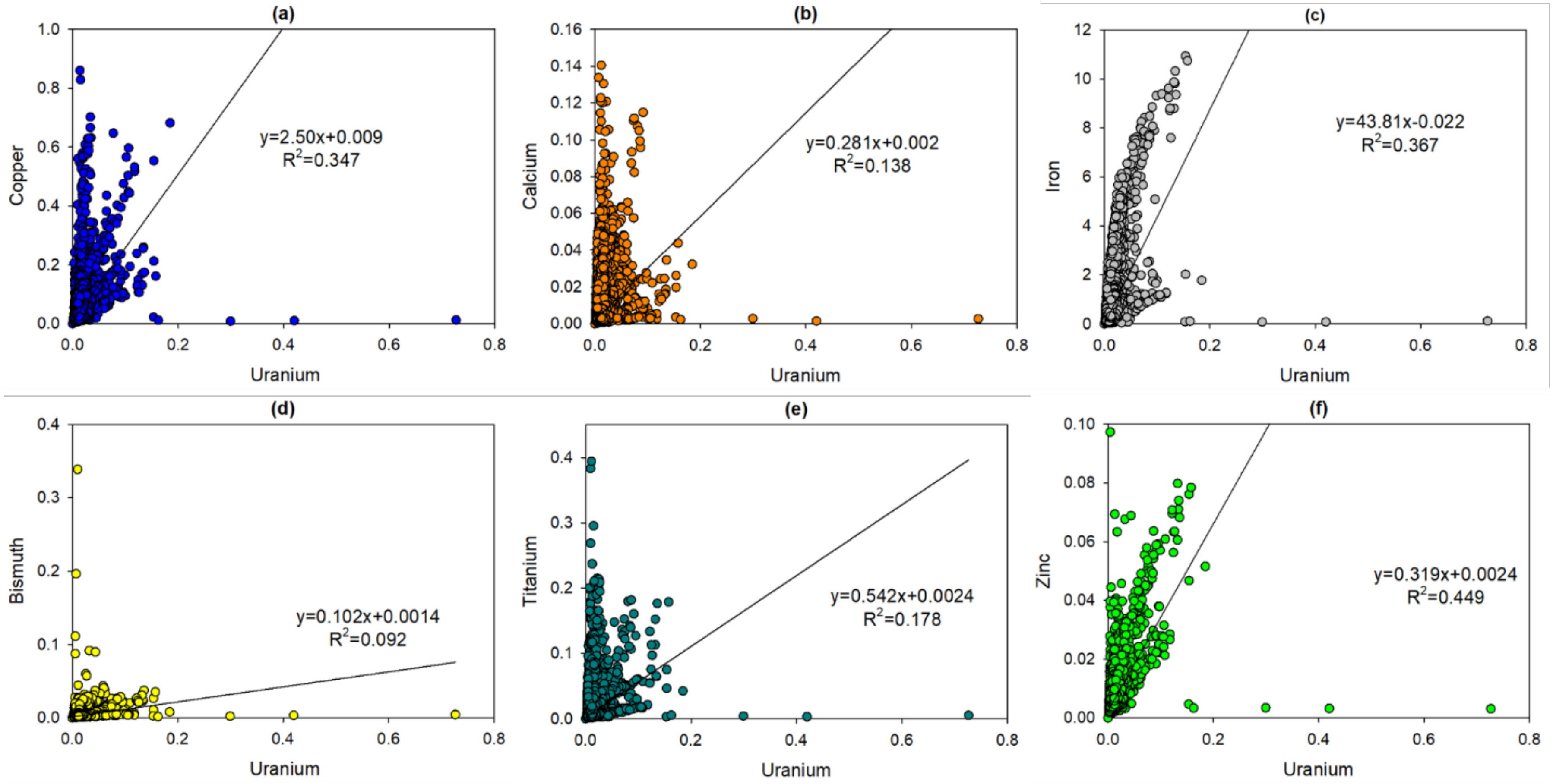

Figure E.2. μ-XRF elemental spectra correlation plots of XMP of C9667 pre-treatment (sample G3_pt2_0001) comparing uranium (x-axis) with (a) copper, (b) calcium, (c) iron, (d) bismuth, (e) titanium, and (f) zinc. All uranium signals are shown. In this pre-treatment sample, uranium is most correlated with copper (r^2=0.35), iron (r^2=0.37) n, and zinc (r^2=0.45).

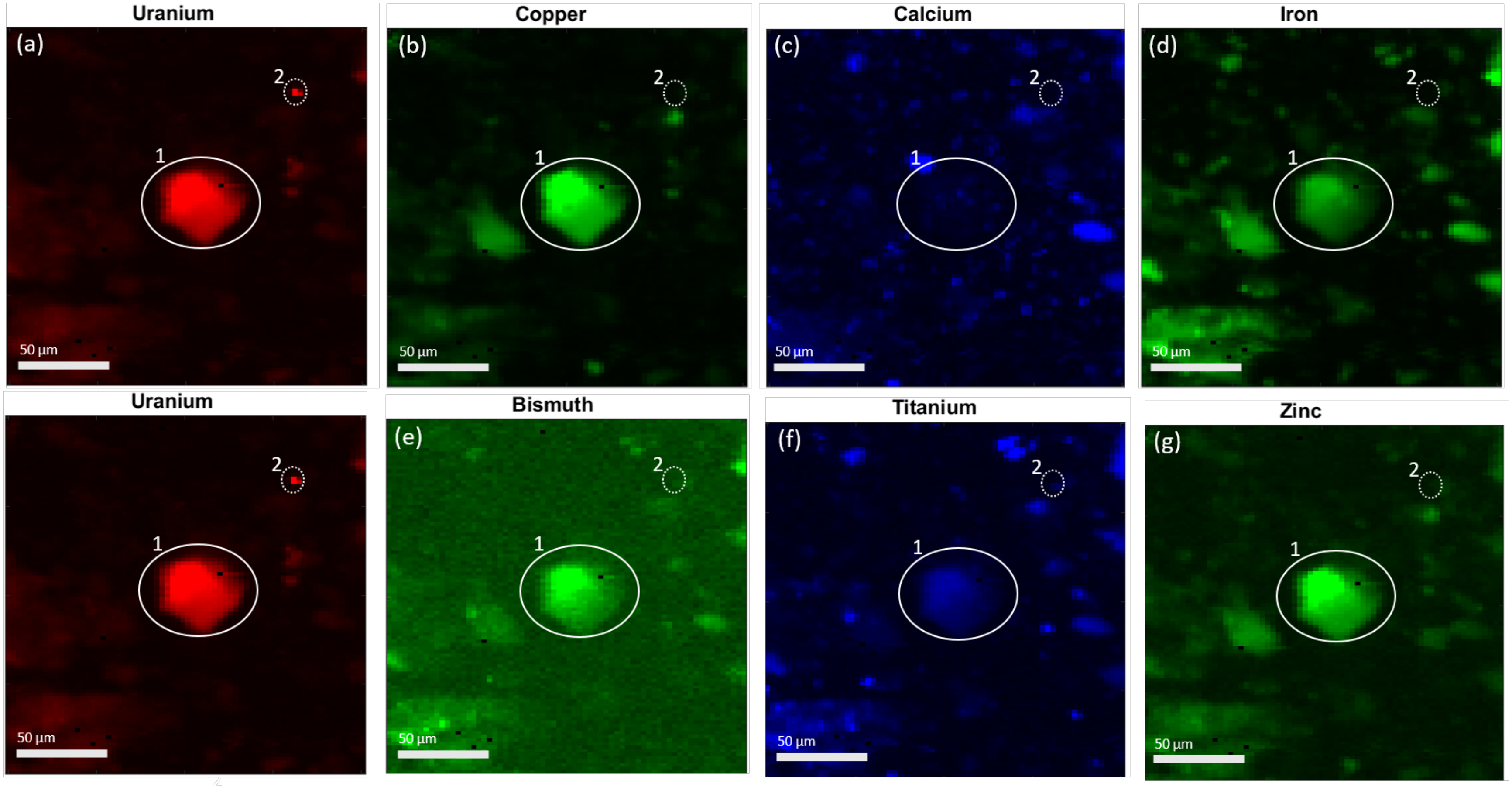

Figure E.3. µ-XRF elemental spectra of sample G3_pt2.002 for: (a) uranium, (b) copper, (c) calcium, (d) iron, (e) bismuth, (f) titanium, (g) zinc. Areas of interest are highlighted with circles 1-2. Circle 1 shows an area of high uranium that corresponds with high copper, iron, bismuth, and zinc (and potentially titanium). Circle 2 shows a small but high uranium area that does not correspond to any other elements.

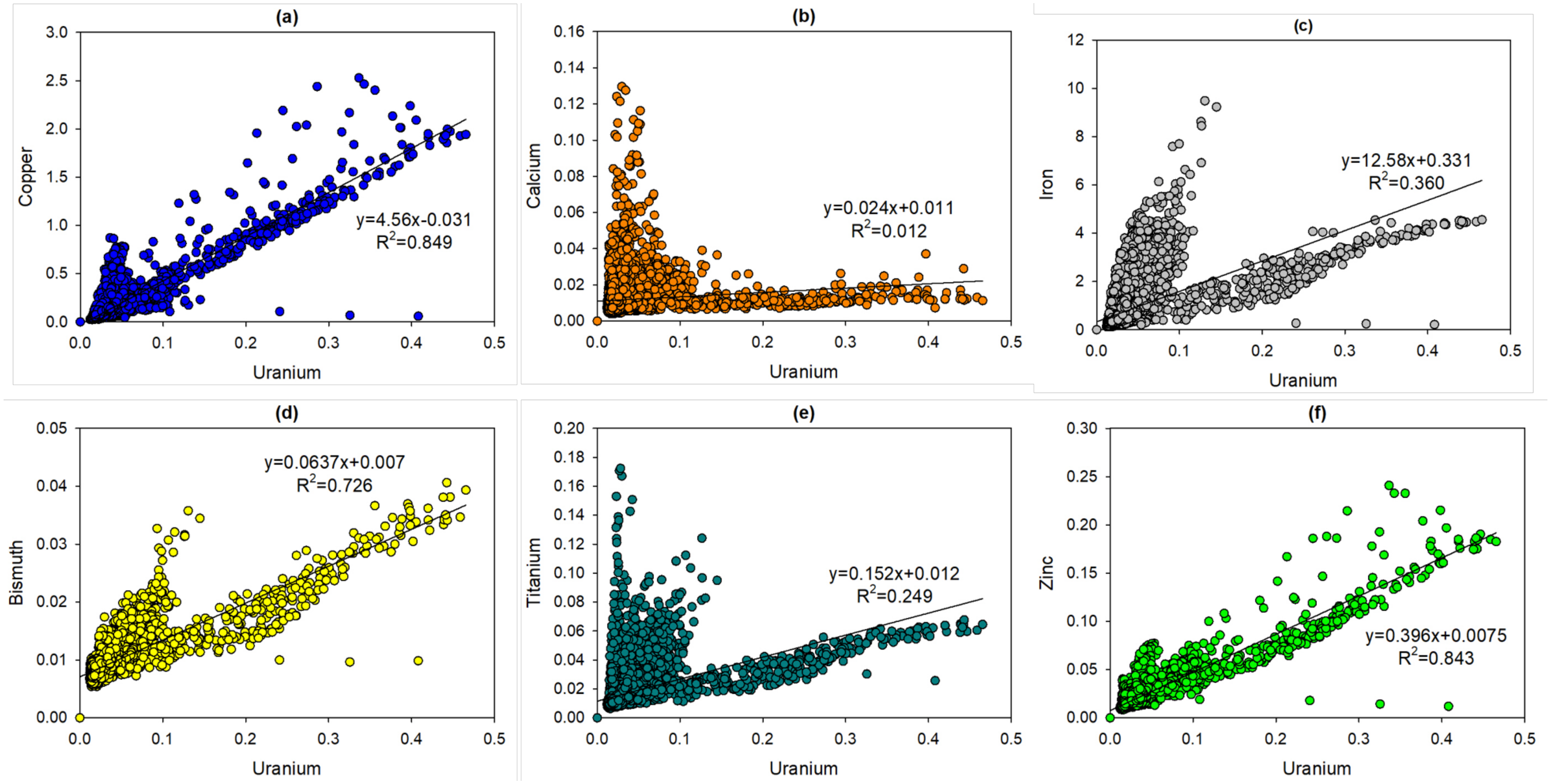

Figure E.4. µ-XRF elemental spectra correlation plots of G3_pt2.002 comparing uranium (x-axis) with (a) copper, (b) calcium, (c) iron, (d) bismuth, (e) titanium, and (f) zinc. All uranium signals are shown. Uranium shows a correlation with copper (r^2=0.85), iron (r^2=0.36), bismuth (r^2=0.73), titanium (r^2=0.25), and zinc (r^2=0.84). Iron and bismuth show two distinct correlations with uranium.

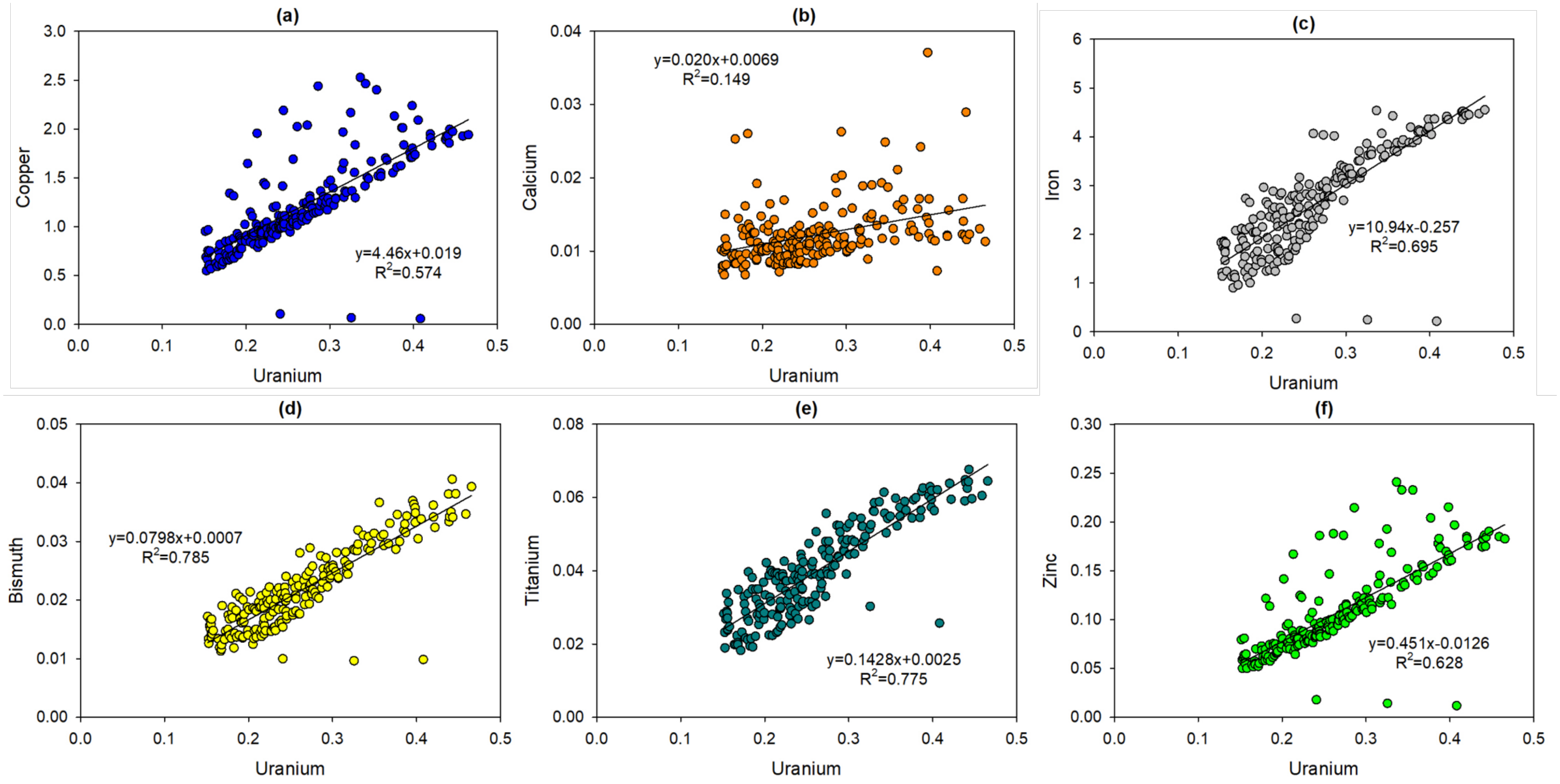

Figure E.5. µ-XRF elemental spectra correlation plots of G3_pt2.002 comparing uranium (x-axis) with (a) copper, (b) calcium, (c) iron, (d) bismuth, (e) titanium, and (f) zinc. Uranium signals above 0.15 are only shown. At higher uranium, there is a correlation with copper (r^2=0.57), iron (r^2=0.70), bismuth (r^2=0.79), titanium (r^2=0.78), and zinc (r^2=0.63).

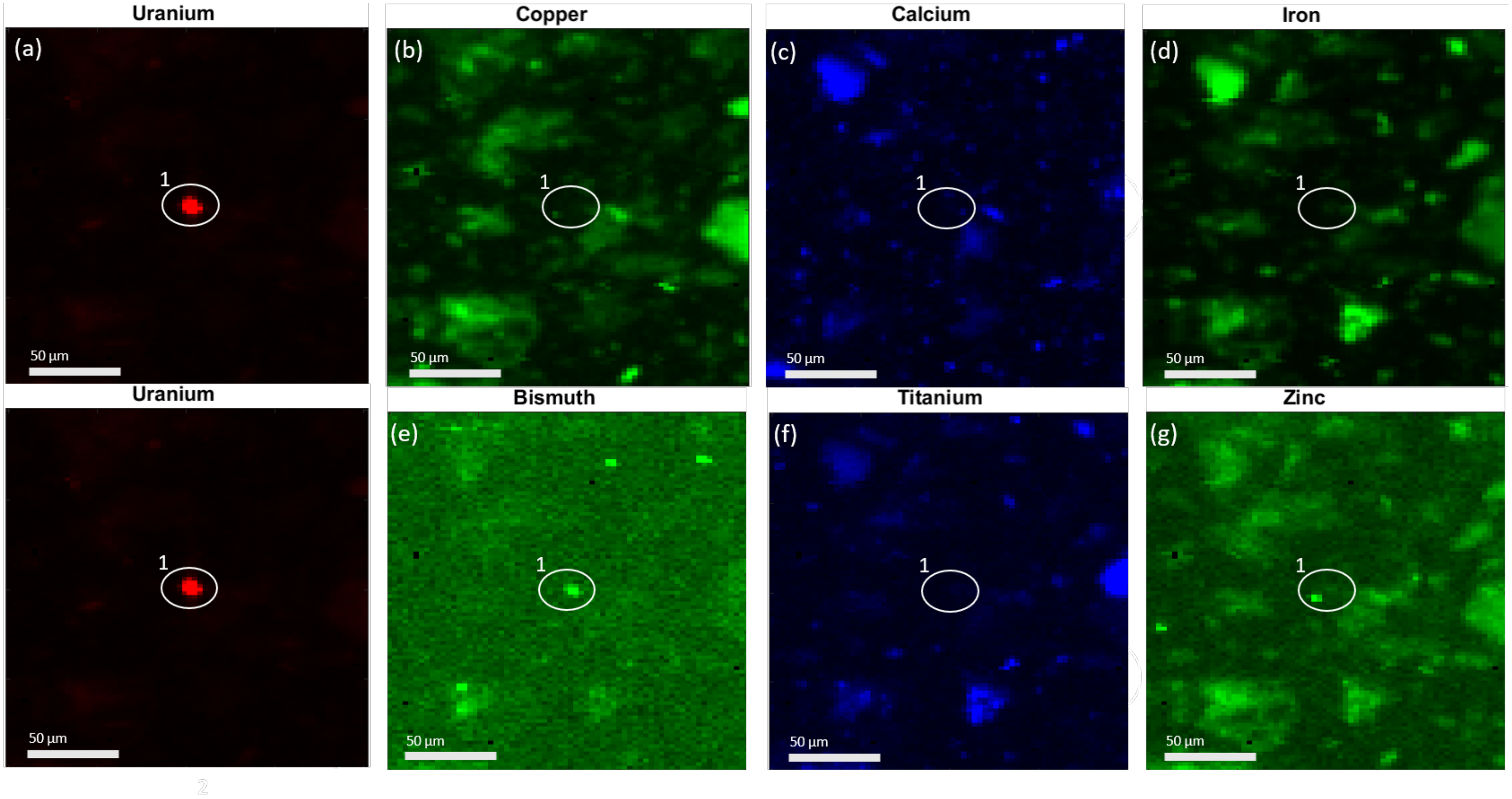

Figure E.6. µ-XRF elemental spectra of sample G3_pt2.003 for: (a) uranium, (b) copper, (c) calcium, (d) iron, (e) bismuth, (f) titanium, (g) zinc. Areas of interest are highlighted with circle 1. Circle 1 shows an area of high uranium that corresponds with high bismuth with an area of high zinc nearby.

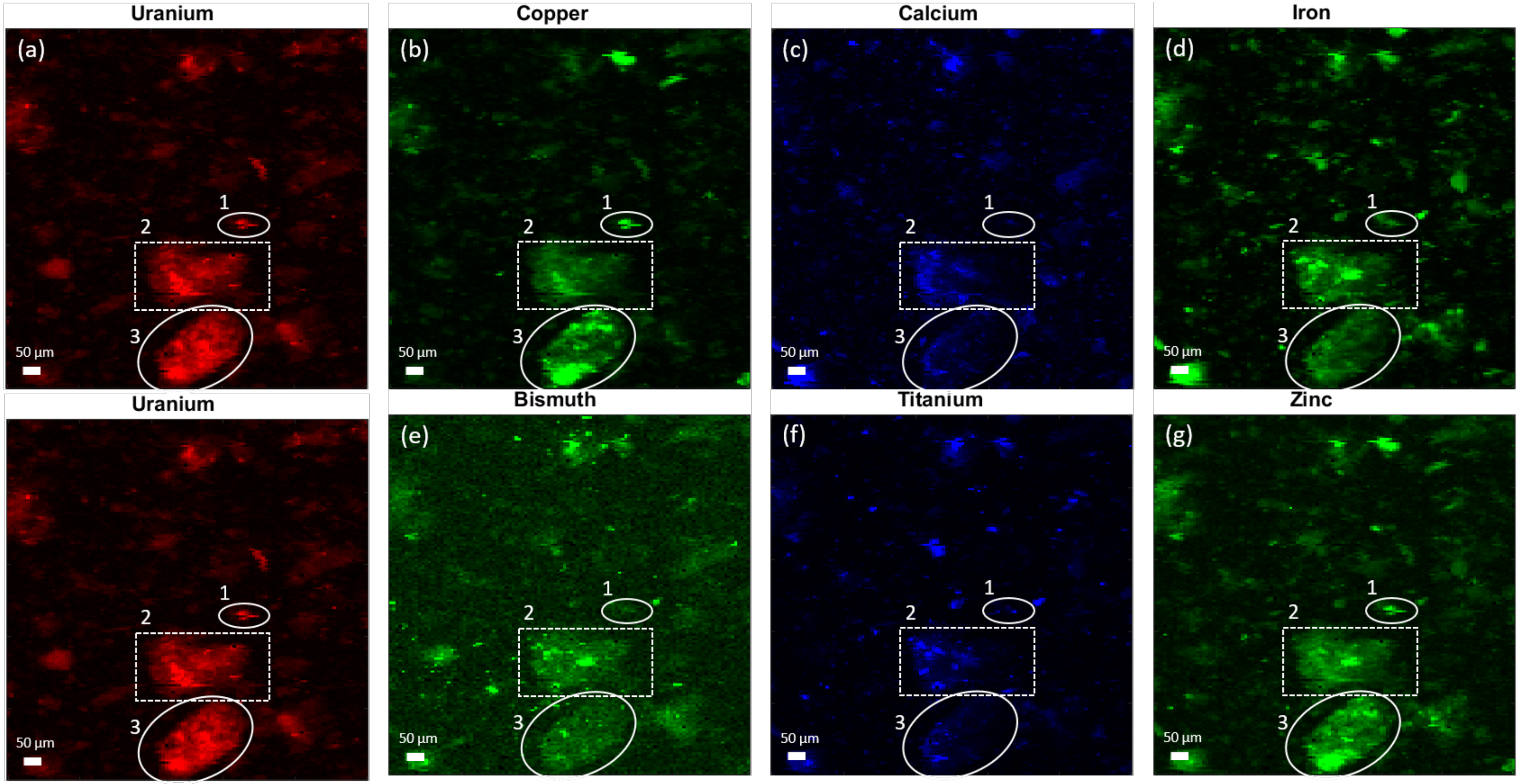

Figure E.7. µ-XRF elemental spectra of sample G3_pt2.004 for: (a) uranium, (b) copper, (c) calcium, (d) iron, (e) bismuth, (f) titanium, (g) zinc. Areas of interest are highlighted with shapes 1-3. Regions 1-3 all show an area with high uranium that is collocated with copper, iron, bismuth, and zinc with some calcium and titanium as well.

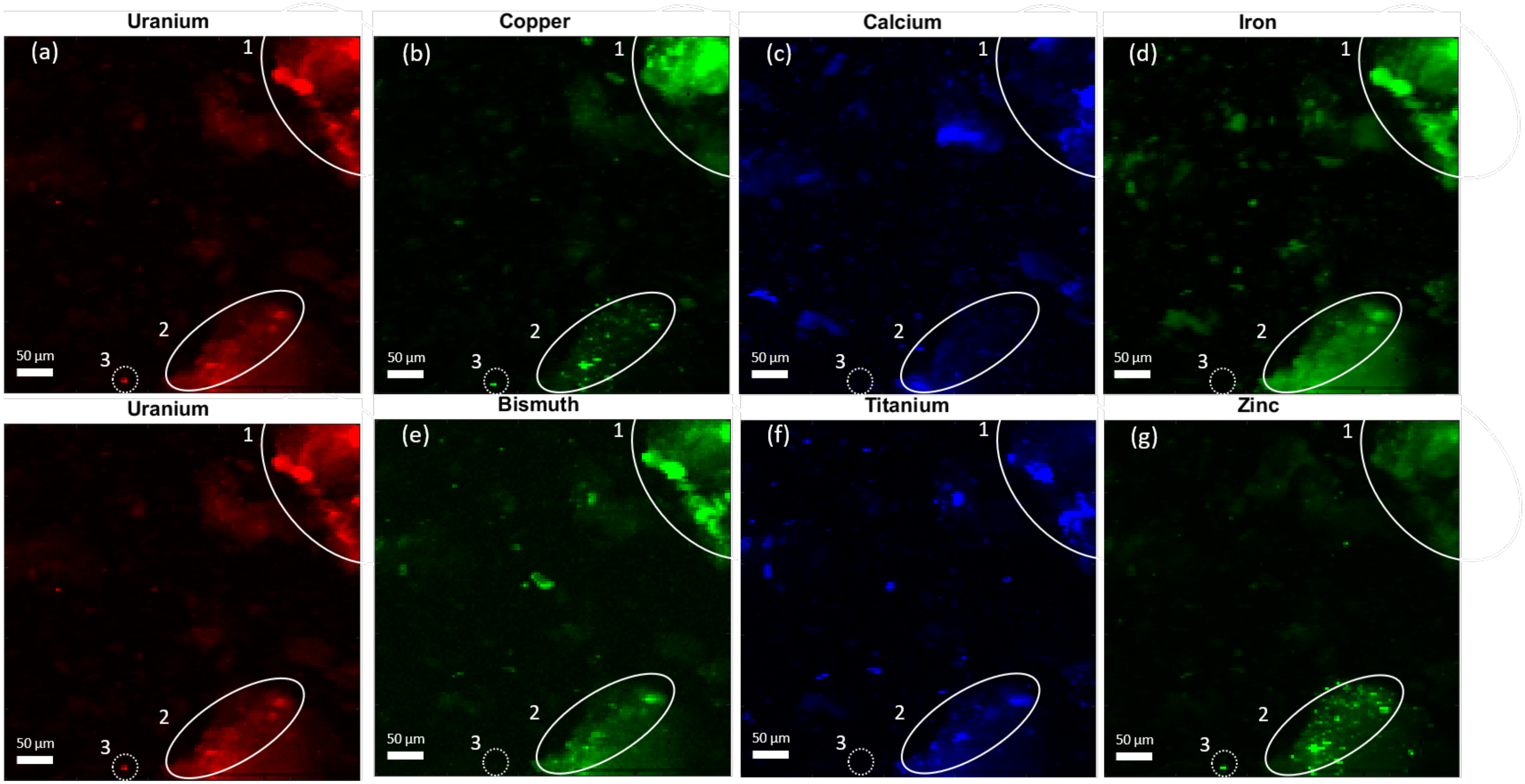

Figure E.8. µ-XRF elemental spectra of sample G4_pt2.001 for: (a) uranium, (b) copper, (c) calcium, (d) iron, (e) bismuth, (f) titanium, (g) zinc. Areas of interest are highlighted with circles 1-3. Circles 1 and 2 show an area with high uranium that is collocated with all the elements shown (i.e., copper, calcium, iron, bismuth, titanium, and zinc). Circle 3 shows a smaller uranium particle which also correlates with high copper and zinc.

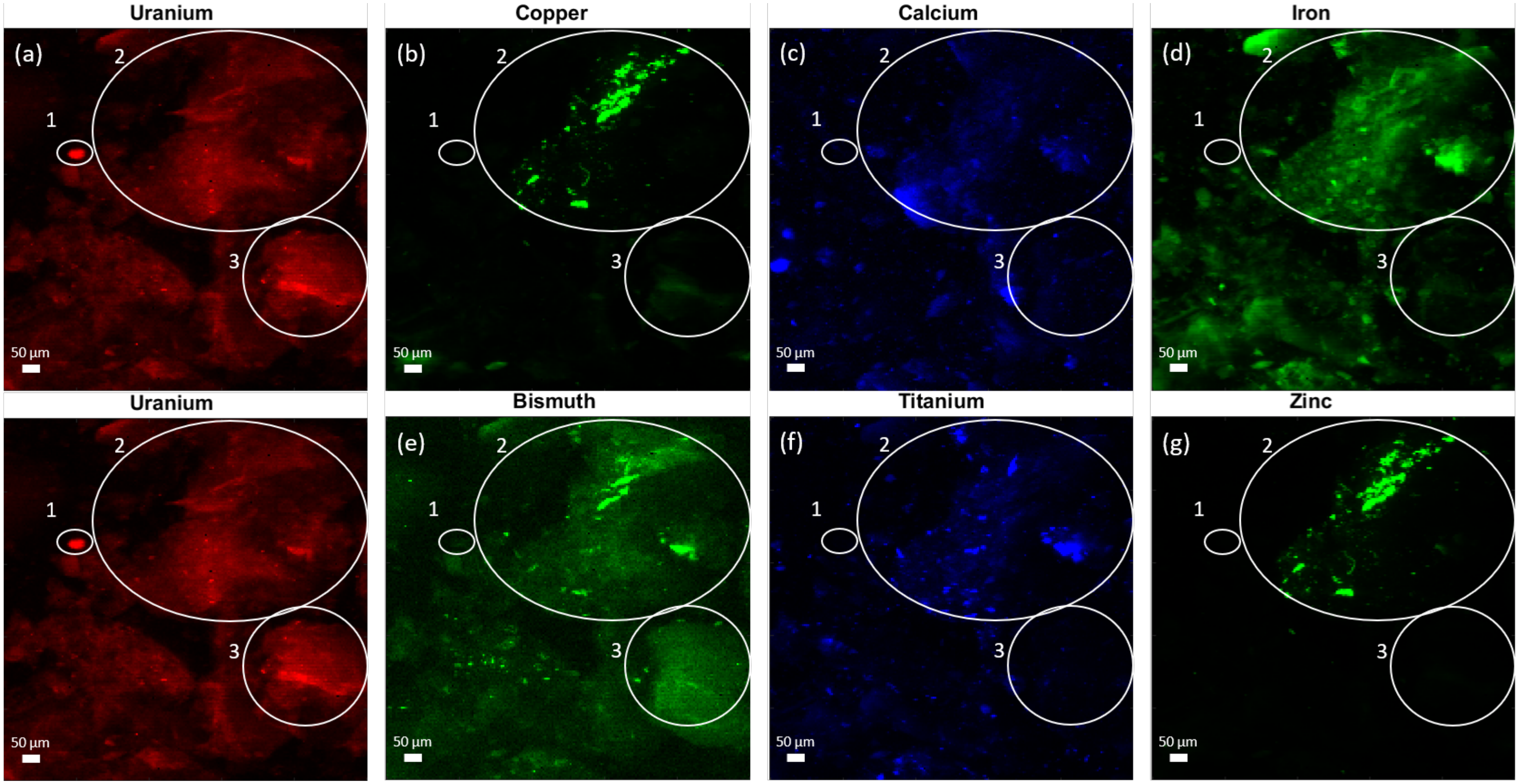

Figure E.9. µ-XRF elemental spectra of sample U_G4_001.001 for: (a) uranium, (b) copper, (c) calcium, (d) iron, (e) bismuth, (f) titanium, (g) zinc. Areas of interest are highlighted with circles 1-3. Circle 1 shows an area of high uranium that does not correspond with other elements. Area 2 indicates a larger area containing all the shown elements (Cu, Ca, Fe, Bi, Ti, and Zn) to some extent. Circle 3 shows an area containing uranium and bismuth.

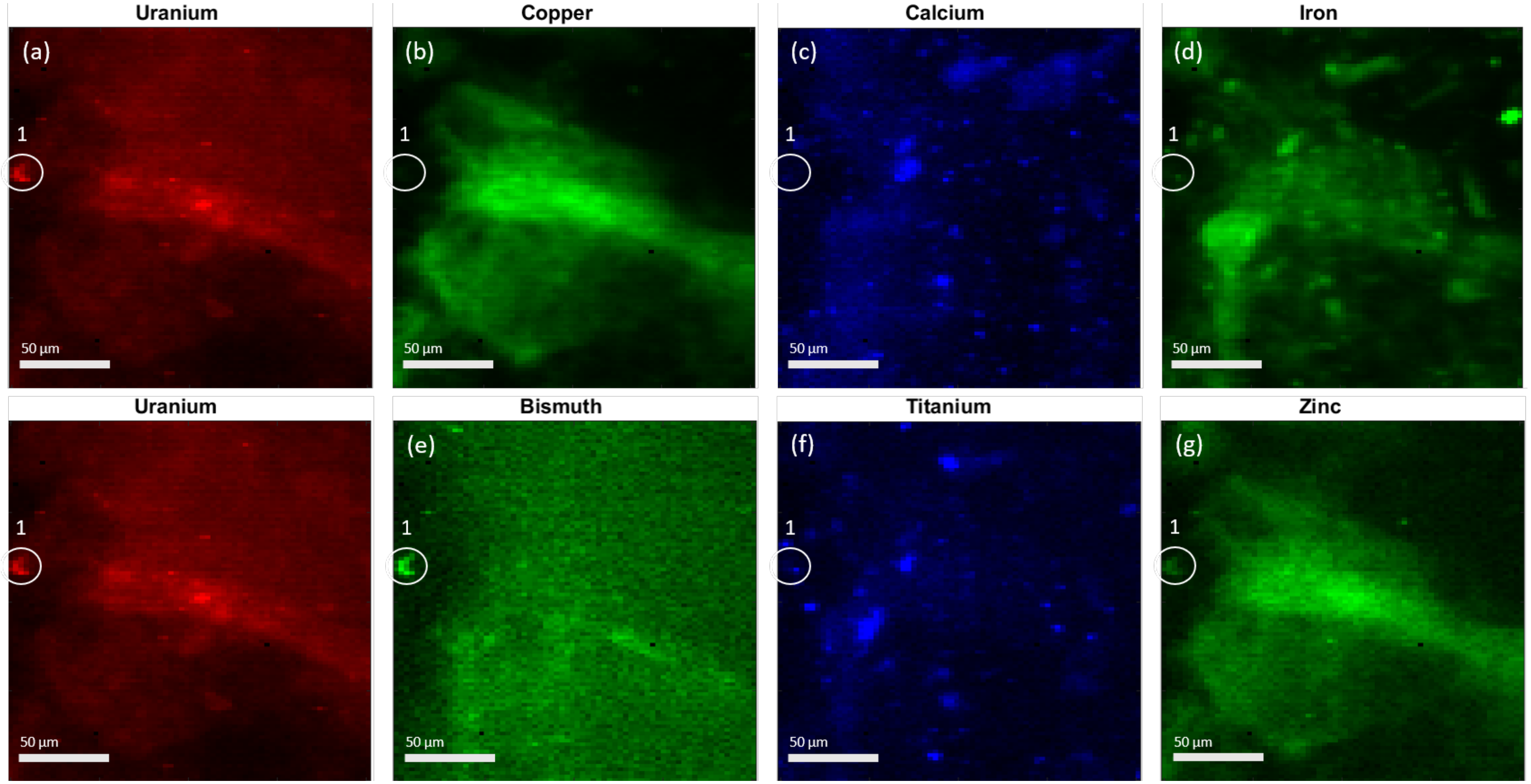

Figure E.10. µ-XRF elemental spectra of sample U_G4_002.001 for: (a) uranium, (b) copper, (c) calcium, (d) iron, (e) bismuth, (f) titanium, (g) zinc. Areas of interest are highlighted with circle 1. Circle 1 shows an area of high uranium that corresponds with high bismuth and some iron, titanium and zinc. In general, the overall distribution of uranium shows a high collocation with copper, bismuth, and zinc with some correlation with iron as well.

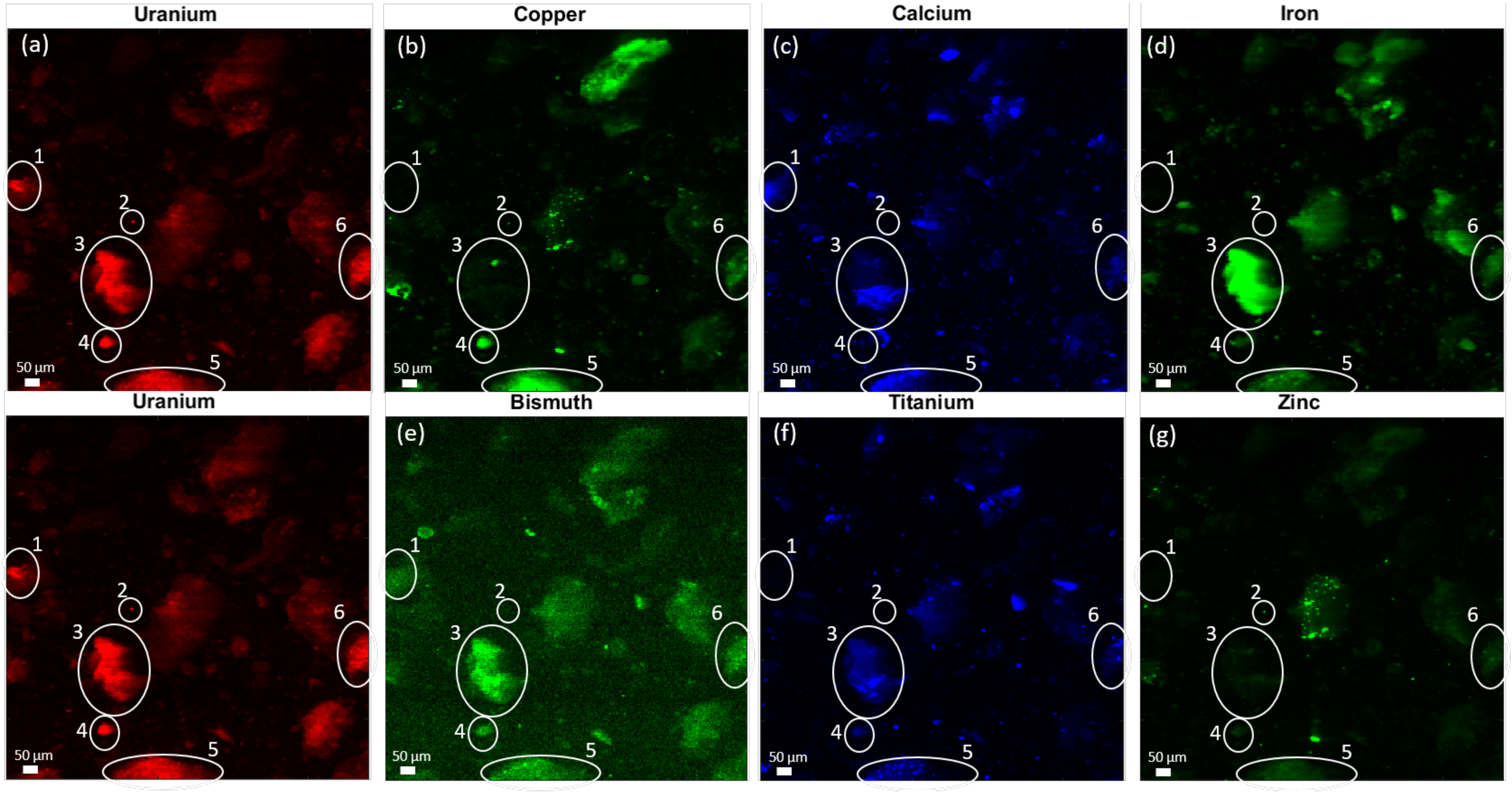

Figure E.11. μ-XRF elemental spectra of sample U_G4_004.001 for: (a) uranium, (b) copper, (c) calcium, (d) iron, (e) bismuth, (f) titanium, (g) zinc. Areas of interest are highlighted with circles 1-6. Circle 1 shows an area of high uranium that corresponds with high calcium and bismuth. Circle 2 shows a small but high uranium, cooper and zinc area. Circle 3 indicates a larger uranium region that correlates with an area of calcium, high iron, bismuth and titanium. Circle 4 shows high uranium with copper, bismuth and potentially some iron and titanium as well. Circles 5 and 6 is an area where all elements are potentially collocated.

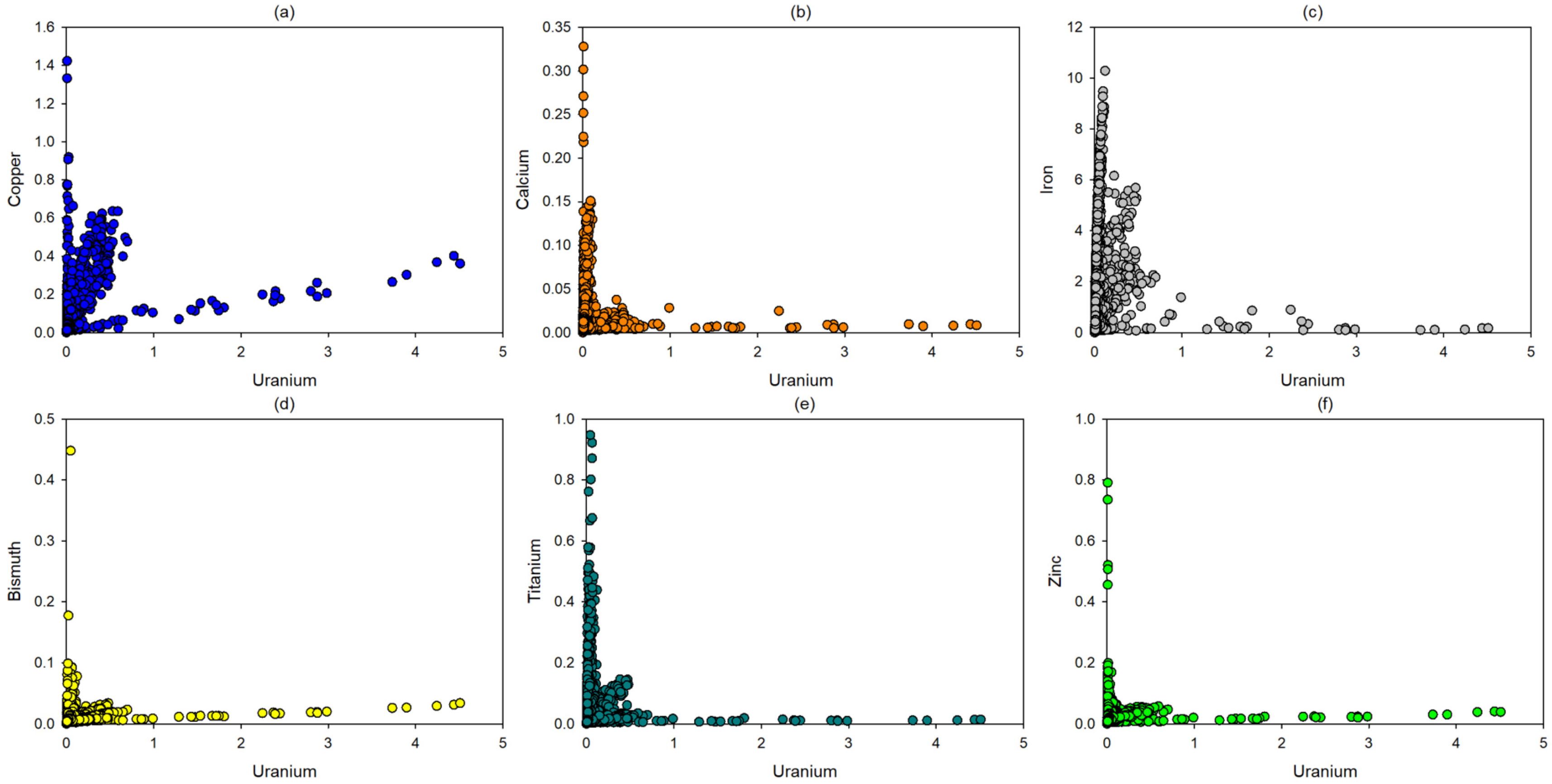

Figure E.12. Correlation plots of μ-XRF elemental spectra for sample U_G5_004.011 comparing uranium (x-axis) with (a) copper, (b) calcium, (c) iron, (d) bismuth, (e) titanium, and (f) zinc. All uranium signals are shown. At higher uranium levels, there is a correlation between uranium and copper, bismuth, titanium, and zinc.

Appendix F – Equilibrium Speciation Modeling

F.1 Uranium Speciation Modeling Methods

A geochemical equilibrium model, Geochemist's Workbench version 10 (GWB), was used to model the speciation of uranium within groundwater and remediation solutions. The Visual Minteq database that was previously converted for GWB by Jon Petter Gustafsson was used for model development with several additions to update uranium species based on new thermodynamic data as described within recent reviews (Guillamont et al. 2003; Gorman-Lewis et al. 2008, 2009). Meta-autunite and metatorbernite species were not included in the model as constants were not available, but autunite and torbernite species were included in predictions. The Davies equation was used for calculation of activity coefficients. The Davies method is applicable up to 0.7 mol/kg (Langmuir 1997) and solutions in this research are within this range. The total bicarbonate (HCO_3^-) concentration was fixed at 166 mg/L and saturated with oxygen (8.4 mg/L) in the model to represent previous groundwater measurements at the Hanford Site based on the average of 11 monitoring wells in the 100D area from 1987 to 1990 (Table F.1). Elevated concentrations of sodium, potassium, bicarbonate, and phosphate were added based on the remediation solution components included in Section 2.0 and actual delivered solution composition. Simulations were conducted where the pH varied from 6 to 8 to consider changes during apatite precipitation with Na^+ for the charge balance. Further, modeling was conducted with mineral precipitation suppressed to allow for comparison of saturation indices as Q/K (reaction quotient divided by the equilibrium constant). Then, models allowed for precipitation in order to compare equilibrium aqueous speciation. Because this modeling is not NQA-1 qualified, simulation results are for information only.

F.2 Phosphate Precipitation Modeling Methods

Batch systems were simulated using a geochemical equilibrium model (PHREEQC Interactive 3.5.0.14000) that was developed by the U.S. Geological Survey with the standard database. The model included the components from a second geochemical equilibrium model (GWB) with the additional equilibration with a partial pressure of $10^{-2.8}$ carbon dioxide gas, which is similar to air ($10^{-3.4}$) but slightly saturated as has been observed at the Hanford Site previously. As with the GWB model, precipitation was allowed and the pH changed as precipitation occurred. In subsequent model runs, precipitation was suppressed to calculate saturation indices. In addition, calcium was added to the system in two different ways: (1) as a variable content of calcite, up to 0.1%; and (2) as aqueous calcium, which may adsorb or exchange from local minerals, up to 50 mg/L.

F.2.1 Input Parameters for Uranium Modeling

Table F.1. Delivered versus targeted concentrations of major cations and anions (mmol/L). Note: the pH fluctuated in the groundwater between approximately 6.5 and 8.0, high bicarbonate may reduce U adsorption due to strong complexation (*delivered* is based on median values measured during injection by CH2M Hill Plateau Remediation Company, CHPRC).

Species	Delivered	Targeted
Ca^{2+}	0.4	-
HCO_3^-	60	-
K^+	45	39
Mg^{2+}	0.6	-
Na^+	113	88
PO_4^{3-}	87.3	87

Table F.2. Speciation modeling inputs (in mmol/L) for Figure 4.42 simulation in GWB with a slide of the ratio of phosphate to bicarbonate beginning with actual injection solution (based on skid 1 and 2 median values across injection period as provided by CHPRC) with an assumed U and Cu concentration.

Species	Delivered (mmol/L)
Ca^{2+}	0.4
Cl^{-}	0.6
HCO_3^{-}	60
H_4SiO_4	0
K^{+}	45
Mg^{2+}	0.6
Na^{+**}	113
O_2(aqu)*	8.4*
PO_4^{3-}	87.3
SO_4^{2-}	0
UO_2^{2+}*	1.0*
Cu^{2+}*	1.0*

Table F.3. Speciation modeling inputs (in mmol/L) for Figure 4.43 simulation in GWB with a slide of the amount of copper in order to compare the Cu:Ca ratios beginning with the targeted injection solution components mixed with groundwater with an assumed U and Cu concentration.

Species	Input (mmol/L)
Ca^{2+}	1.36
Cl^{-}	0.65
HCO_3^{-}	2.72
H_4SiO_4	0.26
K^{+}	3.30
Mg^{2+}	0.55
Na^{+**}	65.0
O_2(aqu)*	8.4*
PO_4^{3-}	70.0
SO_4^{2-}	0.69
UO_2^{2+}*	1.0*
Cu^{2+}*	1.0*

Table F.4. Change in pH and saturation indices (Q/K) for hydroxyapatite following equilibration of groundwater and remediation solution with variable calcite content (by mass).

SI	Calcite (%)	pH	Charge balance (% error)
11.86	0.1	7.73	-0.62
7.66	0.01	7.54	-0.63
<0	0.001	7.5	-0.63

Table F.5. Change in pH and saturation indices (Q/K) for hydroxyapatite following equilibration of groundwater and remediation solution with variable aqueous calcium.

Ca (mg/L)	pH	SI
50	5.37	16.16
35	6.474	15.36
25	6.826	14.6
10	7.211	12.56
5	7.348	11.03
1	7.468	7.52

F.2.2 Thermodynamic database for modeling of uranium

The neutral calcium – uranyl – carbonate species [$Ca_2UO_2(CO_3)_3$] was modified based on previous work (Kalmykov and Choppin 2000; Bernhard et al. 2001; Dong and Brooks 2006). This neutral species was first reported in literature by Bernhard et al. (1996). Additional complexes for ternary uranyl carbonate complexes with alkaline earth metals were also included based on previous work (Dong and Brooks 2006). Notably, the $MgUO_2(CO_3)_3^{-2}$ species was added based on Dong and Brooks (2006) as it was absent from the original database. It should be noted that the neutral calcium – uranyl – carbonate species measured by Kalmykov and Choppin, Dong and Brooks, and Bernhard et al. are all within the experimental error of each other with the $\text{Log}\beta_{213}$ = 29.8±0.7, 30.7±0.05, and 30.55±0.25, respectively. In addition, several uranyl hydroxide and uranyl carbonate species were added or updated based on the OECD NEA update and confirmed by the THEREDA and PSI/NAGRA database updates with only minor differences (Guillamont et al. 2003; Thoenen et al. 2014; Richter et al. 2015).

Although several researchers have previously investigated the thermodynamic properties of the becquerelite [$Ca(UO_2)_6O_4(OH)_6(H_2O)_8$] solid based on the review by Gorman-Lewis et al. (2008), there is still a significant error between measurements (> 6 log units for the K_{sp}). However, Richter et al. (2015) confirmed the suggested value from Guillamont et al. (2003) based on a new study (Gorman-Lewis et al. 2008). Therefore, it is included in the database. Metaschoepite was also included in the database but replaced the schoepite species based on its similarity to the schoepite species from the OECD NEA update (Guillamont et al. 2003; Gorman-Lewis et al. 2008). Further, the species measured in these works are better defined as metaschoepite (Guillamont et al. 2003; Richter et al. 2015).

The most recent thermodynamic data added to the database includes several uranium silicate and oxide minerals. The values for K-boltwoodite, uranophane, and coffinite were added based on recent research (Shvareva et al. 2011; Szenknect et al. 2016). Shvareva et al. (2011) also measured parameters for Na-boltwoodite, which were within the error of the previous value reported in the updated OECD NEA database (Guillamont et al. 2003). Therefore, these values for K-boltwoodite and uranophane are expected to be accurate measurements. K-boltwoodite and uranophane are common uranyl silicates in oxidizing conditions and have been previously identified in the Hanford vadose zone where uranium waste was historically released (Catalano et al. 2004; Um et al. 2010).

The uranophane K_{sp} replaced the highly variable measurements previously summarized by Gorman-Lewis et al. (2008). Further, the coffinite K_{sp} value from Szenknect et al. (2016) is an important addition because it has been reported in many reducing, low-temperature aquatic systems (Guo et al. 2015). Szenknect et al. (2016) reported a standard free energy of formation for coffinite of -1862.3 ± 7.8 kJ/mol, which compares well with the previously measured values ranging from -1872 ± 6 to -1886 ± 6 kJ/mol (Langmuir 1978; Grenthe et al. 1992; Guo et al. 2015). In addition, the size of the coffinite grains used in the study are considered representative of coffinite in nature and as an alteration product of spent nuclear fuel (Szenknect et al. 2016).

Alwan and Williams (1980) previously measured the dissolution of swartzite and liebigite. The authors did not state whether or not the solids were checked for stability and it was assumed but not confirmed that dissolution of major cations was stoichiometric (Gorman-Lewis et al. 2008). Therefore, these data were not selected for the OECD database (Guillamont et al. 2003). However, it is included in some of the simulations in this work for comparison.

Uranium phosphate phases were added or updated based on recent reviews (Gorman-Lewis et al. 2008, 2009). Although saleeite and torbernite were currently included in the initial database, autunite was updated. It should be noted that solubility measurements for the sparingly soluble uranyl phosphate minerals are difficult and are generally conducted under high ionic strength and acidic conditions, therefore, the extrapolation to infinite dilution at neutral pH is challenging. Van Haverbeke et al. (1996) previously measured $LogK_{sp}$ for chernikovite at pH 1 to 2.2 with pre and post solid phase characterization. This value was chosen based on previous reviews and its use by collaborators (Gorman-Lewis et al. 2008; Mehta 2017), although it differs from other reviews (Guillamont et al. 2003). The updated uranyl orthophosphate and autunite values are based on both solubility (from supersaturated and undersaturated conditions) and drop-solution calorimetry measurements up to pH 4.5 (Gorman-Lewis et al. 2009).

Table F.6. Aqueous Species Additions to the Database at 25°C and 0 M ionic strength

Species	Reaction	LogK	Reference
$(UO_2)_{11}(CO_3)_6(OH)_{12}^{-2}$	$(UO_2)_{11}(CO_3)_6(OH)_{12}^{-2} + 12H^+ = 6CO_3^{-2} + 12H_2O$	-36.39	Guillamont et al. 2003
$CaUO_2(CO_3)_3^{-2}$ [(a)]	$CaUO_2(CO_3)_3^{-2} = UO_2^{+2} + 3CO_3^{-2} + Ca^{+2}$	-27.18	Dong and Brooks 2006; Richter et al. 2015
$MgUO_2(CO_3)_3^{-2}$	$MgUO_2(CO_3)_3^{-2} = Mg^{+2} + UO_2^{+2} + 3CO_3^{-2}$	-26.11	Dong and Brooks 2006; Richter et al. 2015
$UO_2(OH)_4^{-2}$ [(a)]	$UO_2(OH)_4^{-2} + 4H^+ = UO_2^{+2} + 4H_2O$	31.92	Guillamont et al. 2003; Richter et al. 2015
$UO_2(SO_4)_2^{-2}$ [(a)]	$UO_2(SO_4)_2^{-2} = UO_2^{+2} + 2SO_4^{-2}$	-4.14	Guillamont et al. 2003
$UO_2(CO_3)_{(aqu)}$ [(a)]	$UO_2(CO_3)_{(aqu)} = UO_2^{+2} + CO_3^{-2}$	-9.94	Guillamont et al. 2003

(a) Species is altered from previous database and does not represent entirely new additions.

*

Table F.7. Solid Species Additions to the Database at 25°C and 0 M ionic strength

Species	Reaction	$\mathrm{LogK_{sp}}$	References
Andersonite	$Na_2CaUO_2(CO_3)_3(H_2O)_6 = Ca^{+2} + 3CO_3^{-2} + 6H_2O + 2Na^+ + UO_2^{+2}$	-37.9	Alwan and Williams 1980; Gorman-Lewis et al. 2008
Autunite[(a)]	$Ca(UO_2)_2(PO_4)_2 11H_2O = 2UO_2^2 + 2PO_4^{3-} + Ca^{+2} + 11H_2O$	-48.36	Gorman-Lewis et al. 2008; 2009
Bayelite	$Mg_2UO_2(CO_3)_3(H_2O)_{18} = 3CO_3^{-2} + 18H_2O + 2Mg^{+2} + UO_2^{+2}$	-36.6	Alwan and Williams 1980; Gorman-Lewis et al. 2008
Becquerelite	$Ca(UO_2)_6O_4(OH)_6(H_2O)_8 + 14H^+ = 6UO_2^{+2} + Ca^{+2} + 18H_2O$	40.5	Guillamont et al. 2003; Richter et al. 2015
Cejkaite	$Na_4UO_2(CO_3)_3 = UO_2^{+2} + 3CO_3^{-2} + 4Na^+$	-27.18	Guillamont et al. 2003; Richter et al. 2015
Chernikovite	$UO_2HPO_4(H_2O)_4 = H^+ + UO_2^{2+} + PO_4^{3-} + H_2O$	-22.73	Gorman-Lewis et al. 2008; VanHaverbeke et al. 1996; Mehta 2017
Clarkeite	$NaUO_2O(OH) + 3H^+ = UO_2^{+2} + Na^+ + 2H_2O$	12.2	Richter et al. 2015
Coffinite	$USiO_4 + 4H^+ = H_4SiO_4 + U^{+4}$	5.246	Guillamont et al. 2003; Richter et al. 2015; Szenknect et al. 2016
Grimselite	$NaK_3UO_2(CO_3)_3(H_2O) = H_2O + 3CO_3^{-2} + 3K^+ + Na^+ + UO_2^{+2}$	-37.1	Gorman-Lewis et al. 2008
Compreignacite	$K_2U_6O_{19}11H_2O + 14H^+ = 6UO_2^{+2} + 2K^+ + 18H_2O$	37.1	Sandino and Grambow 1994; Guillamont et al. 2003
K - boltwoodite	$KUO_2(SiO_3OH)(UO_2)H_2O + 3H^+ = H_2O + K^+ + H_4SiO_4 + UO_2^{+2}$	4.12	Shvareva et al. 2011; Richter et al. 2015
Na - boltwoodite	$NaUO_2(SiO_3OH)(UO_2)H_2O + 3H^+ = H_2O + Na^+ + H_4SiO_4 + UO_2^{+2}$	6.07	Shvareva et al. 2011; Richter et al. 2015
Liebigite	$Ca_2UO_2(CO_3)_3(H_2O)_{10} = 2Ca^{+2} + 3CO_3^{-2} + 10H_2O + UO_2^{+2}$	-36.9	Alwan and Williams 1980; Gorman-Lewis et al. 2008
Metaschoepite[(a)]	$UO_3(H_2O)_2 + 2H^+ = UO_2^{+2} + 3H_2O$	5.8	Bruno and Sandino 1988; Meinrath and Kimura 1993; Sandino and Grambow 1994; Meinrath et al. 1996; Giammar and Hering 2004; Gorman-Lewis et al. 2008; Richter et al. 2015
Saleeite[(b)]	$Mg(UO_2)_2(PO_4)_2 10H_2O = 2UO_2^{2+} + 2PO_4^{3-} + Mg^{2+} + 10H_2O$	-43.65	-
Soddiyite	$(UO_2)_2SiO_4 2H_2O + 4H^+ = 2UO_2^{+2} + H_4SiO_4 + 2H_2O$	6.09	Gorman-Lewis et al. 2008
Swartzite	$CaMg(UO_2)(CO_3)_3 12H_2O = Ca^{+2} + 3CO_3^{-2} + 12H_2O + Mg^{+2} + UO_2^{+2}$	-37.9	Alwan and Williams 1980; Gorman-Lewis et al. 2008
Torbernite[(b)]	$Cu(UO_2)_2(PO_4)_2 12H_2O = 2UO_2^{2+} + 2PO_4^{3-} + Cu^{2+} + 12H_2O$	-45.28	--
Uranophane	$Ca(UO_2)_2SiO3(OH)_2 5H_2O + 6H^+ = Ca^{+2} + 5H_2O + 2H_4SiO_4 + 2UO_2^{+2}$	10.82	Shvareva et al. 2011
Uranyl orthophosphate	$(UO_2)_3(PO_4)_2 4H_2O = 3UO_2^{2+} + 2PO_4^{3-} + 4H_2O$	-49.36	Gorman-Lewis et al. 2008; 2009; Mehta 2017

(a) Species is altered from previous database and does not represent entirely new additions.
(b) Previously included in database but shown for comparison.

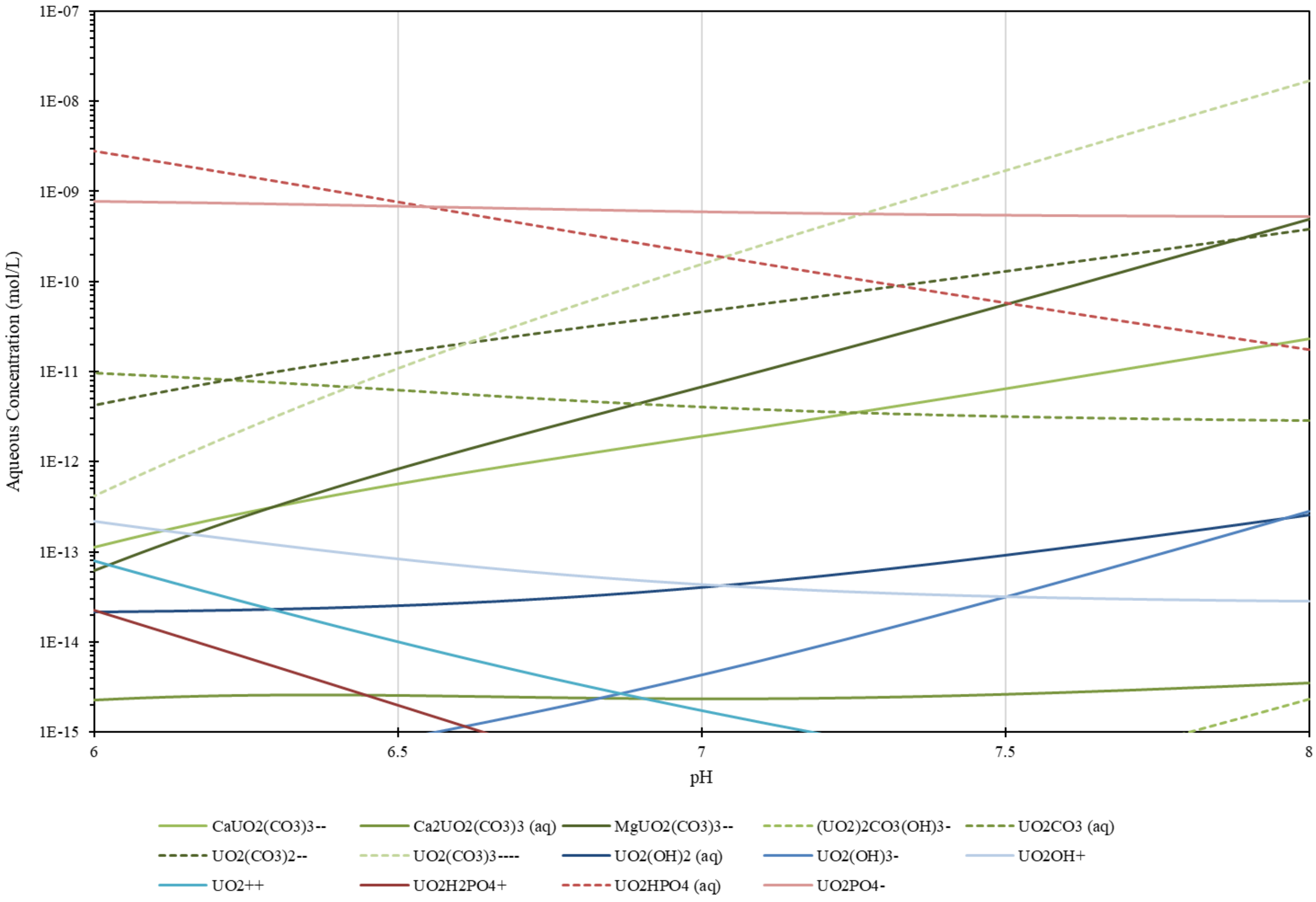

Figure F.1. Aqueous U speciation with pH in remediation solution mixed with groundwater as predicted by GWB with U-carbonate species (*dashed green lines*), Ca/Mg-U-carbonate species (*solid green lines*), U-O/OH species (*blue lines*), and U-phosphate species (*solid red lines*), Note: only select complexes present at concentrations greater than 1 × 10^{-15} mol/L are shown.

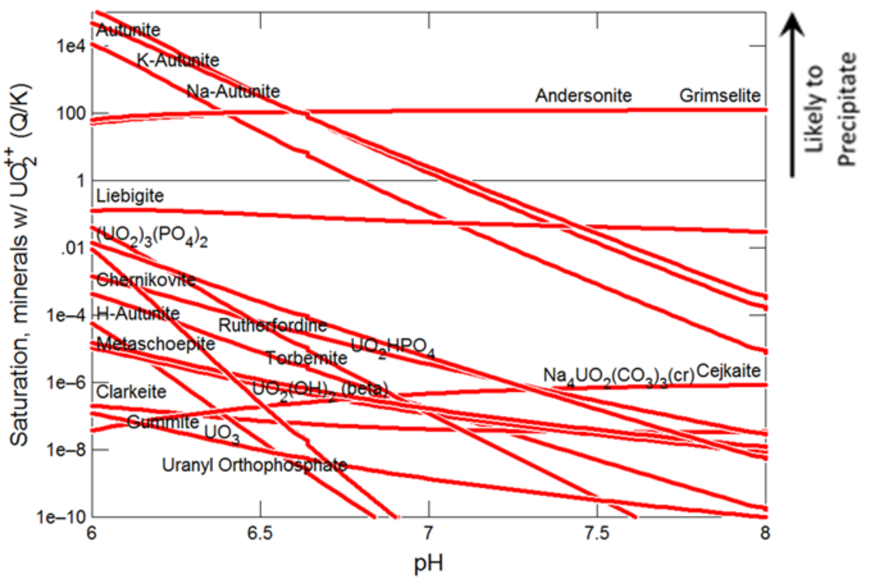

Figure F.2. Thermodynamic favorability of U solid phases based on actual injection solution as described in E.2

F.3 References

Alwan, A., and P. Williams. 1980. The aqueous chemistry of uranium minerals. Part 2. Minerals of the liebigite group. Mineralogical Magazine. 43, 329, 665-667.

Bernhard G, G Geipel, V Brendler, and H Nitsche. 1996. “Speciation of uranium in seepage waters of a mine tailing pile studied by time-resolved laser-induced fluorescence spectroscopy (TRLFS).” *Radiochimica Acta* 74(s1):87-92.

Bernhard G, G Geipel, T Reich, V Brendler, S Amayri, and H Nitsche. 2001. “Uranyl (VI) carbonate complex formation: Validation of the Ca_2UO_2 $(CO_3)_3$ (aq.) species.” *Radiochimica Acta International Journal for Chemical Aspects of Nuclear Science and Technology* 89(8/2001):511.

Bruno, J. and Sandino, A.1988. The solubility of amorphous and crystalline schoepite in neutral to alkaline aqueous solutions, MRS Proceedings. Cambridge Univ Press, p. 871

Catalano JG, SM Heald, JM Zachara, and GE Brown 2004. “Spectroscopic and diffraction study of uranium speciation in contaminated vadose zone sediments from the Hanford site, Washington state.” *Environmental Science & Technology* 38(10):2822-2828.

Dong, W. and Brooks, S.C. 2006. Determination of the formation constants of ternary complexes of uranyl and carbonate with alkaline earth metals (Mg2+, Ca2+, Sr2+, and Ba2+) using anion exchange method. Environmental science & technology 40, 4689-4695.

Giammar, D.E. and Hering, J.G. 2004. Influence of dissolved sodium and cesium on uranyl oxide hydrate solubility. Environmental science & technology 38, 171-179.

Gorman-Lewis D, PC Burns, and JB Fein. 2008. “Review of uranyl mineral solubility measurements.” *The Journal of Chemical Thermodynamics* 40(3):335-352.

Gorman-Lewis D, T Shvareva, K-A Kubatko, PC Burns, DM Wellman, B McNamara, JES Szymanowski, A Navrotsky, and JB Fein. 2009. "Thermodynamic properties of autunite, uranyl hydrogen phosphate, and uranyl orthophosphate from solubility and calorimetric measurements." *Environmental Science and Technology* 43(19):7416-7422.

Grenthe, I., Wanner, H. and Forest, I. 1992. Chemical thermodynamics of uranium.

Guillamont R, T Fanghanel, I Grenthe, V Neck, D Palmer, and MH Rand. 2003. "Update on the chemical thermodynamics of uranium, neptunium, plutonium, americium, and technetium." *Chemical Thermodynamics* 5:959.

Guo X, S Szenknect, A Mesbah, N Clavier, C Poinssot, SV Ushakov, H Curtius, D Bosbach, RC Ewing, and PC Burns. 2015. "Thermodynamics of formation of coffinite, $USiO_4$." *Proceedings of the National Academy of Sciences* 112(21):6551-6555.

Kalmykov SN and GR Choppin. 2000. "Mixed Ca_2+/UO_{22}+/CO_{32}-complex formation at different ionic strengths." *Radiochimica Acta International Journal for Chemical Aspects of Nuclear Science and Technology* 88(9-11/2000):603.

Langmuir D. 1978. "Uranium solution-mineral equilibria at low temperatures with applications to sedimentary ore deposits." *Geochimica et Cosmochimica Acta* 42(6):547-569.

Mehta S. 2017. "Geochemical evaluation of uranium sequestration from field-scale infiltration and injection of polyphosphate solutions in contaminated Hanford sediments." *Applied Geochemistry* 84:133-153.

Meinrath, G., Kato, Y., Kimura, T. and Yoshida, Z. 1996. Solid-aqueous phase equilibria of uranium (VI) under ambient conditions. Radiochimica Acta 75, 159-168.

Meinrath, G. and Kimura, T. 1993. Behaviour of U (VI) solids under conditions of natural aquatic systems. Inorganica chimica acta 204, 79-85

Richter A, F Bok, and V Brendler. 2015. *Data compilation and evaluation for U (IV) and U (VI) for the Thermodynamic Reference Database THEREDA*. HZDR-065, Helmholtz-Zentrum Dresden Rossendorf, Dresden, Germany. https://inis.iaea.org/collection/NCLCollectionStore/_Public/47/081/47081518.pdf.

Sandino, M. and Grambow, B. 1994. Solubility equilibria in the U (VI)-Ca-K-Cl-H2O system: Transformation of schoepite into becquerelite and compreignacite. Radiochimica Acta 66, 37-44.

Shvareva TY, L Mazeina, D Gorman-Lewis, PC Burns, JE Szymanowski, JB Fein, and A Navrotsky. 2011. "Thermodynamic characterization of boltwoodite and uranophane: Enthalpy of formation and aqueous solubility." *Geochimica et Cosmochimica Acta* 75(18):5269-5282.

Szenknect, S, A Mesbah, T Cordara, N Clavier, H-P Brau, X Le Goff, C Poinssot, RC Ewing, and N Dacheux. 2016. "First experimental determination of the solubility constant of coffinite." *Geochimica et Cosmochimica Acta* 181:36-53.

Thoenen T, W Hummel, U Berner, and E Curti. 2014. *The PSI/Nagra Chemical Thermodynamic Database 12/07*. Nuclear Energy and Safety Research Department, Laboratory for Waste Management, Paul Scherrer Institute, Villigen PSI, Switzerland.

https://www.psi.ch/sites/default/files/import/les/DatabaseEN/PSI-Bericht%252014-04_final_druckerei.pdf.

Um, W, ZM Wang, RJ Serne, BD Williams, CF Brown, CJ Dodge, AJ Francis. 2009. "Uranium phases in contaminated sediments below Hanford's U tank farm. *Environmental Science and Technology* 43(12):4280-4286.

Van Haverbeke L, R Vochten, and K Van Springel. 1996. "Solubility and spectrochemical characteristics of synthetic chernikovite and meta-ankoleite." *Mineralogical Magazine* 60(402):759-766.

Pacific Northwest
National Laboratory

902 Battelle Boulevard
P.O. Box 999
Richland, WA 99354
1-888-375-PNNL (7665)

www.pnnl.gov